Title
THE EFFECTS OF METAL PROMOTION ON THE ADSORPTIVE AND CATALYTIC PROPERTIES OF RHODIUM

Author
Levin, M.E.

Publication Date
1987-12-01

Center for Advanced Materials

CAM

The Effects of Metal Promotion on the Adsorptive and Catalytic Properties of Rhodium

M.E. Levin
(Ph.D. Thesis)

December 1987

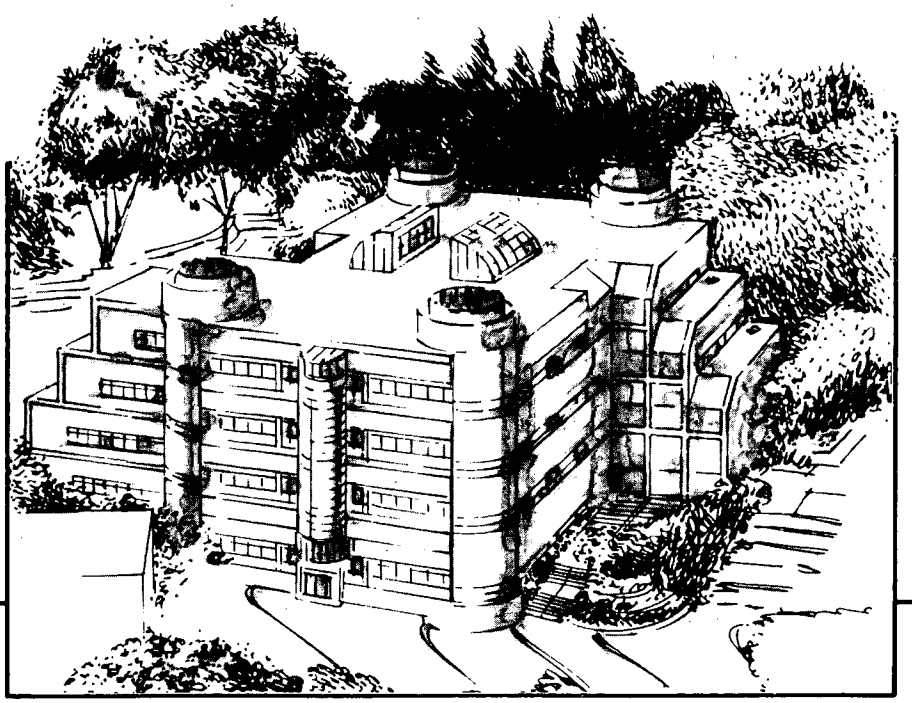

Materials and Chemical Sciences Division

Lawrence Berkeley Laboratory • University of California

ONE CYCLOTRON ROAD, BERKELEY, CA 94720 • (415) 486-4755

Prepared for the U.S. Department of Energy under Contract DE-AC03-76SF00098

DISCLAIMER

LBL-24050

The Effects of Metal Promotion on the Adsorptive and Catalytic Properties of Rhodium

Marc Eliott Levin

(Ph.D. Thesis)

Materials and Chemical Sciences Division
Lawrence Berkeley Laboratory
and Department of Chemistry
University of California
Berkeley, CA 94720

This work was supported by the Office of Basic Energy Sciences, Chemical Sciences Division of the US Department of Energy under Contract DE-AC03-76SF00098.

ABSTRACT

The properties of rhodium with alumina and titania overlayers have been studied to understand the influence of the support oxides in the analogous alumina- and titania-supported catalysts. Aluminum and titanium were deposited on a rhodium foil in ultra-high vacuum and subsequently oxidized. Characterization of the deposits with Auger electron spectroscopy (AES) and x-ray photoelectron spectroscopy (XPS) showed the oxides to be nearly stoichiometric with overlayer growth occurring through the Stranski-Krastanov mechanism (*i.e.*, two-dimensional growth until completion of the monolayer). AES and XPS analysis also showed the titania to be more easily reduced by H_2 or CO at elevated temperatures than was the alumina. Alumina overlayers were found to diminish both CO chemisorption and the activity for atmospheric-pressure CO hydrogenation in direct proportion to the coverage. Titania caused a much sharper suppression in the CO chemisorption capacity (compared with alumina) while enhancing the CO hydrogenation rate at low coverages. The higher rates were accompanied by dramatic changes in the kinetic parameters and hydrocarbon selectivity. Ethylene hydrogenation and ethane hydrogenolysis activities, though, were sharply suppressed by the presence of titania. Titania is believed to exist as two-dimensional islands on the Rh surface at submonolayer coverages. XPS results indicate that Ti^{3+} species appear to populate the perimeter of these oxide islands. These Ti^{3+} species at the oxide perimeter may influence the properties of and the chemical processes taking place at Rh atoms at the oxide/metal interface. The suppression of CO chemisorption when titania is present has been described by a model in which CO does not chemisorb at Rh sites underneath as well as alongside these islands, while an ensemble of Rh and Ti atoms at the oxide/metal interface (along the island perimeter) has been used to model the enhancement in CO hydrogenation rate.

Contents

List of Figures

List of Tables

ACKNOWLEDGEMENTS

This work would not have been possible without the assistance, direction, and support given by those around me. A complete list of the people who have contributed to this research and to my own education would be far too long to present here. Instead, I would like to acknowledge those who have had the most noticeable influence. Among those who have had the most direct impact on this work are the members of the Somorjai and Bell research groups. The wealth of information available from the diverse background of people provided a stimulating environment for doing scientific research. Among those who deserve special mention for enriching my environment here are: (from the Somorjai Group) Dr. Ugo Bardi (thanks(?) for the chamber and the car), (Dr.) Te-Hua Lin, Dr. W.T. Tysoe, (Dr.) Randy Yeates, (Dr.) Mark "Jackson" Logan, (Dr.) Andy Gellman, Dr. Simon Bare, (Dr.) Brian Bent, (*Dr.) Tom "Buck" Rucker, (*Dr.) David Godbey, (*Dr.) Mike Hilton, (*Dr.) José Carrazza, (*Dr.) Gerard Vurens, and (**Dr.) Dan "Tuna" Strongin; (from the Bell Group) (Dr.) Jeff Rieck, (Dr.) Rich Underwood, and (*Dr.) Grant Yokomizo. Tom and Dave deserve recognition for their patience while getting me started on this stupid computer. I would also like to thank Dr. Kevin Ogle for his instruction in the operation of the XPS chamber and to ***Kevin "Cal" Williams for his patience while he "learned the ropes (cables?)" of the UHV chamber. It was quite rewarding to help train someone who always wanted to understand why things behave as they do.

The support staff of the Materials and Molecular Research Division (MMRD) in Bldg. 62 (LBL)deserve special thanks, especially Glenn Baum, James Wu, John Holthuis, Hank Brendel, Jim Severns, Sandy Stewart, Keith Franck, and Dan Colomb. Their efforts made it possible to keep the UHV chamber in operation or, at least, to minimize the down-time. This in turn lessened the frustration historically associated with this UHV chamber and was essential in making this project productive.

I have been quite fortunate to work for two brilliant professors who complement each other so well. I am grateful to Prof. Gabor Somorjai whose insight and creativity are responsible for this project's existence. His ability to view a problem from an entirely dif-

ferent perspective has always inspired me and I hope that I have acquired some of this talent. His refusal to accept limits in pursuing research has made it a pleasure to work in this outstanding research group. Prof. Alex Bell always provided the guidance and stimulus for performing meaningful experiments. His skill for analyzing problems, interpreting results, and developing conclusions with unmatched precision added a strong foundation to our work. In addition, it was his suggestion of pursuing the route of depositing oxide overlayers—a direction which brought with it much successs.

I am deeply indebted to Miquel Salmeron for his never-ending pursuit to understand the fundamental processes taking place in the system under study. His approach to understanding these processes or to resolving problems was refreshing. Conversations with Miquel were always enlightening, no matter what the subject. Those of us who have had the chance to work with him are truly fortunate.

Finally, I wish to express my deep appreciation to my dear friend Tsun-Tsun Tsai and especially to my loving parents. Their continuous encouragement and support gave me the strength to persevere in this project and complete this thesis.

*soon to arrive, with some luck

**not quite as soon as *

***well, ready for the exam

Chapter 1

INTRODUCTION

In recent years, much attention has been devoted to the study of interactions between catalyst metals and their oxide supports. In particular, it has been found that when Group VIII metals (such as Pt, Rh, or Ni) are supported on easily reducible oxides (*e.g.*, TiO_2, V_2O_5, Nb_2O_5), a number of dramatic changes in the morphological, chemisorptive, and catalytic properties take place. A description of the phenomena that have been observed due to "metal-support interaction" and the approaches that have been taken to understand them is now presented.

1.1 HISTORICAL DEVELOPMENT

The catalyst support has traditionally been considered an inert carrier on which the catalyst could be dispersed. By employing a high surface area support, the more valuable catalyst metal is used more effectively than would be the case if there were no support due to the high metal surface-to-volume ratio. A high degree of oxide surface area per support particle volume is also provided and for oxides, the highly porous structure is stable at temperatures where many metals would sinter. These features have often been the design

criteria of oxide supports while the effect on the catalytic properties of the metal have been chiefly overlooked.

This view of the role of the support changed with investigations of the chemical reactivity of metals supported on doped oxides. In the late 1950's, Schwab and co-workers studied the decomposition of formic acid on Al_2O_3-supported Ni where the support was doped with BeO, NiO, TiO_2, GeO_2, or left undoped [1,2,3]. Their results showed a 6 kcal/mole decrease in activation energy for Ni/Al_2O_3 (20.5 kcal/mole) compared with that of Ni alone (26.5 kcal/mole). The addition of tetravalent n-type dopants to the Al_2O_3 was found to increase slightly the activation energy while divalent p-type dopants diminished it. In the case of NiO-doped alumina, an activation energy of just 7.0 kcal/mole was displayed.

During the same time period, this reaction was also studied by Solymosi and co-workers for Ni supported on various semiconductor oxides (TiO_2, Cr_2O_3, and NiO) [4,5,6]. Doping of the TiO_2 and variation of the reduction temperature of the Ni/TiO_2 catalyst were found to strongly influence the catalytic behavior. The influence of NiO on Ni was similarly found to depend on the concentration of positive holes in the NiO. These observations were regarded as evidence of an electronic interaction taking place between the metal and support.

During the next two decades, work continued in monitoring the catalytic properties of metals on doped supports with an emphasis on relating these properties to electrical conductivity behavior [3,6,7]. Changes in the activation energy of CO oxidation were observed for the catalysts in the reverse configuration: metals supporting oxides [3].

Intensive investigation on a wider scale did not occur until the emergence and application of more sophisticated tools capable of monitoring conditions on the surface of the catalyst. In addition, the discovery of metal-support systems and pretreatment conditions that yield reproducible dramatic changes in the chemisorptive properties of the metal provided the spark for innumerable investigations elsewhere.

1.2 CHEMISORPTION PROPERTIES

The influence of the TiO_2 support on the adsorption of CO and H_2 on Group VIII metals has been studied by Tauster and co-workers [8]. They found that after a 473 K H_2 reduction, the H/M and CO/M adsorbate-to-metal ratios were similar to those for the Al_2O_3-supported metals (generally between 0.2 and 1.2). Upon a high temperature reduction (HTR) at 773 K, these ratios decreased markedly, with nearly all ranging between 0 and 0.05. Agglomeration of the metal due to the 773 K reduction treatment was ruled out by x-ray diffraction and transmission electron microscopy (TEM) studies. Oxidation followed by low temperature reduction returned the samples to their original chemisorption behavior.

A subsequent study was performed to evaluate the effect of reduction treatments for Ir supported on various oxides. Tauster and Fung [9,10] showed that H_2 chemisorption could be suppressed by as much as two orders of magnitude when TiO_2, Nb_2O_5, V_2O_3, and Ta_2O_5 supports were used. Only weak dependences ($\leq$factor of 3) were observed when SiO_2, Al_2O_3, Sc_2O_3, HfO_2, MgO, ZrO_2, and Y_2O_3 were the supports and only after more extreme reduction conditions ($773K \leq T_{red} \leq 973$ K). They were also able to correlate the degree of suppression exhibited to the reducibility of the metal oxide; more easily reduced support oxides result in a greater degree of interaction.

Another contribution to the literature by Tauster *et al.* was the term "strong metal-support interaction" or "SMSI". Unfortunately, this terminology has since been applied to virtually any observed effects that could be attributed to the support. The result is a polarized approach to understanding this global "interaction" by numerous researchers whereas, in reality, several different mechanisms may be involved. This term will not be employed in subsequent discussion.

The suppression of H_2 and CO chemisorption on TiO_2-supported metals has been confirmed in other studies [11,12,13,14,15,16,17,18]. A gradual uptake of hydrogen has been noted for Ni and Pt supported on TiO_2 [19] and for Ni on SiO_2 and Al_2O_3 [20] indicating

spillover of adsorbed hydrogen onto the support. A suppression of NO chemisorption has also been observed [21] for Pt/TiO_2 while O_2 chemisorption is reported to be unaffected on TiO_2-supported Ni [11]. Besides pointing to an interaction between the metal and support, the implication of the diminished H_2 and CO chemisorption capacity is that these techniques can no longer be applied to measure the active catalyst surface area in a meaningful manner.

1.3 CATALYTIC BEHAVIOR

Although many of the pioneering studies of metal-support interaction focused on formic acid decomposition [1,2,4,5,7], attention has turned recently toward other reactions which are more closely associated with the formation or restructuring of hydrocarbons. In one particular reaction, CO hydrogenation to form methane and other hydrocarbons, enhancements in activity occur when TiO_2 is the support [13,14,16,22,23,24]. This is observed even when the reaction rate per metal atom is calculated on a basis of 100% dispersion (which is done since the actual exposed metal surface area cannot be determined from the usual chemisorption techniques, as explained above) . This enhancement has been attributed to the reaction taking place at the metal/metal oxide interface where the oxygen of CO is associated with the metal oxide and the carbon with the catalyst metal [14,24]. No conclusive evidence for this has been presented in the literature although this scheme is quite plausible. It should be emphasized that higher rates are seen despite the lower amount of chemisorbed CO. Also, these rates appear to be relatively independent of the pre-reduction treatment [17,22,24,38].

An analogous reaction, reduction of NO by H_2 and CO, has been studied with various support oxides. The reduction of NO by CO over TiO_2-supported Rh, Pt, and Pd catalysts was shown to be higher than on the SiO_2- and Al_2O_3-supported catalysts [25,26,27,28]. The order of activity for NO reduction over rhodium with various oxide supports was

$Rh/TiO_2 \gtrsim Rh/La_2O_3 \approx Rh/SiO_2 \gtrsim Rh/MgO \approx Rh/Al_2O_3$ when CO was the reducing agent and $Rh/TiO_2 \gtrsim Rh/Al_2O_3 \geq Rh/La_2O_3 \gtrsim Rh/SiO_2 \geq Rh/MgO$ when H_2 was used [28]. No appreciable changes in selectivity toward the principal products, N_2O and N_2, were detected among the oxides. Distinctly different rate parameters for the TiO_2-supported catalyst were also found.

Whereas CO hydrogenation was promoted on TiO_2-supported catalysts, the support does not appear to have a significant impact on hydrocarbon hydrogenation reactions, except after high temperature reduction. Mériaudeau *et al.* [12]. observed near order-of-magnitude decreases in rate after HTR for benzene, ethylene and styrene hydrogenation, as well as for cyclohexane dehydrogenation. The catalysts employed were TiO_2-supported Pt, Ir, and Rh. In contrast, for a Ni/TiO_2 catalyst after the HTR treatment, Burch and Flambard [23] found only a slight change in activity for benzene hydrogenation as compared with a Ni/SiO_2 catalyst prepared under similar conditions.

Another class of reactions which has received much attention is the hydrogenolysis of hydrocarbons. Those hydrocarbons most often studied include ethane, n-butane, and n-hexane. In all cases, after HTR of the TiO_2-supported noble metals, the hydrogenolysis activity was sharply suppressed [12,14,23,24,29], sometimes as much as 3–4 orders of magnitude [30]. Ethane hydrogenolysis over a Ni/Nb_2O_5 catalyst was also suppressed after HTR [31]. While the Ni/TiO_2 catalyst shows a much diminished activity after HTR, the activation energy, after successively higher treatments, drops by nearly 20% [14], but still lies in the range of values observed for unsupported and SiO_2-supported Ni [32,33]. The activation energy of the Ni/Nb_2O_5 catalyst remained virtually unchanged after HTR. For ethane hydrogenolysis over Rh/TiO_2, the HTR treatment does not alter the ethane order, but does raise the H_2 order from -2.3 to -1.6 [29]. An analogy was drawn in this last study between Group VIII–Group IB (*e.g.*, Cu, Ag) alloys and the Group VIII-TiO_2 interaction.

1.4 THE NATURE OF THE METAL/METAL OXIDE INTERFACE

The preceding discussion clearly demonstrates the dependence of the chemisorptive and catalytic behavior on the support oxide employed. To understand these effects, other aspects of these systems must be probed. A thermodynamic driving force exists for the interaction of the Group VIII metals with oxides such as TiO_2, V_2O_3, Nb_2O_5, and ZrO_2. As proposed by Brewer [34], overlap of the partially filled d-orbitals of elements in Groups IIIB-VB with the nearly-filled orbitals of the Pt metals may lead to alloys of extraordinary stability between these elements. This was indeed verified and as a case in point, the Gibb's energy of formation for the alloy $ZrPt_3$ was determined to be -30 $\pm$2 kcal/g-atom at 1800 K [35]. Meschter and Worrell [36] calculated the Gibbs' energy of formation for Pt_3Ti and Pt_8Ti at 1150 K to be -17.8 kcal/g-atom and -8.20 kcal/g-atom, respectively.

The oxides of the Group III-VB metals will have a lower valence electron density around the cation and so the overlap of the vacant d-orbitals with those for the Pt metals will be favored even more. The extra bonding provided by the overlap of electrons results in the driving force for interaction between the catalyst metal and support oxide. Also, the oxides that take part in this alloying are not as thermodynamically stable as, say, alumina or silica, and as mentioned in Section 1.2. the more easily reduced oxides were the ones observed to interact the most with the Pt metals.

Several features of the Pt/TiO_2 system were revealed by the molecular orbital calculations of Horsley [37]. First of all, the removal of some of the oxygen anions was necessary for bonding to occur. Titania alone is not easily reduced, but in the presence of a metal capable of dissociatively chemisorbing H_2, the reduction is facilitated [12,39,40,41]. Due to the occurrence of Magnelli phases (composition T_nO_{2n-1}), partial reduction of TiO_2 is certainly feasible from a thermodynamic standpoint, while complete reduction to Ti metal is quite difficult. The formation of Ti_4O_7 on TiO_2-supported Pt upon HTR has been observed by electron diffraction [39,42]. Reduction to Ti_3O_5, however, requires a radical reorganization

of the oxide structure [10].

The calculations of Horsley also incorporated the bonding from the Brewer-Engels interaction, but this turned out to be minor, though, compared with an ionic interaction due to charge transfer from the reduced cation to the adjacent Pt atom. From his work, a charge transfer equivalent to 0.6 electron/Pt atom was determined. Several attempts have been made to experimentally quantify the amount of charge transfer by use of x-ray photoelectron spectroscopy (XPS). In some cases, an additional charge of as much as 0.6 electron/Pt atom for $Pt/SrTiO_3$ was found [43]. For other systems, 0.2 electron/Rh atoms for Rh/TiO_2 [40], 0.13 electron/Ni atom for Ni/TiO_2 [44], and 0.1 electron/Pt atom for Pt/TiO_2 [45] were identified, but the validity of these values rests strongly on the accounting of relaxation effects. Particularly, for Ni/TiO_2, the relaxation shift is much larger than the derived charge transfer making the amount of transfer statistically insignificant.

Other XPS studies have resulted in no observable charge transfer [46], while electrical conductivity measurements seem to indicate that it does occur [47]. It has been argued that for large metal particles with the particle-support boundary comprising the metal/metal oxide interface, that the charge transfer would have an insignificant effect on the properties of the metal compared with the "sea" of delocalized electrons [29,48]. In summary, too many conflicting reports regarding charge transfer have appeared to draw any firm conclusions.

As an attempt to compare the properties of the supported metal systems with the corresponding alloys, experiments have been carried out to characterize the chemical behavior of Brewer-Engels–type alloys. Bardi *et al.* [49] found that the high temperature (530 K) CO desorption peak from Pt is absent on a polycrystalline Pt_3Ti alloy. They also noted a shift to lower temperatures of the 430 K peak of Pt. CO desorption from Pt_3Ti (100) and Pt_3Ti (111) also exhibited lower desorption temperatures than on the analogous Pt single crystals. Oxidation of the polycrystalline Pt_3Ti led to a nearly complete suppression of CO chemisorption and was associated with formation of TiO_2 on the surface. The chemisorption of H_2 on the Pt_3Ti alloy is also suppressed with respect to Pt.

1.5 MORPHOLOGY OF THE METAL/METAL OXIDE SYSTEMS

While the electron transfer studies taken together provide no conclusive results, transmission electron microscopy (TEM) studies show clear-cut changes in the morphology of metal particles on TiO_2 films after HTR. Baker *et al.* [42] observed that hemispherical Pt particles flatten into thin "pill-box" structures after HTR, while portions of the support were reduced to Ti_4O_7. This did not take place for Pt supported on Al_2O_3, SiO_2, and carbon films. After subsequent treatment of the reduced Pt particles in oxygen, the particles retained their hexagonal shape, but grew in thickness. The "pill-box" structure was not observed for Rh/TiO_2 or Ir/TiO_2 after HTR [12].

When silver was supported alone on titania and reduced, no changes in morphology of the silver particles or of the crystal structure of the support occurred. Addition of Pt to this system followed by HTR, though, resulted in both Ag and Pt particles assuming the thin, "pill-box" structures and the conversion of the TiO_2 support to Ti_4O_7 [41]. Platinum evidently acts a supplier of H atoms which facilitates the reduction of the support with wetting by the metal particles eventually taking place.

Many of the efforts already described have focused on fundamental changes taking place between metal and oxide upon activation of the oxide. Small metal particles ($\leq$50 Å) are able to form new bonds or to restructure so as to increase the amount of metal/metal oxide contact. In this way, a high percentage of the surface metal atoms will be affected. In relatively large particles ($\geq$ 160 Å), where similar modifications of the chemisorption and catalytic properties occur [54], the amount of metal/metal oxide contact compared to the number of surface metal atoms would be much smaller. It is also unlikely that electronic effects taking place at a metal/metal oxide interface will have any impact on metal atoms far removed (greater than several atomic distances) from this interface [29,48,50,51,52].

To explain the suppression of CO chemisorption and other effects when large metal particles are supported on TiO_2, it has been proposed that reduced titania species may migrate

onto the surface of the metal particles [53]. Though "encapsulation" of the metal particles was originally discounted [8,12], there has been ample evidence in recent years to support this mechanism. Haller and Resasco [29] observed a decrease in the ethane hydrogenolysis rate of Rh/TiO_2 that was linearly proportional to the square-root of reduction time for temperatures between 474 K and 543 K. This dependence on time can be associated with diffusional phenomena. More direct evidence was provided by depth profile experiments of TiO_2-supported metals. For Rh deposited on a TiO_2 single crystal, Sadeghi and Henrich [55] found that after high temperature reduction, the AES intensities showed minima in the Ti and O signals and a maximum in the Rh signal as a function of sputter time, reflecting a thin surface layer of titanium oxide on top of the rhodium. Confirmation of this was provided by Takatani and Chung [56]. They found a sharp increase in the Ti AES signal (for Ni deposited on an oxidized Ti foil, after HTR) which decayed in an exponential-like manner upon sputtering of the surface.

More evidence was supplied for Rh and Pt on an oxidized Ti(0001) single crystal analyzed with static secondary ion mass spectroscopy (SSIMS) [57]. Masses attributed to Rh and RhO were replaced by peaks characteristic of titanium oxides after annealing to 760 K. Finally, titania deposited onto nickel grids was monitored in a controlled-atmosphere electron microscope [58]. Oxide aggregates on the nickel surface were observed to decrease dramatically in height and surface roughness upon reduction in H_2 at 770 K suggesting wetting of the nickel by the oxide. Re-oxidation returned the oxide overlayer to a three-dimensional structure, having a "saw-toothed" appearance. In addition, heating in 5 torr acetylene resulted in filamentous carbon growth on the nickel surface, predominantly at the metal/metal oxide interface, but not on the titania. Wetting of the metal surface by the oxide was consequently indicated by a sharp reduction in the total amount of carbon deposited as well as the increase in non-filamentous growth.

1.6 DEPOSITION OF OXIDE OVERLAYERS

The migration of oxide species onto the surface of the metal particles under reducing conditions provides the means for establishing more extensive metal/metal oxide contact. Several research groups have investigated the chemisorption and catalytic properties of metals with oxide overlayers to determine the properties of the exposed metal atoms, especially at the metal/metal oxide interface. This work is supported by studies showing that titania-promoted catalysts exhibited catalytic properties identical to those of the analogous TiO_2-supported catalysts. This has been found for CO hydrogenation on Ni/SiO_2 [59] and Pt-black [60], as well as for NO reduction on Rh supported on SiO_2 [61].

Takatani and Chung [56] not only observed migration of the oxide onto the surface of the metal, but they also attempted to calculate the oxide coverage on the metal. Their CO chemisorption results versus oxide coverage indicate, as a function of titania coverage, a non-linear falloff in chemisorption capacity which cannot be explained by mere coverage of sites. Extrapolation at low coverages shows that a single "titania" species deactivates 5 to 6 Ni atoms for CO adsorption. Similar results were obtained by Raupp and Dumesic [62,63] for titania deposited on a nickel foil. In contrast, Ko and Gorte [64,65] studied the effects of titania deposition on the properties of Pt, Rh, and Pd foils. They concluded for all three metals that titania only blocks H_2 and CO chemisorption by physically covering adsorption sites. They have also investigated the effects of niobia, silica, and alumina overlayers on Pt, finding that niobia behaves similarly with TiO_2, while silica and alumina suppress chemisorption to a lesser extent [66]. However, as will be discussed later, their method of coverage determination is questionable. Dwyer *et al.* [67] also studied TiO_2 on Pt and found a linear correlation between the low energy ion scattering spectroscopy (LEISS) signal for Pt and the amount of H_2 chemisorbed. LEISS, though, is prone to neutralization and shadowing problems such that it may not detect any contribution from the metal/metal oxide interface.

General agreement has been found in the effects of TiO_2 on the CO hydrogenation activity. Chung *et al.* [68] noted a 4-fold rise in methanation activity at low titania coverages accompanied by higher rates of C_{2+} hydrocarbon production. Demmin *et al.* [69] and Dwyer *et al.* [60] also observed higher methanation rates as well as significantly lower activation energies for titania on Pt foil (ΔE = -11 kcal/mole) and titania-promoted Pt black (ΔE = -5 kcal/mole), respectively. Similar results were obtained for Nb_2O_5-promoted Pt [70].

1.7 SCOPE OF THE PRESENT WORK

The verification of titania migration onto the metal particle surface during HTR has prompted work in this laboratory, concomitant to the investigations in the previous section, on metal substrates with oxide overlayers. A comparison of the TiO_2-supported and TiO_2-promoted catalysts is depicted in Fig. 1.1. Surface sensitive techniques have been applied to characterize the oxide coverage and oxidation state, thereby facilitating correlation of the chemisorption and catalytic properties of the oxide-covered rhodium with respect to the overlayer coverage.

Experiments were performed in two ultra-high vacuum chambers equipped with atmospheric pressure cells for sample pre-treatment and reaction. Auger electron spectroscopy (AES) was employed for characterization of the surface composition. X-ray photoelectron spectroscopy (XPS) provided information regarding the oxidation states of the oxide overlayers. The chemisorption capacity was measured through temperature programmed desorption (TPD) and the catalytic behavior of the surface was probed with three reactions: CO hydrogenation, ethylene hydrogenation, and ethane hydrogenolysis.

Alumina and titania overlayers were deposited onto rhodium foil and characterized in terms of the mode of overlayer growth, oxidation state dependence on treatment conditions, CO chemisorption, and catalytic behavior. Both alumina and titania overlayers grew until the completion of a two-dimensional monolayer followed by three-dimensional growth, as

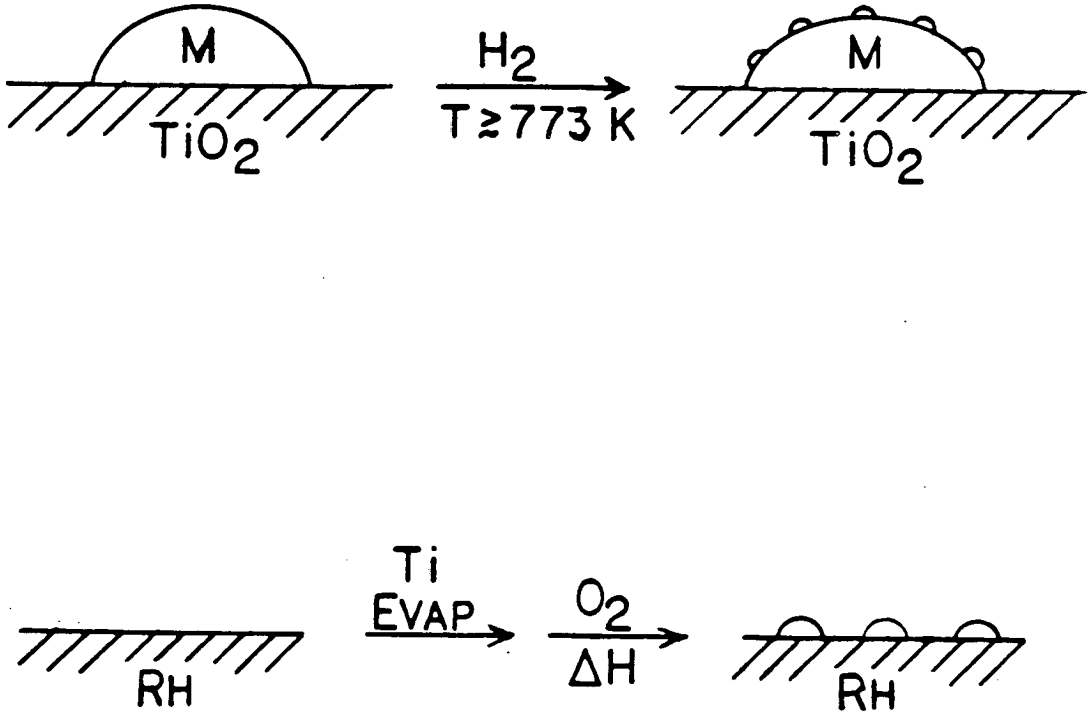

Figure 1.1: A comparison between the metal surface of a TiO_2-supported catalyst and the surface of the analogous TiO_x-promoted metal.

indicated by the AES uptake plots. Alumina inhibited CO chemisorption and CO hydrogenation in proportion to the coverage, while titania suppressed CO chemisorption to a much greater extent and enhanced the CO hydrogenation rate by as much as a factor of three. Both ethylene hydrogenation and ethane hydrogenolysis rates were strongly suppressed when titania overlayers were present, to an extent greater than explained by site blocking by titania.

The XPS results showed that titania was readily reduced while alumina could not be. A model is proposed suggesting there is no CO chemisorption at Rh sites at the periphery of titania islands while Ti^{3+} species along the island periphery interact with CO to enhance CO dissociation and hence, its hydrogenation rate. Good quantitative agreement exists between the model and experimental data; a titania nucleation site density of 4.5 x 10^{13} cm^{-2} and a two-site reaction ensemble at the metal/metal oxide interface at the perimeter of TiO_x islands have been inferred.

Chapter 2

SURFACE ANALYSIS TECHNIQUES–THEORY OF OPERATION

Three principal analytical techniques were employed in this study of metal oxide overlayers on rhodium: Auger electron spectroscopy (AES), X-ray photoelectron spectroscopy (XPS), and temperature programmed desorption (TPD). In what follows, a brief discussion of the basic principles of operation for each of these techniques is presented.

2.1 AUGER ELECTRON SPECTROSCOPY (AES)

2.1.1 The Auger Process

The impingement of a moderately high energy ($\geq$1 kV) beam of electrons upon an atom can cause major rearrangements of the atom's electronic configuration. In the mode of rearrangement commonly referred to as the "Auger process," a core electron is first ejected (see Figure 2.1). The newly formed ion with a core hole then "relaxes" into a lower energy, but doubly ionized, state. This occurs through the collapse of an electron of a higher level

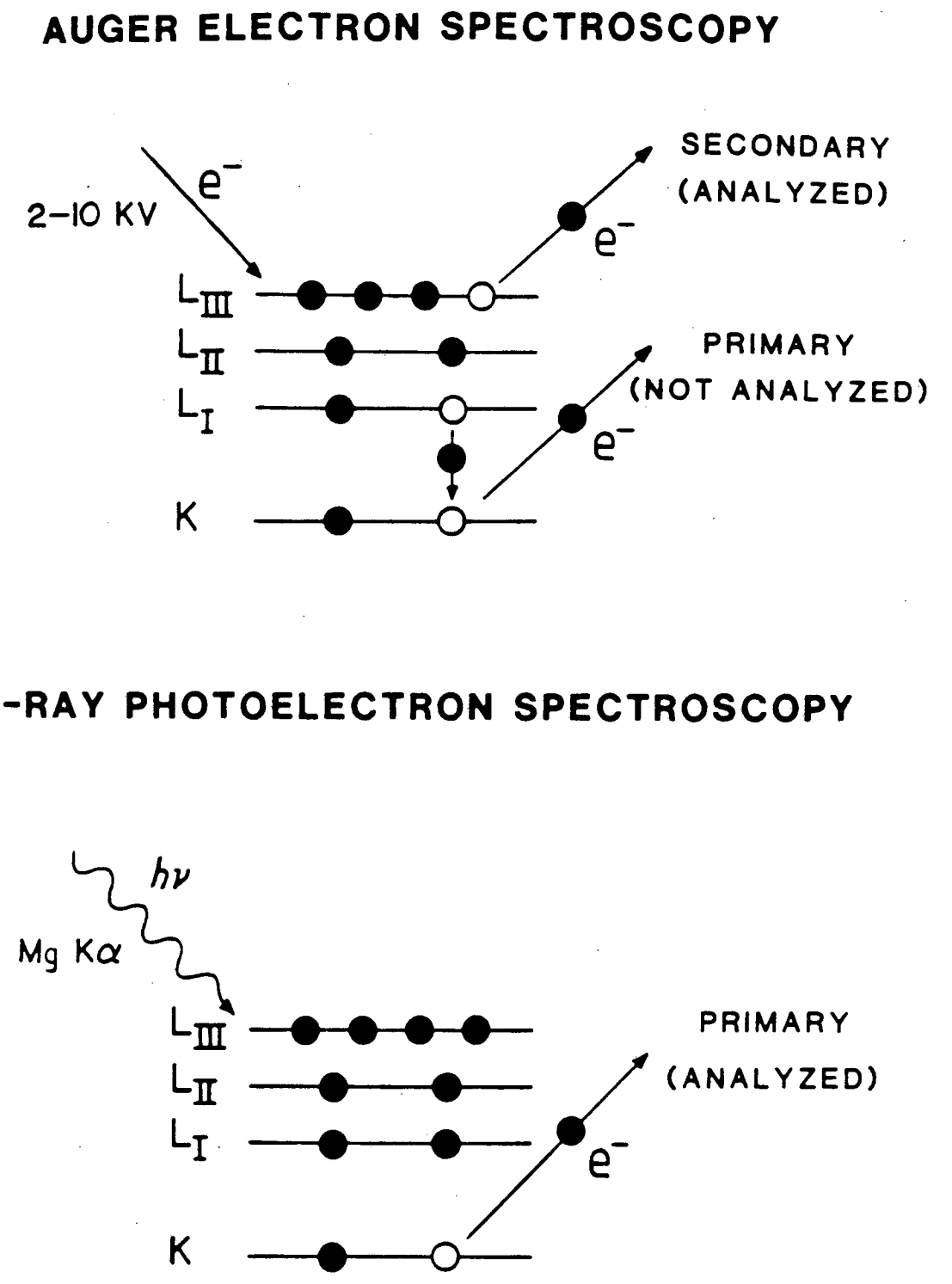

Figure 2.1: The processes for electron excitation in (a) Auger electron spectroscopy and (b) x-ray photoelectron spectroscopy.

shell into the core hole releasing enough energy to trigger the ejection of a second electron. The kinetic energy of the second (or Auger) electron is merely the energy difference between the two electron hole states minus the energy to remove the Auger electron from the atom. Since the electron energy levels are uniquely defined for each element, the energies of Auger electrons can be used for the determination of elemental composition [71].

The typical energy range for the incident (primary) electron beam is 2–10 kV. From the corresponding penetration depths (without inelastic losses) of the electrons [72], the Auger process will be induced in atoms ranging from 20 to 50 Å into the bulk of the sample. However, the Auger electrons are typically between 40 and 1000 eV in energy [73], limiting the escape depth to under 15 Å for emergence normal to the surface. For the energy values characteristic of this study ($\leq$500 eV), the mean free path of the Auger electrons will be less than 10 Å so that AES is sensitive to the uppermost three or four surface layers.

2.1.2 Determination of Overlayer Coverage

The attenuation of a substrate's AES peak intensity by the addition of an overlayer of different composition can yield information on the coverage and growth mode of the overlayer. Overlayer growth can be categorized into four growth modes [74,75]: layer-by-layer, three-dimensional island growth, a mixture of the two (completion of one or more monolayers followed by three-dimensional growth), and alloying.

The simplest case to describe is the layered-growth mechanism, also known as Frank and Van der Merwe growth. When a single, two-dimensional monolayer is deposited, the substrate signal will be attenuated by an amount designated as α. Between 0 and 1 monolayer, a fraction of the substrate signal corresponding to the surface that is covered will be attenuated by α while the remaining exposed surface signal emerges unattenuated. Thus the degree of attenuation changes linearly with coverage as follows:

$$I = I_0\theta\alpha + I_0(1-\theta)$$

$$I = I_0 - (1-\alpha)I_0\theta \tag{2.1}$$

where I_0 denotes the intensity of the bare substrate and I the intensity of the substrate with an overlayer of coverage θ.

For two monolayers, the attenuation of the substrate signal is α^2; therefore, I varies from α to α^2 linearly between 1 and 2 monolayers. Similar arguments follow for higher coverages. The slope of each successive monolayer, then, diminishes by a factor of α. The AES signal of the overlayer grows in a corresponding manner. These trends are depicted in Fig. 2.2a. Layer-by-layer growth is often exhibited by metal-on-metal deposition [74,76,77,78]. In the case of three-dimensional island growth, also known as Volmer-Weber growth, clusters form on the surface which tend to grow in height as well as laterally. These clusters leave bare substrate patches that are covered relatively slowly while the AES contribution, already attenuated from the covered substrate, is diminished even further with increasing deposition. The overall substrate signal therefore diminishes more slowly and in a more continuous manner than in the layer-by-layer case (Fig. 2.2b); no sharp breaks occur demarking monolayer coverage. The clustering of metals on oxide surfaces is an example of three-dimensional growth.

In the third growth mechanism, known as Stranski-Krastanov growth, the first (or several) monolayer is completed. Thereafter, three-dimensional clustering occurs. While layered growth is taking place, the AES signal of the substrate decreases in linear segments until clustering causes a shift to the more continuous decrease (Fig. 2.2c). Stranski-Krastanov growth has been seen for metal-on-metal growth and in oxide-on-metal growth [74,79].

The final growth mode, alloying, occurs upon rearrangement of the overlayer atoms with those of the substrate and is indicative of very strong adsorbate-substrate bonding. A typical AES uptake plot is shown in Fig. 2.2d.

The degree of attenuation, α, is dependent on the mean free path of the detected Auger electrons, λ, and on the thickness of the layer, h, covering the substrate

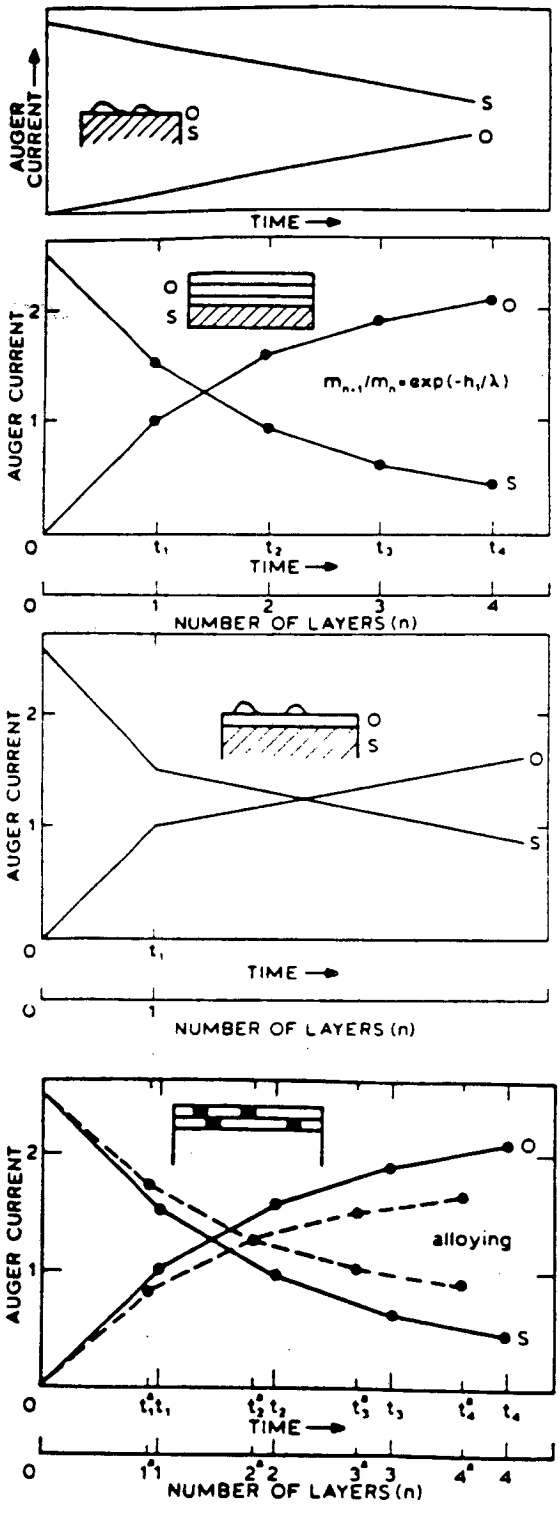

Figure 2.2: Characterization by Auger electron spectroscopy of the growth of overlayers on substrates: (a) three-dimensional growth, (b) layer-by-layer growth, (c) layered growth followed by three-dimensional growth, and (d) alloy formation between the overlayer and substrate.

$$\alpha = I/I_0 = \exp(-h/\lambda\cos\phi) \tag{2.2}$$

The $\cos\phi$ term arises from the sampling of electrons entering the electron energy analyzer at an angle of ϕ from the surface normal. The mean free path is, of course, dependent on the energy of the Auger electrons [72]; however, it is more practical to determine α from the plots of AES intensity versus overlayer coverage. A list of attenuation coefficients for various overlayer/substrate systems is displayed in Table 2-1.

Finally, it should be mentioned that in determining the coverage and growth mode, it is convenient to plot AES intensities versus dosing time (assuming the evaporation rate is fairly constant). From the position of breaks in the plot (if Frank–Van der Merwe or Stranski–Krastanov growth occurs), information is obtained regarding the evaporation rate as well.

2.1.3 Detection of Auger Electrons

To produce the Auger electrons, a high voltage (between 2 and 10 kV) electron gun is required. When a cylindrical mirror analyzer (CMA) is employed as an electron energy analyzer, the electron gun is often located concentrically inside the CMA (Fig. 2.3). This then gives an electron beam of normal incidence; a gun may also be located external to the CMA to generate a glancing incidence beam which is inherently more "surface sensitive" due to the longer average path length of Auger electrons emerging from the sample.

The CMA is comprised of two concentric cylindrical shells with an electrostatic potential applied to the outer cylinder. Electrons from the sample enter the gap between the cylinders through "windows" in the inner cylinder at the end closest to the sample (Fig. 2.3). Once inside the gap, the electrons are deflected away from the outer cylinder by an applied negative voltage. Electrons with the appropriate kinetic energy will be directed through a second set of "windows" at the opposite end of the inner cylinder and into the detector

Table 2.1: ATTENUATION COEFFICIENTS FOR METAL-ON-METAL SYSTEMS AS A FUNCTION OF SUBSTRATE AUGER ELECTRON ENERGY

SUBSTRATE	ADSORBATE	α	REFERENCE
Cu (60 eV)	Mn	0.37	[80]
	Pb	0.44 - 0.51	[81,82,75]
	Bi	0.42	[83]
	Ag	0.29	[76]
	Co	0.38	[84]
Pt (64 eV)	Au	0.48	[77]
	Pb	0.48	[85]
	Zr	0.29	[86]
	Ag	0.30	[87]
Al (68 eV)	Pb	0.22	[88]
	Sn	0.25	[88]
Au (69 eV)	Ag	0.31	[89]
	Pb	0.40	[90]
	V	~0.35	[91]
Ge (87 eV)	Au	0.51	[92]
Si (92 eV)	Sb	0.38	[93]
Cu (105 eV)	Ni	0.29	[94]
	Co	0.46	[95]
Pt (150 eV)	Cu	0.19	[78]
	Re	0.41	[96]
W (169 eV)	Fe	0.46	[97]
	Zr	0.53	[98]
	Pd	0.50 - 0.53	[76,99]
	Ag	0.58	[74]
Mo (179 eV)	Pd	0.58	[100]
Re (181 eV)	Fe	0.33	[101]
Re (215 eV)	Pt	0.42	[102]
Pt (237 eV)	Cu	0.38 - 0.50	[84,78]
	Zr	0.63	[103]
	C	0.56	[75]
Ru (281 eV)	Cu	0.49	[104]
	Au	0.58	[105]
Ag (356 eV)	Pt	0.64	[84]
	Pt	0.65	[87]
	Au	0.51	[106]
	Pb	0.58	[107]
	Fe	0.66	[108,109]
Fe (650 eV)	K	~0.6	[110]
	Se	0.72	[111]
Ni (850 eV)	Ag	0.72	[112]
Cu (920 eV)	Pt	0.70	[84]

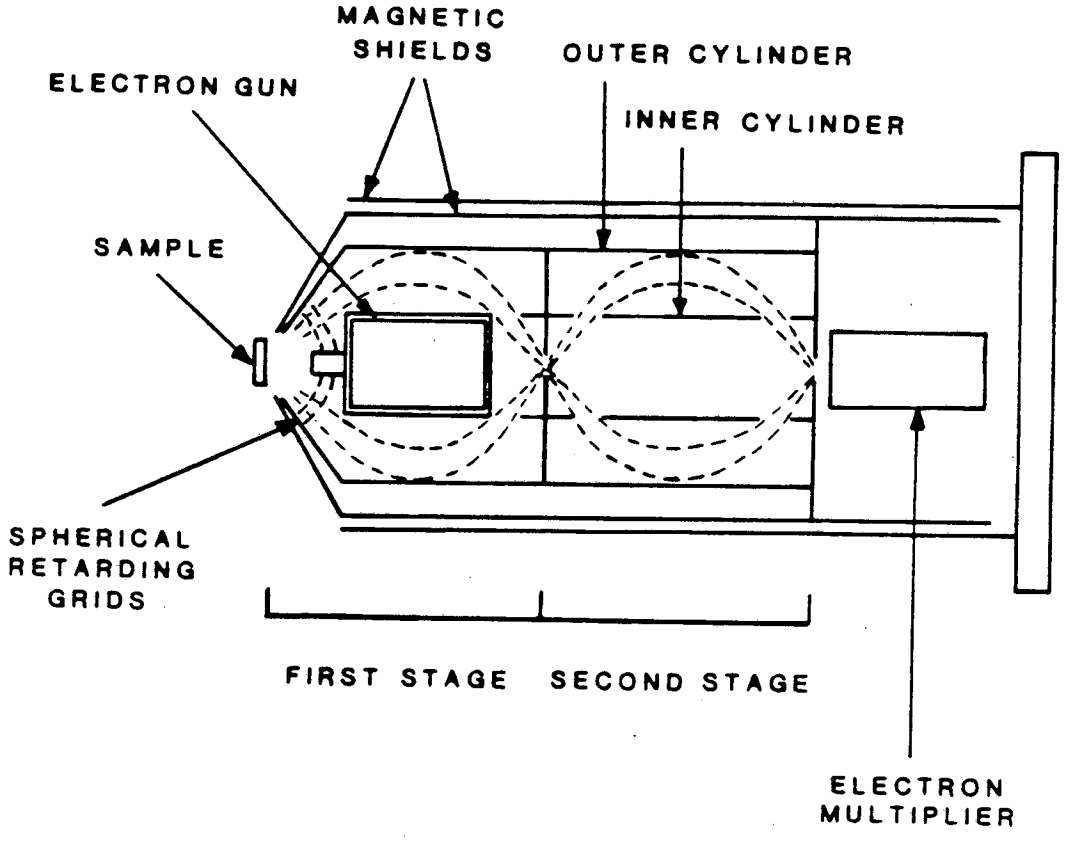

Figure 2.3: Schematic of a double-pass cylindrical mirror analyzer (CMA). (The second stage is absent in a single-pass CMA.)

(usually a "channeltron" or a multiple dynode electron multiplier). By ramping the outer cylinder voltage, a spectrum of electron signal intensity versus electron kinetic energy can be generated. The electron energy tends to be about 1.6 times the voltage applied to the outer cylinder of the CMA.

The description just given applies for a single-pass CMA. A double-pass CMA is nearly identical except that two sequential energy filter sections are incorporated before electrons are detected. Operated in the manner of the preceding paragraph, the relative resolution, $\Delta E/E$, is constant over the range of energy values. For XPS, a double-pass CMA is used

and operated in an alternative energy analyzing mode, as will be discussed in the next section.

Since the contribution to the total signal by Auger electrons for a given energy is small, it is common practice to enhance the Auger signal by plotting the derivative spectrum, dN(E)/dE, as a function of electron energy. By superimposing a modulating voltage of amplitude U_m and frequency ω on the outer cylinder voltage, the signal current, i, which can be written as a Taylor series,

$$i(U_r + U_m \sin\omega t) = i(U_r) + i'(U_r)\cdot U_m \sin\omega t + \frac{i''(U_r)}{2!} U_m^2 \sin^2\omega t + \ldots \qquad (2.3)$$

has a component containing the first derivative [113]. The value of this derivative is then isolated with a phase-sensitive lock-in amplifier tuned to the frequency ω and the desired AES spectrum can then be plotted. Peaks corresponding to Auger transitions will usually occur as paired upward and downward deflections due to the derivative mode. Peak-to-peak heights are measured to indicate an element's abundance on the surface.

2.2 X-RAY PHOTOELECTRON SPECTROSCOPY (XPS)

2.2.1 X-Ray Excitation

As with AES, XPS may be used for analysis of surface composition, but one of its principal advantages lies in the information it yields on the oxidation state of surface species. Electrons of atoms near the surface ($\leq$20 Å—for the same reasons discussed in Section 2.1) can be ejected upon illumination with soft x-rays (Fig. 2.1b). The kinetic energy, E_K, of the emitted electrons can be related to the binding energy, E_B, and the incident radiation energy, $h\nu$, by

$$E_K = h\nu - E_B - \phi \tag{2.4}$$

where ϕ is the work function of the analyzer (when the sample is a conductor). When the number of "counts" for a given binding (or kinetic) energy is plotted as a function of binding (or kinetic) energy, distinct peaks are observed. These peaks may correspond to individual electron orbitals (core-level transitions) or to x-ray–induced Auger peaks (Auger transitions) [71]. In addition, at low binding energies, features reflecting the density of filled states near the valence band are observed (valence-level transitions). Example "wide scan" spectra for Rh, Au, Ti, Al, and O appear in Figs. 2.4 to 2.8 [114].

Of the three categories of transitions, only core-level transitions reveal direct information regarding the oxidation state of species on the surface. Since core-level electrons of energy less than the incoming radiation will be ejected, for a Mg Kα source (1253.6 eV), only the 4s, 3d, 3p, and 3s orbitals of Rh (see Fig. 2.4) and the 3s, 2p, and 2s orbitals of Ti (see Fig. 2.6) are of low enough binding energy to be emitted. It is also apparent that the non-s orbitals are doublets. This arises from spin-orbit coupling involving the "parallel" and "anti-parallel" states of the remaining electron (spin quantum number, s, equal to 1/2 and -1/2, respectively). These two energy states occur only if the orbital quantum number, l, is greater than zero. The ratio of peak areas for a doublet can be related to the respective degeneracies (2j + 1, where j = l + s) of each peak. The observed peak widths are dependent on the characteristic widths of the x-ray source, the electron emission process, and the analyzer. The inherent peak width of the core-level can be related to the lifetime of the generated core-hole through the Heisenberg uncertainty principle. Faster relaxation times, such as would occur through Auger transitions in atoms with a higher valence electron densities, result in broader peaks. Typical line-width values are 1–2 eV.

Qualitative information regarding the oxidation state of a compound can be obtained from the valence band region of the spectrum. Since the structure of the highest filled orbitals is reflected in this region, the compound can be identified as an insulator or a

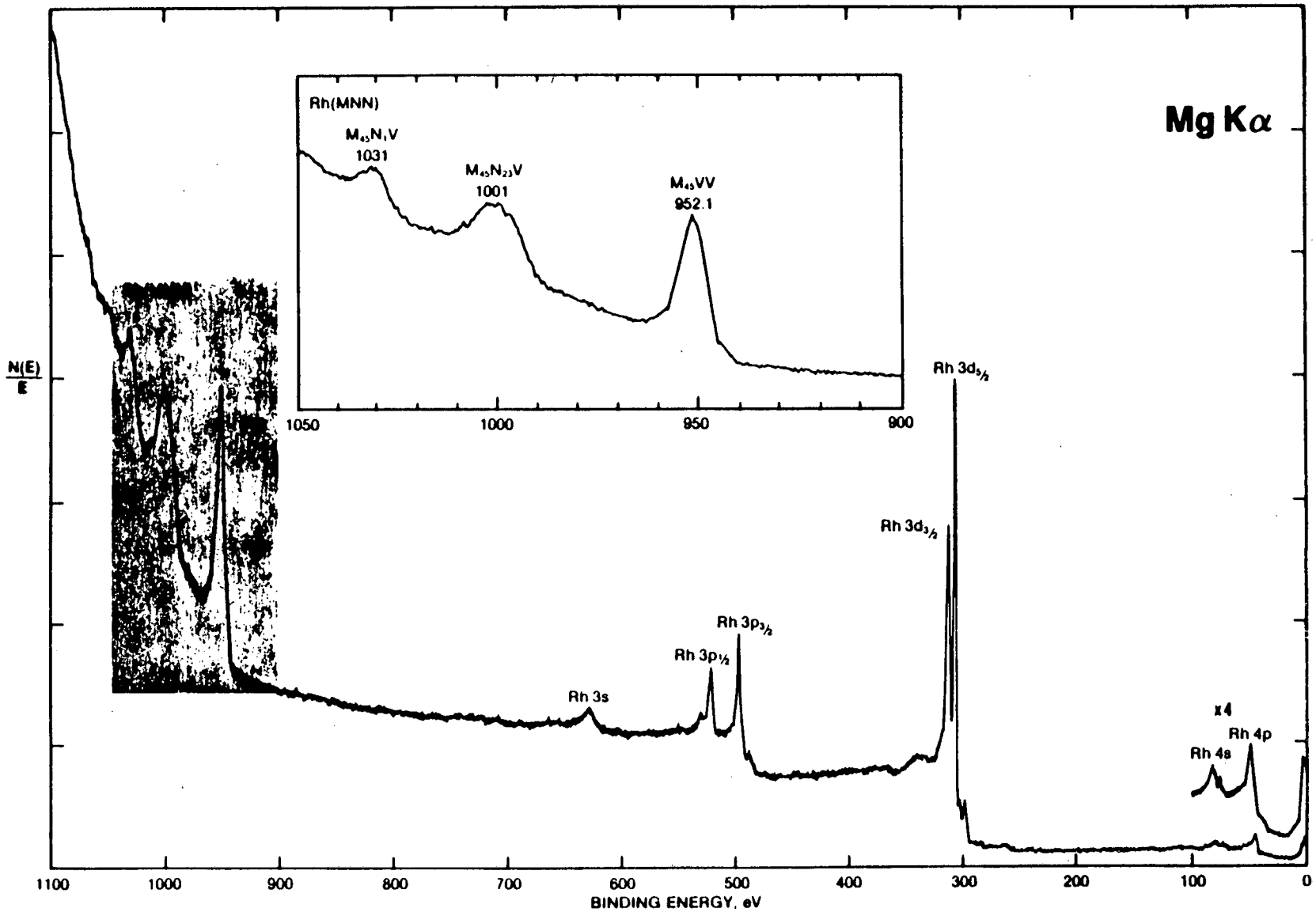

Figure 2.4: An XPS spectrum of rhodium (Mg Kα anode) [114].

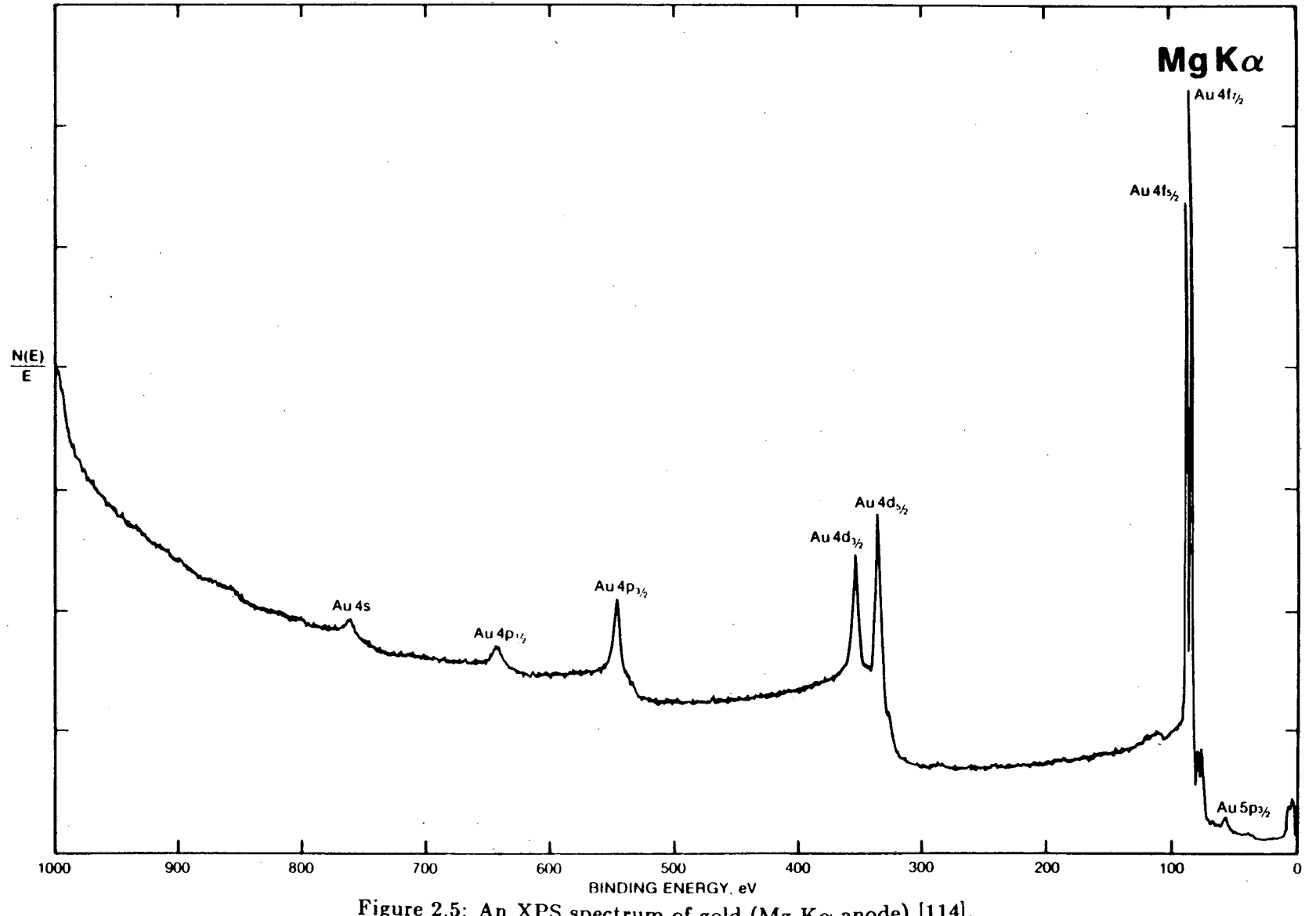

Figure 2.5: An XPS spectrum of gold (Mg Kα anode) [114].

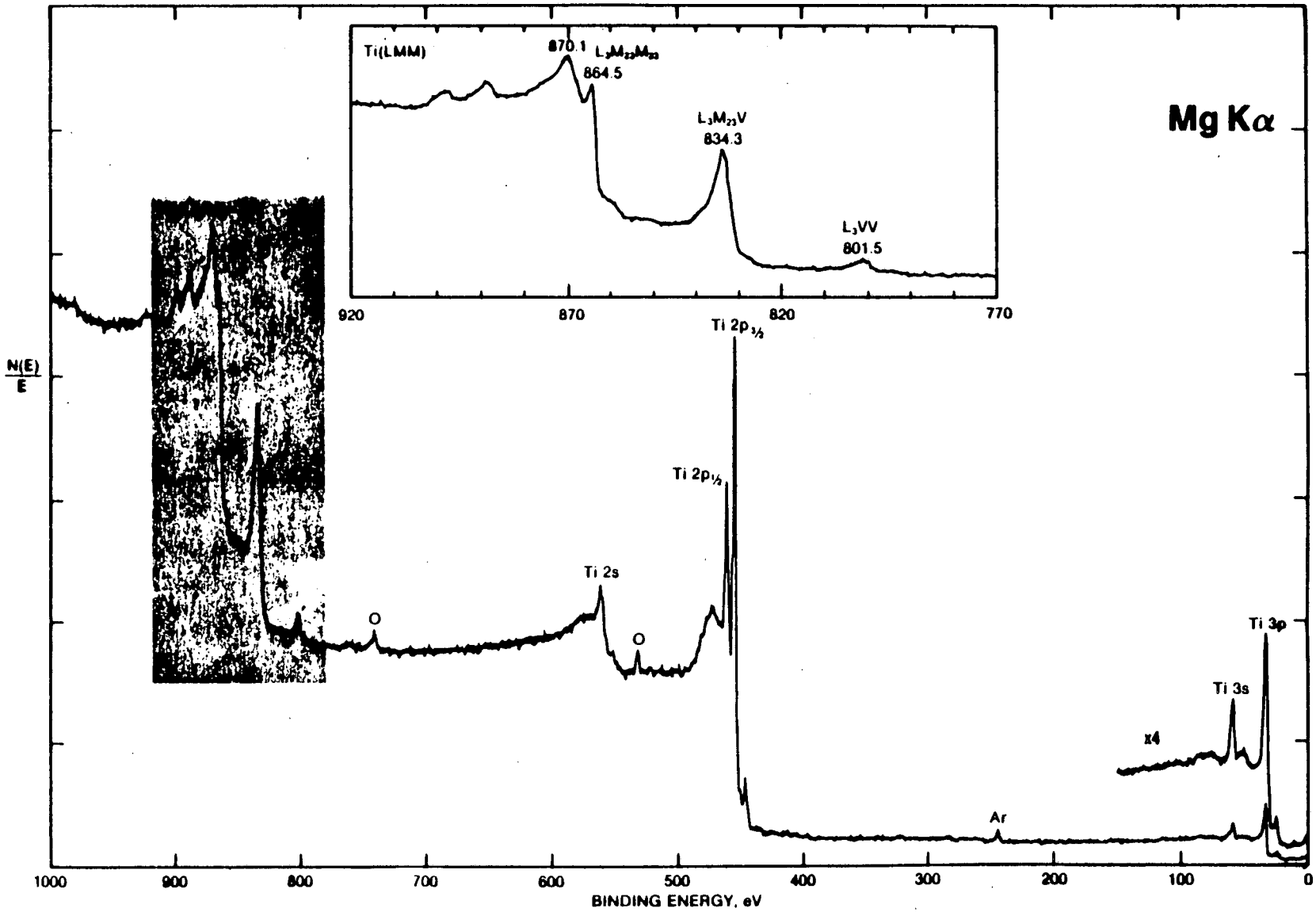

Figure 2.7: An XPS spectrum of titanium (Mg Kα anode) [114].

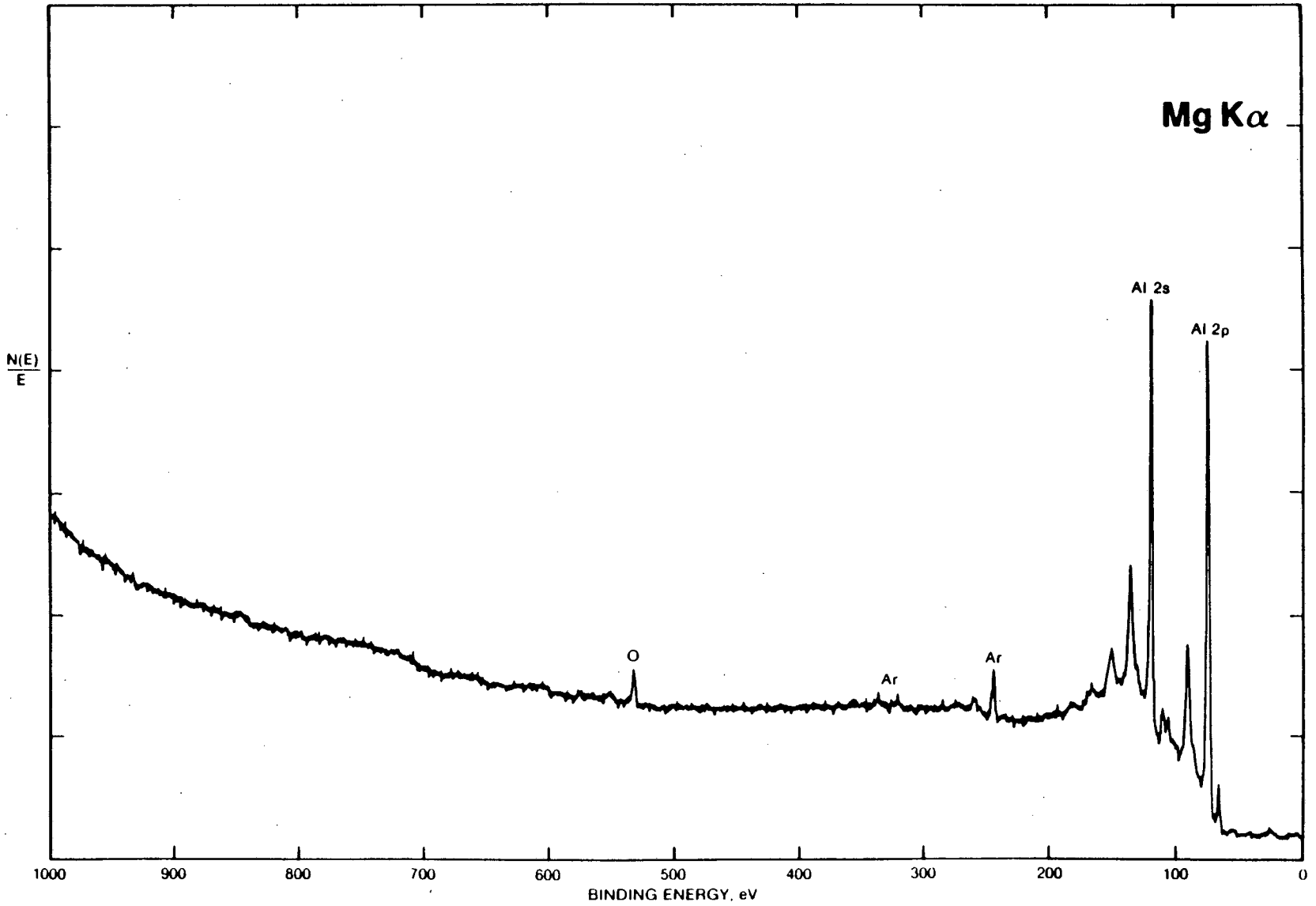

Figure 2.6: An XPS spectrum of aluminum (Mg Kα anode) [114].

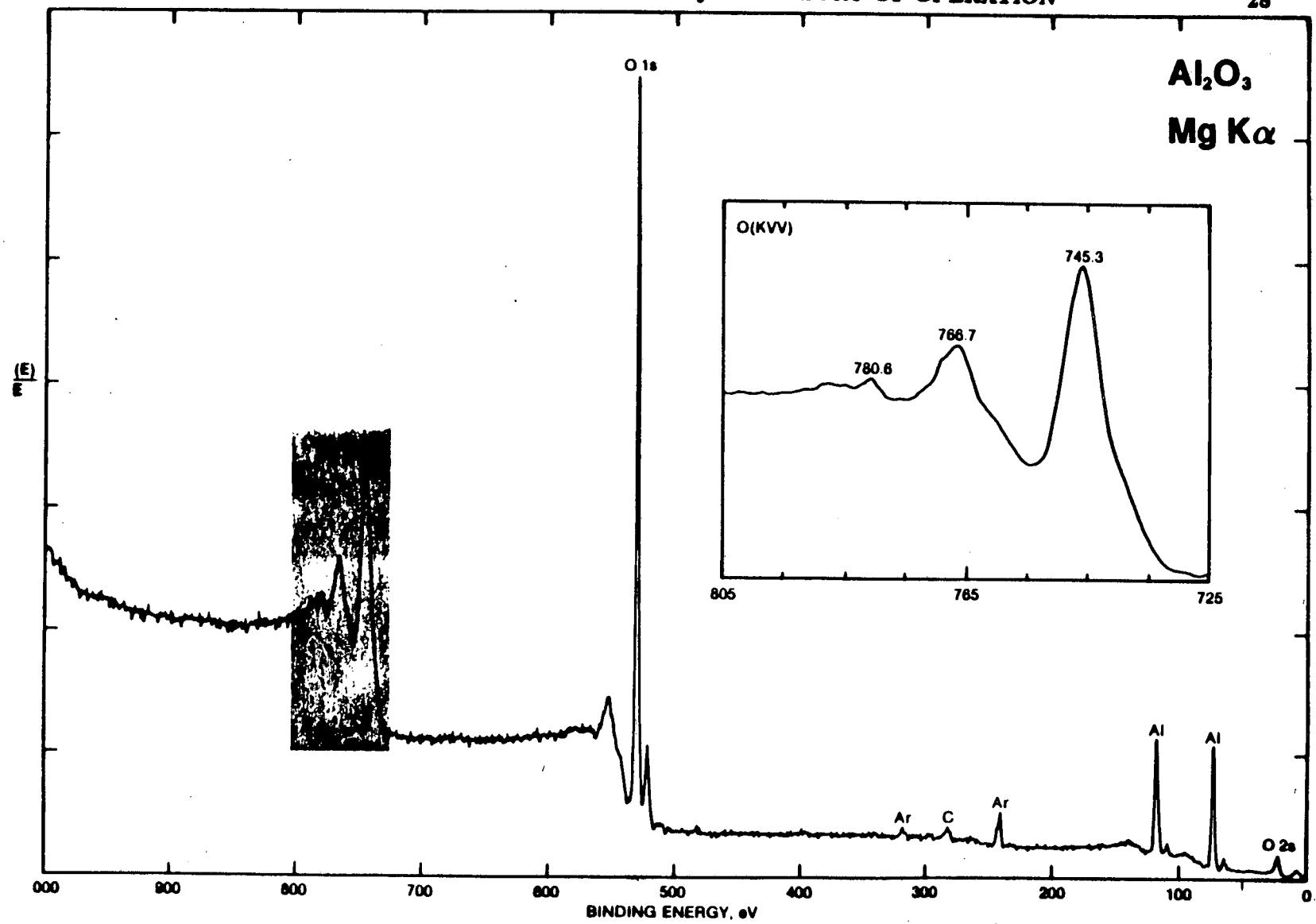

Figure 2.8: An XPS spectrum of oxygen (Mg Kα anode) [114].

conductor depending on whether a band-gap is present or not. Thus for oxides of metals, such as iron or vanadium, the predominance of a particular oxidation state may be identified. This feature was not applied in the work presented here.

2.2.2 Core-Level Chemical Shifts

The binding energy of core-level electrons is heavily influenced by the surrounding electronic environment—both from electrons within the same atom and from nearby atoms. Consider a core electron of an atom with multiple oxidation states. To that electron, the electronic environment of inner level electrons and the nucleus will appear relatively unperturbed for the various valence electron densities. If the valence charge, q, comprised of the valence electrons, is considered to be dispersed uniformly on a sphere of radius r, then a change in the valence electron density, *i.e.*, a valence charge change of Δq, corresponds to a change of potential within the sphere of $\Delta q/r$. Therefore, traversing down a column in the periodic table, where Δq is constant, but r increases, a reduced effect of valence level changes on the core electron is expected.

An increased charge density should lessen the binding energy, due to electrostatic repulsion, while a decreased density should raise the binding energy. For example, electron-withdrawing species (*e.g.*, O or Cl) on an atom would result in a higher binding energy of electrons from that atom than if the atom were not bound to these species. In the same manner, electron-donating elements, such as K or Mg, would diminish the binding energy by increasing the valence charge density. Of course, if the atom initially was negatively charged, the electron would have a higher binding energy. These concepts can be summarized in the following equation for the binding energy, E_B, of the core electron of an atom in two different environments

$$E_B(2) - E_B(1) = -k[q(2) - q(1)] - [\sum_j \frac{q_j(2)}{r_j(2)} - \sum_j \frac{q_j(1)}{r_j(1)}] \quad (2.5)$$

where q_j is the charge on neighboring atoms located at a distance of r_j from the central atom. Changes in the electrostatic field of the central atom due to valence changes appear in the term with the proportionality constant, k. This model does not take into account final state effects, where the electronic state of the newly-formed ion is different than that of the initial atomic state. The model also neglects the effect of the core hole on electrons of neighboring atoms.

More likely than not, for an oxide affected by reduction conditions, a mixture of oxidation states will occur. These states appear in the XPS spectrum as overlapping peaks from which information must be obtained. Deconvolution of these peaks into the component peaks can be performed if the number of contributory peaks is known and characteristic peak shapes assumed. Peaks of Gaussian lineshape are often employed requiring three parameters per peak: position (binding energy), amplitude, and the width at half-maximum.

Lineshapes of Lorentzian character, however, have a theoretical basis [115] and can be modified to account for inelastic interaction between the emitted electrons and the delocalized electrons for metal samples. This effect is responsible for the asymmetry favoring higher binding energies (including the step increase in the background) for metal peaks. A fourth parameter, α, the asymmetry index, is then associated with this lineshape, sometimes referred to as a Doniach-Šunjić lineshape

$$F(E) = \frac{\Gamma(1-\alpha)}{(E^2+\gamma^2)^{(1-\alpha)/2}} \cos\{\frac{\pi\alpha}{2} + (1-\alpha)\tan^{-1}(\frac{E}{\gamma})\} \quad (2.6)$$

where γ is a characteristic peak width. Aside from the asymmetry factor, the major difference in peak shapes between the Doniach-Šunjić and Gaussian lineshapes is that the base of the Gaussian rises more slowly initially and thereby overestimates the contribution of other peaks in that region.

Table 2.2: HIGH-ENERGY SATELLITE LINES FROM MG AND AL TARGETS

X-ray line	Separation from $K\alpha_{1,2}$ (eV) and relative intensity ($K\alpha_{1,2}$ = 100)	
	Mg	Al
K α'	4.5 (1.0)	5.6 (1.0)
K α_3	8.4 (9.2)	9.6 (7.8)
K α_4	10.0 (5.1)	11.5 (3.3)
K α_5	17.3 (0.8)	19.8 (0.4)
K α_6	20.5 (0.5)	23.4 (0.3)
K β	48.0 (2.0)	70.0 (2.0)

2.2.3 Additional Features of the XPS Spectrum

Satellites in the spectrum may arise from secondary lines of lower intensity originating from the x-ray source. The primary radiation, $K\alpha_{1,2}$, occuring from the $2p_{3/2,1/2} \rightarrow 1s$ transition, may be accompanied by radiation of less probable transitions (*e.g.*, valence band $\rightarrow$ 1s: Kβ) or of transitions from multiply ionized atoms (*e.g.*, $K\alpha_{3,4}$). The observed separations and relative intensities of these secondary XPS signals have been tabulated for magnesium and aluminum anodes [71] and are reproduced in Table 2-2.

Secondary electrons striking the aluminum window (which prevents escape of the electrons into the chamber) or the presence of impurities in the anode result in additional features in the x-ray radiation spectrum, which in turn, produce ghost peaks in the XPS spectrum. The common impurities include copper (from the backing behind a worn out anode), oxygen, and carbon. The location of the ghost peaks from these elements and from aluminum lie several hundred eV from the primary peaks so that overlap is not a problem; however, they do complicate the overall spectrum.

Additional peaks may also occur through electronic interactions during relaxation of the newly-generated ion. One example in this category is multiplet splitting where there is exchange interaction between the remaining electron in a core orbital and several unpaired

electrons in the valence levels. Here, the spin of the lone core electron may be parallel or antiparallel to the spin of the valence electrons resulting in the splitting of the original XPS peak. Another relaxation effect involves rearrangement of the valence electrons because of the apparent increase in nuclear charge (as it appears to these electrons). The promotion of one of these electrons into a higher, unfilled level removes energy from the primary excitation process and thereby yields a peak of apparently higher binding energy. This is known as a "shake-up" satellite.

Numerous peaks, *e.g.*, core-level, valence level, and Auger transitions as well as satellites and ghost peaks, can be attributed to just a single element. Though some of the satellites may not be present in certain systems and for certain samples, these features do serve as a warning that the complexity of the XPS spectrum grows rapidly with the number of species present.

2.3 TEMPERATURE PROGRAMMED DESORPTION (TPD)

2.3.1 General Description

The chemical environment of atoms on the surface of a sample can be probed by measuring the strength of adsorption of certain test molecules. One such technique involves exposing the sample to molecules at a particular temperature and pressure followed by heating until the adsorbed species desorb. This is commonly referred to as temperature programmed desorption (TPD). For experiments in ultra-high vacuum (UHV), exposures expressed in units of "Langmuirs" (1 L = 10^{-6} torr-s) are appropriate. The samples are often directly heated and desorbed species detected with a mass spectrometer.

Species adsorbed to a surface may be categorized as either "physisorbed" or "chemisorbed"—terms reflecting the type and strength of interaction between the adsorbate and substrate. Physisorption arises through dispersion forces and/or dipole forces. In the present work,

this mode of interaction is not significant with exposure temperatures no lower than 150 K and diatomic adsorbate molecules. Chemisorption indicates the formation of a "chemical bond" between adsorbate and substrate and consequently, chemisorbed species will provide more information about the surface chemical environment.

2.3.2 Kinetics of TPD

Temperature programmed desorption is by definition a dynamic process. The temperature of the substrate is ramped, causing desorption of adsorbed molecules, which eventually are pumped out of the system. The number of molecules detected by the mass spectrometer is therefore dependent on the rate of temperature increase, kinetics of desorption, alternative processes occurring on the surface as the temperature rises, and the pumping speed of the system's pumps. These factors are combined to give [116,117]

$$\frac{dp}{dt} = k(p_{eq} - p) - \frac{A}{cV}\frac{dn}{dt} \tag{2.7}$$

where dp/dt represents the change in system pressure at a particular time, $k(p_{eq} - p)$ the pumping speed, and the final term the rate of gas evolution from a sample of area A into a system of volume V. The latter term is, in turn, dependent on the heating rate. For a low surface area sample in a typical UHV chamber and a relatively low heating rate, the pumping speed will be much greater than the rate of gas desorption. This means the change in system pressure will be relatively small compared with the pumping speed, or

$$\frac{dp}{dt} \ll k(p_{eq} - p) \tag{2.8}$$

$$\frac{dn}{dt} = \frac{cV}{A}k(p_{eq} - p) \tag{2.9}$$

The kinetics of desorption can be described as an expression incorporating an Arrhenius term as well as a dependence on the species' surface coverage, n

$$-\frac{dn}{dt} = \nu n^a \exp(-\frac{E_d}{R_G T}) \tag{2.10}$$

for an "a-th" order desorption process, a desorption energy E_d, and a frequency factor ν. A linear heating rate, β, with time reduces the number of independent variables

$$-\frac{dn}{dT} = \frac{\nu}{\beta} n^a \exp(-\frac{E_d}{R_G T}) \qquad \text{where } T = T_o + \beta t \tag{2.11}$$

The pressure corresponding to the desorbing species is monitored with the mass spectrometer (set at the mass of that species) and so dn/dT is linearly proportional to the mass spectrometer signal. A plot of dn/dT as a function of temperature (or time) will exhibit a peak with a maximum at some temperature, T_p. At the peak temperature, $d^2n/dT^2 = 0$, which can further simplify Eq. 2.11 in terms of T_p. For a first-order process, a = 1 and

$$\frac{E_d}{R_G T_p^2} = \frac{\nu}{\beta} \exp(-\frac{E_d}{R_G T_p}) \tag{2.12}$$

which indicates T_p is independent of the surface coverage. Second-order desorption (a = 2) yields

$$\frac{E_d}{R_G T_p^2} = 2\frac{\nu}{\beta} n_p \exp(-\frac{E_d}{R_G T_p}) \tag{2.13}$$

so that T_p increases for lower surface coverages, n_p, at the peak temperatures. Estimates of the desorption energy, E_d, can be made from Eqs. 2.12 and 2.13, and by assuming a value of ν (usually taken to be 10^{13} s^{-1}). Hydrogen desorption, which shows a peak shift to lower temperatures at higher exposures, is an example of a second-order process.

In the case of CO chemisorbed to the surface, dipole-dipole repulsion results in a weakening of the bond strength of CO to the surface. This interaction also causes bonding at different types of sites, relative to the surface lattice, at high coverages (>0.3 ML), as CO rearranges to minimize the effects of the repulsion. Consequently, as higher CO exposures

are employed, the degree of repulsion increases, and the desorption temperature decreases. Correlating the desorption kinetics with the governing parameters is considerably more complicated than warranted by the results in this work and will not be treated here.

Chapter 3

EXPERIMENTAL APPARATUS

The techniques employed for characterizing interactions between the metal oxide overlayers and the metal substrate include Auger electron spectroscopy (AES), x-ray photoelectron spectroscopy (XPS), temperature programmed desorption (TPD), and chemical reaction analysis. To accomplish this, two different ultrahigh vacuum (UHV) chambers were used: one equipped with all of the above techniques except for XPS and a second for AES and XPS analysis. The features of these two chambers will now be discussed separately.

3.1 VARIAN LEED CHAMBER

Though originally designed as a LEED chamber, a Varian 240 LEED chamber (Model 981-0030) UHV chamber was modified to serve primarily for sample analysis by AES, TPD, and chemical reactivity. This stainless steel chamber of roughly 25 liters volume has a variety of 6- and 2- inch ports along with two 8-inch ports (for the LEED optics and the window). With the exception of the LEED optics, all analytical equipment was mounted on the front half of the chamber (Figure 3.1) while the pumps, ion gauge, and leak valves were connected

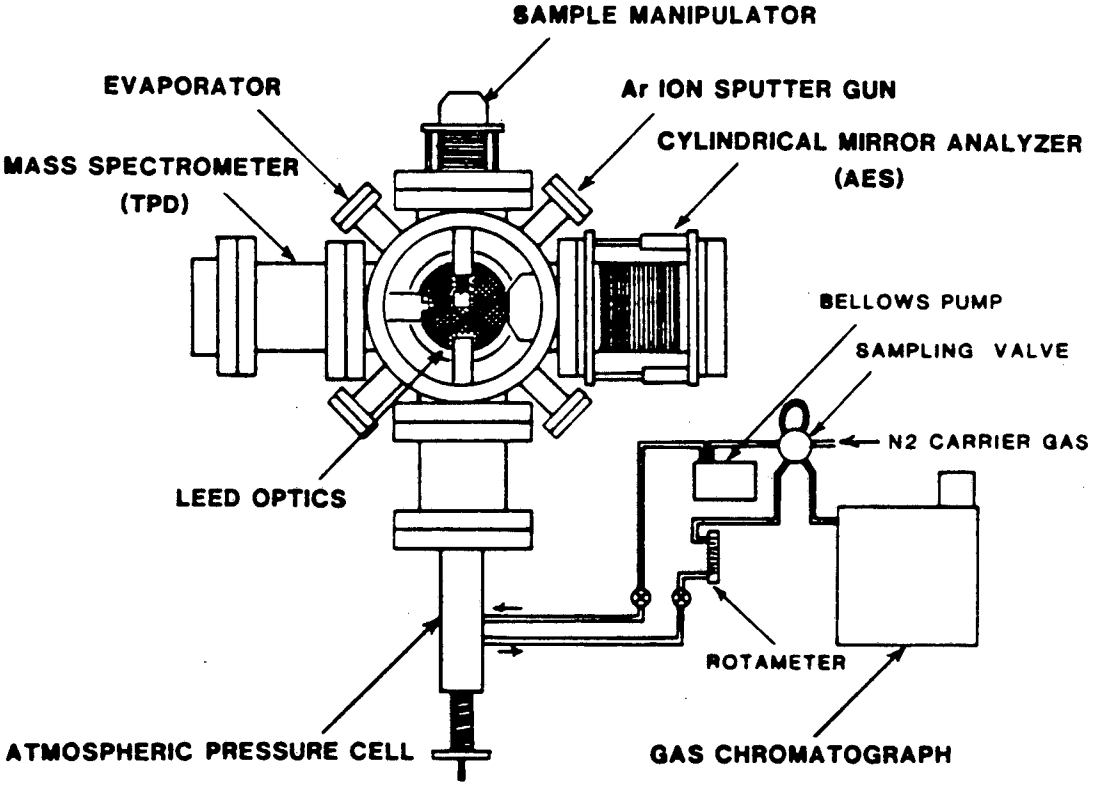

Figure 3.1: Ultra-high vacuum chamber for surface science/reaction studies.

through the back half. The chamber was also equipped with gas handling and reaction loop systems for the introduction of gases to the chamber or reaction network.

3.1.1 Pumps and Pressure Measurement

Three pumps were attached to the UHV chamber: a Varian 4-inch oil diffusion pump, a Varian VacIon pump, and a titanium sublimation pump. The diffusion pump, equipped with a liquid nitrogen trap and backed-up by a rotary-vane mechanical pump, was charged with SantoVac5 oil. Despite its location about 2-1/2 feet from the chamber, connected by 4-inch conduit, a base pressure of 2 x 10^{-10} torr could be achieved in the chamber—

especially after limited operation of the titanium sublimation pump. The poor condition of the ion pump made it unsatisfactory for use during experiments; however, it was adequate for maintaining an acceptable base pressure at night, when the equipment was not operated and the diffusion pump was valved off. The pressure in the chamber was measured with a Bayard-Alpert–type ion gauge.

After opening to air for maintenance or repairs, the chamber was "roughed" with a sorption pump filled with 8 Å molecular sieve and cooled with liquid nitrogen. Pressures at this stage were measured with a thermocouple gauge.

3.1.2 Sample Manipulators and Reaction Cell

Two different sample manipulators were employed in the course of the experiments: one for room temperature chemisorption (for TPD) and for reactions; the other for low temperature chemisorption (for TPD). Both manipulators had the capability for X–Y–Z displacement as well as tilt in the X and Y directions. However, none of these motions were calibrated against any measuring devices. Rotary motion was also allowed in both manipulators.

The low temperature manipulator was equipped with three cryogenic feedthroughs to provide liquid nitrogen cooling inside the chamber. The ends of the feedthroughs were connected to the sample by copper braids. The configuration of this sample holder restricted sample preparation and analysis to only one side of the sample. A chromel/alumel thermocouple was used for temperature measurement.

Mounted on the reaction manipulator was a sample holder consisting of a stainless steel disk with four copper feedthroughs: two for heating lines and two for the thermocouple. A sample foil was spot-welded to 0.020 inch Pt or Rh support wires which, in turn, were bound to the heating feedthroughs by copper-berylium "barrel" connectors. A chromel/alumel thermocouple was used for temperature measurement during the TPD ex-

periments; a platinum/platinum-10% rhodium thermocouple was used during reactions.

The sample holder disk mentioned above was machined to seal against the atmospheric reaction cell, with a N-buna o-ring inbetween to make the seal. This arrangement allowed encapsulation of the sample with subsequent exposure to reaction gases while the rest of the chamber remained in ultra-high vacuum. The cell was mounted on a bellows allowing vertical motion to either "close" or "open" the cell. Two 1/16 in holes bored partially through the cell walls were connected to 1/4 inch stainless steel tubing and thereby to the reaction loop. With this set-up, gases could be admitted to the cell for either reactions or sample treatment.

3.1.3 Reaction Loop and Gas Handling Systems

Reactions were run in a batch mode by circulation of the reaction gases through the reaction loop and cell (Fig. 3.2). The reaction mixture was prepared by admitting gas from the gas manifold to the loop to the desired pressure, as indicated by a -30 to 0 in Hg pressure gauge. Gas flows of up to 200 cm^3/min were achieved by a metal bellows pump and flow was detected by a Matheson #601 rotameter. Gas samples for hydrocarbon analysis were taken from the reaction loop through a 6-port sampling valve. A 3 liter Wallace and Tiernan 0-30 in Hg pressure gauge served as a reservoir for a CH_4/Ar calibration gas mixture. Finally, the loop could be evacuated through the gas manifold with either the mechanical pump or the sorption pump, and a nearby thermocouple gauge indicated the pressure.

The gas manifold was set up to supply the reaction loop, leak valves, or chamber with the appropriate gases. The above-mentioned mechanical pump and sorption pump were used for evacuation and the pressure measured with a thermocouple gauge. Two gas lines were devoted to hydrogen and carbon monoxide while a third line was shared between O_2 and Ar. Ethylene and ethane were also passed through the CO gas line.

3.1.4 Ion Sputtering Gun

A Varian ion bombardment gun equipped with a home-built power supply was used for coarse sample surface cleaning. This sputtering gun had x- and y-deflection capability also making it suitable for Low Energy Ion Scattering Spectroscopy (LEISS).

3.1.5 Titanium and Aluminum Evaporators

Titanium was deposited on samples by operation of the titanium evaporator which consisted of a U-shaped tungsten wire (0.020–0.030 in diameter, cleaned in a 2% HF/10% HNO_3 mixture) wrapped with a 0.020 in titanium wire (99.999% purity). The tungsten wire branched two 1/4 in copper feedthroughs mounted on a 2-3/4 in flange. Controlled exposures were accomplished with an externally-operated shutter. A stainless steel shield with an opening directed toward the sample encapsulated the assembly to prevent titanium evaporation elsewhere in the chamber. A collimator tube mounted on the shield also helped in directing the evaporation beam.

Aluminum evaporation required a different evaporator design. A 3/8 in alumina crucible with a 1/8 in hole in the bottom face was loaded with 0.060 in aluminum wire (99.9995% purity). This crucible, in turn, fits inside another slightly larger crucible so that aluminum was visible only through the 1/8 in hole. This second crucible was wrapped with 0.020 in tungsten wire (about 10–15 turns), each end of which was bound to 1/4 in copper feedthroughs on a 2-3/4 in flange. The crucibles and wire wrappings were covered by a third alumina crucible with a 1/16 in hole in the bottom face for one end of the tungsten wire to pass through. This evaporator assembly also had an externally-operated shutter for controlled exposures.

3.1.6 Analytical Equipment

Auger Electron Spectroscopy (AES): Analysis of Auger electrons for determination of surface composition was accomplished with a Varian 6-in cylindrical mirror analyzer (CMA) (Model 981-2607). A home-built internal electron gun, concentrically aligned in the CMA, produced a normal incidence, 2 kV electron beam. Electrons emerging from the single pass filter section were detected by a "channeltron" multiplier. The CMA, mounted on a metal bellows, could be moved closer or farther from the sample by means of a hydraulic pump. The theory of operation behind AES is discussed in Chapter 2.

Mass Spectrometer: An EAI 250B Quadrupole Mass Spectrometer served as residual gas analyzer and mass detector during TPD experiments. During the initial room temperature desorption experiments, the ionizer section was fitted with a tantalum collimator. The entire ionizer section was encapsulated prior to the series of low temperature desorption experiments with a tantalum shield, thus diminishing the background contribution to the desorption spectra. A description of TPD was given in the previous chapter.

Low Energy Electron Diffraction (LEED) Optics: A Varian LEED optics assembly, consisting of an electron gun, a high voltage grid, two retarding grids, and a phosphorescent screen, was mounted on the 8-in flange at the rear of the chamber. LEED was not employed as a primary analytical tool of the titania and alumina overlayers on the rhodium foil, so the discussion regarding it is limited to what has just been presented here.

Gas Chromatograph (GC): Separation and analysis of hydrocarbons sampled from the reaction loop was performed with a Hewlett-Packard Model 1720A Gas Chromatograph. A 1/8 in stainless steel column, 3 ft long, packed with Porapak N (active ingredient—cross-linked polymers) was maintained at 328 K with a nitrogen carrier gas flow of about 30 cm^3/min. The effluent gases from the column entered the flame ionization detector (FID) directly. The detector was supplied with hydrogen (about 30 cm^3/min at 40 psig) and compressed air (roughly 200 cm^3/min at 20 psig) and kept at 483 K. The interpretation of the GC output will be addressed at a later point.

3.2 XPS CHAMBER

Experiments were carried out in a Perkin-Elmer PHI Model 548 XPS Chamber on a short-term basis. Consisting of a stainless steel bell jar with a transfer cell attached (Fig. 3.3), a horizontal transfer rod (also referred to as the "probe") moved the sample between the two sections. All analytical and surface-modifying equipment was located at ports directed toward the axis of the probe. The CMA was located along the axis of the probe at the opposite end of the chamber from the transfer cell. A gas handling system was built for the chamber and transfer cell for treatment of the sample under a variety of conditions.

3.2.1 Pumps and Pressure Measurement

A chamber base pressure of 3 x 10^{-9} torr with the probe in the chamber (8 x 10^{-10} torr with the probe removed from the chamber) was maintained by a Perkin-Elmer ion pump. A Perkin-Elmer titanium sublimation pump aided in bringing the pressure down after large doses of gases (during sample preparation) or after exposure of the chamber to the transfer cell (during sample transferral). A Balzers turbomolecular pump was provided to maintain vacuum in the transfer cell or for pumping the UHV chamber during sputtering and oxidation treatments. The chamber could be "roughed" (after being brought up to atmospheric pressure for maintenance or modifications) with a liquid nitrogen-cooled sorption pump packed with molecular sieve. The chamber pressure was measured with a Bayard-Alpert type ion gauge; most of the chamber's electronics were interlocked with the ion gauge controller so as to shut off when the pressure reached the upper 10^{-5} torr range.

3.2.2 Sample Probe and Transfer Cell

The probe consisted of a 2-ft long, hollow, stainless steel tube, 1-1/2 in in diameter, welded at the chamber end to a disk with four feedthroughs: two for the chromel/alumel thermocouple and two for heating and support. The mounting of the sample was similar to that of the reaction manipulator of the Varian chamber—except that the sample had to be tilted about 45° off the axis of the probe to ensure that the photons from x-ray source could strike the surface and eject electrons that would enter the CMA.

Teflon seals in the housing around the circumference of the probe, sealing against the probe's outer diameter, prevented air from entering the transfer cell along the probe's length. Additional seals between the transfer cell and the chamber, along with pumping of the transfer cell by the turbo pump, isolated the chamber from the cell. Differential pumping inbetween the cell and ambient was available with a rotary-vane mechanical pump.

Two degrees of motion were available to the probe: horizontal motion along the axis of the probe and a rotary motion around the axis. The linear motion, which was motor-driven, allowed transport of the sample between the chamber and the transfer cell. Once the sample was in the transfer cell, a gate valve between the two sections could be closed to maintain UHV in the chamber. At this point, the sample could even be removed from the entire apparatus by continued withdrawal of the probe. Otherwise, the sample could be treated in the cell with various gases and simultaneous heating, and then later returned to the main chamber.

3.2.3 Gas Handling System

The chamber operated with two leak valves: one devoted to supplying argon to the chamber and the other for all other gases. The gas manifold could be filled with hydrogen, carbon monoxide, or oxygen. Evacuation of the manifold was accomplished with the rotary-

vane mechanical pump and the pressure was measured with a thermocouple gauge. Gases from the manifold could also be directed to the transfer cell; a -30 to 0 in Hg pressure gauge indicated the amount of gas admitted to the cell.

3.2.4 Ion Sputtering Gun

The sample surface could be cleaned with a Perkin-Elmer PHI (0-2 kV) ion sputtering gun. Positioned above the CMA, but at an angle so that the sample could be in its line of sight, the gun was situated for carrying out LEISS experiments; however, the CMA filter section was not set up for this function.

3.2.5 Titanium and Aluminum Evaporators

Samples were dosed with titanium and aluminum from evaporators of the same design employed in the reaction chamber. However, in the XPS chamber, the evaporators were located as far as 6 inches from the samples, as opposed to only about 2–4 in the reaction chamber.

3.2.6 Analytical Equipment

X-Ray Photoelectron Spectroscopy (XPS): XPS was employed for the determination of core electron binding energies of species in the near-surface region. The x-ray source, a Perkin-Elmer Model 04-548, consisted of a water-cooled assembly with two filaments, a magnesium anode and a aluminum window. The kinetic energy of emitted electrons was analyzed in the Perkin-Elmer double-pass CMA (Model 15-255GAR). The CMA included features for selection of energy window width and for angle resolving of the photoelectrons.

A "Channeltron" multiplier detected the filtered electrons. Data acquisition, storage, and analysis of XPS spectra was accomplished with an IBM PC interfaced with a Tracor Multichannel Analyzer.

AES: As in the reaction chamber, located along the axis of the CMA was internal an electron gun for producing a 2 kV beam of electrons. The CMA could be operated in either constant pass energy (XPS) or constant analyzer energy (AES) modes so it served as electron filter and detector for AES as well.

Mass Spectrometer: The chamber was equipped with a Balzers mass spectrometer; however, TPD experiments were not performed in this chamber.

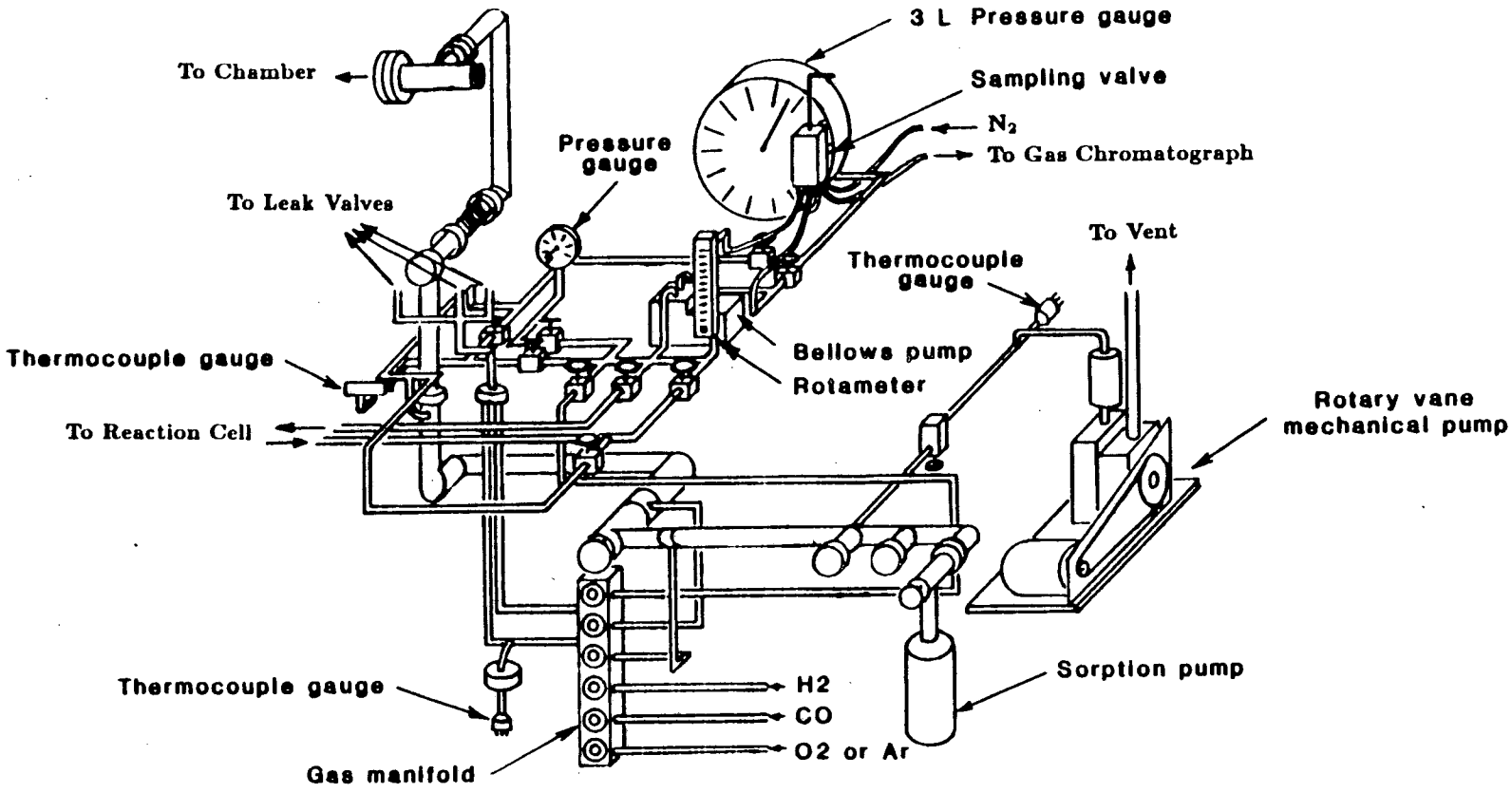

Figure 3.2: Reaction loop and gas handling system.

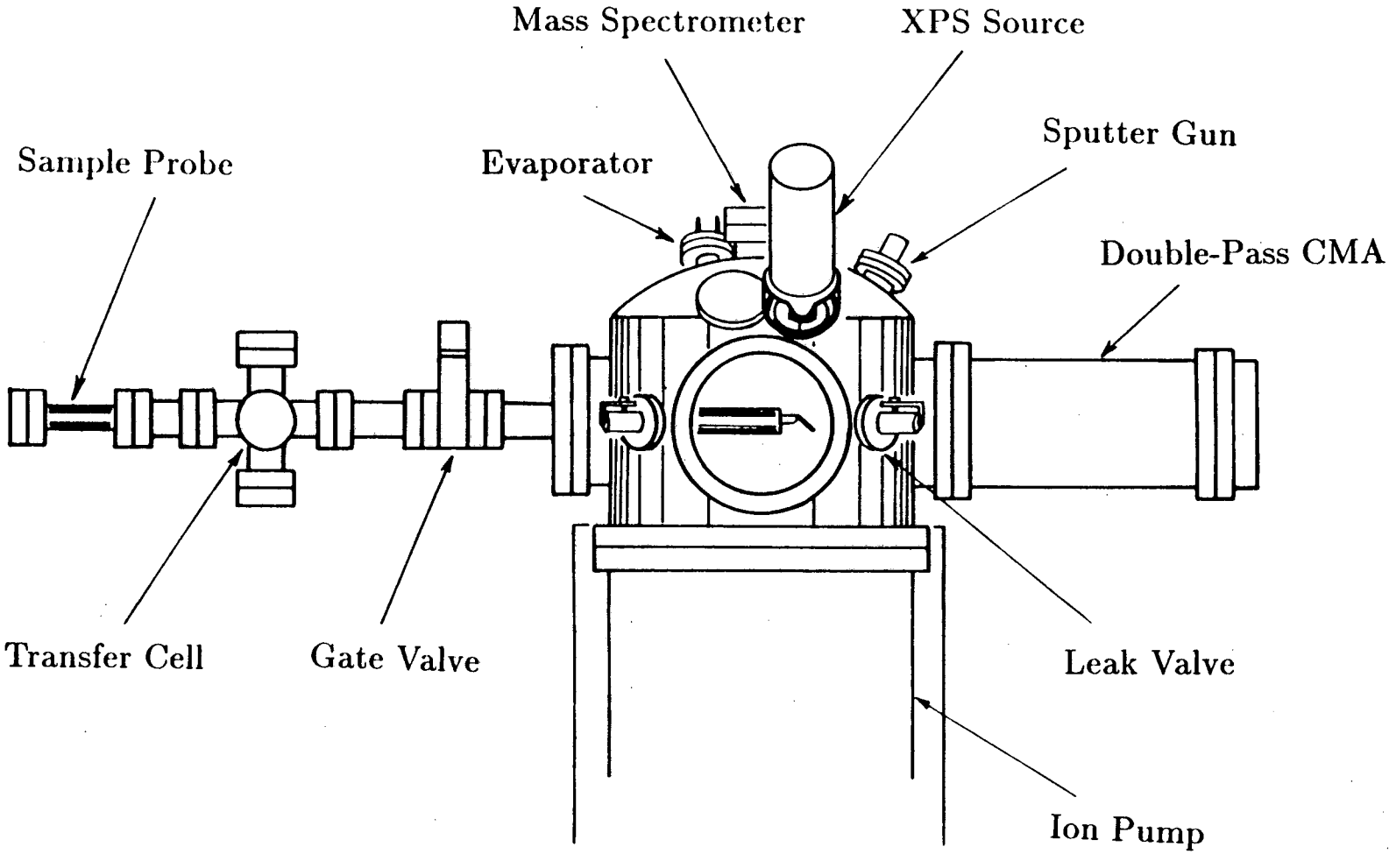

Figure 3.3: Ultra-high vacuum chamber for XPS analysis.

Chapter 4

EXPERIMENTAL PROCEDURES AND ANALYSIS

4.1 SAMPLE PREPARATION AND EXPERIMENTAL PROCEDURES

4.1.1 Preparation of Clean Rhodium Surfaces

Prior to chemisorption, reaction, or XPS analyses, fresh rhodium foil samples (99.8% purity) were cleaned by a variety of techniques to remove the most common impurities: carbon, oxygen, sulfur, chlorine, and calcium. Other contaminants from external sources included iron, nickel, and copper introduced from the sample holders, thermocouples, and spot-welder probes, respectively. Sometimes palladium was an impurity, as well, and probably arose from grains of palladium already present in the foil. Sample contaminants were detected by AES.

Removal of chlorine and calcium from the foil was most effectively accomplished with cycles of annealing and sputtering treatments. Annealing was done *in vacuo* at temperatures between 1270 and 1370 K and argon ion sputtering was performed at a pressure of 7-8 x 10^{-5} torr Ar. This method proved ineffective for Pd removal, necessitating sample replacement when palladium was a contaminant. Annealing alone was sufficient for oxygen removal, provided no other impurities were present.

Ion sputtering was the preferred technique for cleaning iron, nickel, copper and also alumina and titania from the surface. Small amounts of CO in the argon resulted in carbon and oxygen left on the surface following sputtering. Carbon, as well as sulfur, were easily oxidized off the surface by heating in the 10^{-7} to 10^{-5} torr range of O_2 at temperatures between 500–800 K.

During the oxidation treatment, the rhodium is likewise oxidized and this oxygen must be removed to ensure meaningful catalytic and especially chemisorption experiments. Annealing to temperatures of 1270–1370 K, as mentioned above, was quite effective for complete oxygen removal; however, heating to such high temperatures is not suitable when metal oxide overlayers are present due to dissolution of the overlayers into the bulk. A second method for surface oxygen removal was reactive titration with CO to form CO_2 and will be described in more detail in Section 5.1. Nearly all of the rhodium-bound oxygen was removed by cycles of CO exposure with subsequent heating to 773 K.

4.1.2 Deposition of Metal Oxide Overlayers

Alumina and titania overlayers were deposited on the Rh foil by operation of the evaporators described in the previous chapter. The procedure for aluminum evaporation involved positioning of the sample to obtain an even distribution and heating of the evaporator crucible with a DC power supply delivering roughly 15 amps at 8 volts. Preheating of the crucible for 5 minutes (with the shutter closed) brought the aluminum charge up to temperature, ensuring a steady evaporation rate. Utilizing the shutter for timed exposures, controlled amounts of aluminum could be deposited on the surface. An aluminum flux of $\sim 10^{12}$–10^{13} atoms/cm^2 s (estimated from the AES growth curves in Section 5.2) was typical. Prolonged operation of the evaporator for more than 30 min caused substantial heating of that portion of the chamber.

Titanium deposition was performed in a manner similar to that for aluminum. A preheat

period of no more than 30 seconds was necessary since the titanium metal was directly heated by the tungsten wire. Again, after positioning the sample, controlled exposures of the foil to the source were possible through use of the shutter. The power requirements of this evaporator depended on the tungsten wire gauge. No more than 3 VDC were needed and the current required ranged from ~20 amps for a 0.020 in W wire, ~26 amps for a 0.025 in wire, to ~35 amps for a 0.030 wire. The Ti flux, as estimated from titania monolayer growth rates in Chapter 5, was roughly 8 x 10^{12}–8 x 10^{13} atoms/cm^2 s.

Analysis by AES immediately after aluminum or titanium deposition showed surfaces with a substantial amount of oxygen and carbon on the surface. As will be seen later, XPS results indicate that for titanium, oxygen was associated with the Ti. It was not possible to prepare and maintain clean metal-on-metal surfaces even with base pressures in the 2–5 x 10^{-10} torr range. During evaporation, sufficient heating of nearby hardware in the chamber easily raised the pressure to the 10^{-8} to 10^{-6} torr range, making control of background H_2O, CO_2, and CO virtually impossible. Metal oxide overlayers were deposited on only one side of the Rh foil for the chemisorption and XPS studies, but on both sides for the reaction studies.

To assure complete oxidation of the deposited alumina or titania, the sample was treated in O_2 at pressures between 2 x 10^{-7} to 5 x 10^{-6} torr and 500–700 K, depending on the extent of carbon contamination and the oxygen deficiency. The steps in overlayer preparation are depicted in Fig. 4.1. Excess oxygen bound to the Rh was then removed by titration with CO to form CO_2. The formation of a nearly-stoichiometric titanium oxide was facile and could at times be done without heating above 470 K. As will be seen, the order of sensitivity of the analytical techniques to the ultimate oxidation state of the oxide overlayer, from most to least, was XPS, AES, CO TPD, and finally reaction analysis (CO hydrogenation). XPS analysis was quite sensitive to variations in oxide stoichiometry barely detectable by AES. For that reason, more extreme oxidation conditions (773 K, 2 x 10^{-6} torr O_2) were generally used in the XPS-related experiments to form a near-stoichiometric oxide.

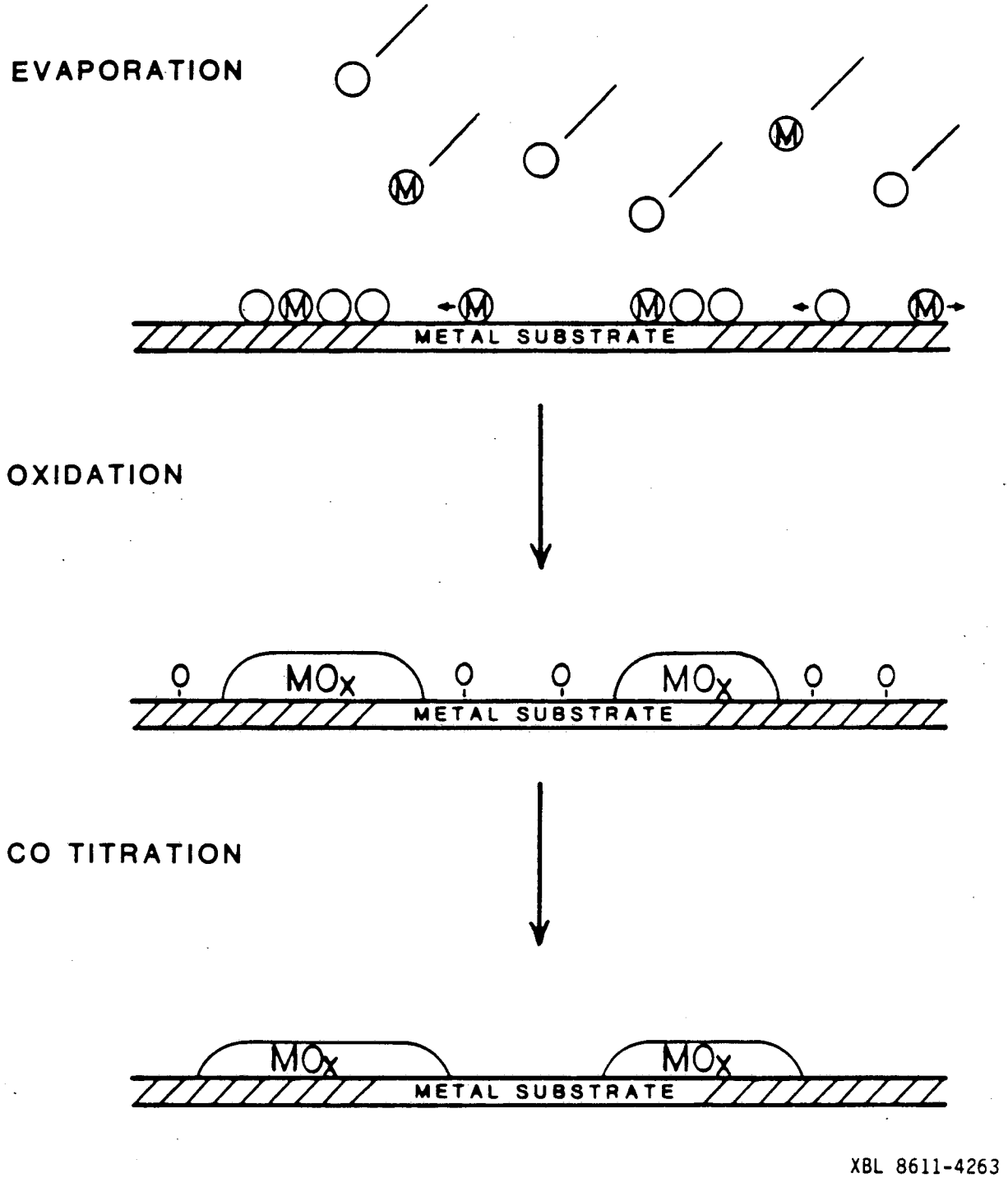

Figure 4.1: Schematic representation of metal oxide overlayer deposition on metals.

4.1.3 Operation of AES and XPS

Analysis of the sample by AES, especially with metal oxide overlayers present, consisted of scans at three points per face from the top of the sample to the bottom. This ensured identical compositions across the sample. Variations of less than ±0.05 ML were considered acceptable.

During AES analysis in the reaction chamber, the AES electron gun was operated at a beam voltage of 2 kV with a beam current (as measured by the gun power supply) of 50–100 μamps. This corresponded to an actual beam current hitting the sample of between 10^{-7} to 10^{-6} μamps. Low beam currents are preferred, in spite of weaker signals, to lessen damage to the surface. (For example, on occasion, reduction of the titania overlayer from $\sim TiO_2$ to $\sim$TiO has occurred.)

Auger electrons were energy analyzed by sweeping the voltage on the outer cylinder of the cylindrical mirror analyzer linearly with time from -20 eV to as much as -1000 eV. A ramp rate of roughly -30 eV/s was used. A modulating voltage of 2 V peak-to-peak at a frequency of roughly 3000 hz was superimposed upon the sweeping voltage to facilitate differentiation of the spectrum. Electrons emerging from the filtering section were detected with a "channeltron" multiplier operated at voltages ranging from 1.2 to 2.2 kV (as warranted by the detector sensitivity).

Conditions for AES analysis in the XPS chamber were similar to those in the reaction chamber. A 2 kV electron beam was used at about 50–200 μamps beam current (as measured by the gun control) while a 2 volt peak-to-peak modulation was employed. The ramping voltage rate was -20 eV/s and the multiplier voltage used was 900–950 V.

The XPS source was operated at a voltage between 13.5 and 15.0 kV with a total power to the anode of 300 W divided equally between the two filaments. No detectable amount of heating of the sample by the source occurred during XPS analysis.

The photoelectrons were energy analyzed with ramping voltages for the inner and outer cylinders at a pass energy of 25 eV. The principal core level peaks of Rh, Au, Ti, Al,

and O were sampled with an spectrum energy window of ~25 eV width. Electrons were detected by a "channeltron" multiplier operated between 1.8 and 2.5 kV (as warranted by the sensitivity) and in a pulse-counting mode. Pulse counts were displayed on a video monitor divided into 256 channels for the 25 eV sweep width.

4.1.4 Temperature Programmed Desorption Operation

The removal of chemisorbed species from the surface of the Rh foil by TPD was performed with ramp rates of 50 K/s and 15 K/s. The 50 K/s rate was employed for CO chemisorption on the TiO_x/Rh and TiO_x/Rh (H_2 reduced) systems; the 15 K/s rate was used on all later studies (CO on TiO_x/Rh at low temperatures and CO on AlO_x/Rh). No significant effects from different ramp rates on the normalized amount of CO chemisorbed as a function of titania coverage were observed.

Typical conditions for mass spectrometer operation during TPD were: filament current–250 ma, electron energy–90 V, and an electron multiplier voltage of 2–3 kV, as needed. The mass spectrometer signal was amplified with a picoammeter and plotted as a function of time on a chart recorder. For any given coverage, cycles of CO exposure and flashing to 773 K were repeated until the peak area no longer changed. Calibration of the mass spectrometer signal, by leaking CO into the chamber to an observed pressure, followed each series of thermal desorptions.

Temperature programmed desorption of hydrogen was attempted, but problems associated with sample cooling and background gas adsorption prevented acquisition of meaningful results. The lowest steady operating temperature available with a liquid nitrogen-cooled manipulator was 150 K and during the time required for cooling (after flashing), background water and CO were found to chemisorb on the surface.

4.1.5 Operation for Reaction Studies

After a sample was prepared for a catalytic study, the manipulator was raised until the sample holder rested against the sample holder support. The lower part of the reaction cell was then brought up high enough to enclose the sample and was seated against the sample holder. Evacuation of the entire reaction loop followed.

The next step in preparation for a reaction involved admission of the reactant gases into the reaction loop to form the reaction mixture. Argon was admitted into the loop directly from the bottle after evacuation of the gas line. Both the hydrogen and carbon monoxide lines contained molecular sieve traps. The hydrogen (99,95% purity) was purified by immersion of its trap in liquid nitrogen while metal carbonyls were removed from the CO (99.5% purity) by resting the CO trap just above the surface of the liquid nitrogen. Hydrogen had to be added last to enable usage of the sorption pump for evacuating the gas lines. Ethylene (99.5% purity) and ethane (99.95% purity) entered the loop without further purification.

Pressures in the loop were measured by a mechanical gauge (30 cm^3 volume) that could be valved shut during reaction. Typical reaction gas mixtures were: CO hydrogenation—0.33 atm CO, 0.67 atm H_2; ethylene hydrogenation—25 torr C_2H_4, 25 torr H_2, and 710 torr Ar; and ethane hydrogenolysis—25 torr C_2H_6, 25 torr H_2, and 710 torr Ar. Reactions were always carried out at a total pressure of 1 atm so as not to exceed chamber design limitations and to facilitate circulation by the metal bellows pump. In the case of partial pressure dependence studies for CO hydrogenation, argon was used as a make-up gas while a lower reactant partial pressures was used.

When the desired gas mixture was attained, the pressure gauge was isolated and circulation of the gases began. Flow rates from the pump were usually around 200 cm^3/min, as determined by an in-line rotameter. For the CO hydrogenation reaction, the gases were circulated for 20 minutes prior to heating the sample to reaction temperature. For ethane hydrogenolysis this time period was 10 minutes and for ethylene hydrogenation, less than

a minute. In the case of the latter reaction, the activity at room temperature prompted immediate heating of the sample. From the plots of reactant consumption-vs.-time, a 10-minute circulation period appeared to be sufficient for adequate mixing of the reactants in the reaction loop.

During the CO hydrogenation reaction, gas samples were taken 5 minutes after heating began and then at 10–15 minute intervals thereafter. The reaction was maintained for 1–2 hours. Similar gas sampling intervals were employed for ethane hydrogenolysis and ethylene hydrogenation and these reactions were monitored for roughly one hour.

The gas samples reached the gas chromatograph via a nitrogen carrier gas with a flow rate of 20–30 cm^3/min. Separation of the hydrocarbons took place in a 6-ft Porapak N column (1/8 in diameter) held at 328 K. (During the ethylene hydrogenation reaction, the temperature was lowered to 300 K to enhance the C_2 separation). All C_1–C_2 hydrocarbon products could be easily separated within 10 minutes while the propylene overlapped time-wise into that sample (but usually separate from the next sample's peaks). The separation of ethylene and ethane in ethylene hydrogenation required a total time of 20 minutes, but these two hydrocarbons emerged within a time frame of only 10 minutes. The signal was plotted versus time on the X–Y chart recorder.

The reaction was terminated by cutting power to the temperature controller and evacuating the reaction loop with the mechanical pump. The reaction cell was then isolated from the reaction loop and the pressure brought to under 25 microns by use of the sorption pump. The cell was then opened, causing a pressure burst in the UHV chamber up to the 10^{-6} torr range. While the chamber pressure dropped back to the 10^{-8} torr region, the reaction loop (now by-passing the reaction cell) was filled with a 1% CH_4/Ar mixture stored in the 3 L pressure gauge. The gas was then circulated for a few minutes while 2 or 3 gas samples were taken to calibrate the gas chromatograph. The pressure of the calibration gas was read from the 3 L pressure gauge (prior to gas circulation) as part of the calibration procedure. (After numerous reactions, when the calibration gas mixture was depleted to 1/2 or 1/3 of atmospheric pressure, more argon was added to increase the lifetime of the

mixture and facilitate pumping by the metal bellows pump. The dilution of the gas was incorporated into the calibration calculations.)

The final step involved characterization of the surface after reaction by AES. In particular, the amount of carbon deposited during reaction was of interest. Again, three scans were taken of each side before the sample was prepared for another experiment.

4.2 METHODS OF ANALYSIS

4.2.1 AES Data Analysis

The standard method of extracting information from Auger spectra is measurement of peak-to-peak heights for each elemental peak. In a multi-component system, these heights do not directly convey information regarding surface composition without knowledge of the surface atoms' configuration (*e.g.*, whether the top surface layers have a uniform composition or alternating layers of specific compositions) and the sensitivities for each element (*e.g.*, the cross-section for AES and the penetration depth of Auger electrons). For the case of uniform surface composition, the following form has been suggested [73]

$$c_i = \frac{(I_i/S_i)}{\sum_j (I_j/S_j)} \tag{4.1}$$

where the surface concentration, c_i, of species i is expressed in terms of the signal intensities, I_j, and the corresponding sensitivity factors, S_j, of all species present. The sensitivity factors were determined by comparison of signals from (usually) single-component samples. This approach though, is not appropriate for the study of deposited overlayers on a substrate.

There is an additional complication, as well. The total signal strength depends upon the sample position relative to the CMA. In the process of preparing and analyzing metal oxide overlayers, the sample must be moved to various positions in the UHV chamber. Because a precision manipulator is not employed in this study, each time the sample is returned for

AES analysis, it ends up in a different position, and hence, gives a different signal intensity.

To counteract this problem, it is assumed that the relative contribution of each element in the spectrum is constant. These signals are weighted by the elemental sensitivities described above [73]. When the signals are normalized with respect to the total contribution, an equation identical to Eqn. 4.1 is obtained, but its interpretation is different. As in Eqn. 4.1, only one peak, the "principal" peak, is considered per element. The sum of the normalized elemental contributions, then, is unity.

Sensitivity factors for most elements have been published [73] for incident beam voltages of 3, 5 and 10 keV. These were obtained in a system also equipped with a single-pass CMA. To determine the appropriate values for a beam voltage of 2 kV, quadratic interpolation was employed. Sensitivity factors for all four beam voltages for the pertinent elements are listed in Table 4.1.

A different procedure was employed to determine the aluminum sensitivity factor. Upon oxidation, a new aluminum peak emerges at an energy of 55 eV (metallic aluminum appears at 68 eV), so a sensitivity factor for aluminum metal may not be applicable for aluminum in aluminum oxide. The value for aluminum oxide used in this study was calculated from

Table 4.1: AES SENSITIVITY FACTORS

	10 keV*	5 keV*	3 keV*	2 keV (from interpolation)
C (272 eV)	0.075	0.12	0.19	0.236
Ca (291 eV)	0.22	0.40	0.46	0.487
K (252 eV)	0.35	0.90	0.77	0.630
O (510 eV)	0.35	0.40	0.50	0.567
Rh (302 eV)	0.48	0.67	0.64	0.602
S (152 eV)	0.57	0.73	0.80	0.836
Si (92 eV)	0.30	0.28	0.35	0.402
Ti (418 eV)	0.24	0.33	0.44	0.511
Al (68 eV)	0.075	0.18	0.23	0.257
Al (55 eV)				0.505 (from an Al_2O_3 sample)

*From Ref. [73]

an AES spectrum of a bulk alumina sample.

In a manner described in Chapter 2, AES intensities-versus-evaporation time plots can provide information regarding the overlayer coverage. After determination of this relationship, the AES spectra for each part of the sample (3 per side) were converted into their corresponding coverages. The global coverage, which is plotted as the abscissa in many of the figures, is taken as the average over these localized coverages.

Modifications of the AES data handling procedure had to be made when small amounts of carbon or oxygen contaminants were present on the surface. Carbon usually attenuated the Rh signal relative to that of Ti indicating the carbon was covering Rh sites. As mentioned above, some residual oxygen was left on the rhodium, even after CO titration, so that at very low titania coverages, the AES O/Ti ratio was much higher than expected. The "normal" raw O/Ti ratio for coverages above 0.30 ML was about 1.7. To account for these species on the surface when calculating the overlayer coverage, the AES intensities of carbon and excess oxygen were lumped into the Rh intensity.

4.2.2 XPS Data Analysis

Of the elemental transitions investigated (Ti(2p), O(1s), Rh(3d), Al(2p), and C(1s)), data analysis was performed only on the Ti(2p) and O(1s) transitions. The Rh(3d) transitions showed no shifts or additional features to warrant extensive analysis. The objective in the analysis was to find the areas of the individual peaks contributing to the overall spectrum. For titanium, these peaks represented the presence of Ti^{3+} and Ti^{4+}, whereas for oxygen, Ti–O–M (M = Ti, Rh) and Ti–OH species.

A modified version of Dr. Bruce Beard's XPS analysis program was employed (the modification will be discussed shortly). The first step involved smoothing of the data. The routine compared the signal for each channel with the average of the neighboring 6 data points. A "discriminator value" input was required which related the difference between

the signal and average for a channel to the square of the maximum value of the signal in the spectrum. Larger discriminator values resulted in a lower degree of smoothing. The discriminator value typically employed was between 1.5 and 2. Smoothing was found to be necessary for the Ti(2p) spectra, especially at low coverages and after a hydrogen reduction treatment. Satellite peaks arising from secondary emissions of the Mg source were then removed from the spectrum.

At this stage, the spectrum was ready for peak deconvolution. The program was originally written to sum Gaussian-shaped peaks and compare with the collected spectrum. The position and shape of each Gaussian was determined by input parameters given by the operator. To modify the fit of the peaks, changes needed to be made to these parameters. The baseline was determined from 2 points (specified by the operator) and the reversed "sigmoidally-shaped" line calculated from an exponentially-based function.

The program was modified to allow fitting of the peaks with Doniach-Šunjić lineshapes [115] (see Chapter 2) as well. These lineshapes have a theoretical basis related to interactions between ejected electrons and the delocalized metal electrons. The shape of these peaks is essentially Lorentzian with an asymmetry factor to account for the electron interaction at higher binding energies (= lower electron kinetic energies) as in Eqn. 2.6. With this feature, a "signoidally-shaped" baseline is not required. Instead, a routine to draw a parabolic baseline based on three spectrum points (operator-chosen) was incorporated.

For the Ti and O peak deconvolutions, asymmetry factors of zero were employed, since titania is not metallic. The Ti(2p) region was fitted with four component peaks and the O(1s) region with two. Again, all peak parameters were adjusted by the operator. Example spectra with the individual peaks and their sums are shown in Fig. 4.2.

4.2.3 TPD Data Analysis

A simple procedure was employed for thermal desorption analysis. Applied usually to

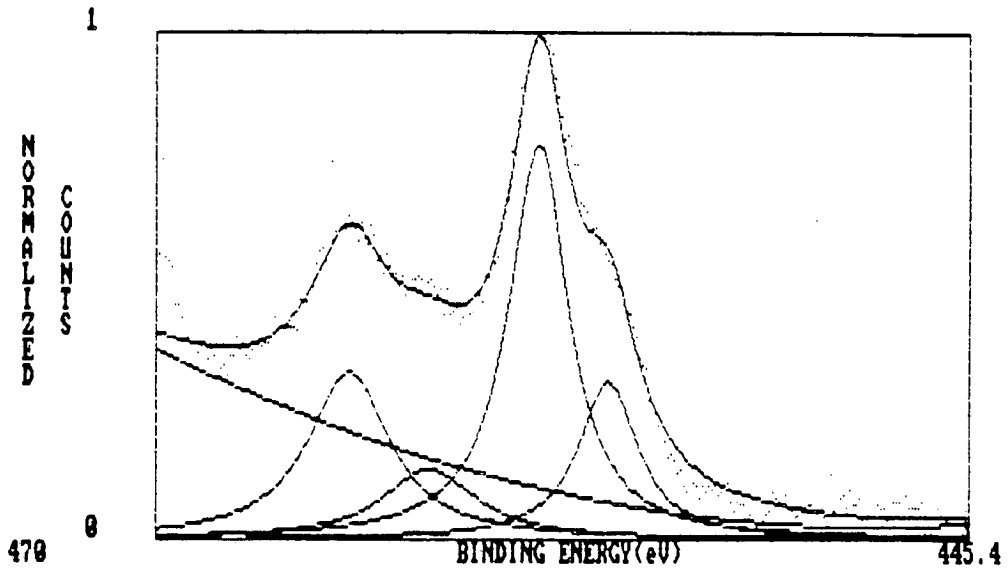

(a)

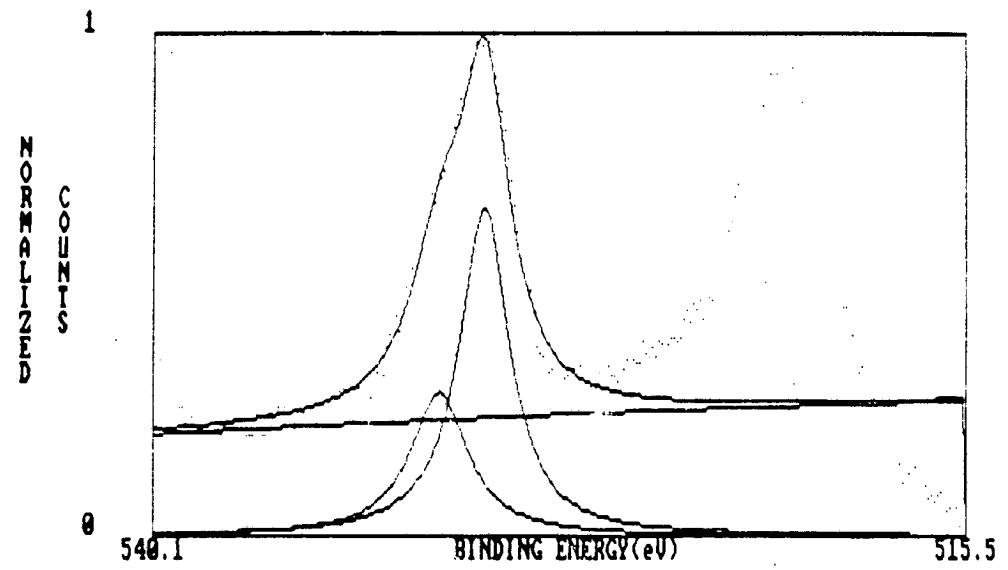

(b)

Figure 4.2: Examples of XPS aquisition program output, each with the sum of the deconvoluted peaks for (a) Ti(2p) and (b) O(1s).

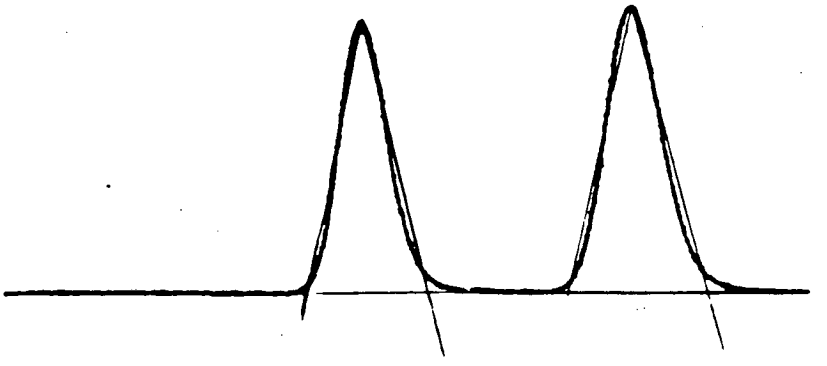

Figure 4.3: Examples of gas chromatograph peaks with lines drawn in for determination of the area.

CO and CO_2 peaks, the areas were found by reproducing the desorption curves on graph paper, reading off 11–17 curve heights at regular intervals, and implementing Simpson's rule integration. The area was then adjusted according to the calibration signal for the spectrum. Peak temperatures were interpolated from temperature markings taken on the spectrum. This information was then related to the overlayer coverage or pretreatment conditions.

4.2.4 Reaction Rate Data Analysis

Gas chromatograph peaks were first integrated to determine the areas, then converted into moles from calibration data, and then plotted as a function of time to find the reaction rate. Integration was carried out by triangulation—a baseline was drawn for each peak and a triangle made that approximated the area of the peak. Peak areas missed by the triangulation, such as at the beginning and end of the baseline, were compensated by extra area included in the mid-section of the peak (see Fig. 4.3).

The areas of the methane calibration peaks were also calculated in this manner. Com-

parison of the average of the calibration gas peak areas with those of the reaction gas, and taking into account the respective gas pressures, the temperature, and reaction loop volume, the areas could be converted into moles of hydrocarbon. Peak areas were divided by the corresponding species carbon number since the area from a flame ionization detector is roughly proportional to the total number of carbon atoms of that species. When all of the above factors are incorporated into one equation, the result is

$$n_{HC} = 57.25 \times 10^{-6} \frac{P_{cal}}{m_c} \frac{A_{HC}}{A_{CH_4,cal}} \tag{4.2}$$

where n_{HC} is the number of moles of a given hydrocarbon, A_{HC} the corresponding GC peak area, and m_c the carbon number. The quantities, P_{cal} and $A_{CH_4,cal}$ refer to the calibration gas pressure and GC peak area, respectively. The constant incorporates the reaction loop volume and other invariant factors. When originally calculated, a reaction loop volume of 140 cm^3 was used. It was later found that the actual volume was only 125 cm^3. All reaction rates are therefore overestimated by about 12%. However, when it is considered that this applies to all rates, and taking into account the inherent error in experimental reaction rate measurement of this kind (~20%), the error in reaction loop volume is probably of little consequence.

Reaction rates were found from the initial slope of product accumulation-versus-time curves. Linear regression was applied to the first 4–6 data points, representing the initial 30–40 minutes of reaction. Rates were usually expressed in terms of moles/s, not molecules/site-s, since, when the surface is partially covered by a metal oxide, the number of active sites (and of which type) is not known. In addition, since reactions were performed on a foil rather than a single crystal, the actual number of surface atoms is not known.

Chapter 5

EXPERIMENTAL RESULTS

5.1 THE PROPERTIES OF RHODIUM FOIL

5.1.1 TPD from Clean Rhodium

The chemisorption behavior of CO on rhodium was investigated prior to the deposition of metal oxides. The amount of CO chemisorbed at room temperature, as indicated by temperature programmed desorption, was measured as a function of CO exposure. Typical TPD spectra appear in Fig. 5.1 and the corresponding curve areas are plotted in Fig. 5.2. Above exposures of 1.6 Langmuirs (L) (1 L = 10^{-6} torr-sec), the amount of CO chemisorbed becomes relatively insensitive to coverage. In all subsequent CO TPD experiments, exposures of 4 L were used, equivalent to roughly 75% of saturation coverage.

The position of the peak maximum and the peak development with CO exposure correspond well with that for the Rh (111) [118,119] and Rh (110) [120] surfaces. The low temperature contribution characteristic of the Rh(100) surface was not observed for the Rh foil. No irreversible decomposition of CO was detected after thermal desorption, as indicated by AES.

Since, as will be seen later, deposited aluminum and titanium are oxidized to form oxide overlayers, the effect of oxidation on the chemisorption behavior of CO on rhodium has been investigated. Exposure of the oxidized Rh foil (773 K in 9 x 10^{-6} torr O_2 for 5 minutes) to

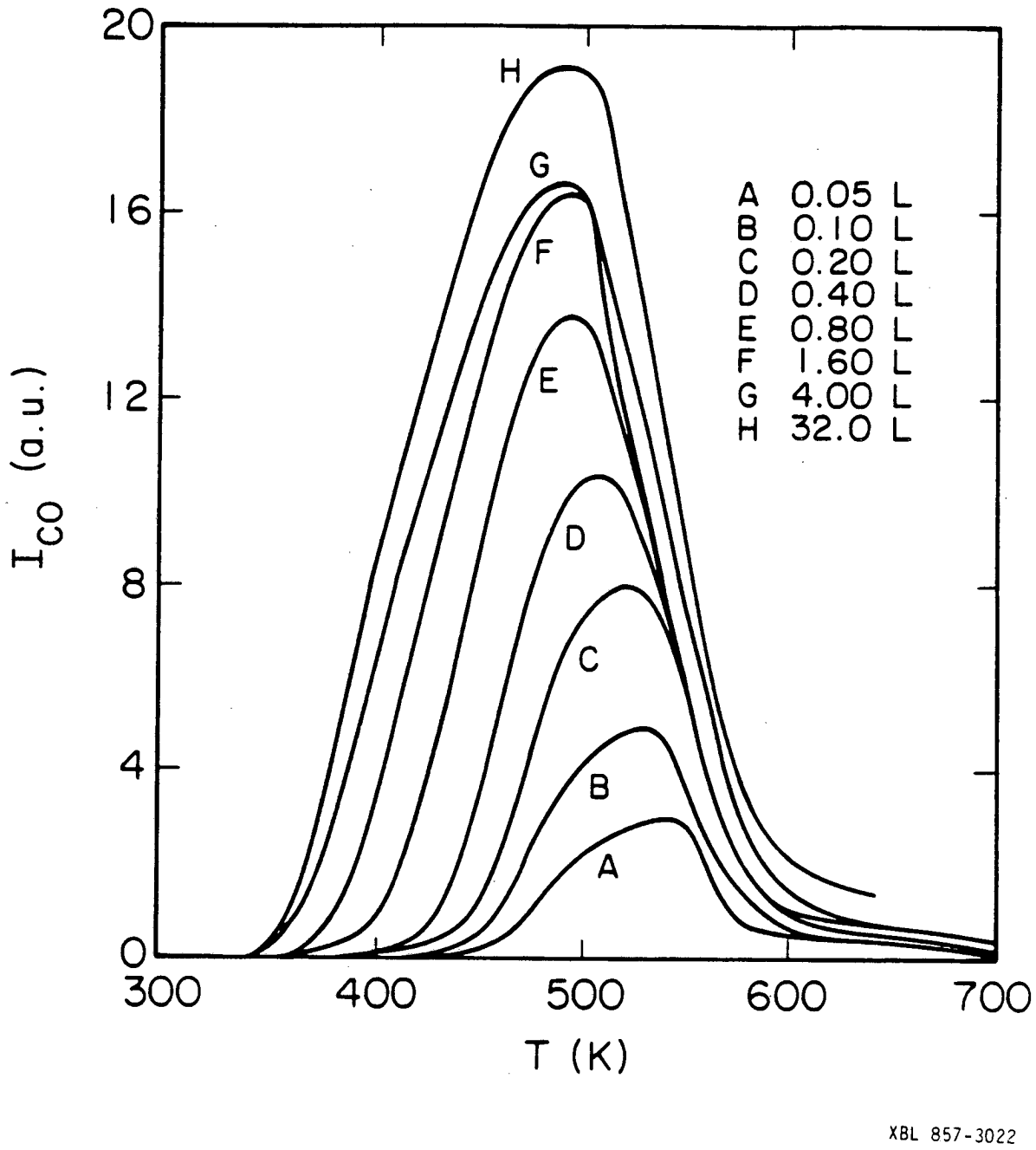

Figure 5.1: Temperature programmed desorption spectra of CO from clean Rh foil with varying exposures (CO adsorbed at room temperature).

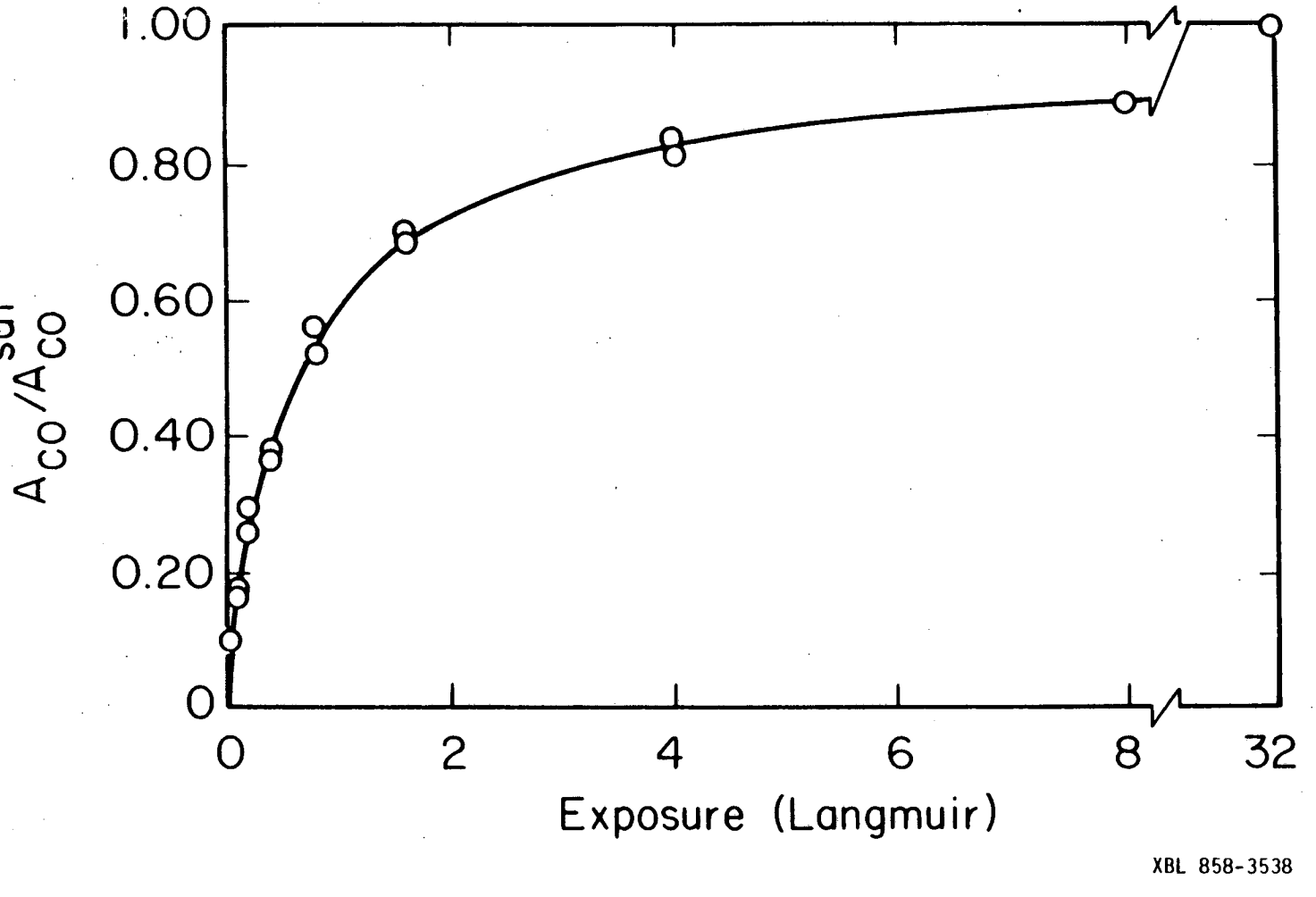

Figure 5.2: Surface CO coverage (normalized) as a function of exposure.

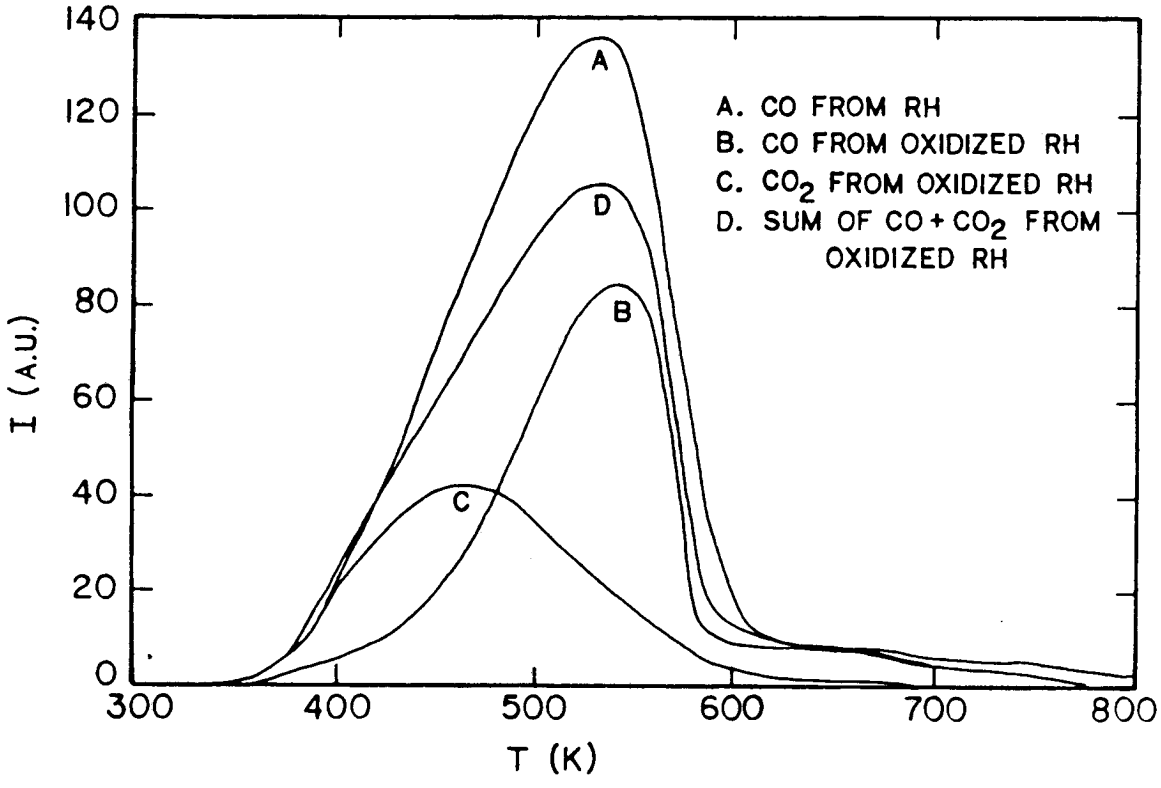

Figure 5.3: Temperature programmed desorption spectra of CO and CO_2 from Rh foil: (a) CO TPD from clean Rh foil, (b) CO TPD from an oxidized Rh foil, (c) CO_2 TPD from an oxidized Rh foil, (d) the sum of the CO and CO_2 TPD spectra.

4 L CO followed by heating results in the evolution of CO_2 as well as CO. Examples of CO and CO_2 TPD spectra are shown in Fig. 5.3 (curves a and b). The sum of these two peak areas (curve c) is seen to be roughly 70 - 80 % of the peak area for CO chemisorbed on clean Rh (curve d). The removal of surface oxygen by CO to form CO_2 was also observed by Watson and Somorjai for bulk rhodium oxides [121].

Not all surface oxygen is removed during the first CO titration. The behavior of the CO_2 TPD spectrum during subsequent CO exposures to remove the remaining surface oxygen is quite complicated. The peak temperature has been observed to shift as much as 120 K,

while the desorption area progresses through a maximum. At the same time, the CO peak area converges toward its clean Rh value. After 5 or 6 such exposures, virtually no CO_2 is formed and the CO TPD area has converged to the clean Rh value.

Oxidation was also performed by exposing the sample to 50–150 torr O_2 at 420 K in the reaction cell. Initially, no CO was observed upon heating. After the third treatment, CO was seen during desorption and after 10 or 11 exposures, only CO was observed. Coinciding with this process, the AES oxygen peak intensity decreased monotonically with each additional CO treatment.

5.1.2 CO Hydrogenation Kinetics

The reaction kinetics for methane formation from CO and H_2 over rhodium were investigated. The methanation rate at 553 K and 1 atm of H_2 and CO (H_2:CO = 2:1) was 19.4 x 10^{-11} mole/s corresponding to a turnover frequency of 0.037 molecules/site-s based on a Rh site density of 1.6 x 10^{15} cm^{-2} for each side of the foil. (This site density is calculated for a Rh(111) surface with a Rh atomic diameter of 2.69 Å). Logan *et al.* [122] found a turnover frequency of 0.26 molecules/site-s for a H_2:CO ratio of 2:1, 573 K and 6 atm. Based on their observed activation energy of 25 kcal/mole, their turnover frequency at 553 K would be 0.12 molecules/site-s. The discrepancy in the absolute reaction rates can be partially attributed to the different operating pressures (1 atm vs. 6 atm). In addition, it was not uncommon to see variations in the rate by factors of 2 or more for different Rh foil samples taken from the same Rh sheet. These differences are presumably due to variations in the defect densities of the samples.

The kinetic parameters of this reaction were determined, based on a power law model of the form

$$R_{CH_4} = A\exp(-\frac{E_A}{R_G T})p_{CO}^{m} p_{H_2}^{n} \qquad (5.1)$$

where R_{CH_4} denotes the methanation rate, T the absolute temperature, and p_{CO} and p_{H_2} the reactant partial pressures, and R_G the gas constant. An activation energy, E_A, of 24.4 ± 0.3 kcal/mole was found for methane formation, in agreement with other published results [122,123]. The hydrogen reaction order, n, was found to be 1.0 ± 0.2 and the carbon monoxide reaction order, m, -1.0 ± 0.5. These results are summarized in Table 5.1. The selectivities observed match those of Logan and Somorjai except that the specific product identification differs. In their results, all C_2 hydrocarbons were assigned as ethane and the C_3 hydrocarbons as propane. Calibration studies in this work indicate the formation of ethane, ethylene, and propylene—ethylene being the principal C_2 product.

5.1.3 C_2H_4 Hydrogenation and C_2H_6 Hydrogenolysis Kinetics

The hydrogenation of ethylene to ethane at temperatures between 293 K and 343 K was also studied. With Pt support wires at room temperature, a significant background hydrogenation rate was observed. To reduce the relative contribution of the reaction loop and support wires, the Rh foil was mounted on gold support wires and reactions were performed at 323 K. The background rate was then subtracted from the measured rate. The reaction rate at 323 K (for 25 torr of ethylene, 25 torr of hydrogen, and 710 torr argon) was 25.2 x 10^{-9} mole/s (TOF = 4.7 molecules/site-s) with an apparent activation energy

Table 5.1: KINETIC PARAMETERS FOR CO HYDROGENATION

$$R_{CH_4} = A\ EXP(-\frac{E_A}{R_G T}) p_{CO}^m p_{H_2}^n$$

	Rh	AlO_x (0.4 ML)	TiO_x (0.2 ML)
E	24.4	24.7	19
m	-1.0	-0.6	-0.3
n	1.0	1.1	2.4

of 6.1 kcal/mole. Possible explanations for the low activation energy (compared with 12–13 kcal/mole elsewhere [124,125]) will be discussed later.

The rate of methane formation from the cracking of ethane was 15.7 x 10^{-9} mole/s (TOF ~2.4) at 513 K. The reactant gas consisted of 25 torr ethane, 25 torr hydrogen, and 710 torr argon. The activation energy at 513 K was 12 kcal/mole while at 160 K, it was 35.4 kcal/mole.

5.2 THE PROPERTIES OF RHODIUM WITH ALUMINA OVERLAYERS

5.2.1 Alumina Overlayer Deposition and Characterization

Aluminum was vapor-deposited onto the Rh surface according to the procedure outlined in the previous chapter. An example AES spectrum of the alumina/rhodium surface (≈ 1 ML) is given in Fig. 5.4. To determine the overlayer growth characteristics, changes in the AES peak intensities (after oxidation and CO titration) were analyzed with respect to increasing alumina dosage. The AES peak intensities, both raw and normalized, are plotted in Figure 5.5 as a function of dosing time. The trends in each are similar, so attention will be focused on the plot of normalized signals where the noise level is diminished. (The process of signal normalization with the employment of sensitivity factors is described in detail in Chapter 4.) Initially, the Rh substrate peak decays linearly with deposition time, while the Al and O peaks grow linearly. After about 5 minutes of Al evaporation, the suppression of the Rh signal diminishes to a lesser extent with increasing coverage, with corresponding changes for the overlayer signals.

The initial region of linear decay for the substrate can be attributed to the growth of a two-dimensional monolayer. Monolayer coverage is assigned to the point where the deviation from linearity occurs. The development of the second and third layers would be expected

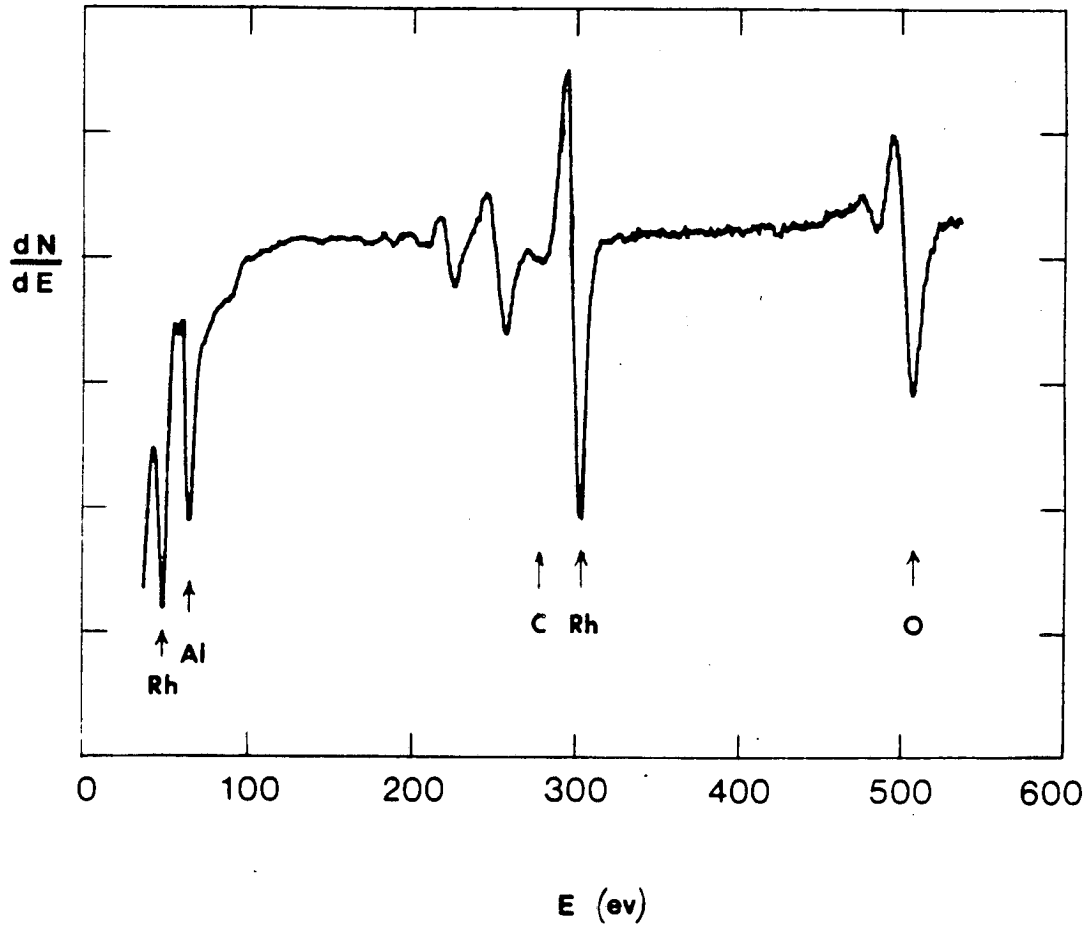

Figure 5.4: AES spectrum for ~1 ML of AlO_x on Rh.

to follow the dashed lines in this plot. Three-dimensional growth follows completion of the monolayer since the substrate intensities lie above these lines. This growth mode is commonly referred to as "Stranski-Krastanov" growth (see Chapter 2).

Monolayer coverage corresponds to an attenuation of the Rh (302 eV) peak intensity to 45% of the bare Rh value. Since an attenuation to 50–60% is typical for electrons of this energy (see Table 2.1), the alumina "monolayer" may actually be thicker than typical metal monolayers. This does not seem unreasonable for a multi-component (Al and O) overlayer. The linear decay in the Rh signal up to a coverage of 1 ML allows calculation of coverages in this range by linear interpolation.

The method of Gorte *et al.* [64] for monolayer determination, which consists essentially

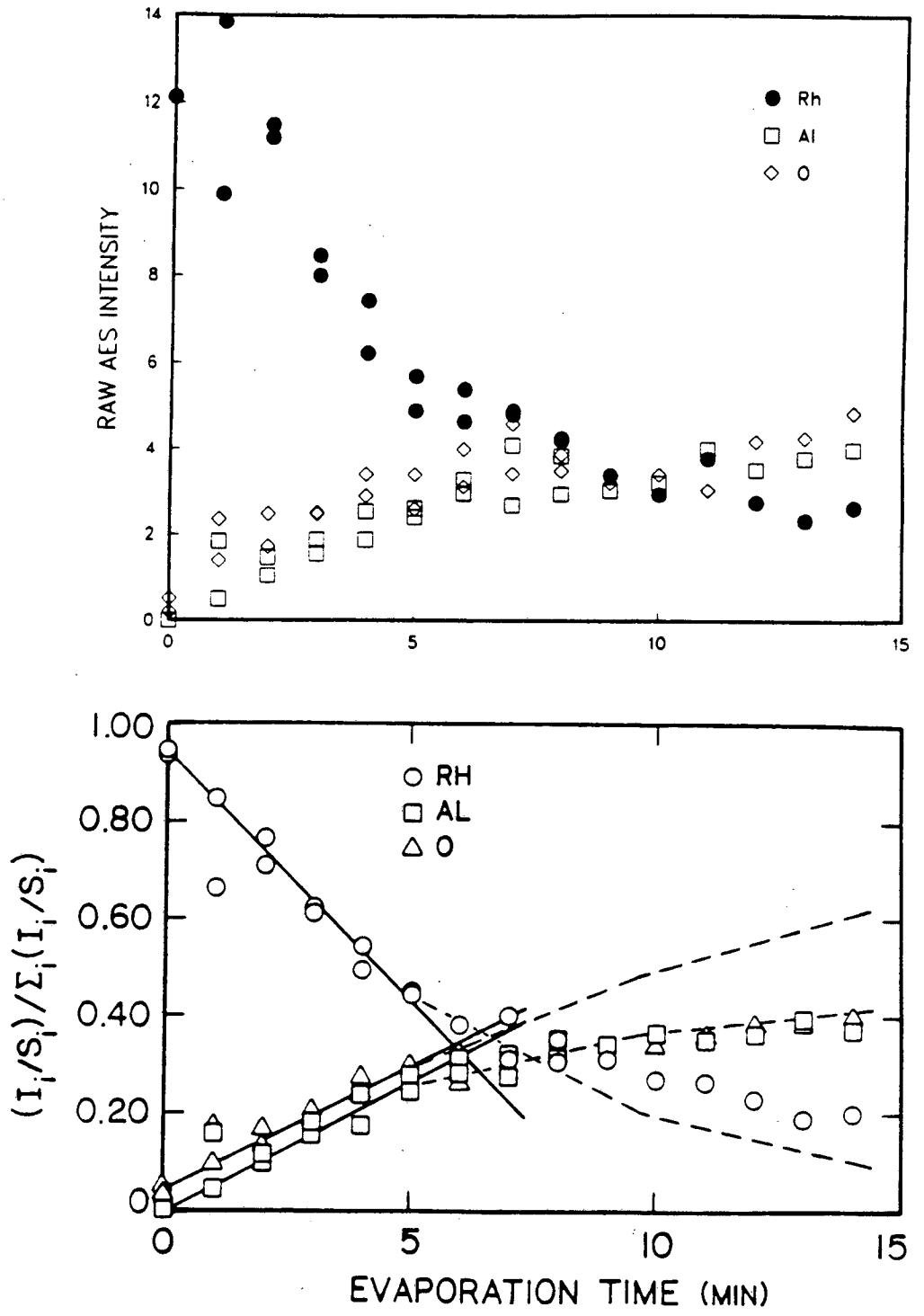

Figure 5.5: Auger peak-to-peak intensities corresponding to the growth of the AlO_x overlayer on Rh foil. Plot (a) shows the raw AES intensities and plot (b) the normalized AES intensities as functions of Al dosing time. The expected trends for two-dimensional (layered) growth are depicted by the solid (< 1 ML) and dashed (> 1 ML) lines.

of counting the number of surface oxygen atoms relative to the substrate atoms, has been applied to the alumina/rhodium system. These results may be found in Appendix A along with a discussion of the appropriateness of the method.

The stoichiometry of the alumina overlayer was determined by comparison of the AES O/Al ratio with that of a bulk Al_2O_3 sample. A correction for Auger electron escape depths in the bulk sample must also be considered. Assuming attenuation factors of 0.30 for the Al (55 eV) electrons and 0.65 for the O (510 eV) electrons (see Table 2.1), the apparent overlayer AES ratio is expected to be about one-half that for bulk alumina.

Typical AES O/Al ratios of ~0.78 were observed at monolayer coverage of alumina. With the correction for electron escape depth, this would be equivalent to a ratio of 1.6 ± 0.2, compared with the ratio of 1.68 measured for bulk alumina. Uncertainty in the attenuation factors accounts for the wide error margin. It appears from AES that a nearly complete stoichiometric alumina overlayer exists on the surface, but this is strongly dependent on the attenuation factors assumed. Verification of near-stoichiometry was provided by XPS studies. Nevertheless, the alumina overlayer will be referred to as AlO_x, where $x \approx 1.4$.

5.2.2 XPS Analysis of the AlO_x/Rh Surface

XPS spectra of the Al (2p), O (1s), and Rh (3d) regions for ~0.2 ML AlO_x on rhodium appear in Figure 5.6. Due to a large secondary electron intensity in the low energy section of the AES spectrum when collected in the XPS chamber, determination of the alumina coverage with AES was not possible. Instead, a rough estimate was made from the O (1s) peak area of alumina by comparing with the corresponding peak areas of titania overlayers and correcting for the oxide stoichiometries.

Following oxidation of the surface in 2 x 10^{-6} torr O_2 at 753 K for 5 minutes, one aluminum peak corresponding to Al^{3+} was observed. (The broad, lower energy peak to the left arises from the Rh (4s) transition.) After three exposures to 4 L CO, with intermedi-

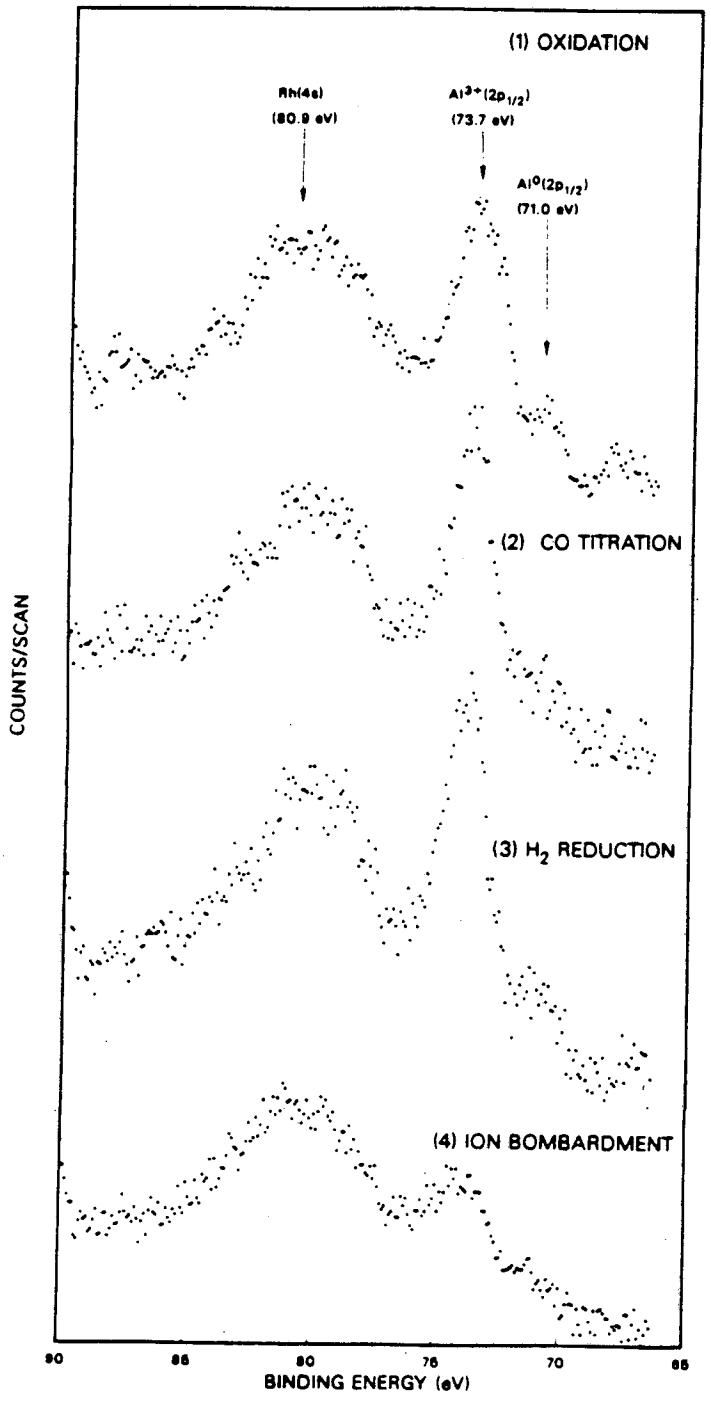

Figure 5.6: (a) XPS spectra of the Al(2p) region for 0.2 ML of AlO_x on Rh. Spectra 1, 2, and 3 were observed after oxidation, CO titration, and H_2 reduction of the surface,respectively. (See text for pretreatment conditions.) Ar ion sputtering resulted in spectrum 4. The Rh(4s) peak appears at high energy to the left in these spectra.

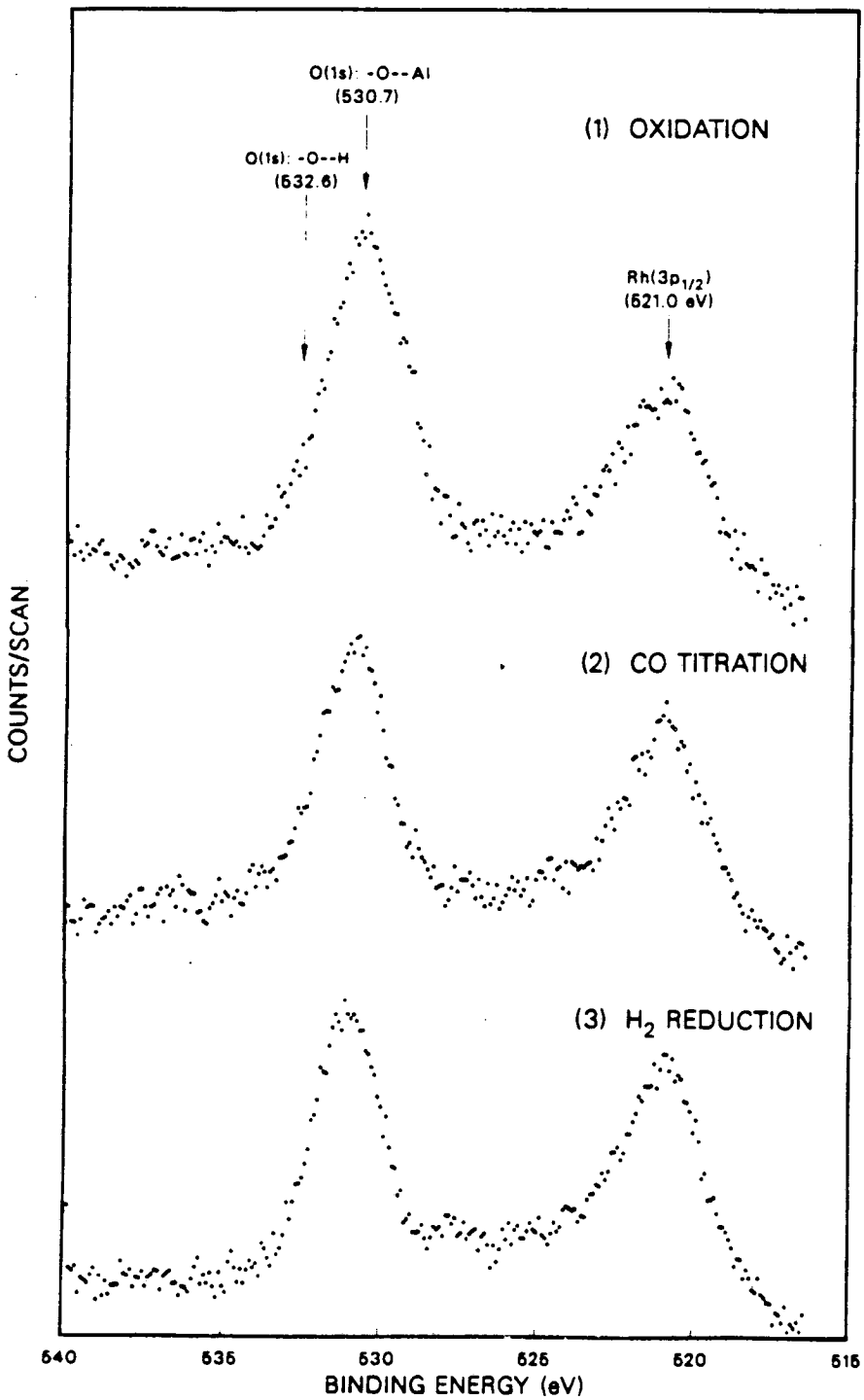

Figure 5.6: (b) XPS spectra of the O(1s) region for 0.2 ML of AlO_x on Rh. Spectra 1, 2, and 3 were observed following conditions identical to those prior to spectra 1, 2, and 3 in Fig. 5-6a. The $Rh(3p_{1/2})$ peak appears at lower energy to the right in these spectra.

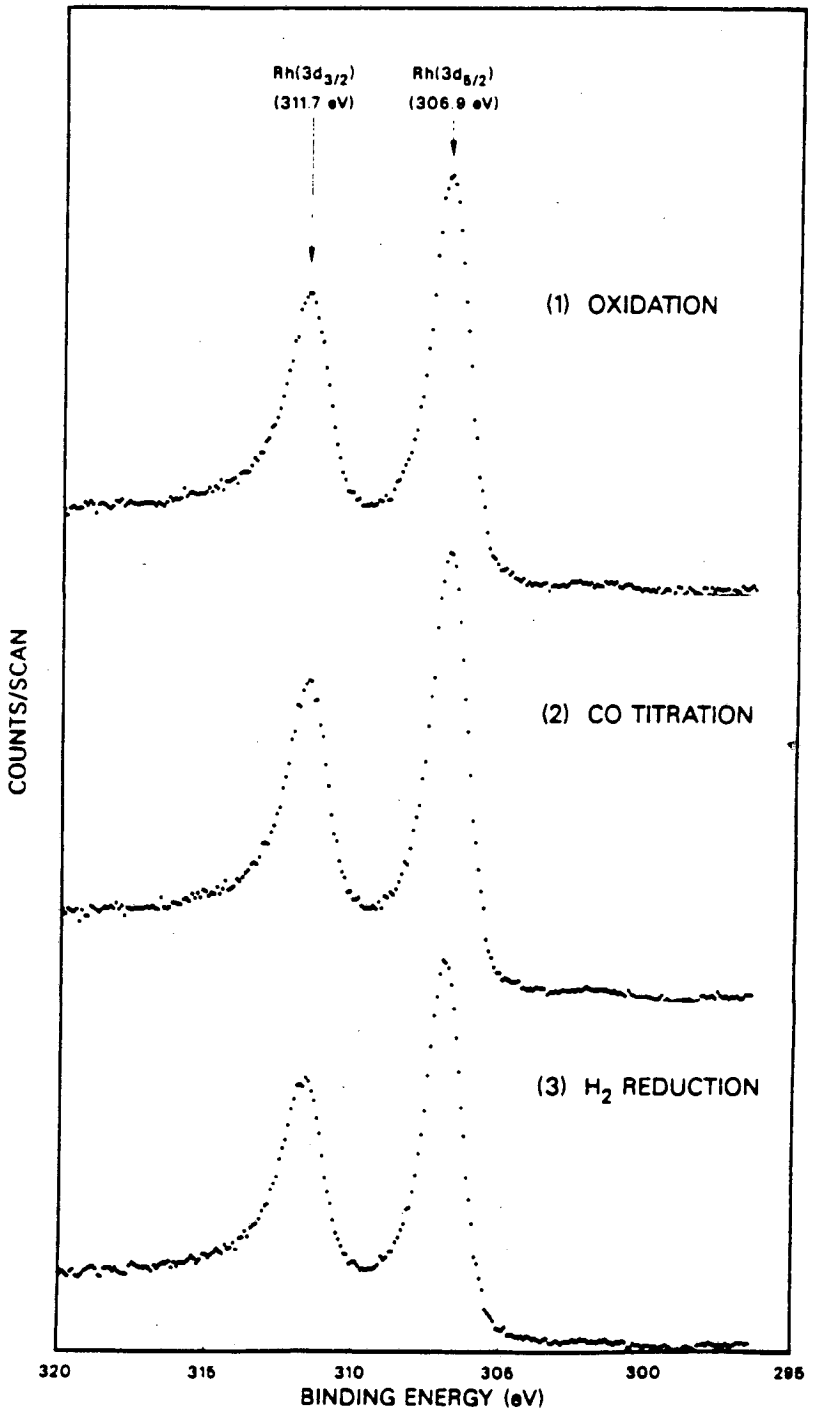

Figure 5.6: (c) XPS spectra of the Rh(3d) region for 0.2 ML of AlO_x on Rh. Spectra 1, 2, and 3 were observed following conditions identical to those prior to spectra 1, 2, and 3 in Fig. 5-6a.

ate flashes to 773 K, no significant changes in the Al spectrum occurred. A new feature ascribable to Al^0 (2.7 eV higher binding energy) appears after reduction in 50 torr H_2 at 753 K for 5 minutes, but this peak comprises less than 10% of the total Al signal. Argon ion sputtering of the sample followed by XPS analysis confirmed the identity of the Rh (4s) and Al (2p) peaks. No significant changes were observed in the O (1s) and Rh (3d) XPS spectra after the three pretreatments.

5.2.3 CO Chemisorption on AlO_x/Rh

The determination of monolayer coverage in the previous section provides the means for quantitatively assessing the effect of alumina overlayers on CO chemisorption. Thermal desorption spectra of CO (chemisorbed at room temperature) from Rh with various alumina coverages are shown in Fig. 5.7. Note the absence of any new desorption features, the fairly constant peak maximum temperature, and the monotonic decline in total peak area. As curve g indicates, residual CO desorption occurs at 1 monolayer. This could be reduced by further alumina deposition.

A plot of the CO TPD area, normalized to that of the bare Rh surface, as a function of AlO_x coverage appears in Fig. 5.8. Clearly, the CO desorption area decreases linearly with coverage, suggesting the blocking of Rh chemisorption sites by alumina. This will be discussed at greater length later. CO does not chemisorb on the alumina at room temperature to any significant extent as evidenced by TPD studies at high AlO_x coverages.

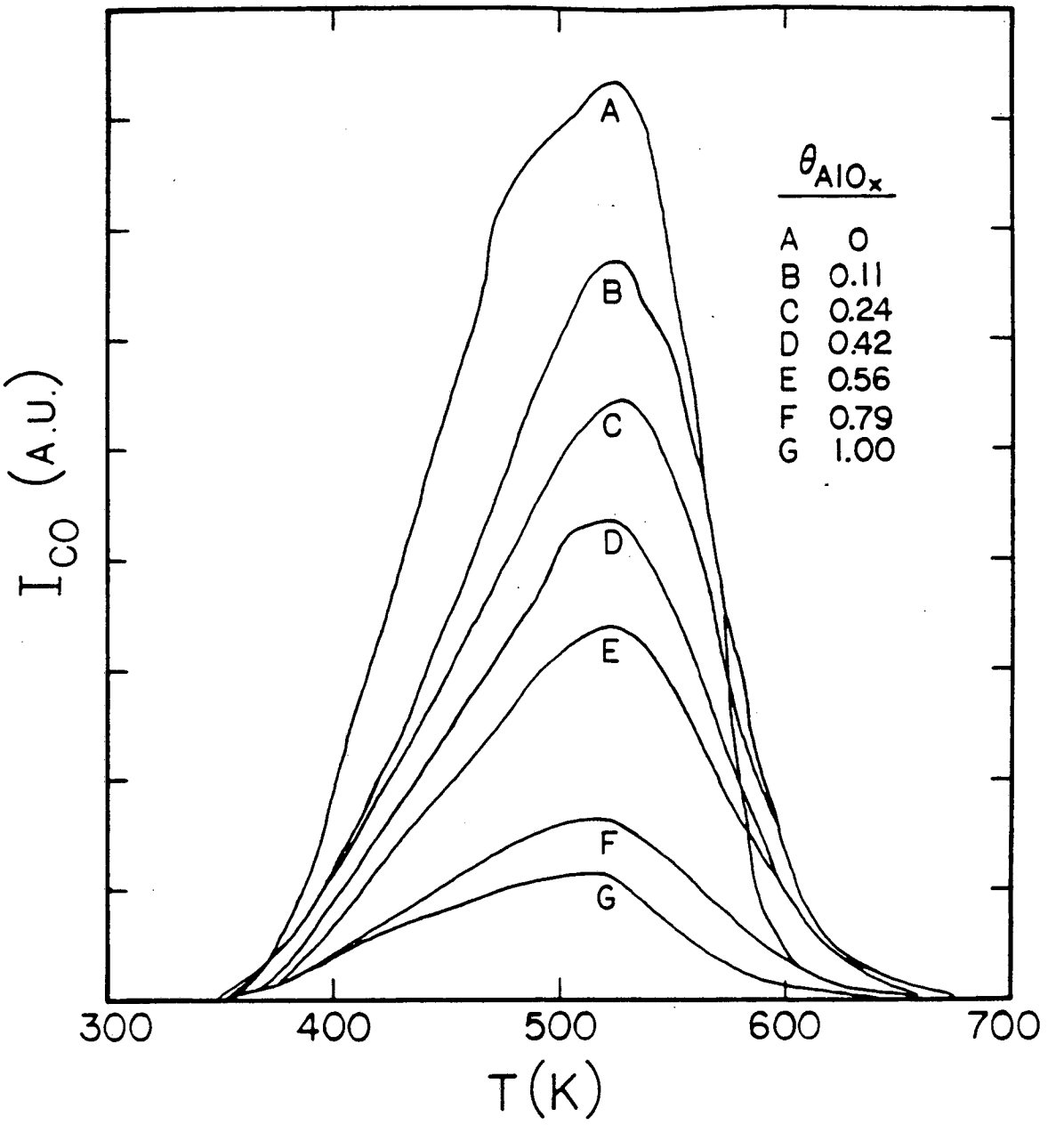

Figure 5.7: CO TPD spectra from Rh foil with varying amounts of AlO_x deposited on the surface (CO adsorbed at room temperature).

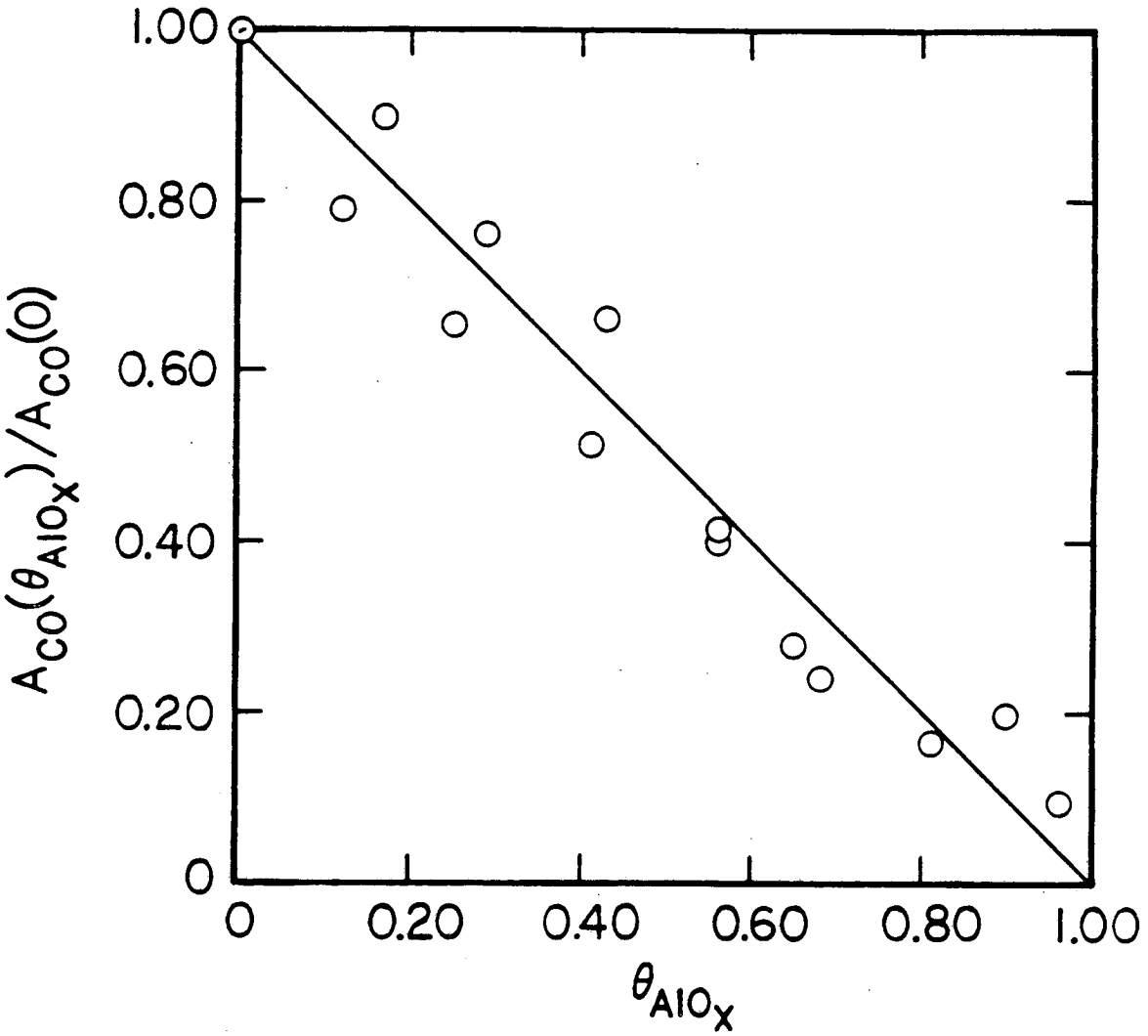

Figure 5.8: The effect of AlO_z coverage on the amount of CO adsorbed on Rh foil. Solid line indicates the profile expected for physical blockage of adsorption sites by AlO_z.

5.2.4 CO Hydrogenation on AlO_z/Rh

The effect of AlO_z overlayers on the chemistry of CO hydrogenation to methane and other hydrocarbons at atmospheric presssure was studied. The rate of methanation, at the same conditions as for clean Rh (namely, 553 K and H_2:CO = 2:1) decreases linearly with coverage (Fig. 5.9). The reaction rate for this particular Rh foil ($\theta_{AlOx} = 0$) is significantly different than that measured and presented for clean Rh in the previous section (~5.5 x 10^{-11} mole/s vs. 19.4 x 10^{-11} mole/s, respectively). The existence and possible cause

of such variations have already been noted (Section 5.1.3) and will not be dwelled upon further.

The decline in methanation rate was accompanied by similar decreases in the rates of formation of the other hydrocarbons. This is illustrated in Fig. 5.10 where hydrocarbon selectivities (based on reaction rates) are plotted versus AlO_x coverage. The propylene mole fraction, which lies between those of ethylene and ethane, has been omitted for the sake of clarity. The hydrocarbon mole fractions are invariant with coverage and approximate

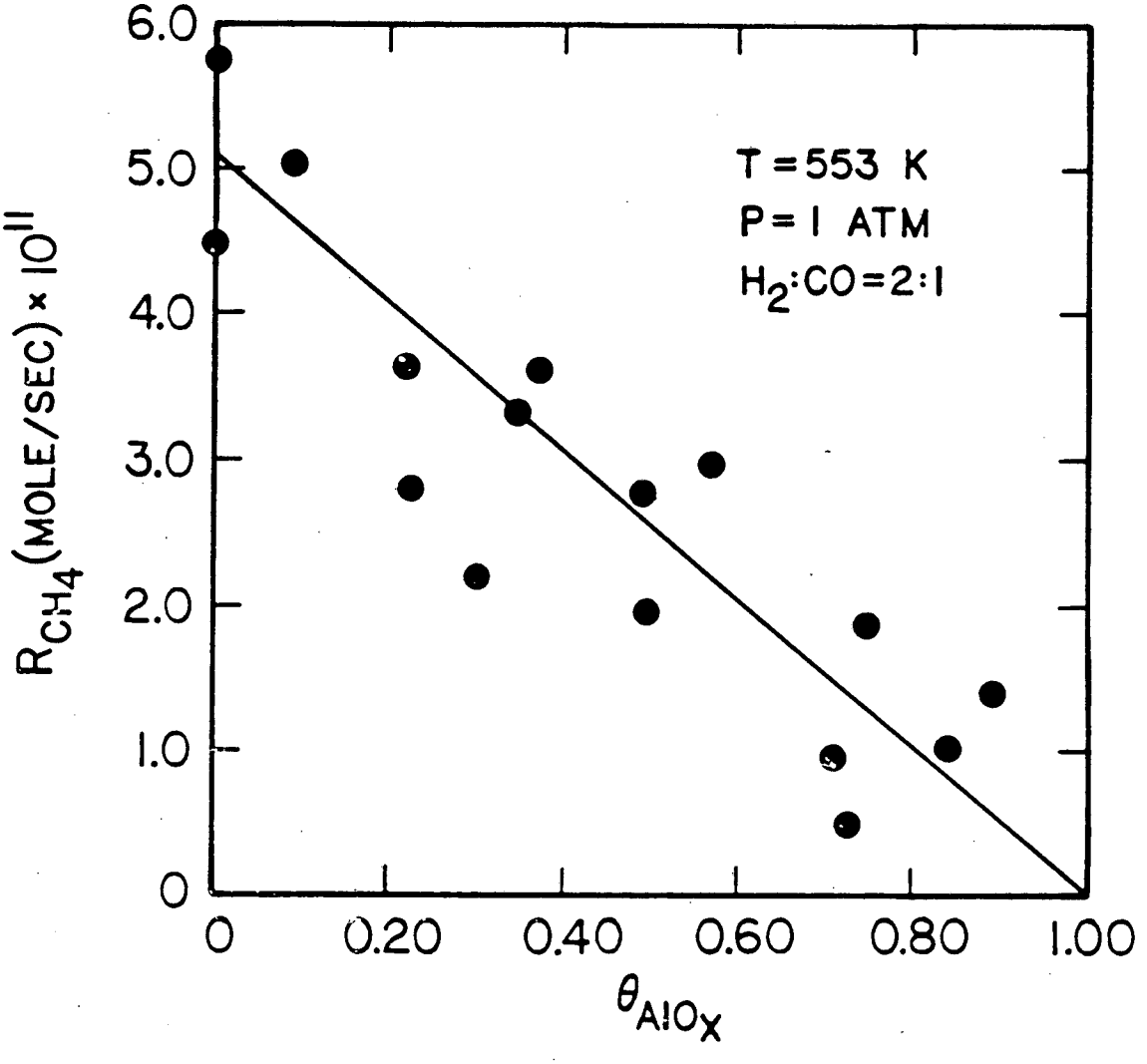

Figure 5.9: Methanation rate on AlO_x-promoted Rh as a function of AlO_x coverage. Reaction conditions were: 553 K, 1 atm total pressure, and a H_2:CO ratio of 2:1.

those of the bare Rh catalyst; alumina overlayers appear to have no effect on the product distribution for this reaction.

The kinetic parameters for methane production, as prescribed by Eqn. 5.1, were found for coverages of 0.37 and 0.49 ML. These appear in Table 5.1 along with values typical of bare Rh and of the titania/Rh system. Comparison of the parameters for the AlO_x/Rh system with bare Rh adds further evidence that alumina does not dramatically affect the

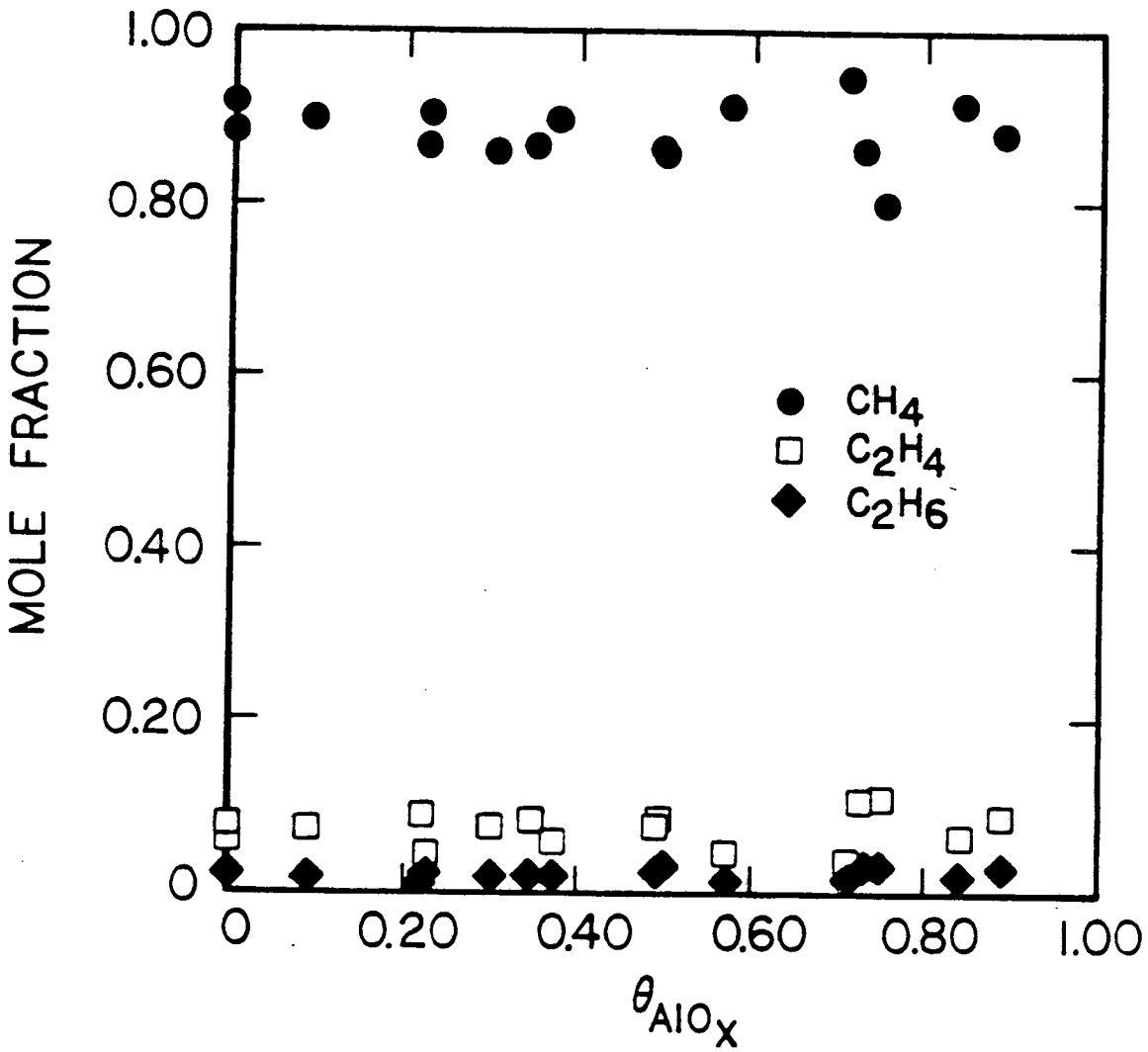

Figure 5.10: Hydrocarbon product selectivity as a function of AlO_x coverage: T = 553 K, P = 1 atm, H_2:CO = 2:1. The propylene mole fraction (omitted in the plot) was generally inbetween those of ethane and ethylene.

kinetics of CO hydrogenation.

It should be remarked that the activity of the sample did not decline significantly after one hour of reaction. The average amount of deactivation was roughly 20% of the initial value (Fig. 5.11, open squares) and was not dependent on the alumina coverage. (The large degree of scatter is due, in part, to the low methanation activity). This was accompanied by a mild build-up of carbon on the surface ($\leq$0.2 ML) detected immediately after reaction by AES (Fig. 5.11, solid circles).

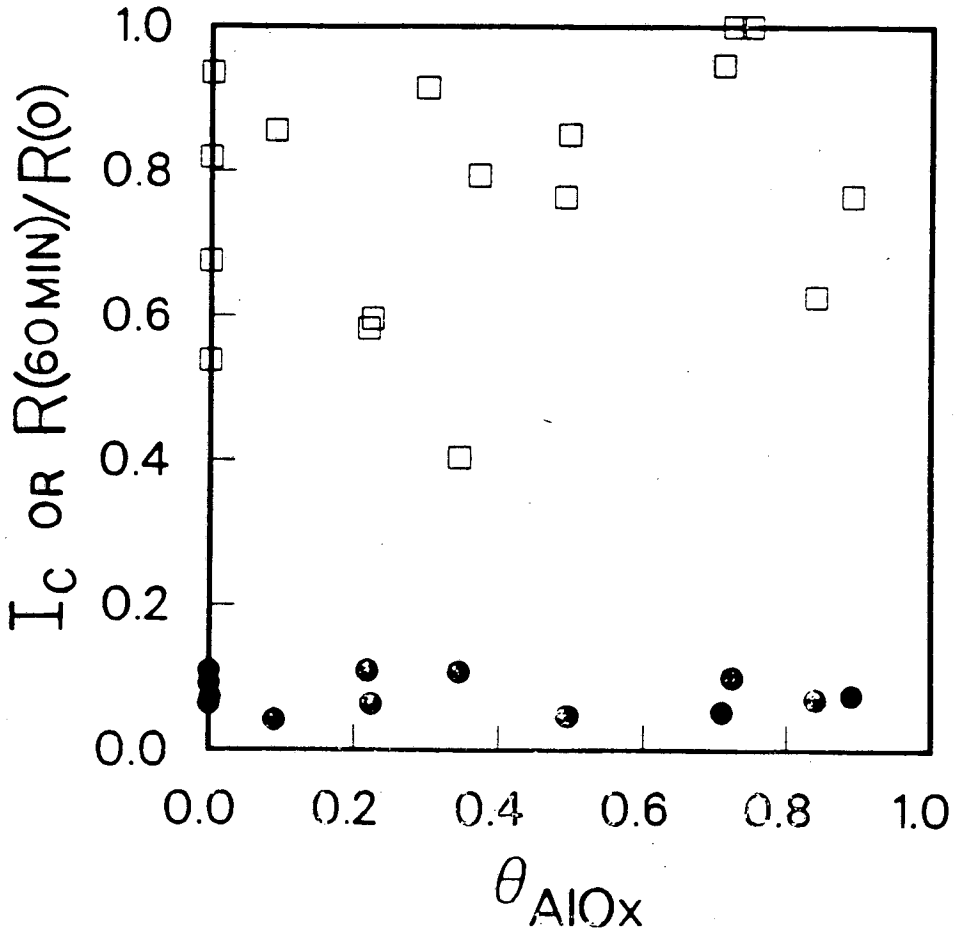

Figure 5.11: Properties of the AlO_x/Rh sample after one hour of reaction (CO hydrogenation). The relative amount of deactivation (open squares) and the AES carbon intensity (solid circles) are shown as a function of AlO_x coverage.

5.3 THE PROPERTIES OF RHODIUM WITH TITANIA OVERLAYERS

5.3.1 Titania Overlayer Deposition and Characterization

As in the case of alumina overlayers, the growth of titania overlayers was characterized by plotting the normalized AES peak intensities as a function of evaporation time. Figure 5.12 shows an AES spectrum of rhodium with a titania overlayer (~0.3 ML). The appropriate sensitivity factors have been tabulated in Chapter 4. The raw and normalized signal intensities are shown in Fig. 5.13 as a function of Ti dosing time. As was seen for alumina overlayers on rhodium, an initial linear decline in the substrate peak intensity occurs, signaling the development of the first monolayer. Further deposition yields signal intensities that deviate from this linearity and do not quite match the trends expected for layer-by-layer growth. The overlayer peaks behave analogously. Therefore, as with alumina, Stranski-Krastanov growth is exhibited.

The degree of attenuation of the substrate peak at the monolayer break is 0.34 ± 0.05. This high degree of attenuation, as compared with that of adsorbate-on-metal growth (~0.55, Table 2.1), may reflect a bi-layer structure of the oxide monolayer. Calculation of submonolayer coverages from AES spectra is performed by linear interpolation of the substrate signal between bare Rh and monolayer coverage on Rh.

The approach of determining monolayer coverage by comparing AES O/Rh ratios has been applied to this system and the results appear in Appendix A. No severe discrepancies exist if a bilayer structure of complete stoichiometry (TiO_2) is assumed.

The effect of evaporator current on the deposition rate was also explored. Rhodium AES intensity-vs.-dosing time profiles for four different evaporator currents appear in Fig. 5.14. Explicit oxidation of the sample was not carried out in these studies, although the titanium inherently was partially oxidized by reaction with background water, CO_2, or CO. The slopes of the uptake curves, for both Rh and Ti, reveal an exponential dependence of

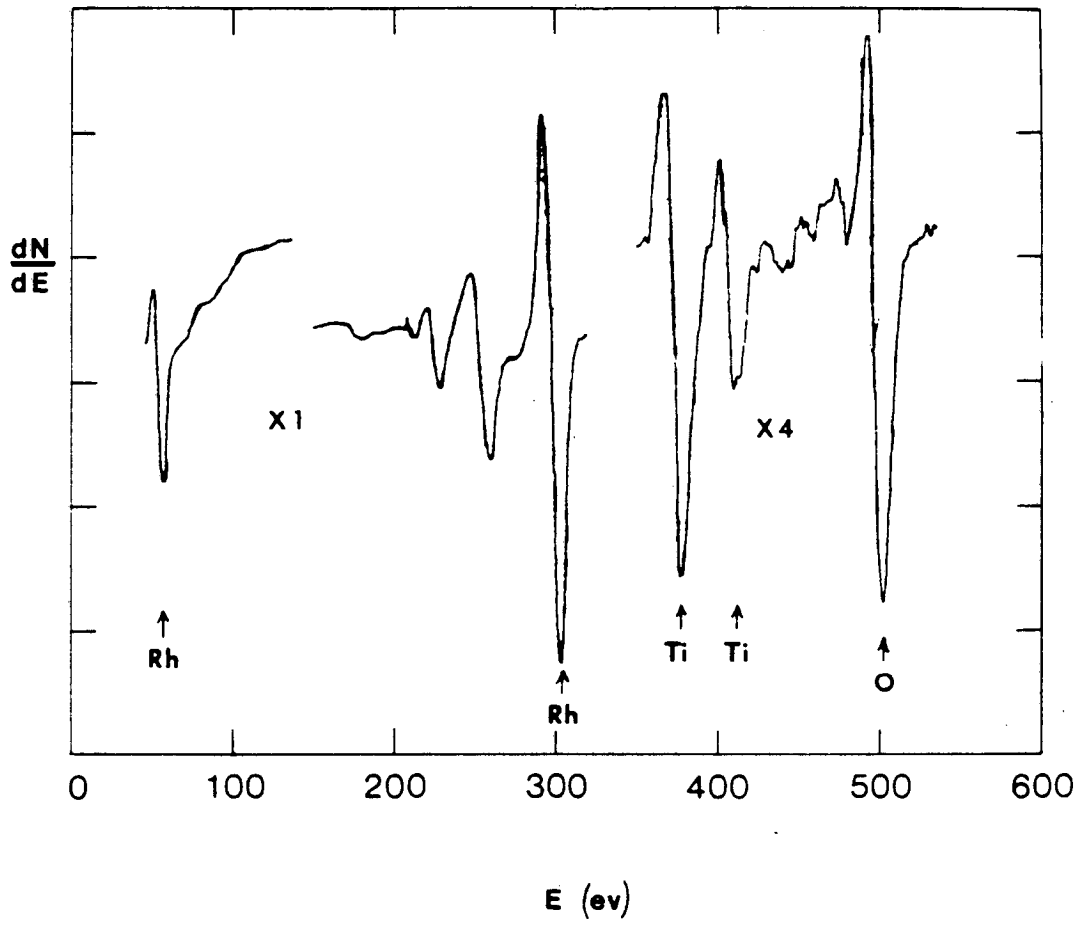

Figure 5.12: AES spectrum for ~0.3 ML of TiO_x on Rh.

deposition rate on the evaporation current (Fig. 5.15).

Raw AES O(510 ev)/Ti(387 ev) ratios of roughly 2 for stoichiometric TiO_2 have been reported [57,126]. This value depends on the type of electron energy analyzer and the sample-analyzer geometries. In this study, an O/Ti ratio of 1.2 (for oxidized TiO_x on Rh) was observed in the reaction chamber and a value of 1.3 in the XPS chamber. The appearance of a shoulder at about 398 eV in the Ti AES region often signals the presence of Ti^{4+} [127]. This was sometimes observed for the titania/rhodium system, but is an imprecise measure of the overlayer stoichiometry.

Other approaches were employed to find the stoichiometry of the deposited titania overlayer. Comparison of the overlayer AES O/Ti ratio with that of a TiO_2 single crystal

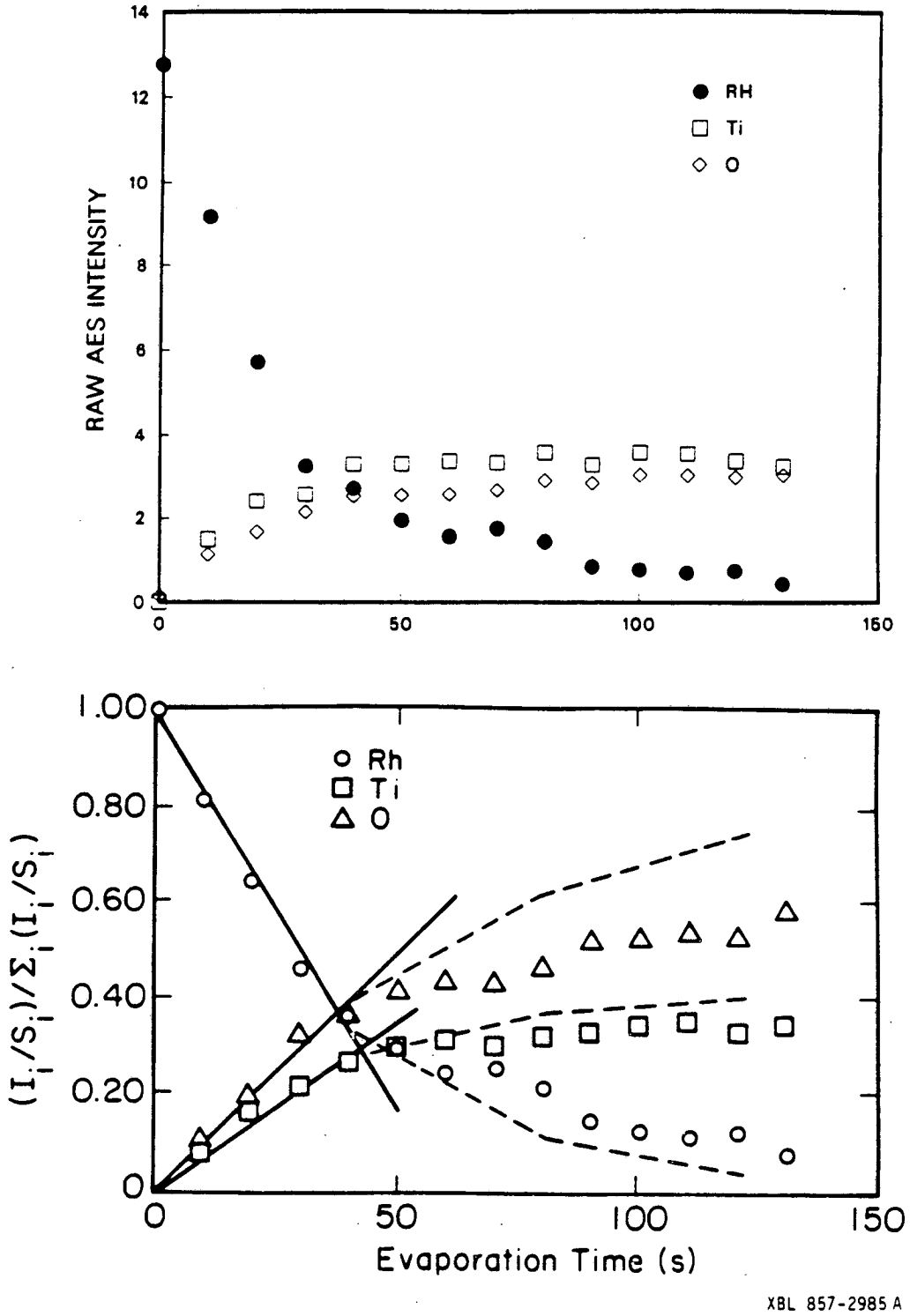

Figure 5.13: Auger peak-to-peak intensities corresponding to the growth of the TiO_x overlayer on Rh foil. Plot (a) shows the raw AES intensities and plot (b) the normalized AES intensities as functions of Ti dosing time. The expected trends for two-dimensional (layered) growth are depicted by the solid (< 1 ML) and dashed (> 1 ML) lines.

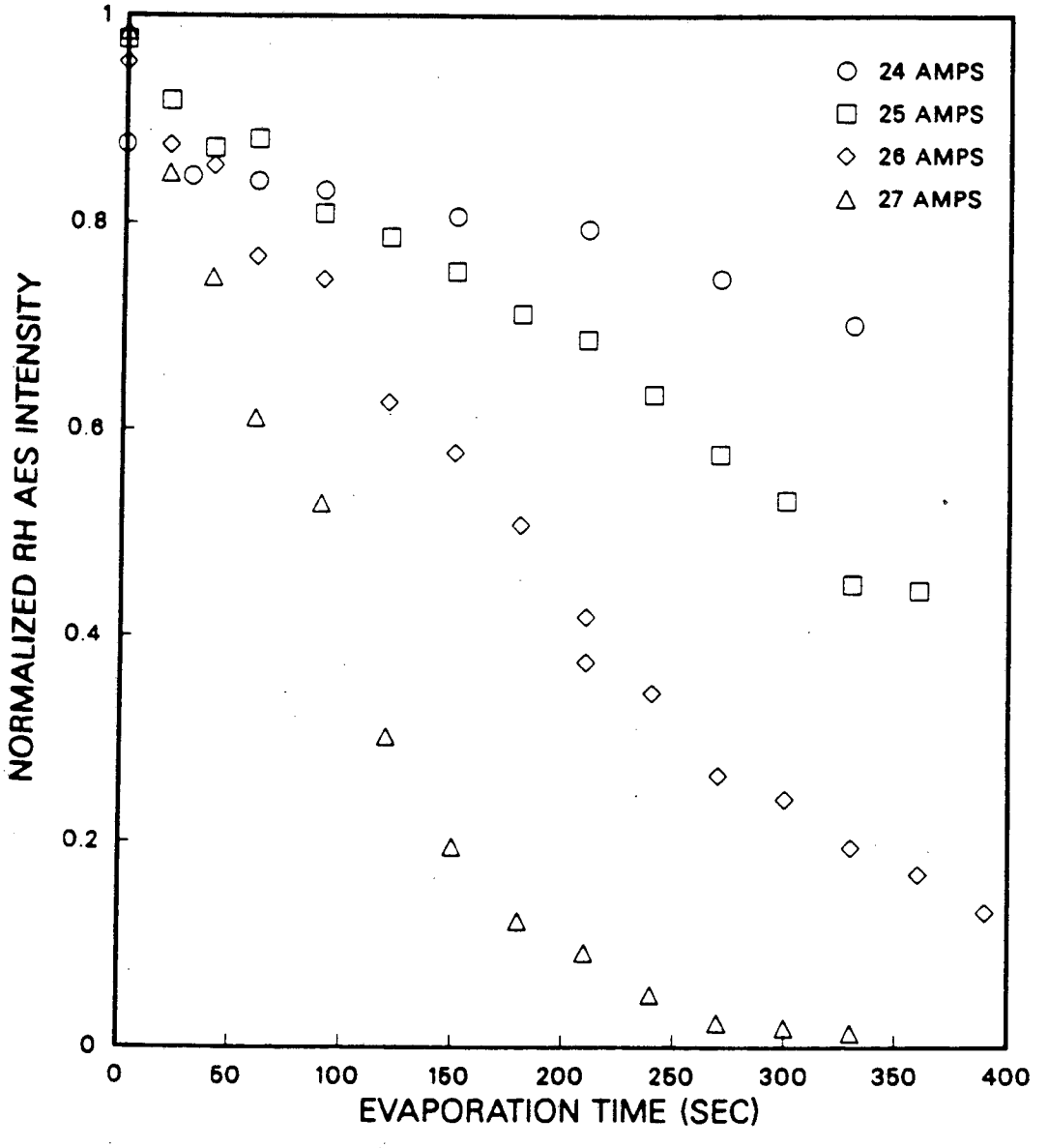

Figure 5.14: Titania deposition rate as a function of evaporator current—as indicated by the normalized AES Rh intensity.

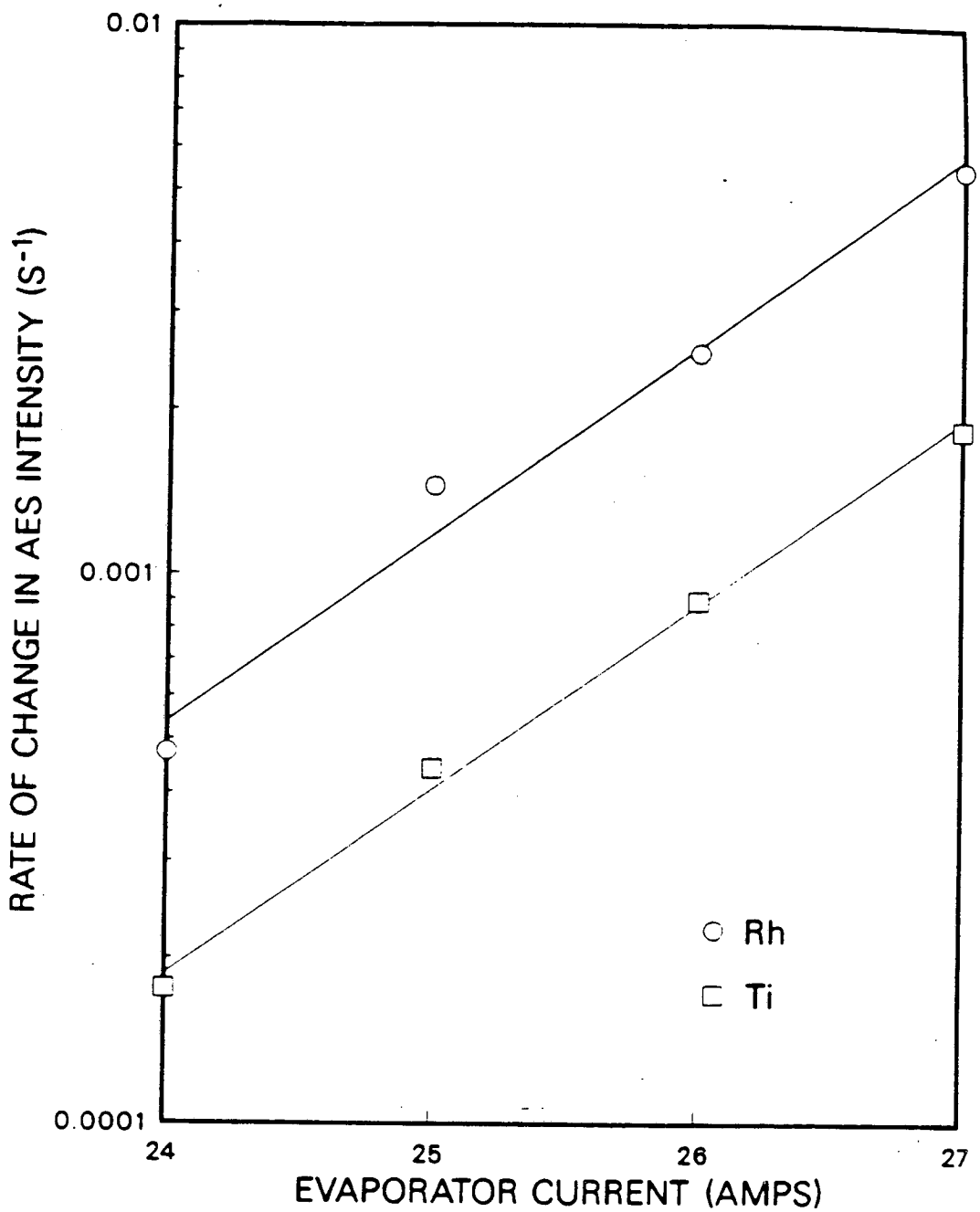

Figure 5.15: The effect of evaporator current on the titania deposition rate as indicated by the rates of change of the AES Rh and Ti intensities.

indicated an apparent overlayer O/Ti atom ratio of 1.65. A similar figure was obtained upon comparison with an oxidized Ti foil (produced in flowing O_2, ~523 K, overnight). Correction for the different escape depths of Ti (387 ev) and O (510 ev) electrons (since a surface compound is being compared to a bulk compound) raises the ratio to 1.95. For this calculation, values of $\alpha(Ti) = 0.59$ and $\alpha(O) = 0.65$ were taken. Verification of the nearly-complete stoichiometry was provided by XPS spectra of the Ti (2p) region. Above 0.25 ML TiO_x, less than 10% of the XPS peak areas could be attributed to Ti^{3+}, *i.e.*, an atomic O/Ti ratio greater than 1.95. As with alumina, the titania overlayer will also be referred to as TiO_x. The value of x will be seen to vary, depending on the coverage and the pretreatments employed.

5.3.2 XPS Analysis of the TiO_x/Rh Surface

The existence of Ti species in different oxidation states has been monitored by x-ray photoelectron spectroscopy. The results for titania overlayers on rhodium and gold after a variety of treatment conditions will discussed presently.

The first series of experiments involved four pretreatment steps: (1) oxidation, (2) CO titration, (3) H_2 reduction, and (4) re-oxidation. The oxidation step, similar to that described earlier, consisted of exposure to 2 x 10^{-6} torr O_2 at 753 K for 5 minutes. Removal of rhodium-bound oxygen with CO to form CO_2 was considered a separate step consisting of three 4 L exposures to CO, each exposure followed by flashing to 753 K. More extreme reduction of the surface was accomplished by treatment in 50 torr H_2 at 753 K for 5 minutes. Finally, re-oxidation under the conditions of step 1 was performed.

Following each pretreatment step, the TiO_x/Rh surface was analyzed with XPS. A series of XPS spectra of the Ti (2p), O (1s), and Rh (3d) regions for a TiO_x coverage of 0.15 ML appears in Fig. 5.16. In spectrum 1 of Fig. 5.16a, two peaks are prominent. The low binding energy peak (to the right in the figure) corresponds to the Ti^{4+} ($2p_{3/2}$) transition,

while the high binding energy peak corresponds to the Ti^{4+} ($2p_{1/2}$) transition. Note the slight degree of asymmetry in the Ti ($2p_{3/2}$) peak reflecting the presence of a low energy shoulder. This additional feature appears in the Ti ($2p_{1/2}$) region as well, but is not as clear. These additional features comprise the Ti^{3+} contribution to the spectrum. The increased charge density in the Ti^{3+} state, as compared with the Ti^{4+} state, results in a lower binding energy for the Ti^{3+} transition.

Titration of surface oxygen with CO causes the emergence of distinct Ti^{3+} peaks (spectrum 2). While Rh-bound oxygen is removed in this process, clearly some oxygen is removed from the TiO_x islands as well. Enhancement of the Ti^{3+} peaks is achieved by reduction in H_2 (spectrum 3). In this particular case, much of the Ti exists in the Ti^{3+} state after the reduction step. Similar spectra were obtained by Raupp *et al.* [128] for TiO_x on Ni following reduction and by Greenlief *et al.* [129] for TiO_x on Pt following annealing treatments. Re-oxidation of the sample returns the spectrum to one showing mostly Ti^{4+} (spectrum 4).

Inspection of the O(1s) peak reveals a high binding energy shoulder at low TiO_x coverages (Fig. 5.16b) due to the change in bonding from Ti–O–M (M = Ti or Rh) to Ti–OH. After H_2 reduction, the total O (1s) peak area becomes noticeably smaller. While changes occur in the Ti and O spectra, no modifications of the Rh spectrum are observed after any of the pretreatments (Fig. 5.16c). This is, in part, due to the sampling of bulk rhodium (the kinetic energy of Rh (3d) electrons is $\sim$ 940 eV).

Similar experiments were performed for a gold foil with a TiO_x coverage of 0.19 ML. (The coverage was determined by comparing the relative intensity of the AES Ti signal of the TiO_x/Au sample with the signal from TiO_x/Rh samples in the XPS chamber.) The Ti (2p) spectra (Fig. 5.17a) show narrow and highly symmetric $2p_{1/2}$ and $2p_{3/2}$ peaks—indicating pure Ti^{4+} (within instrumental resolution). Even H_2 reduction failed to produce any Ti^{3+} in the TiO_x overlayer.

Deconvolution of the spectra into peaks with Doniach-Šunjić lineshape [115], allows determination of the Ti^{3+} and OH fractions in the overlayer. Example spectra with the fitted peaks superimposed appear in Figs. 5.18 and 5.19. Multiplication of the Ti^{3+} fraction

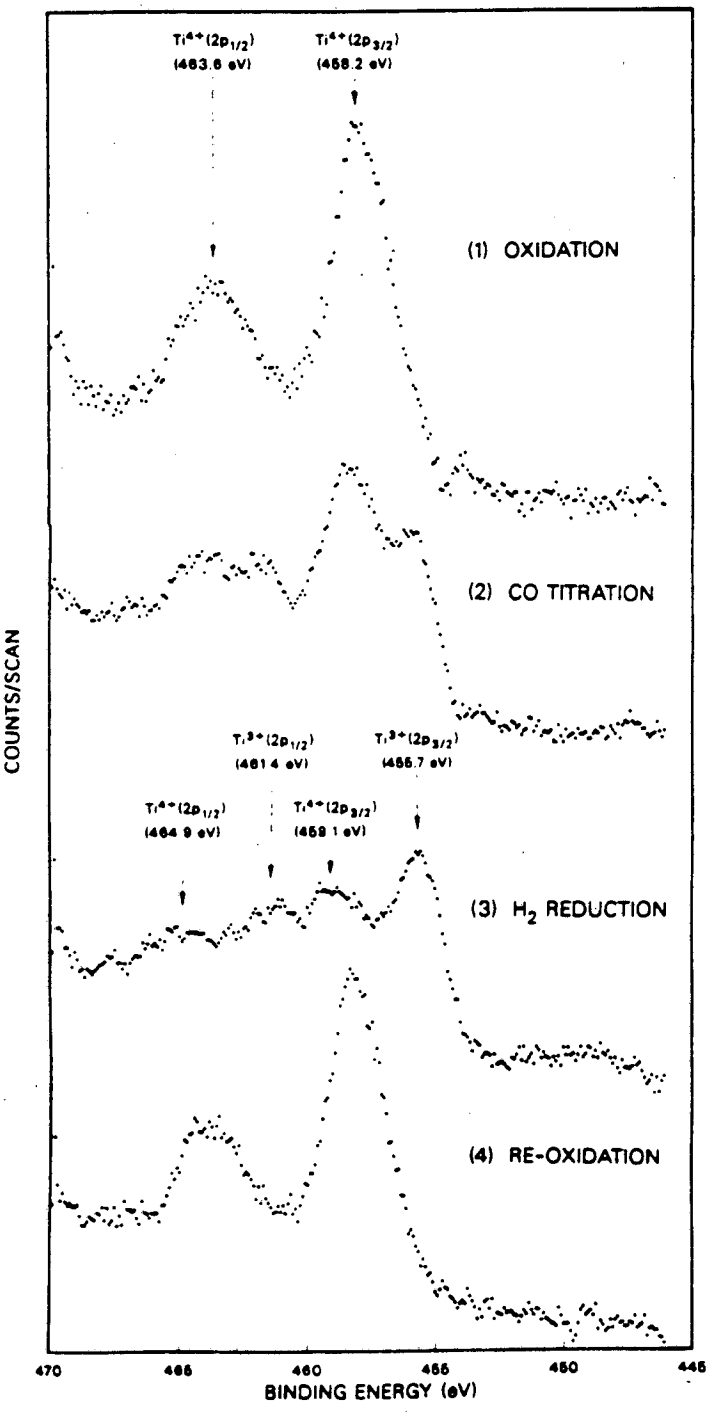

Figure 5.16: (a) XPS spectra of the Ti(2p) region for 0.15 ML of TiO_x on Rh. Spectra 1, 2, and 3 were observed after oxidation, CO titration, and H_2 reduction of the surface. (See pretreatment conditions in text.) Re-oxidation under the conditions preceding spectrum 1 yielded spectrum 4.

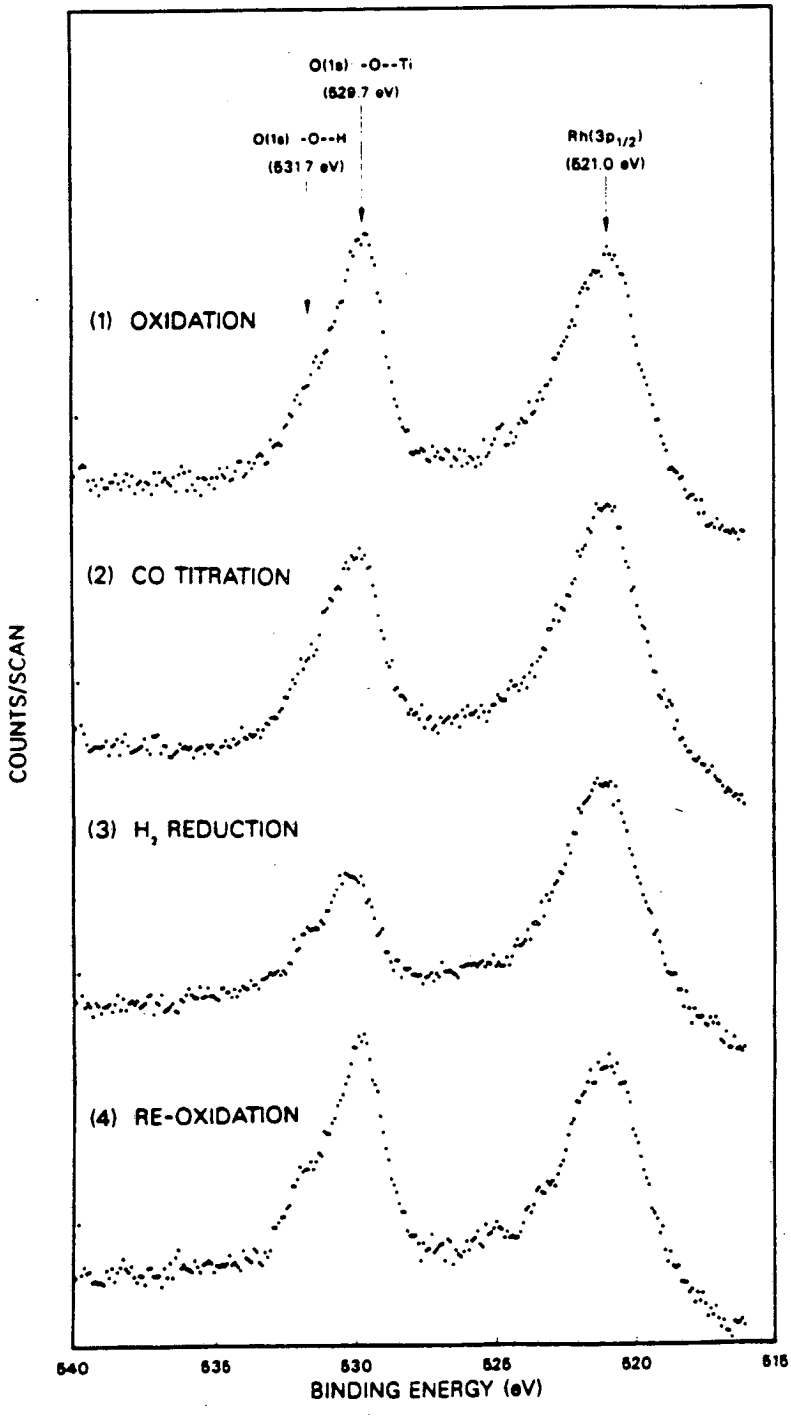

Figure 5.16: (b) XPS spectra of the O(1s) region for 0.15 ML of TiO_x on Rh. Spectra 1, 2, 3, and 4 were observed following conditions identical to those prior to spectra 1, 2, 3, and 4 in Fig. 16a. The $Rh(3p_{1/2})$ peak appears at lower energy to the right in these spectra.

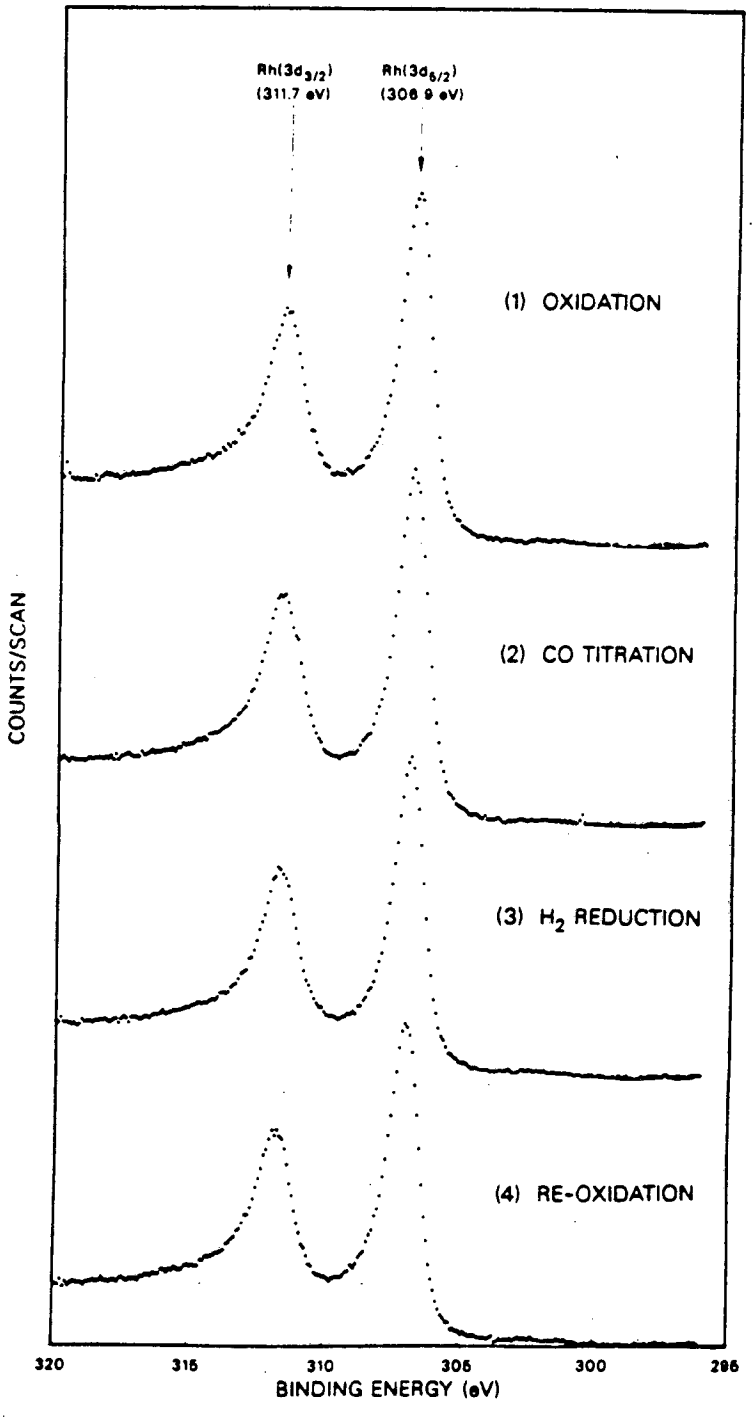

Figure 5.16: (c) XPS spectra of the Rh(3d) region for 0.15 ML of TiO_x on Rh. Spectra 1, 2, 3, and 4 were observed following conditions identical to those prior to spectra 1, 2, 3, and 4 in Fig. 5.16a.

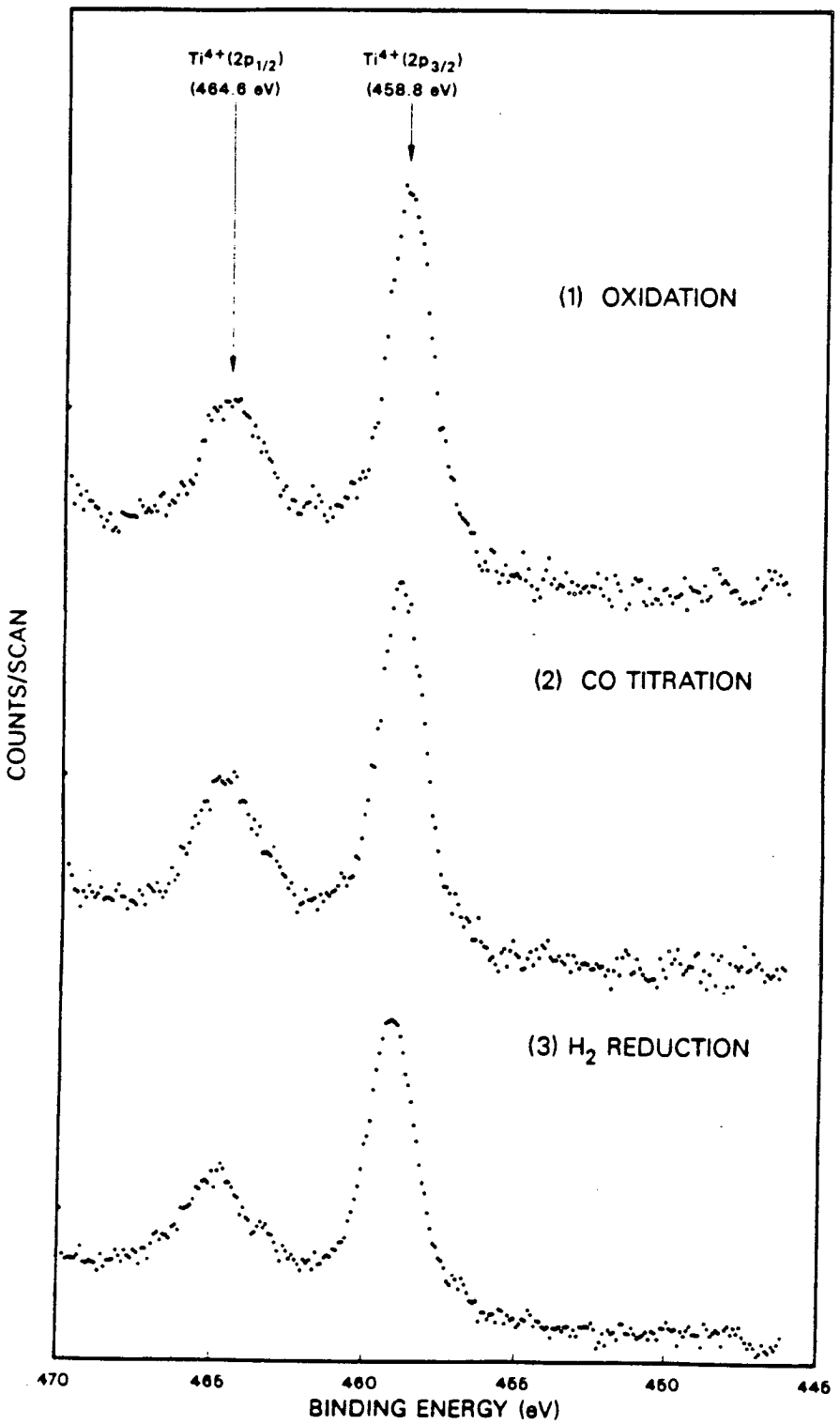

Figure 5.17: (a) XPS spectra of the Ti(2p) region for 0.19 ML of TiO_x on Au. Spectrum 1 was observed after oxidation of the surface (2 x 10^{-6} torr O_2, 753 K, 5 min). Following CO titration (4 L CO with heating to 773 K—repeated 3 times), spectrum 2 resulted. H_2 reduction (50 torr H_2, 753 K, 5 min) yielded spectrum 3.

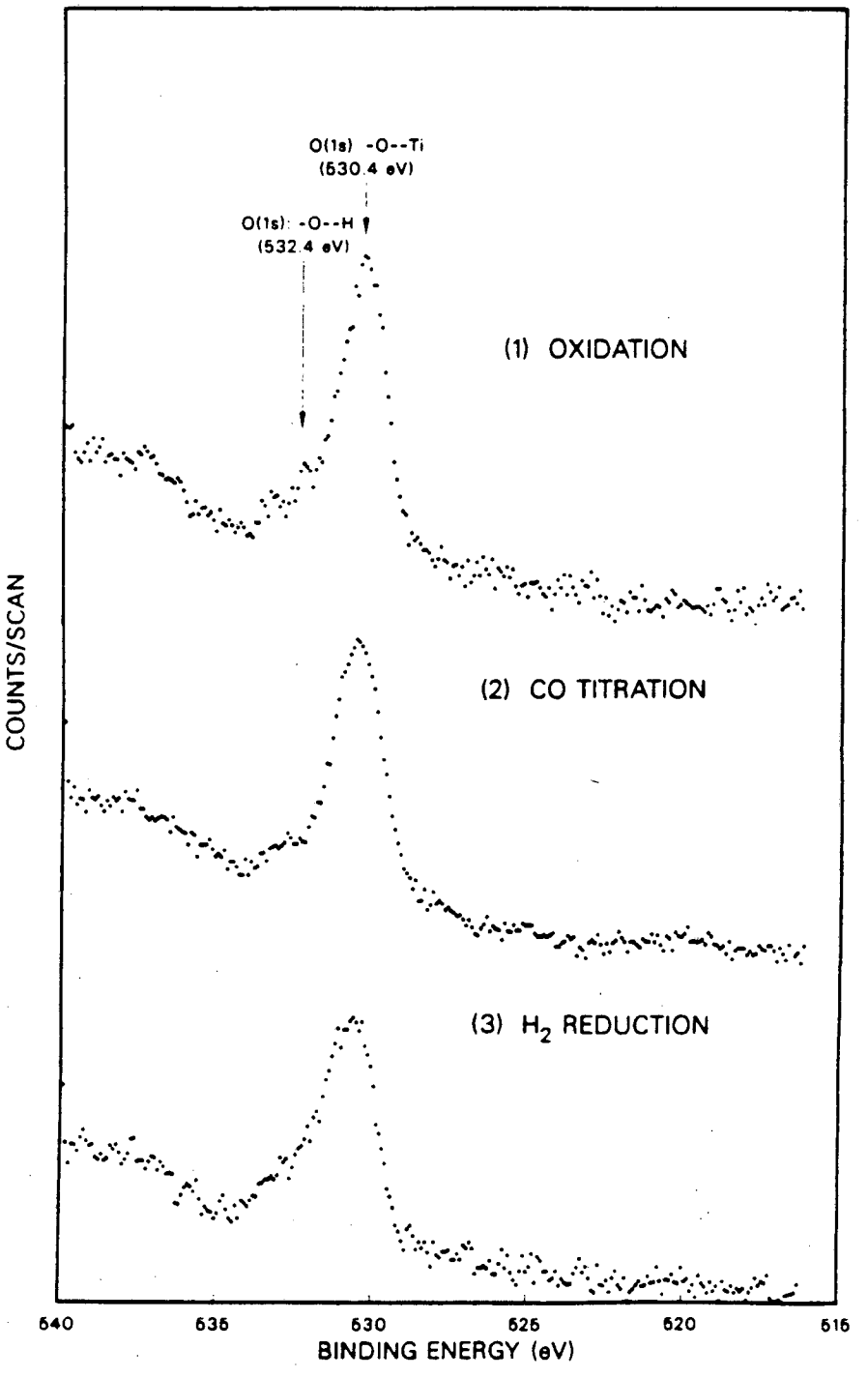

Figure 5.17: (b) XPS spectra of the O(1s) region for 0.19 ML of TiO_x on Au. Spectra 1, 2, and 3 were observed following conditions identical to those prior to spectra 1, 2, and 3 in Fig. 17a.

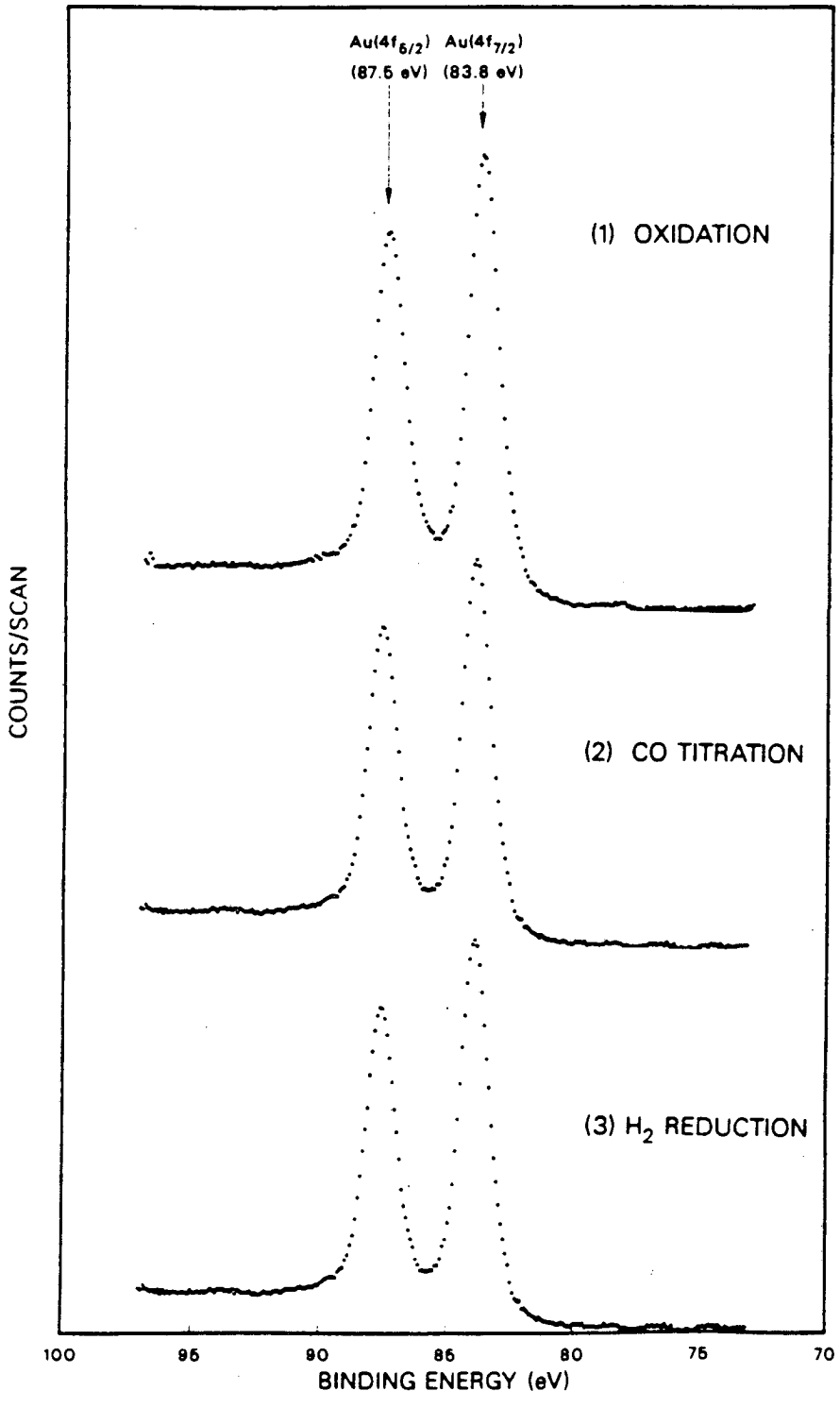

Figure 5.17: (c) XPS spectra of the Au (4f) region for 0.19 ML of TiO_x on Au. Spectra 1, 2, and 3 were observed following conditions identical to those prior to spectra 1, 2, and 3 in Fig. 5.17a.

with coverage yields a measure of the total number of Ti^{3+} sites. These quantities are presented as a function of coverage in Figs. 5.20 and 5.21, respectively. Except at very low coverages ($\leq$0.2 ML), less than 10% of the Ti atoms are in the 3+ oxidation state following oxidation. CO titration causes an increase in the Ti^{3+} content, especially at the low coverages, where as much as 50% of the Ti is in that state. (A 50% Ti^{3+} content corresponds to a stoichiometry of $TiO_{1.75}$.) A significantly higher baseline is observed for the case of H_2 reduction ($\geq$0.6 ML) and as much as 65% of the Ti is Ti^{3+} for 0.04 ML TiO_x ($\sim TiO_{1.68}$). The total Ti^{3+} content after each pretreatment in Fig. 5.21 shows continual increases as the coverage rises, with most of the change occurring below coverages of 0.5 ML.

Deconvolution of the O (1s) spectra for various TiO_x coverages into Ti–O–M and –OH peaks indicates that the OH percentage is higher with lower TiO_x coverage and that this percentage is not strongly dependent on the pretreatment conditions (Fig. 5.22). The total O (1s) peak area as a function of TiO_x coverage and pretreatment conditions is shown in Fig. 5.23. A decrease in the total amount of oxygen in the overlayer occurs after H_2 reduction.

The rapidity of the reduction of titania on rhodium in H_2 was also investigated. Fig. 5.24 shows the Ti^{3+} content of the overlayer as a function of reduction time at 753 K for a coverage of 0.55 ML. After only 10 seconds of reduction, the Ti^{3+} percentage has nearly attained the maximum value for the reduction conditions.

The effect of annealing at temperatures above 850 K on the TiO_x overlayer was checked. This was done for TiO_x coverages of 0.19 ML (not oxidized) and 0.71 ML (oxidized and titrated with CO). XPS analysis of the 0.19 ML sample showed Ti predominantly in the Ti^{3+} oxidation state. (Partial oxidation of titanium, even in UHV, is unavoidable due to the presence of water in the background.) Annealing at 1123 K caused a decrease in the AES and XPS Ti and O signals and converted the Ti^{3+} to Ti^{2+} (Fig. 5.25). However, full reduction to titanium metal could not be achieved. The O/Ti peak ratios from both AES and XPS remained nearly constant, reflecting the dissolution of both Ti and O into the

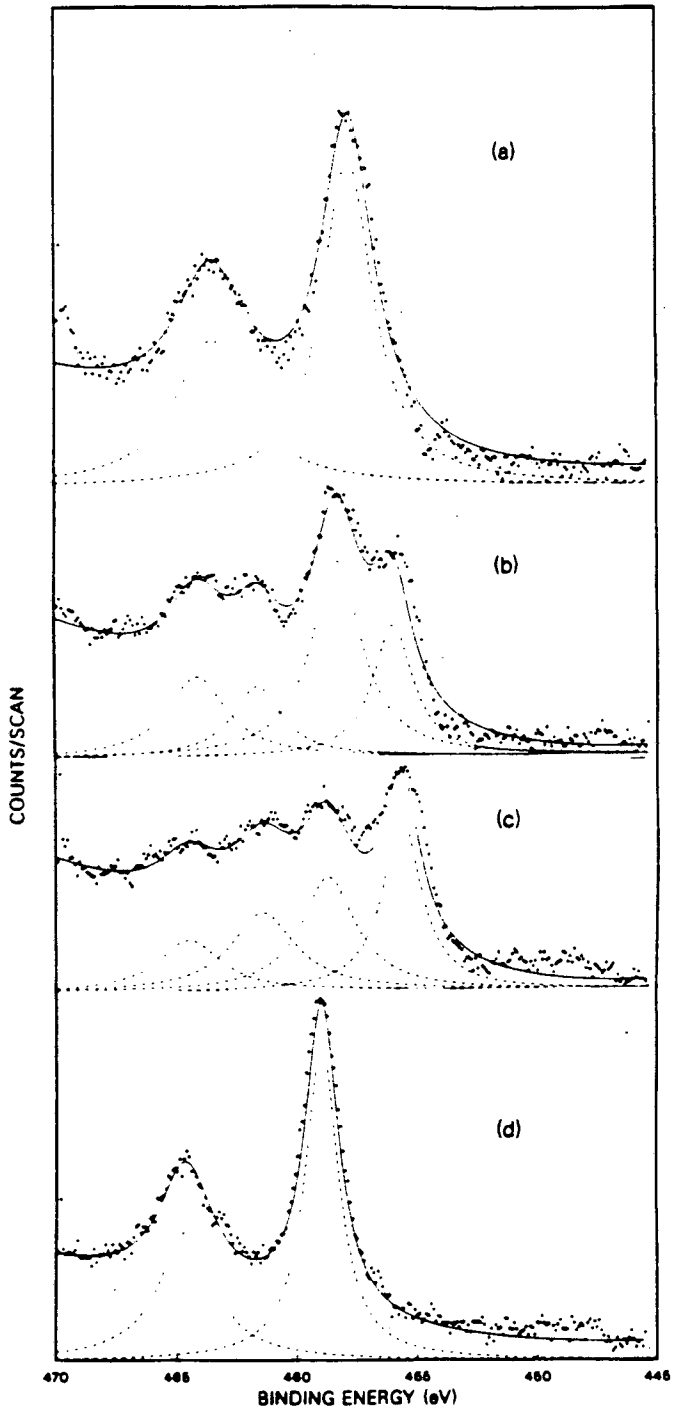

Figure 5.18: Examples of peak deconvolution of the Ti(2p) region. Spectra a, b, and c show the individual peaks and the sum of the individual peaks corresponding to spectra 1, 2, and 3 in Fig. 5.16a, respectively. Spectrum d corresponds to spectrum 3 in Fig. 5.17a. Doniach-Šunjić lineshapes were employed.

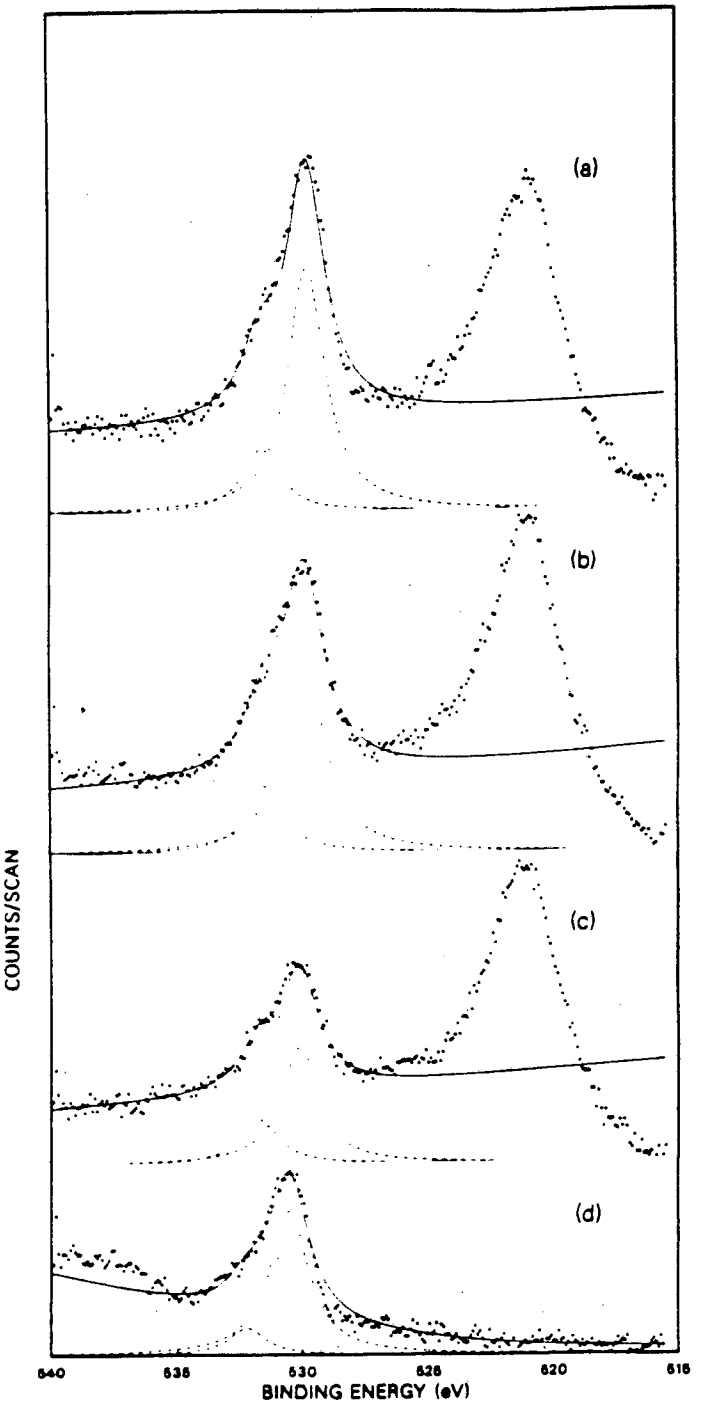

Figure 5.19: Examples of peak deconvolution of the O(1s) region. Spectra a, b, and c show the individual peaks and the sum of the individual peaks corresponding to spectra 1, 2, and 3 in Fig. 5.16b, respectively. Spectrum d corresponds to spectrum 3 in Fig. 5.17b. Doniach-Šunjić lineshapes were employed.

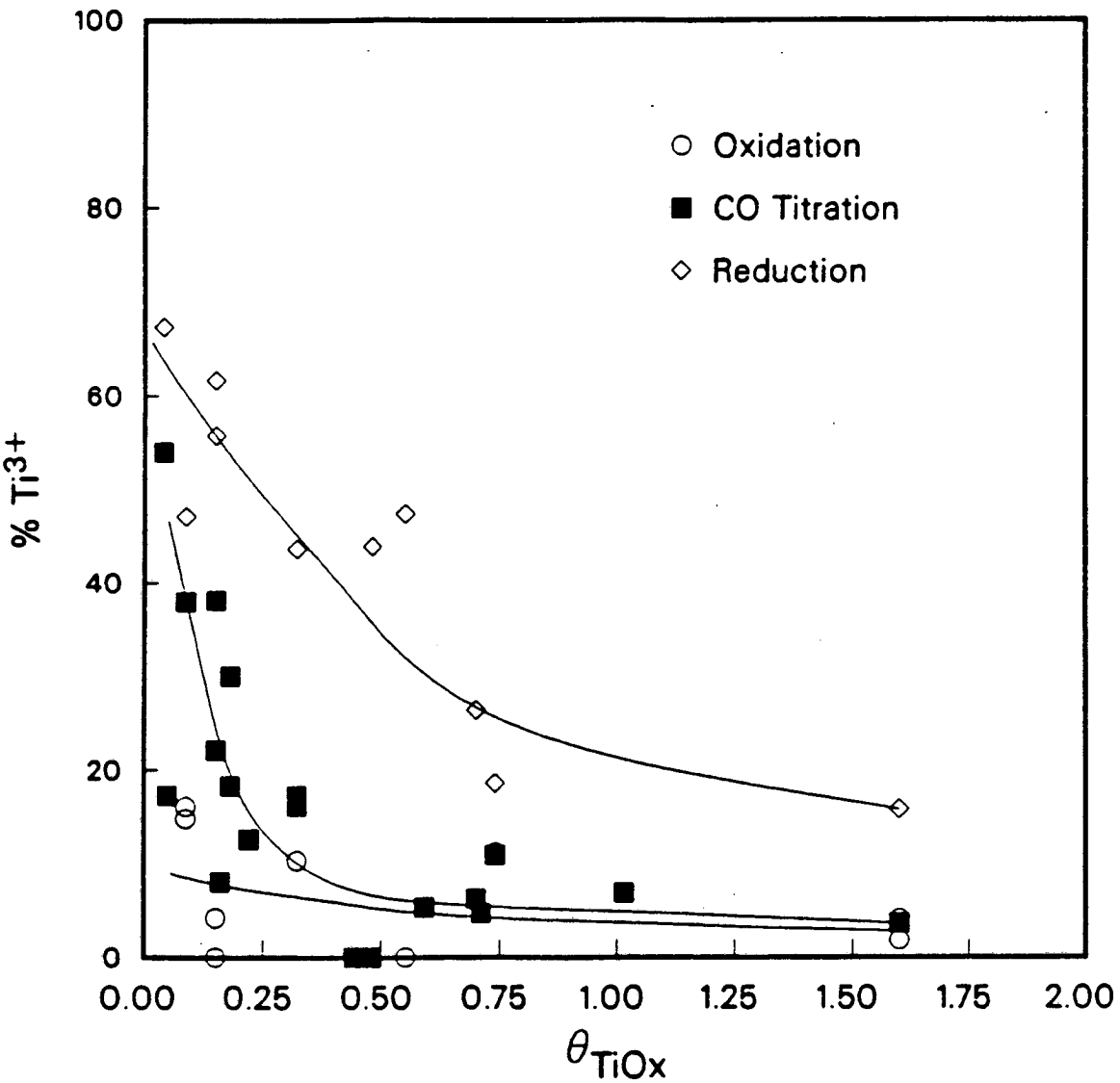

Figure 5.20: Percentage of titanium as Ti^{3+} (as determined by deconvolution of XPS spectra) as a function of coverage and pretreatment conditions. The pretreatment conditions consisted of the oxidation, CO titration, and H_2 reduction steps described in the text.

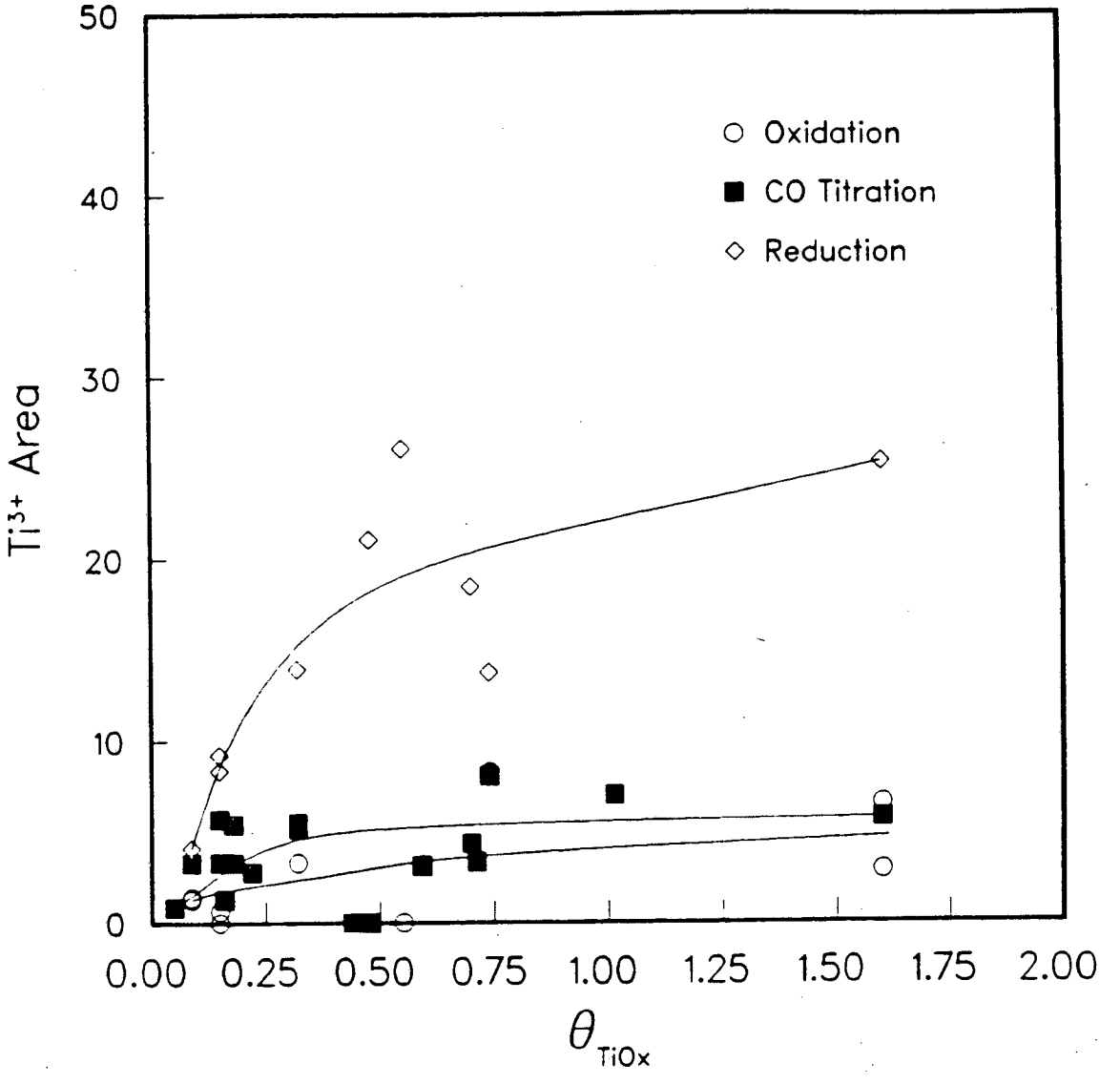

Figure 5.21: Total amount of Ti^{3+} as a function of coverage and pretreatment conditions. The total was calculated from multiplication of the Ti^{3+} percentage with the TiO_x coverage.

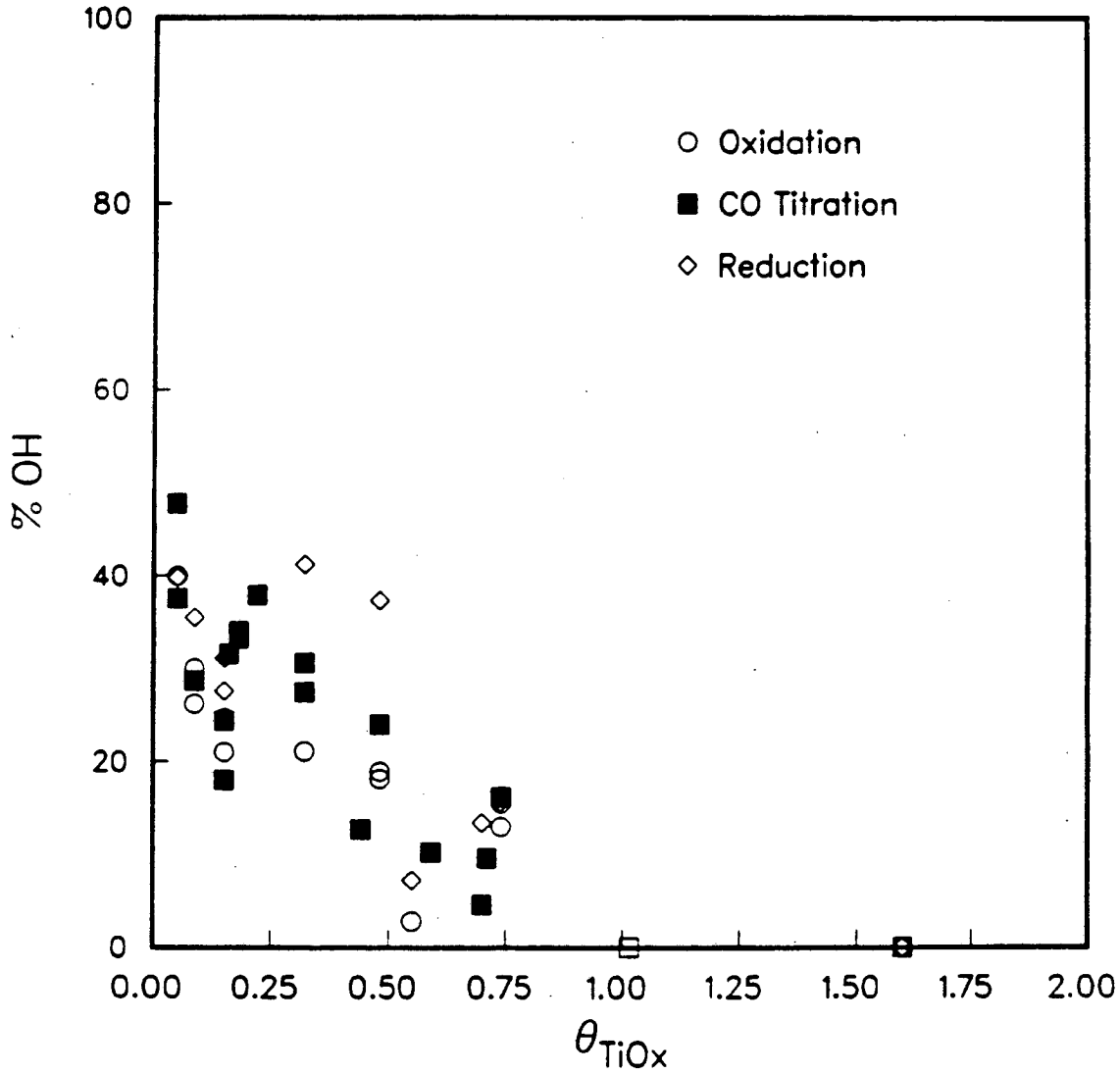

Figure 5.22: Percentage of oxygen as OH (as determined by deconvolution of XPS spectra) as a function of coverage and pretreatment conditions. The pretreatment conditions consisted of the oxidation, CO titration, and H_2 reduction steps described in the text.

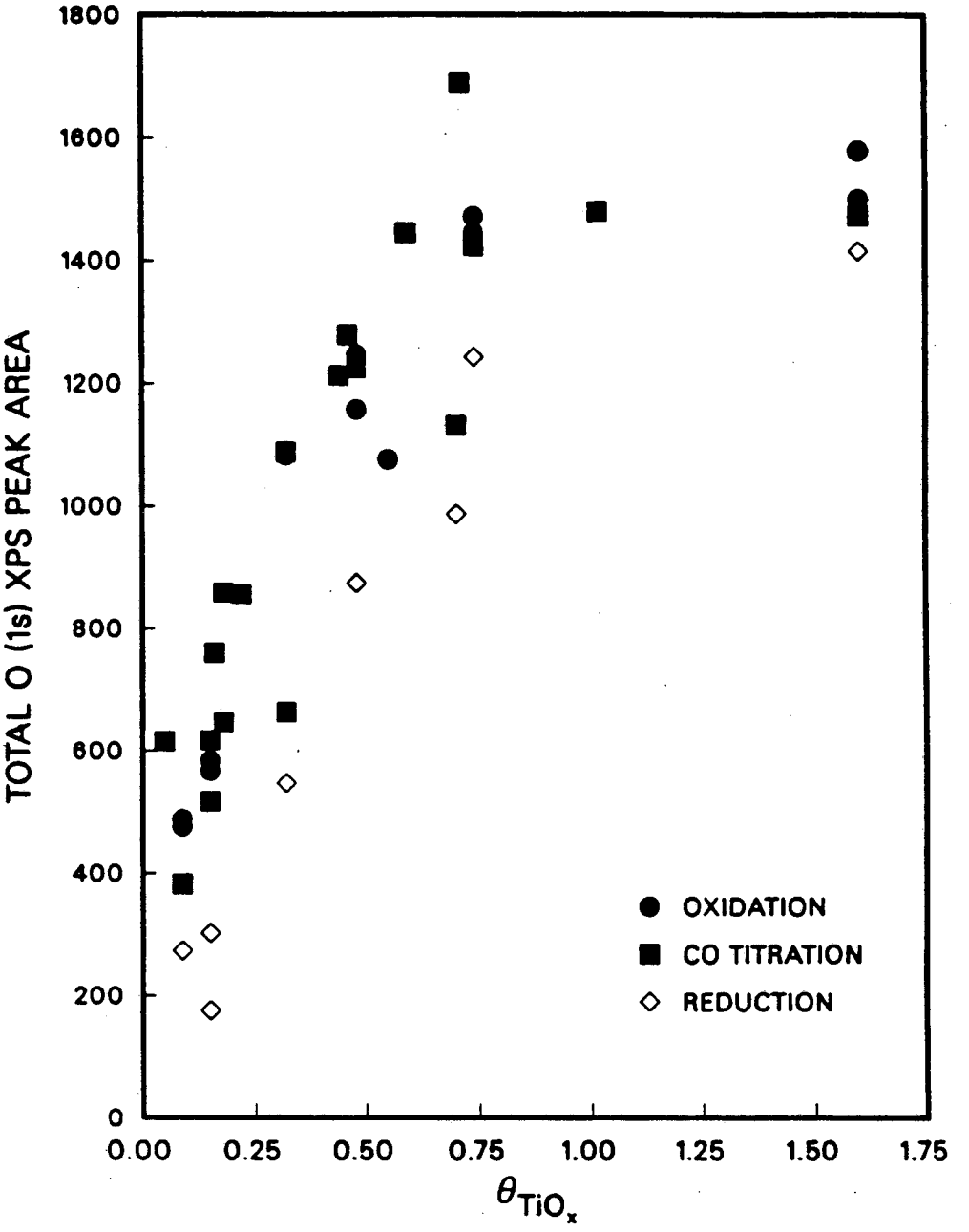

Figure 5.23: Total amount of oxygen in the form of OH as a function of coverage and pretreatment conditions.

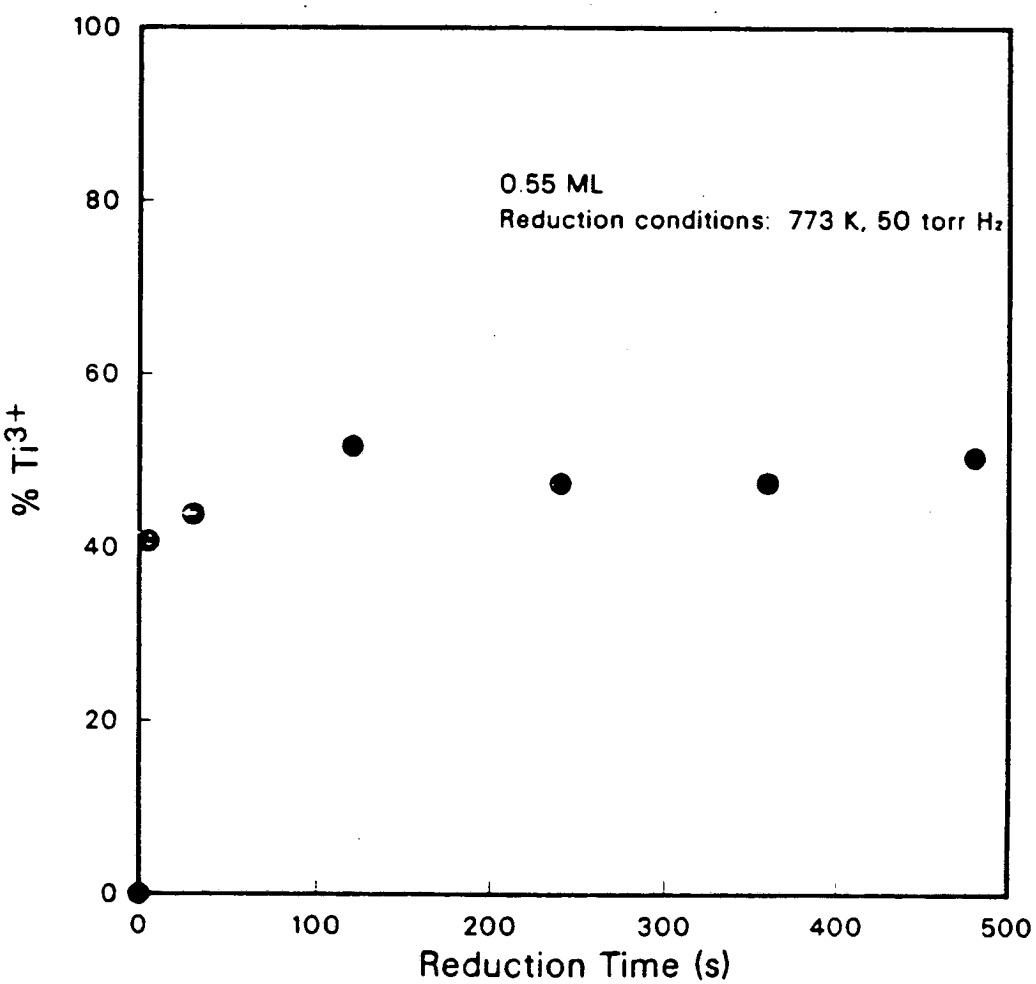

Figure 5.24: Extent of Ti^{3+} generation as a function of H_2 reduction time for a TiO_x coverage of 0.55 ML. Reduction conditions: 50 torr H_2, 773 K.

bulk, presumably as TiO species. Annealing of the 0.71 ML TiO_x/Rh sample also resulted in reduction of Ti and migration of the TiO_x into the bulk. XPS Ti (2p) spectra after 30 second treatments at successively higher temperatures are shown in Fig. 5.26. The Ti^{3+} content varied from 5% (before annealing) to 44% (after a 1173 K treatment) while the apparent TiO_x coverage dropped to 0.58. No Ti^{2+} was observed in this annealing study.

XPS analyses of the sample following conditions used for CO hydrogenation (553 K, 1 atm, H_2:CO = 2:1, 5 min) comprised the final series of experiments. Exposure to reaction conditions was carried out for coverages of 0.15 and 0.70 ML. At both coverages, exposure to the reaction conditions was carried out after the oxidation/CO titration steps as well as after the H_2 reduction step. After reaction, the Ti^{3+} content was seen to lie inbetween the values corresponding to the CO titrated and the H_2 surfaces, as depicted in Fig. 5.27. Subsequent flashing of the sample to 773 K, which removed adsorbed species from the surface, increased the amount of Ti^{3+} present, but not to the extent of H_2 reduction.

5.3.3 CO Chemisorption on TiO_x/Rh

A plot of CO TPD area versus exposure (Fig. 5.28) at a coverage of 0.15 ML shows that 4 L exposures of CO result in near saturation of the surface. Temperature programmed desorption spectra of CO (chemisorbed at room temperature) for various TiO_x coverages are shown in Fig. 5.29. The desorption peak area is rapidly attenuated as titania is added to the surface and at coverages above 0.50 ML, a shoulder at 410 K appears. When normalized with respect to the bare Rh peak area and plotted as a function of TiO_x coverage, as in Figure 5.30, the CO TPD areas are suppressed to a much greater extent with coverage than was observed for the case of alumina overlayers. If the TiO_x species on the surface only blocked CO chemisorption at Rh sites underneath, a linear falloff in chemisorption capacity would be exhibited. No residual carbon was detected on the surface by AES after TPD. CO chemisorption on titania at room temperature is negligible as evidenced by TPD studies at

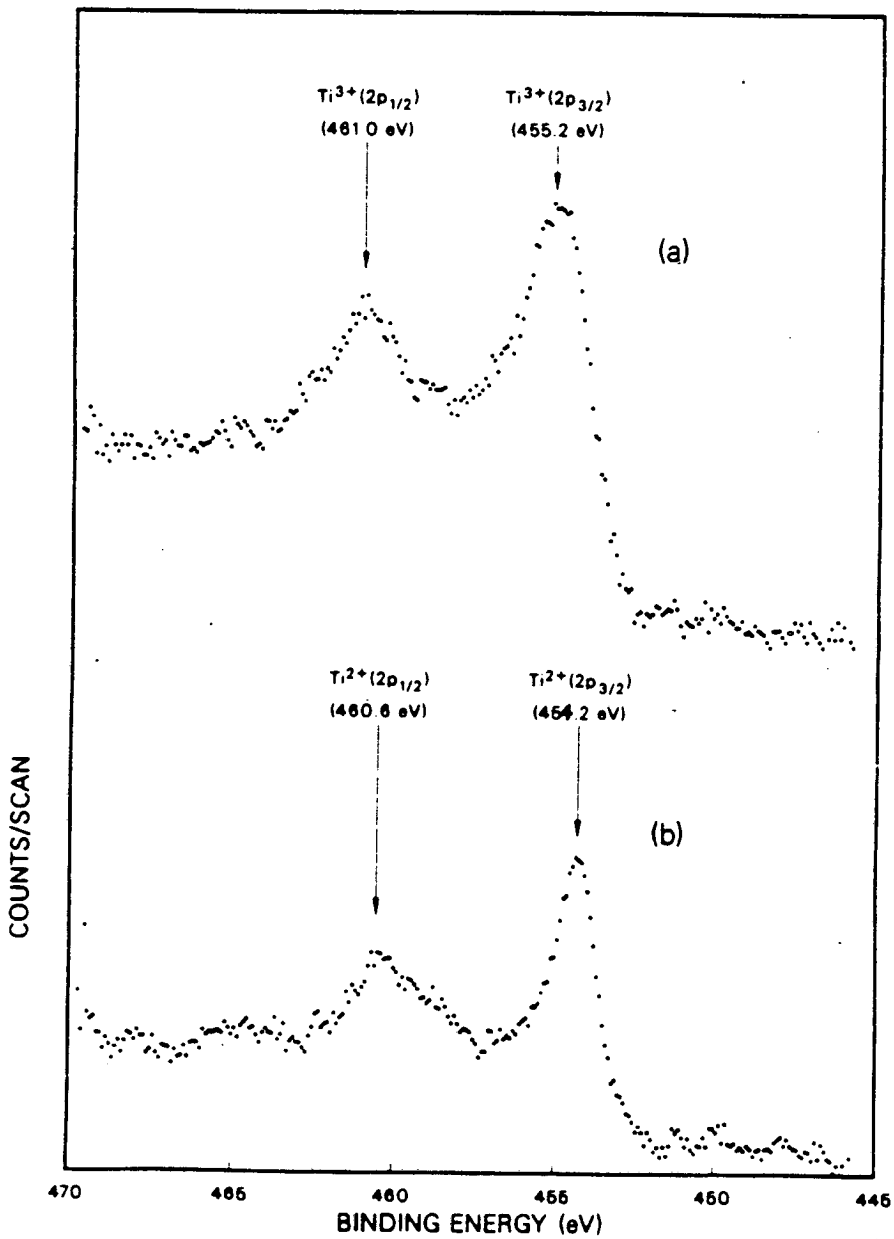

Figure 5.25: Effect of annealing on the oxidation state of Ti in the TiO_x overlayer. (a) The Ti(2p) region for a partially oxidized TiO_x overlayer (0.19 ML). (b) Annealing to 1123 K converted the Ti^{3+} to Ti^{2+}.

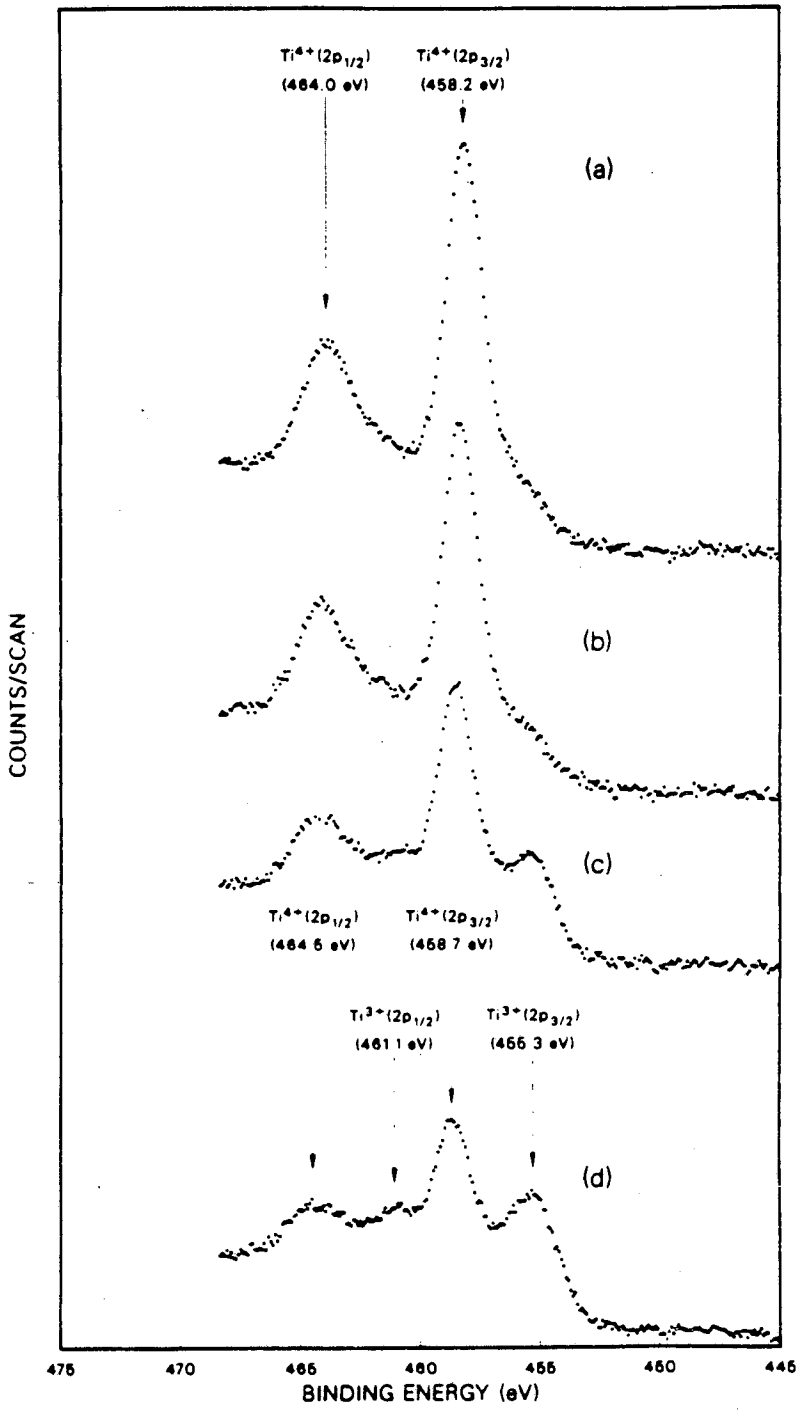

Figure 5.26: Effect of annealing on the oxidation state of Ti in the TiO_x overlayer. (a) The Ti(2p) region for an oxidized TiO_x overlayer (0.71 ML). (b) Annealed at 973 K (30 s). (c) Annealed at 1073 K (30 s). (d) Annealed at 1173 K (30 s).

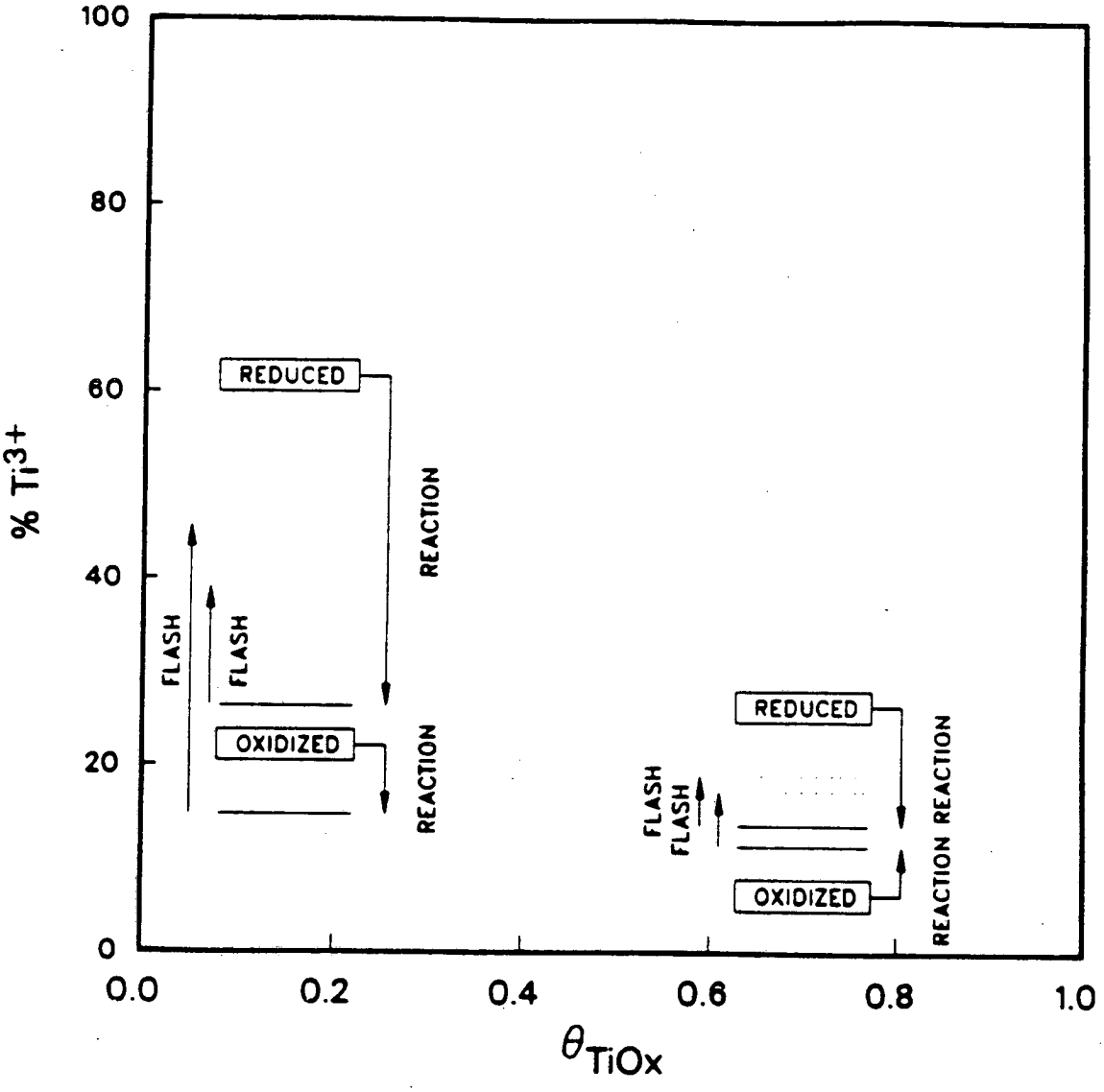

Figure 5.27: Oxidation state of Ti prior to and following reaction conditions (see text) for TiO_x coverages of 0.15 and 0.70 ML. CO titration and H_2 pretreatments were employed, as indicated. The Ti^{3+} percentages after reaction (solid lines) and with subsequent flashing to 773 K (dashed lines) are shown.

high TiO_x coverages.

Residual CO desorption occurred at monolayer coverage equivalent to about 5% of the total for bare Rh. In principal, this could be due to desorption from the Rh support wires, the back side and edges of the sample, or from imperfections in the TiO_x monolayer (where patches of Rh metal would be exposed). Further deposition of titania on the surface continued to reduce the amount of CO chemisorbed, indicating that most of the residual chemisorption is not due to the contribution from the back side of the Rh foil.

A similar series of experiments was performed with liquid nitrogen cooling of the sample. The configuration of the low temperature manipulator limited the lowest attainable temperature to roughly 140 K. The CO TPD spectra for 150 K exposures (Fig. 5.31) appear essentially the same as for room temperature exposures except that the low temperature onset is more pronounced. However, no new peaks are observed that could be attributed to the additional CO chemisorption suppression given in Fig. 5.30.

Figure 5.32 illustrates the effect of TiO_x coverage on CO TPD area at the low temperature exposures. Note that the temperatures of Ti deposition and oxidation have no appreciable effect on the results. Repeated heating of the sample to 773 K during thermal desorption may cause titania on the surface to react with adsorbed species, such as water, or to rearrange to a more favorable configuration. The points coincide with the curve defined by room temperature CO adsorption (Fig. 5.30), but converge to zero area above coverages of 0.60 ML. In these experiments, Pt support wires were used and the mass spectrometer was fitted with an improved collimator. These results suggest that imperfections in the TiO_x monolayer are not the principal cause of the residual desorption area.

Another CO chemisorption study was performed to ascertain whether pre-sputtering of the Rh surface would alter the TiO_x growth characteristics and hence, the CO chemisorption versus coverage plot. Apparently, this is not the case (Fig. 5.33). This may be due to rearranging of the surface from heating of the sample during TPD.

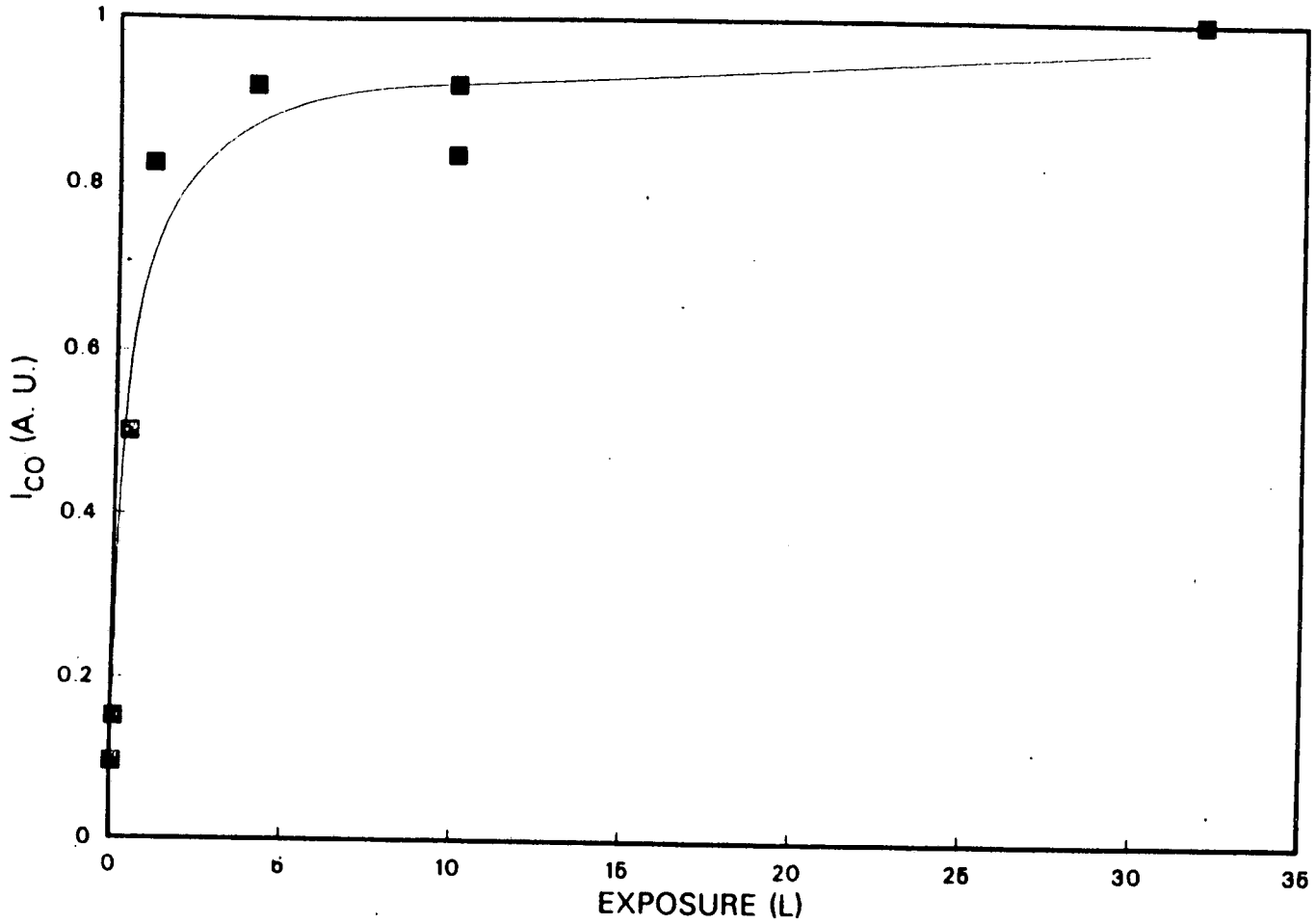

Figure 5.28: Surface CO coverage (normalized) as a function of CO exposure on Rh with 0.20 ML TiO_x.

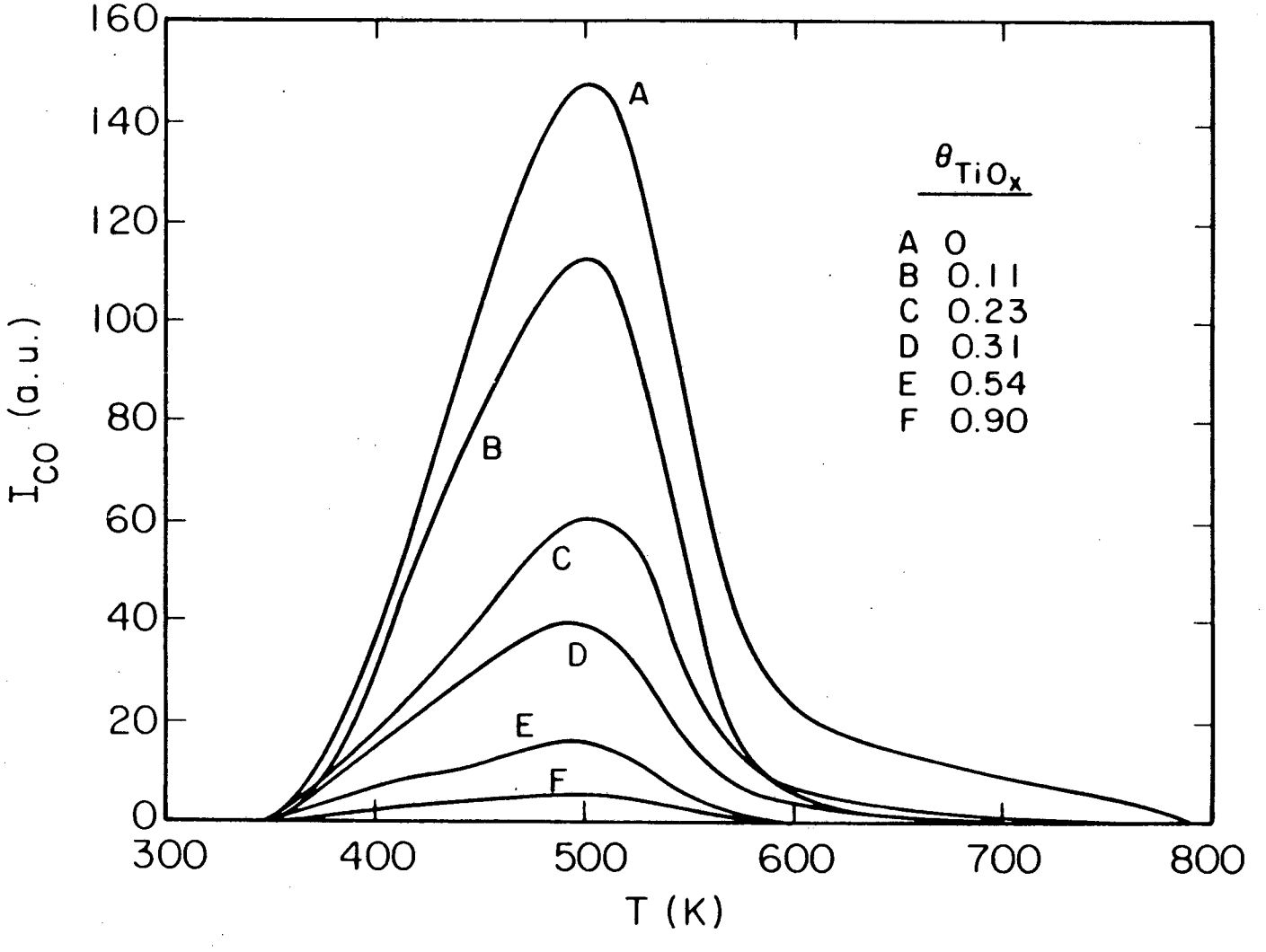

Figure 5.29: Effect of TiO_x coverage on the TPD spectra after 4 L CO exposure to the Rh foil.

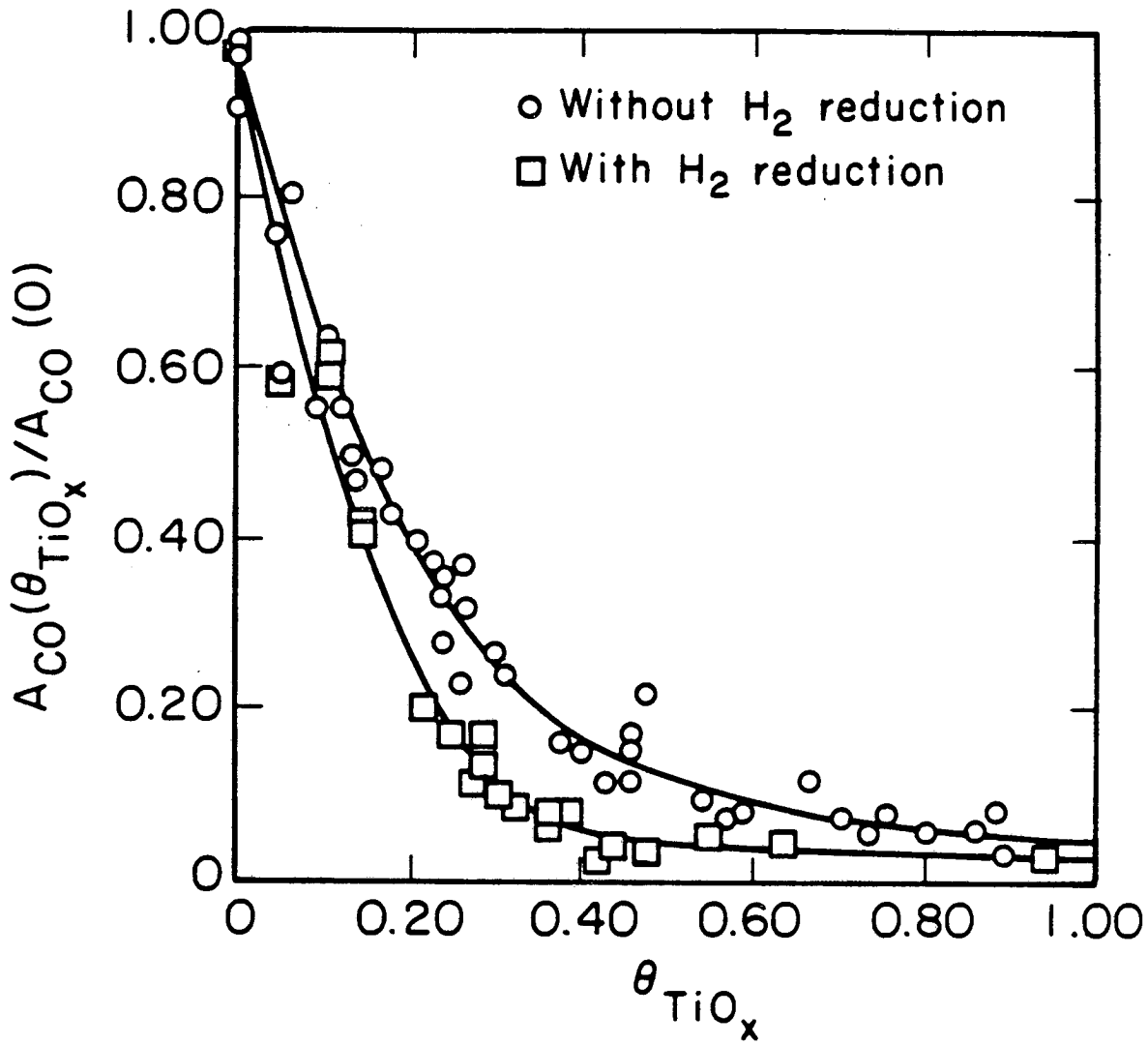

Figure 5.30: The effect of TiO_x coverage on the amount of CO adsorbed on Rh foil. Circles denote the amount of CO adsorbed following CO titration of the sample; squares denote the amount of CO adsorbed following H_2 reduction of the sample (50 torr H_2, 753 K, 5 min).

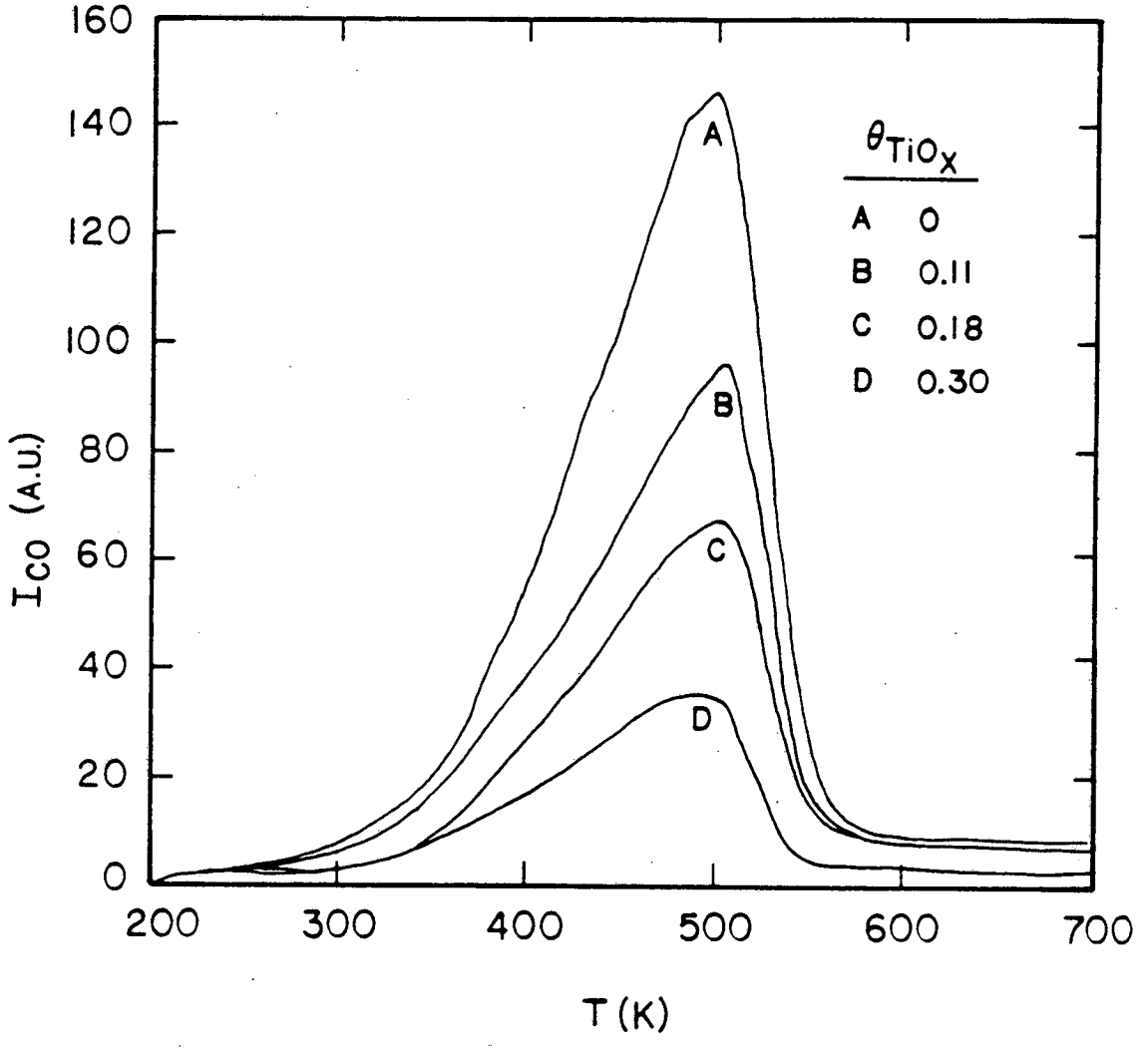

Figure 5.31: Effect of TiO_x coverage on the TPD spectra after exposure of the Rh foil to 4 L CO at 150 K.

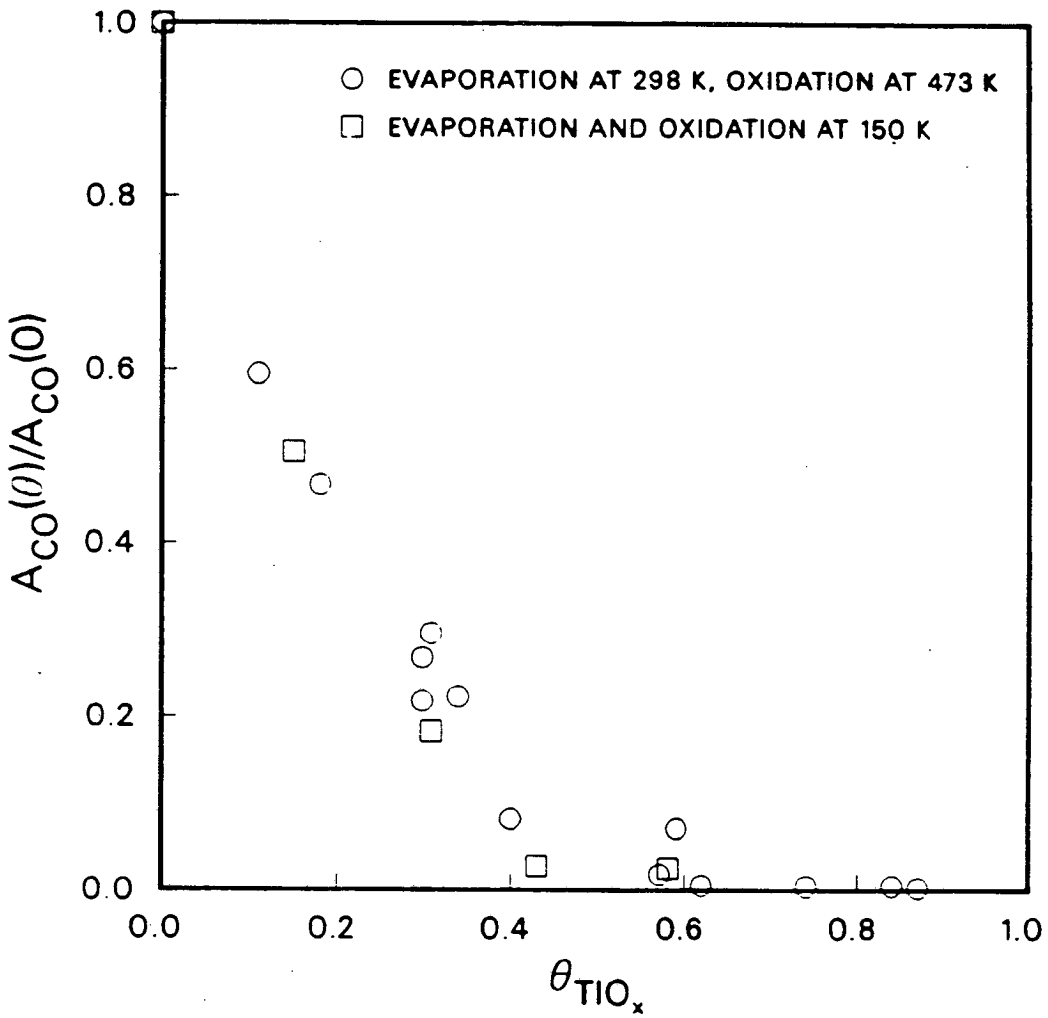

Figure 5.32: Amount of CO adsorbed at 150 K on Rh foil as a function of TiO_x coverage. Circles denote room temperature Ti deposition with oxidation at 473 K, while the squares denote evaporation and oxidation at 150 K.

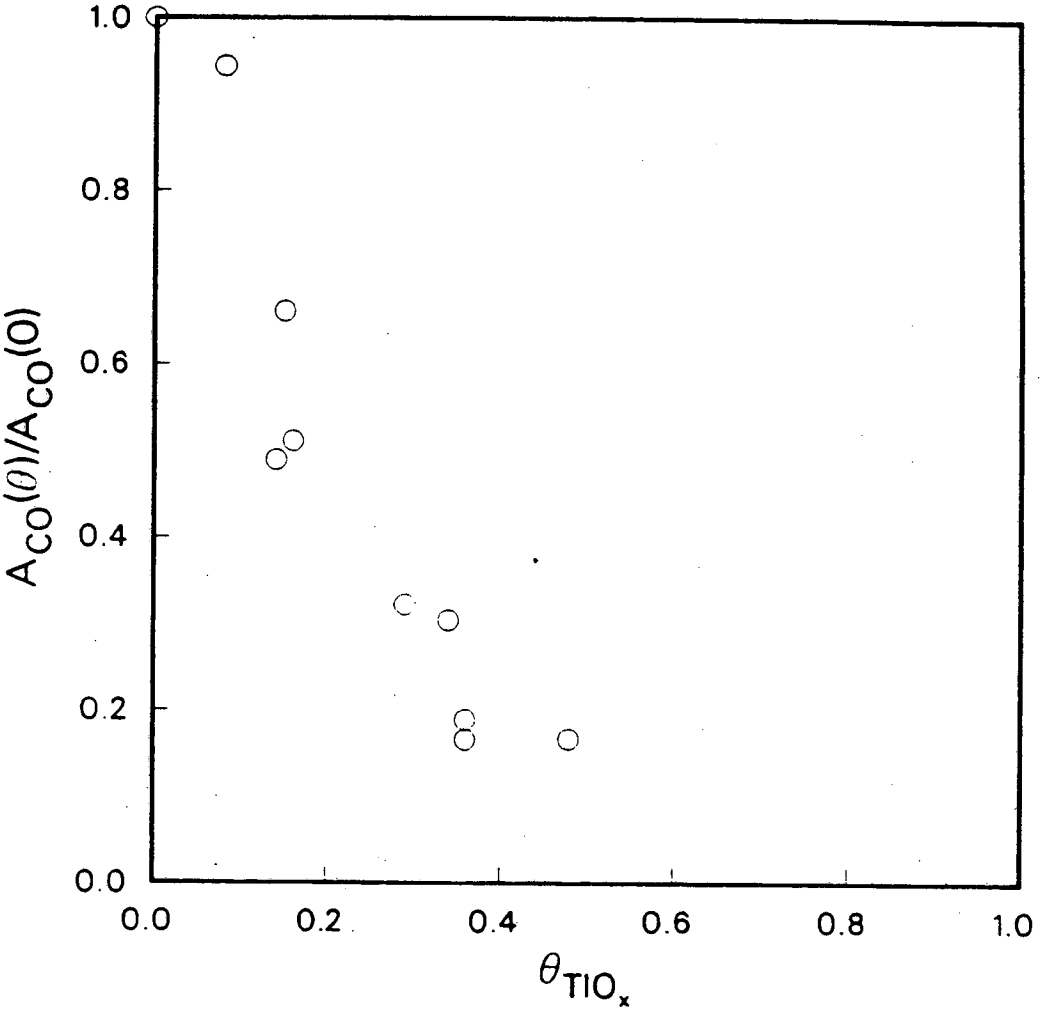

Figure 5.33: Amount of CO adsorbed at 150 K on Rh foil as a function of TiO_x coverage. Titania was deposited (at 150 K) immediately after argon ion sputtering of the surface.

5.3.4 CO Chemisorption on TiO_x/Rh after H_2 Reduction

Since the suppression of CO chemisorption on TiO_2-supported Group VIII metals was originally observed after reduction in hydrogen at temperatures near 773 K [8,9], it was natural to study the effect of H_2 reduction on CO chemisorption in the TiO_x/Rh system. CO TPD spectra, after reduction in 50 torr H_2 at 753 K, for TiO_x coverages up to 1 ML are displayed in Fig. 5.34 and a comparison of spectra for the non-reduced and reduced samples are shown in Fig. 5.35. Not only is the CO TPD area more sharply attenuated with higher coverages, but the low temperature feature is more prominent. A plot of CO TPD area after reduction as a function of coverage (Fig. 5.30) reveals more extensive suppression of CO chemisorption by about a factor of 2. It should be noted that the CO peak area-versus-coverage plot converges to the value for clean rhodium at low coverages, indicating that the adsorption capacity of the clean rhodium foil is unaffected by H_2 reduction.

The temperature of H_2 reduction was also found to be important. Figure 5.36 illustrates the temperature at which further suppression is induced for TiO_x coverages of 0.16, 0.25, and 0.66 ML. Normalized to the areas for the same non-reduced TiO_x coverages, the CO TPD areas indicate that the reduction step, when carried out below 500 K, does not alter CO chemisorption on the surface. At 600 K, the onset of the additional suppression is seen.

Analysis of the sample by AES after H_2 reduction reveals two trends (1) the apparent TiO_x coverage after reduction at 753 K is within a few percent of the pre-reduction value and (2) the O/Ti ratio decreases during the H_2 reduction (Fig. 5.37). Although there is a significant amount of scatter in the data, it is clear that the more extreme the reduction conditions, the more reduced the oxide overlayer becomes. The average atomic O/Ti ratio (after correction for electron escape depths) changes from roughly 2 to 1.3 (after 753 K reduction), a range substantiated by the XPS results (Fig. 5.16a).

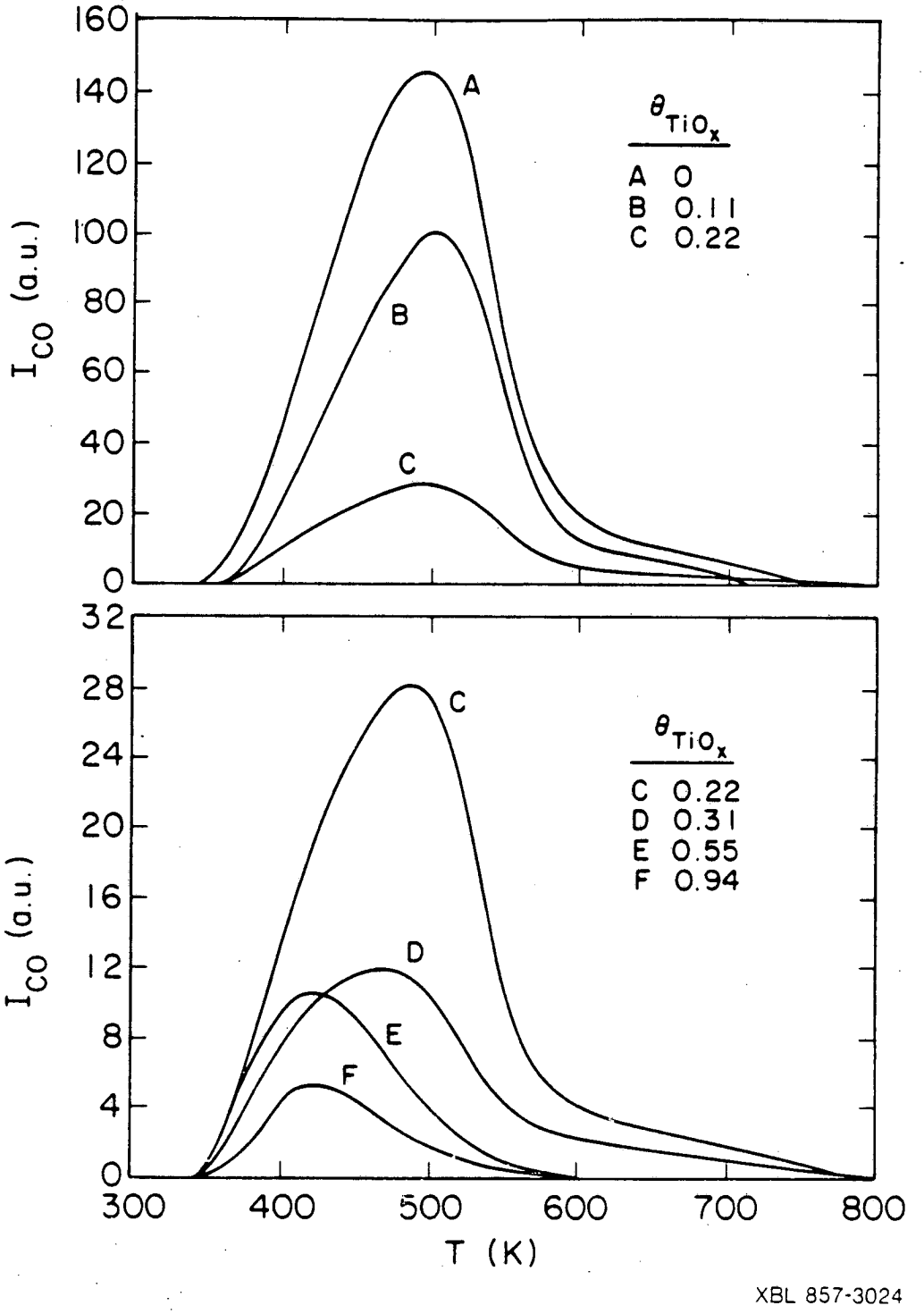

Figure 5.34: Effect of high-temperature reduction (50 torr H_2 at 750 K, 5 min) of TiO_x on the TPD spectra of CO from Rh foil: (a) $\theta \leq 0.22$; (b) $\theta \geq 0.22$.

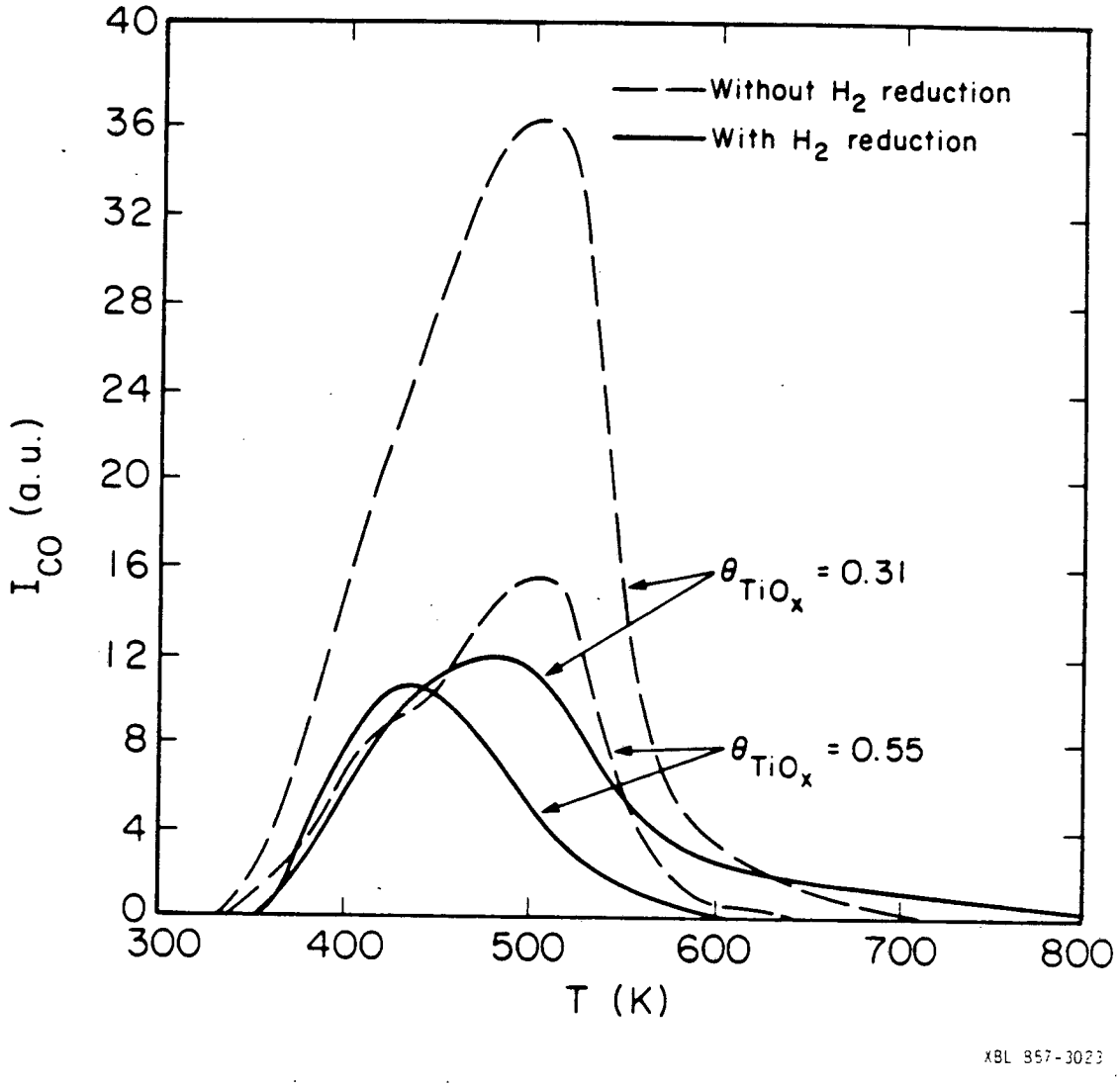

Figure 5.35: Effect of high temperature reduction of TiO_x on the CO TPD spectra for a fixed θ_{TiO_x} coverage.

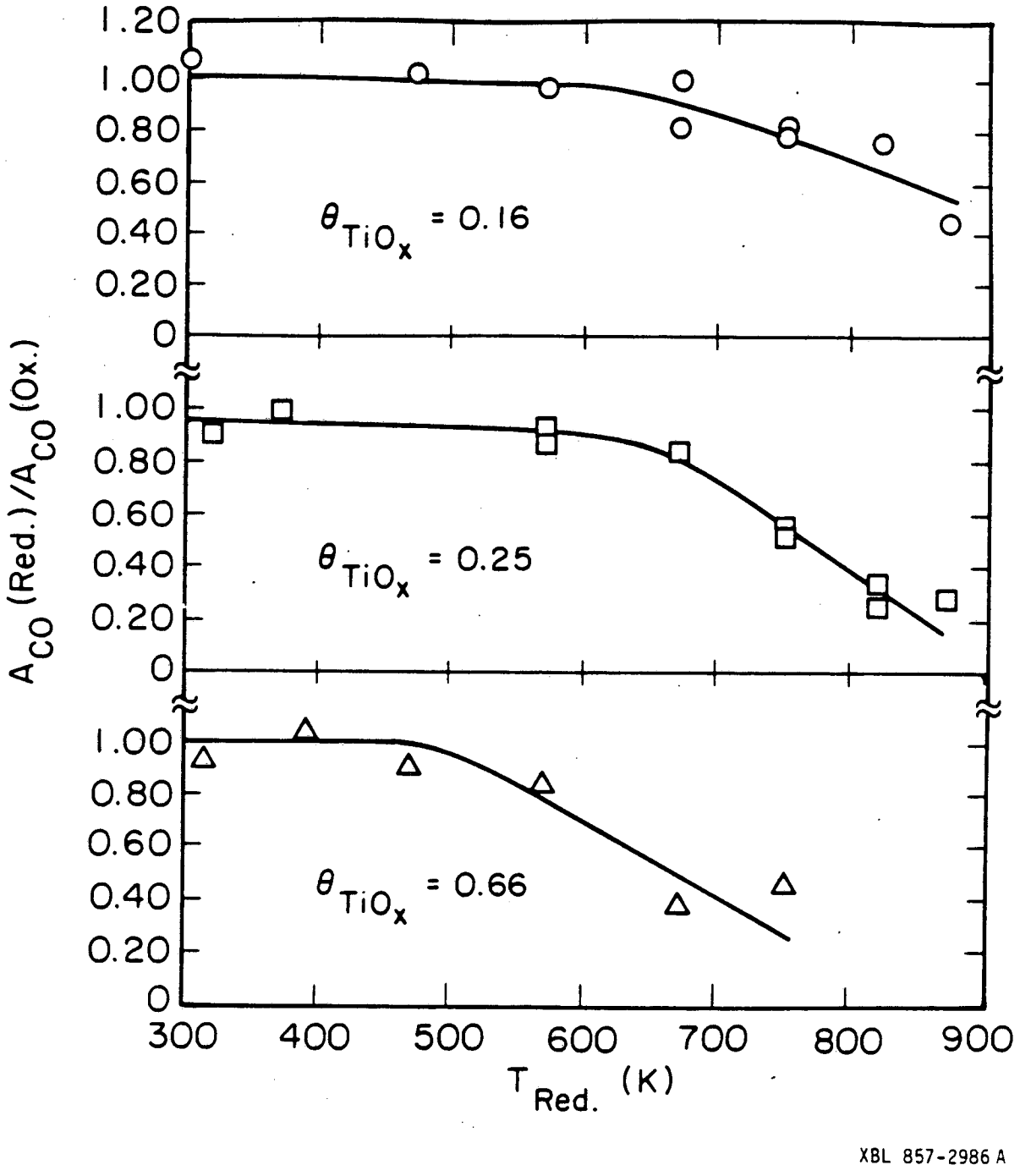

Figure 5.36: Effect of reduction temperature on the amount of CO adsorbed for various coverages of TiO_x on Rh foil relative to the amount without reduction.

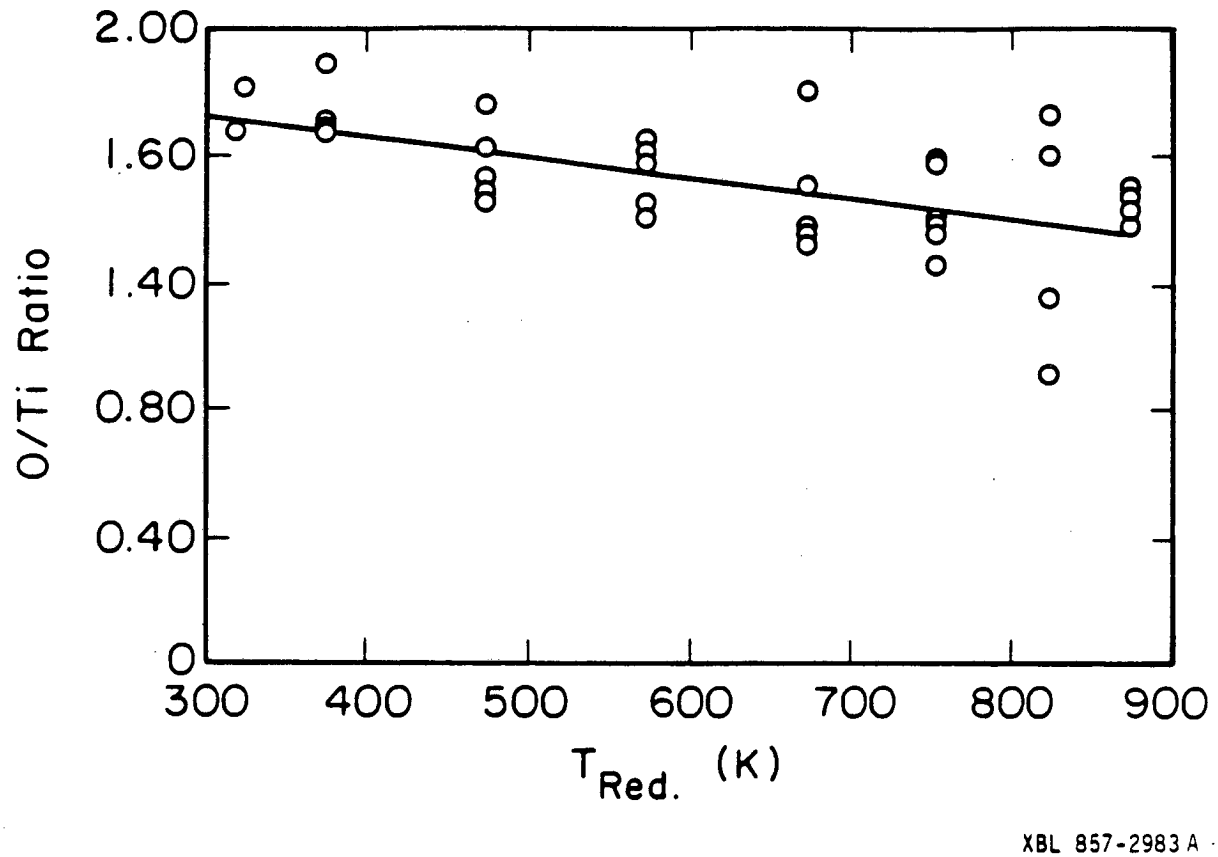

Figure 5.37: Effect of reduction temperature on the apparent O/Ti ratio (as measured by AES).

5.3.5 CO Hydrogenation on TiO_x/Rh

The rate of methane formation as a function of TiO_x coverage is shown in Fig. 5.38. At conditions of 553 K, 1 atm pressure, and a 2:1 H_2-to-CO ratio, the reaction rate rose as TiO_x was added to the surface, reaching a maximum at 0.15 ML. The maximum corresponded to a three-fold increase in rate. Thereafter, the rate decayed sharply until about 0.30 ML and decreased more gradually beyond that coverage. Residual methanation activity occurred at monolayer coverage and could be reduced further by additional TiO_x deposition. A gold foil mounted on the Pt support wires showed negligible activity under identical reaction conditions indicating an insignificant contribution to the reaction rate by the support wires or cell walls. For five different TiO_x coverages, the sample was also pre-reduced in 50 torr H_2 at 753 K for 5 minutes. No significant effects from the hydrogen pre-treatment could be discerned.

More dramatic enhancements are observed in the formation of C_2 and C_3 hydrocarbons at low coverages as seen in Figure 5.39. Most notable are the more than order-of-magnitude increases in rates at $\theta_{TiO_x} = 0.20$ ML for ethylene and propylene. As with methane, the rates quickly diminish as higher coverages are reached. As seen in Figure 5.40, the methane content of the hydrocarbon product falls from a value of 94 mol% when no titania is present to nearly 60 mol% for $\theta_{TiO_x} = 0.20$. Ethylene and propylene are the predominant higher hydrocarbon species comprising roughly 34% of the total hydrocarbon product. At higher coverages, the selectivities return to values more characteristic of clean Rh.

The influence of TiO_x on the kinetic parameters of CO hydrogenation on Rh was also investigated. The variations of the activation energy, along with the H_2 and CO partial pressure dependences, as described by Eqn. 5.1, are presented in Figs. 5.41 to 5.43. The plot of activation energy (Fig. 5.41) shows a minimum of 16.8 $\pm$ 0.5 kcal/mole at a coverage just above 0.2 ML. This represents a downward shift of about 7.7 kcal/mole from the clean Rh value.

The hydrogen reaction order displayed in Fig. 5.42 rises sharply from a value of 1.0 $\pm$

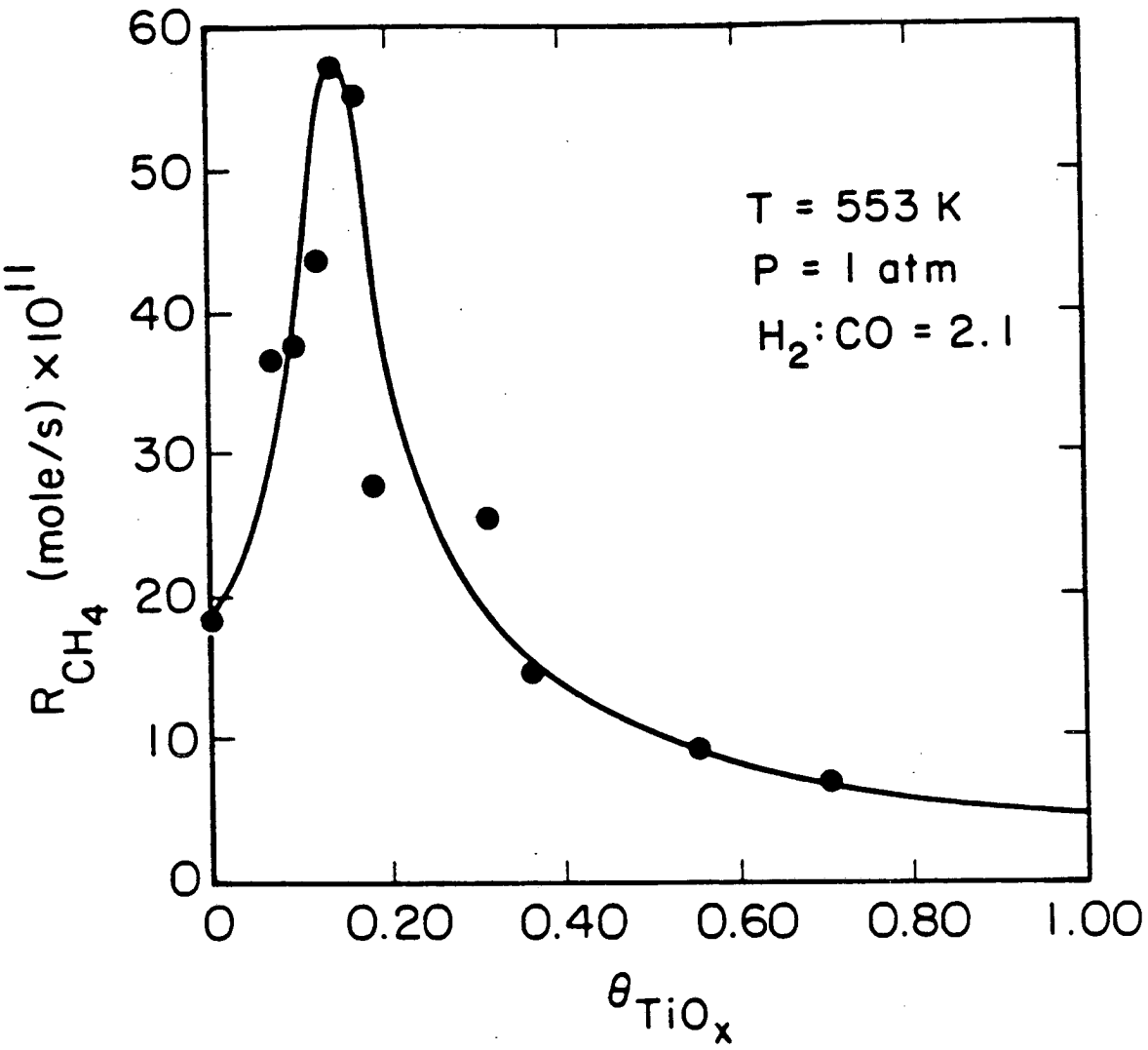

Figure 5.38: Methanation rate on TiO_x-promoted Rh as a function of TiO_x coverage. Reaction conditions were: 553 K, 1 atm total pressure, H_2:CO = 2:1.

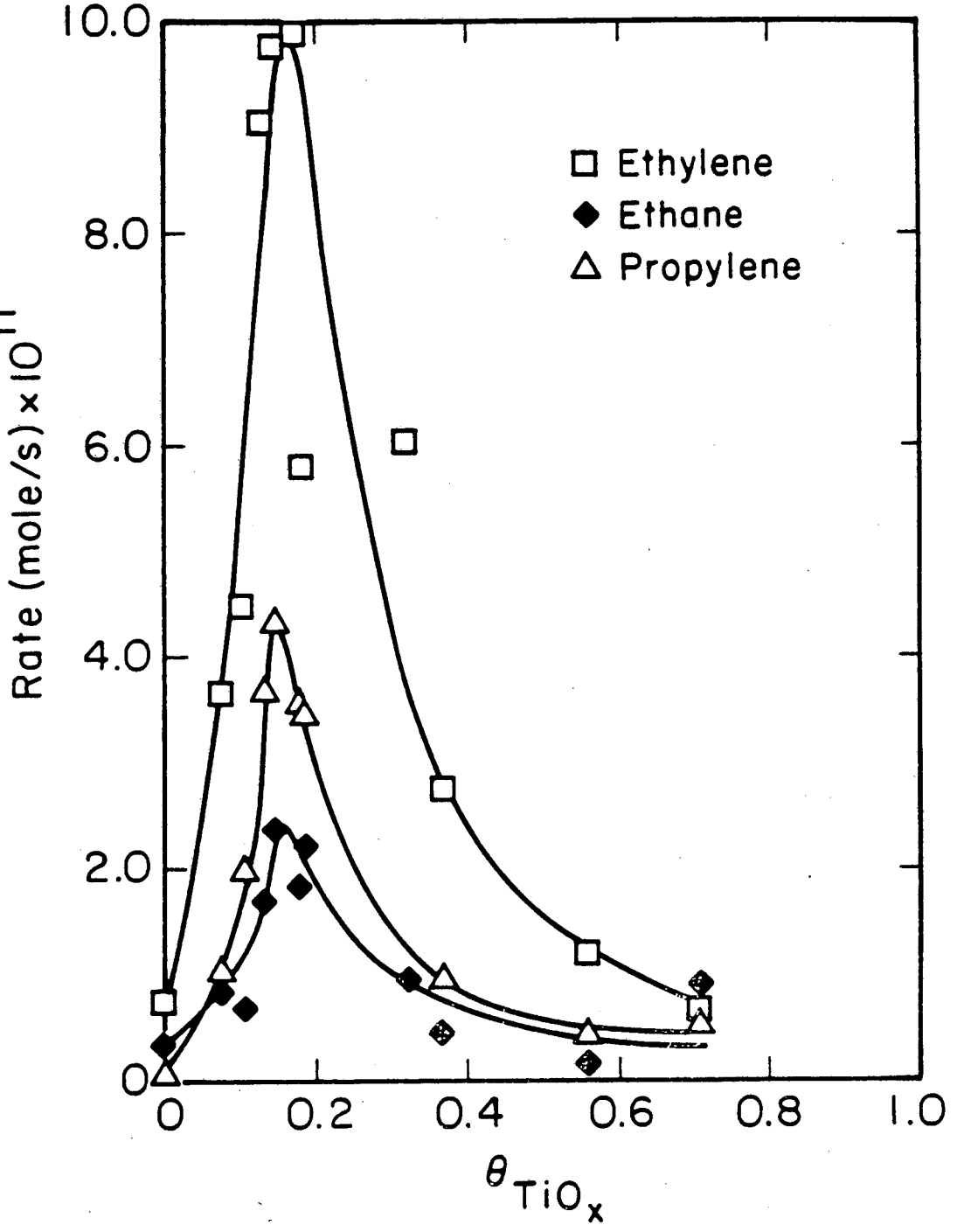

Figure 5.39: Higher hydrocarbon formation rates on TiO_x/Rh as a function of TiO_x coverage. Reaction conditions were: 553 K, 1 atm total pressure, and H_2:CO = 2:1.

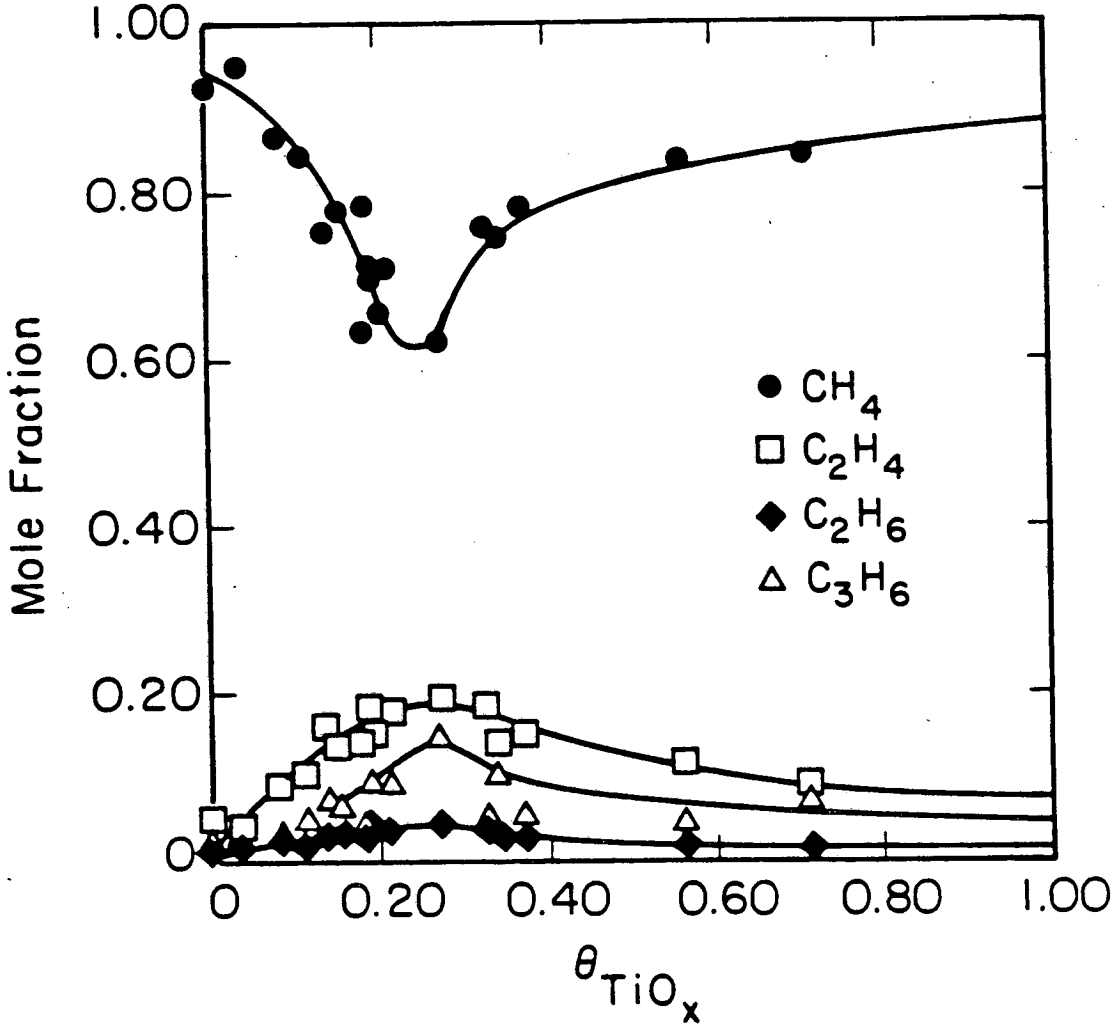

Figure 5.40: Hydrocarbon product selectivity as a function of TiO_x coverage. Reaction conditions were: 553 K, 1 atm total pressure, and H_2:CO = 2:1.

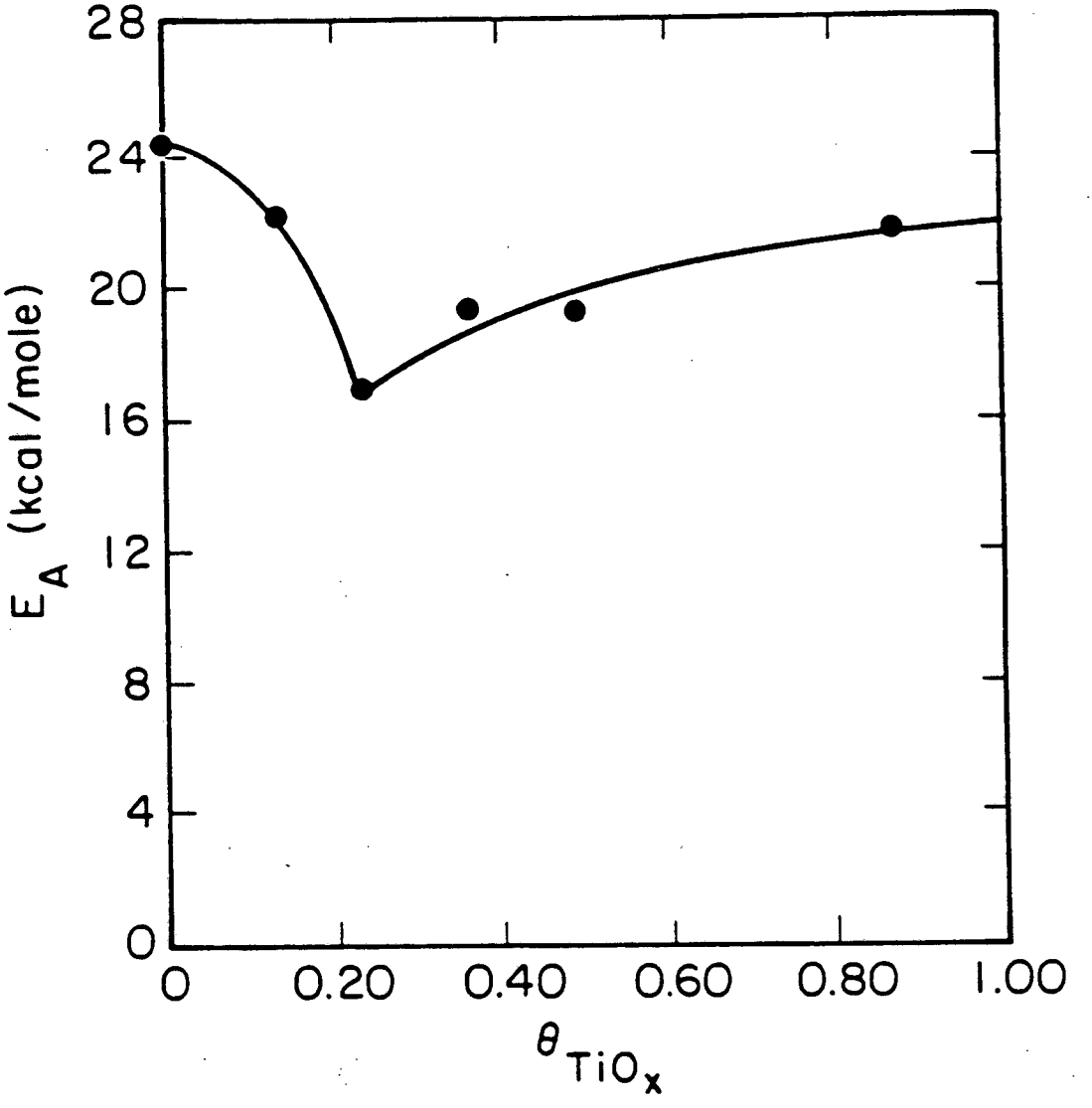

Figure 5.41: Activation energy for methane formation as a function of TiO_x coverage. Reaction conditions were identical to Fig. 5.40 except the temperature was varied between 473 and 633 K.

0.1 to 2.6 ± 0.1 at $\theta_{TiO_x} = 0.10$ and then slowly decays to a value of 1.5 near monolayer coverage. This trend is repeated in the CO partial pressure dependence plot (Fig. 5.43), but to a lesser extent. The CO reaction order passes through a maximum at $\theta_{TiO_x} = 0.15$ with m = -0.3 ± 0.1, compared with -1.0 ± 0.1 for clean Rh. Kinetic parameter values corresponding to $\theta_{TiO_x} = 0.20$ are listed in Table 5.1.

The rate parameters for higher hydrocarbon formation were also modeled with power-law expressions of the form of Eqn. 5.1 and the parameter values are plotted in Figures 5.44 to 5.46. As in the case for methane, a decrease in the activation energy at low coverages is observed for ethane (Fig. 5.44) followed by a gradual rise above 0.3 ML. However, the presence of TiO_x has virtually no effect on the activation energies of ethylene and propylene formation.

For all three hydrocarbons, the H_2 reaction orders increase significantly between 0 and 0.10 ML (Fig. 5.45). Ethane appears to follow the same trend as methane, while the olefins rise from near zero-order dependence to 1.5 order and fall slightly thereafter. The trends for the CO reaction orders are particularly interesting. Unlike methane, where a -1.0 order is encountered, positive orders between 0.5 and 1.5 are seen for the other hydrocarbons on the clean surface (Fig. 5.46). With the addition of titania, the CO reaction orders for the C_2 hydrocarbons decrease to -1.0. Propylene, though, exhibits a broad minimum at about 0.4 ML where the reaction becomes zero order in CO.

Coinciding with the higher activities for hydrocarbon formation on the TiO_x/Rh surface was a greater degree of carbon deposition, as determined by AES immediately after reaction. The normalized carbon signal is plotted in Fig. 5.47 versus TiO_x coverage and shows a maximum of 0.4 at a coverage of 0.4 ML. At higher coverages, the carbon content returns to the value typical of bare Rh and of AlO_x on Rh. Figure 5.47 also shows that the relative activity after one hour of reaction is lowest at the same coverages where the maximum in initial methanation activity occurs, *i.e.*, the higher methanation rates are accompanied by significantly higher deactivation rates. A cross-plot of the percentage deactivation as a function of surface carbon coverage for both alumina and titania overlayers reveals an

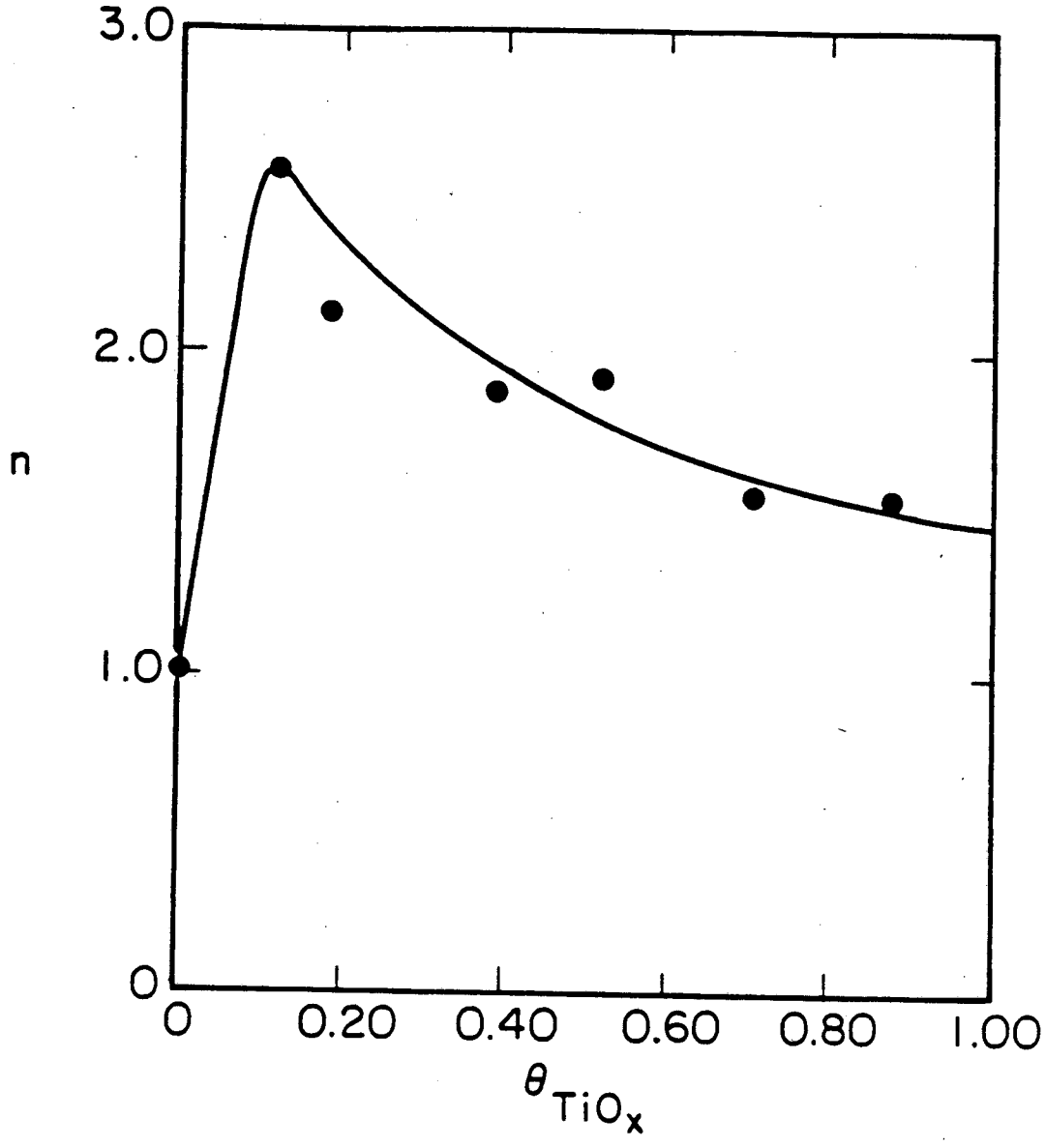

Figure 5.42: Hydrogen partial pressure dependence as a function of TiO_x coverage. Reaction conditions were identical to Fig. 5.40 except the hydrogen partial pressure was varied from 0.23 to 0.67 atm.

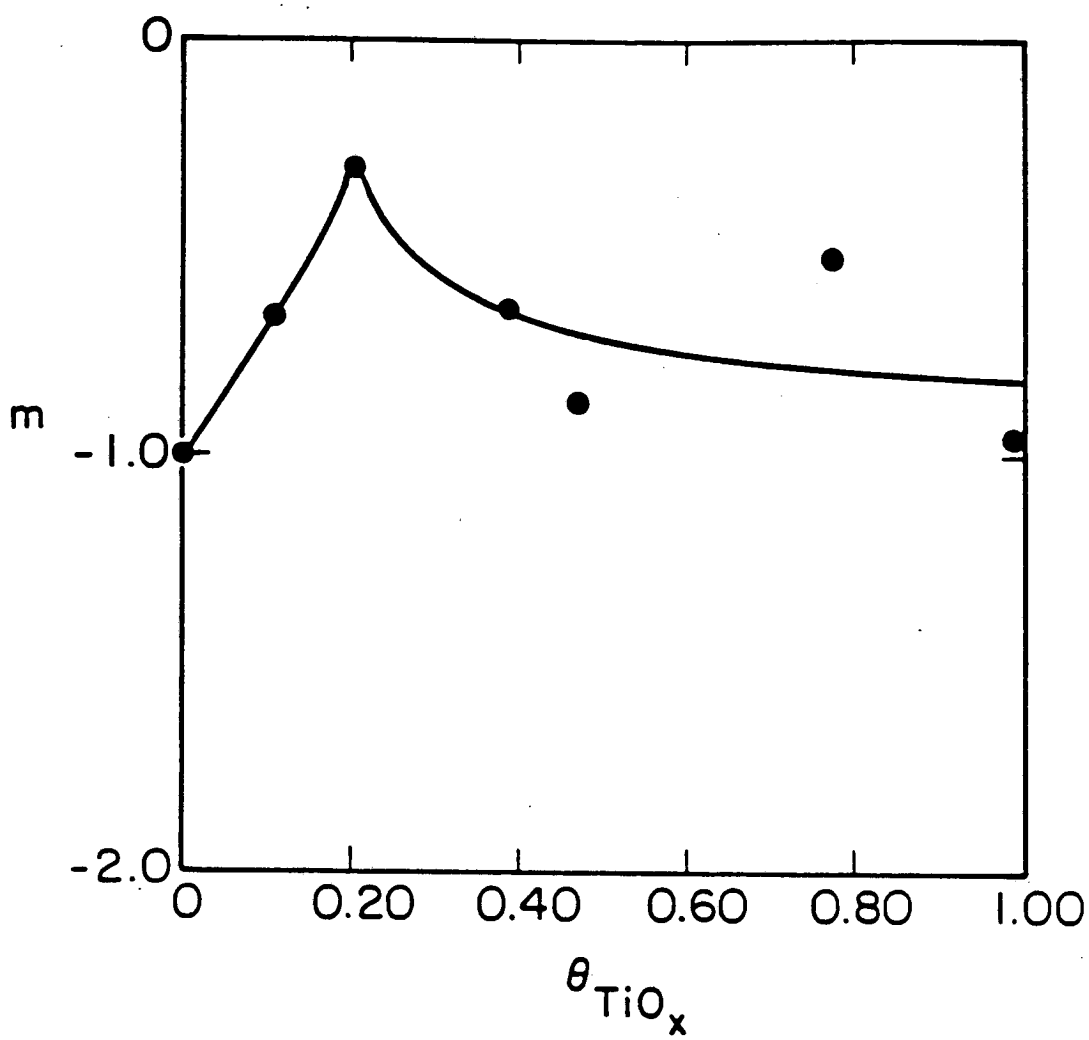

Figure 5.43: CO partial pressure dependence as a function of TiO_x coverage. Reaction conditions were identical to Fig. 5.40 except the CO partial pressure was varied between 0.037 and 0.33 atm.

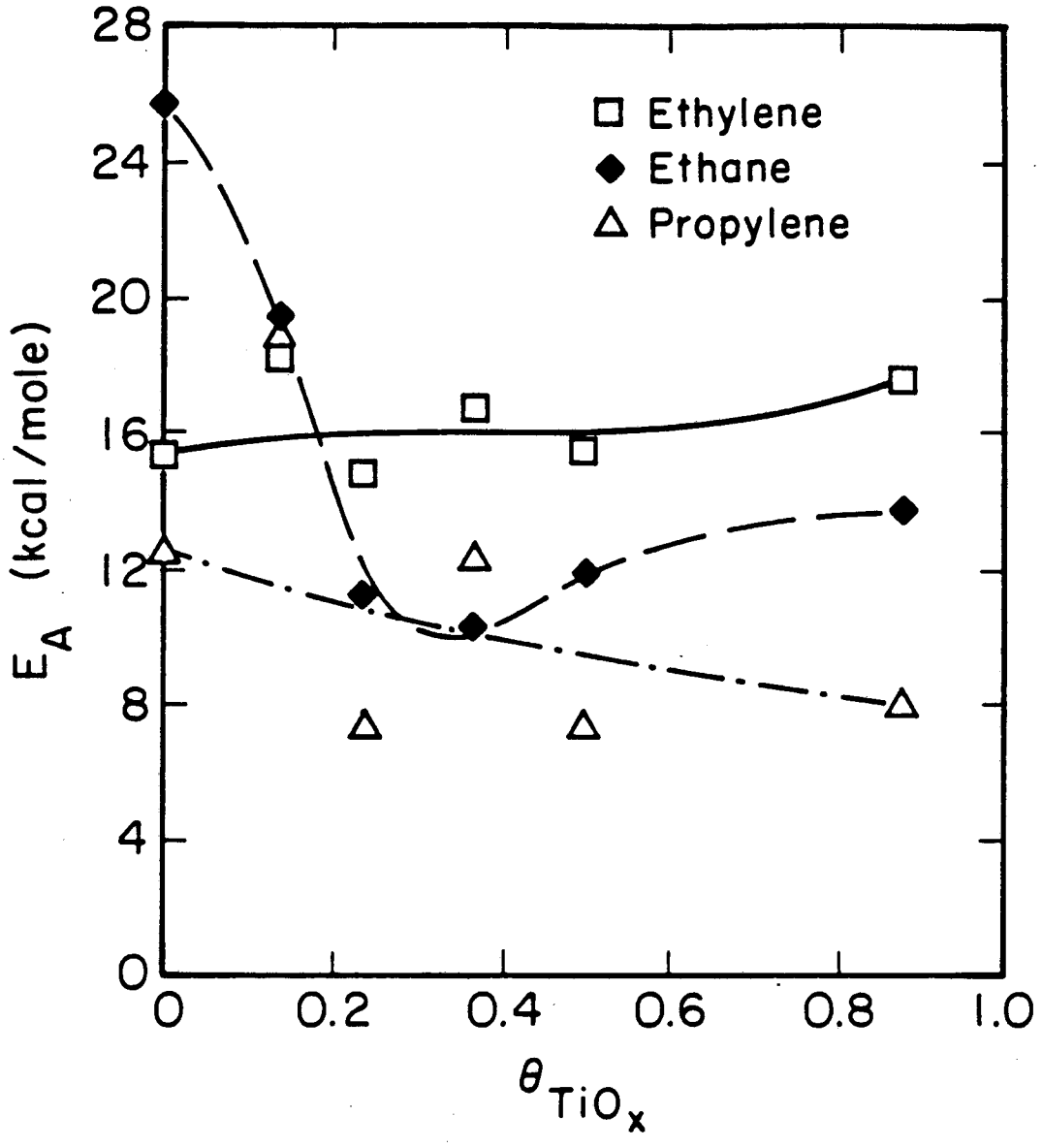

Figure 5.44: Activation energy for C_{2+} hydrocarbon formation as a function of TiO_x coverage.

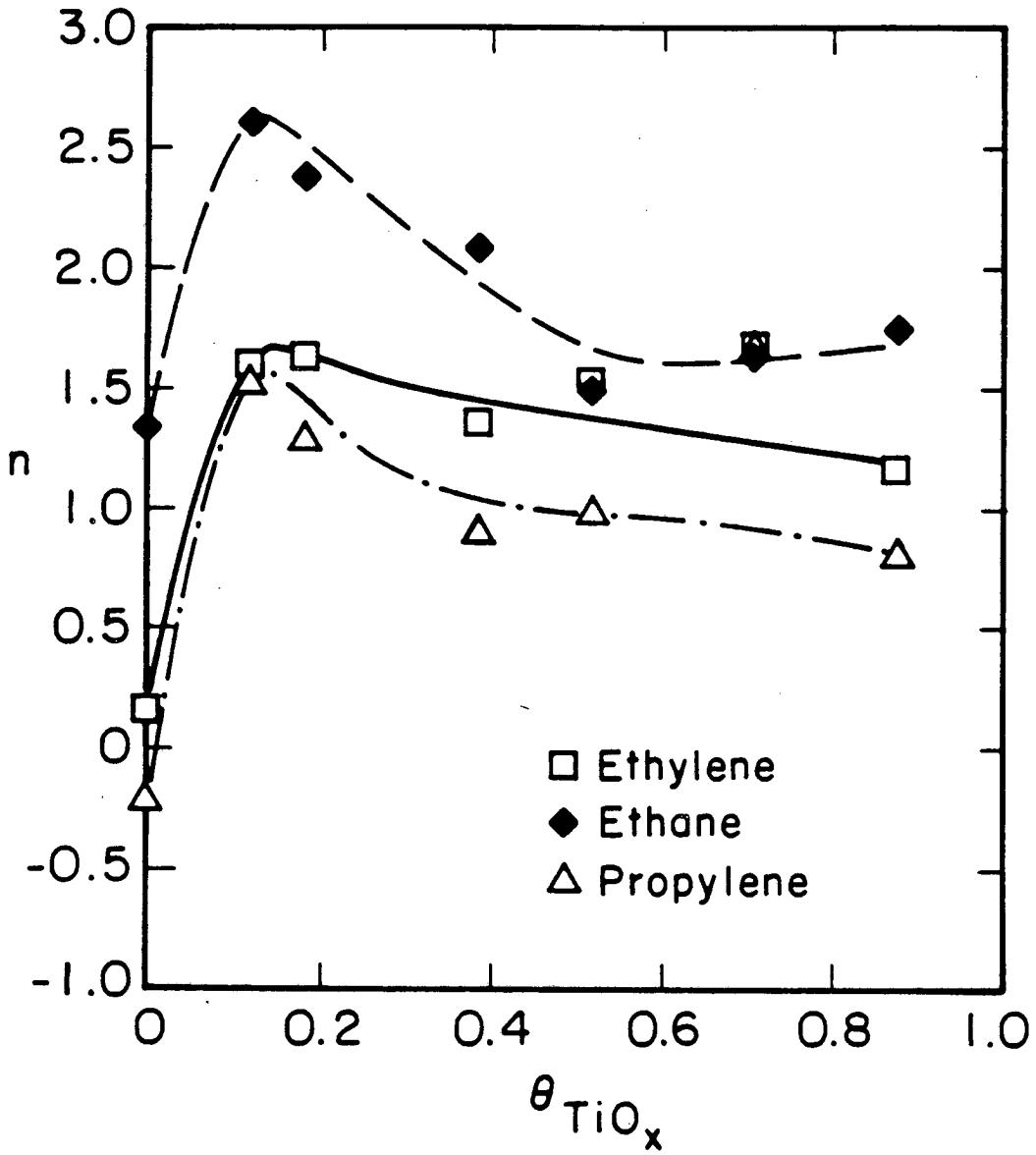

Figure 5.45: Hydrogen partial pressure dependence for C_{2+} hydrocarbon formation as a function of TiO_x coverage.

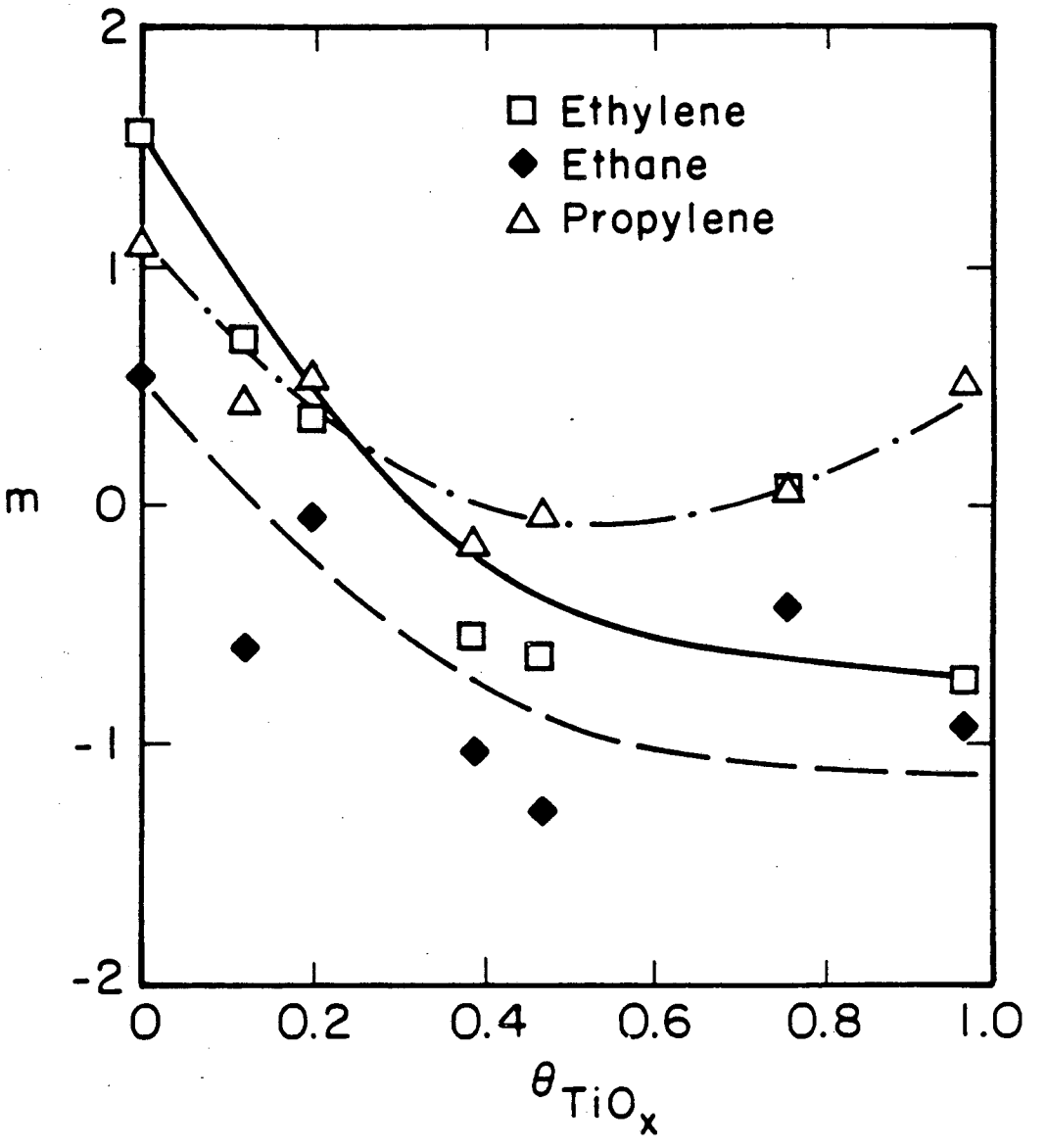

Figure 5.46: CO partial pressure dependence for C_{2+} hydrocarbon formation as a function of TiO_x coverage.

exponential-like decay with surface carbon (Fig. 5.48).

5.3.6 Ethylene Hydrogenation on TiO_x/Rh

The enhancement of CO hydrogenation prompted the study of other reactions of simple molecules. Ethylene hydrogenation was carried out with 25 torr of ethylene and 25 torr of hydrogen, with argon making up the balance to 1 atm, as in Section 5.1.3. The effect of titania coverage on the reaction rate is illustrated in Fig. 5.49. The activity was found to decrease strongly with coverage in a manner resembling the CO chemisorption-versus-coverage plot of Figure 5.30. Titania therefore suppresses this hydrogenation reaction beyond that expected from the covering of active sites. No other reaction products were observed. Explanations for this behavior will be discussed later.

The temperature dependence for ethylene hydrogenation appears in Fig. 5.50 for bare rhodium and for a TiO_x coverage of 0.21 ML. Both curves yield activation energies slightly above 6 kcal/mole and exhibit "flattening out" of the rate at the higher temperature. The similarity between the bare and partially covered surfaces suggests that there are no dramatic changes in the reaction mechanism when titania is added to the surface.

5.3.7 Ethane Hydrogenolysis on TiO_x/Rh

The reports by investigators [12,14,23,24,29] of sharply diminished hydrocarbon hydrogenolysis activities when the platinum metals are supported on titania make ethane hydrogenolysis an excellent model reaction for the TiO_x/Rh system. Ethane hydrogenolysis rates at 513 K, with 25 torr ethane, 25 torr hydrogen, and 710 torr argon are plotted in Fig. 5.51 as a function of TiO_x coverage. The dependence on TiO_x coverage is similar, though steeper, than that observed for ethylene hydrogenation. Titania appears to suppress the hydrogenolysis reaction to the extent of CO chemisorption. At $\theta_{TiO_x} = 0.60$, virtually

no activity is seen. The only product observed (at all titania coverages) was methane.

Figure 5.52 shows the temperature dependence for this reaction for both clean Rh and for low TiO_x coverages. Below 453 K, both samples display activation energies near 35.5 kcal/mole which compares with values of 36 kcal/mole for TiO_2-supported Rh [30] and 42 kcal/mole for SiO_2-supported Rh [133]. Above 453 K, the slopes are diminished resulting in activation energies of about 12 kcal/mole. Evidently this behavior at the higher temperatures is not particular to the TiO_x/Rh catalyst. The origin of this effect will be discussed later. As in the case of ethylene hydrogenation, the trends with temperature for the bare and TiO_x-covered surfaces are very similar, suggesting no dramatic changes in the mechanism when TiO_x is present.

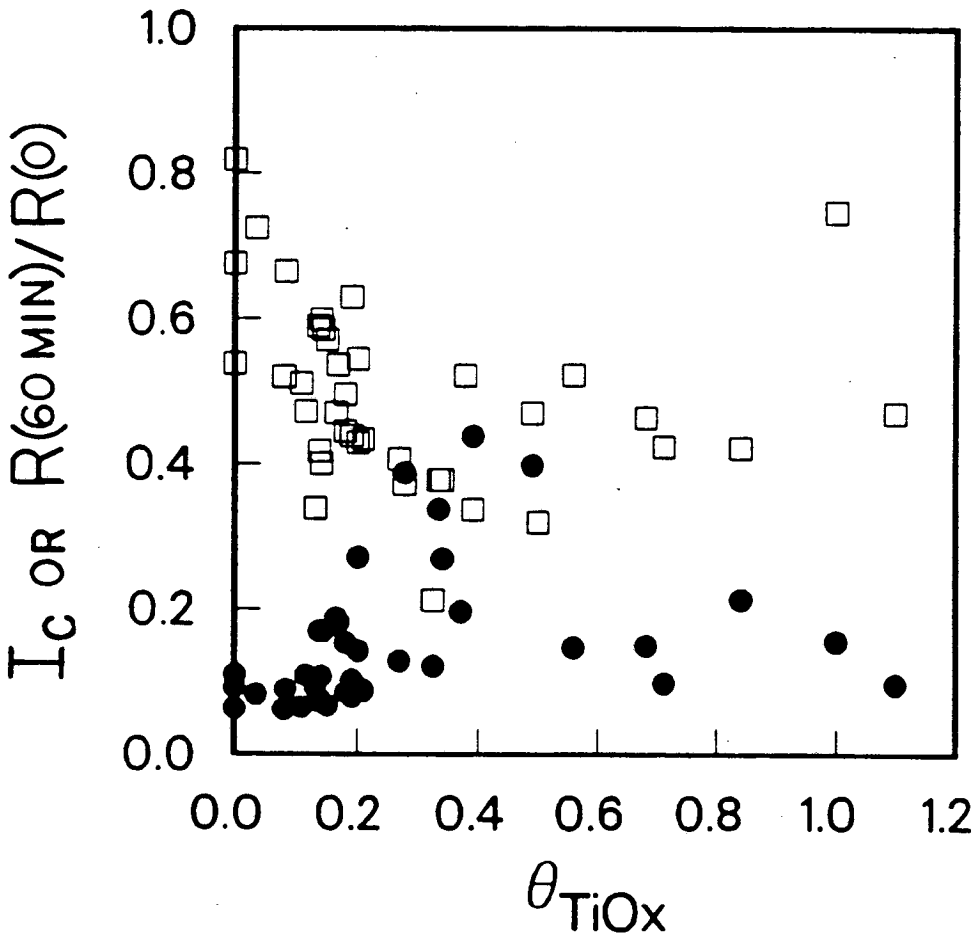

Figure 5.47: Properties of the TiO_x/Rh sample after one hour of reaction (CO hydrogenation). The relative amount of deactivation (open squares) and the AES carbon intensity (solid circles) are shown as a function of TiO_x coverage.

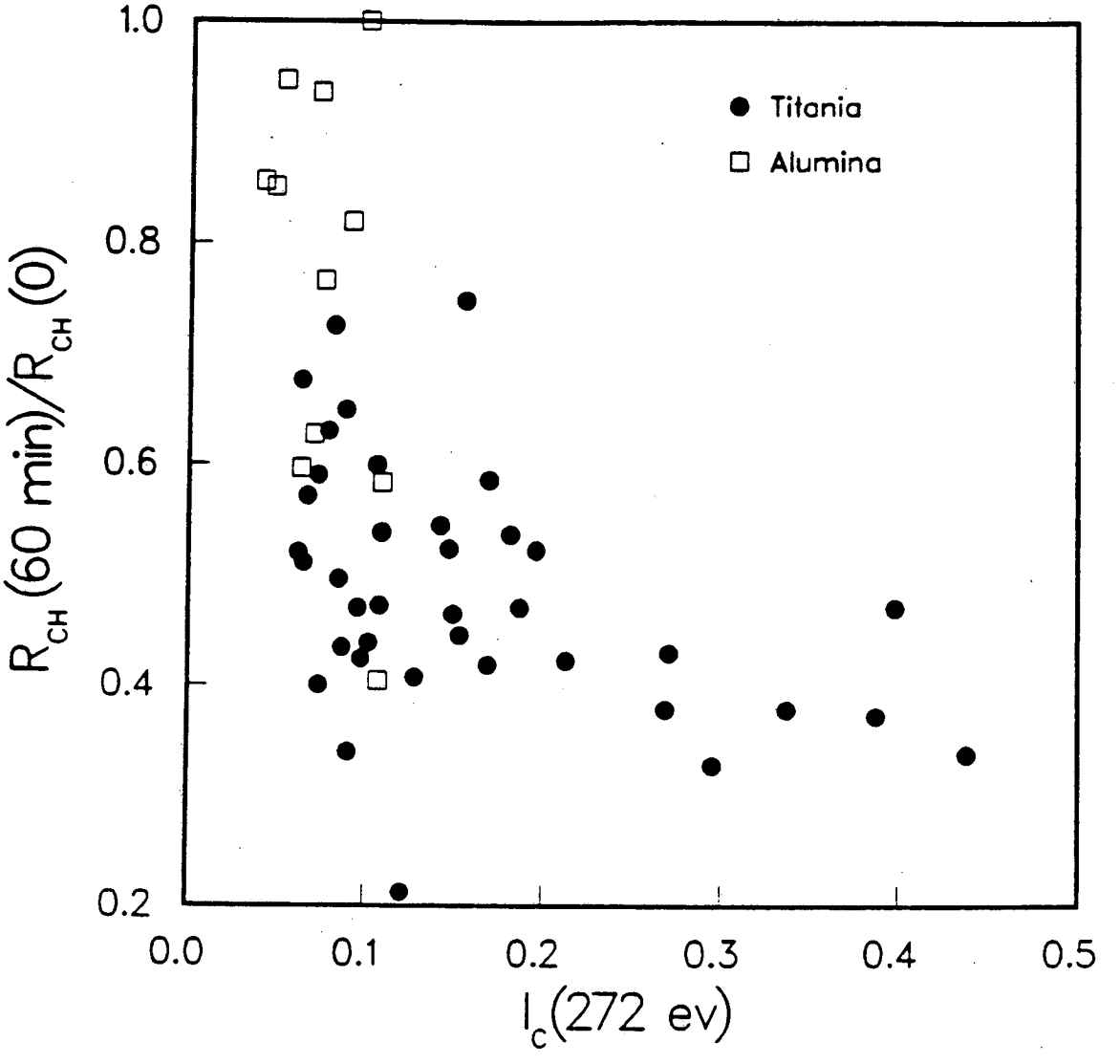

Figure 5.48: Cross-plot of relative amount of deactivation with the AES carbon intensity after one hour of reaction. Open squares denote the results for the AlO_x/Rh samples while the solid circles denote those for the TiO_x/Rh samples.

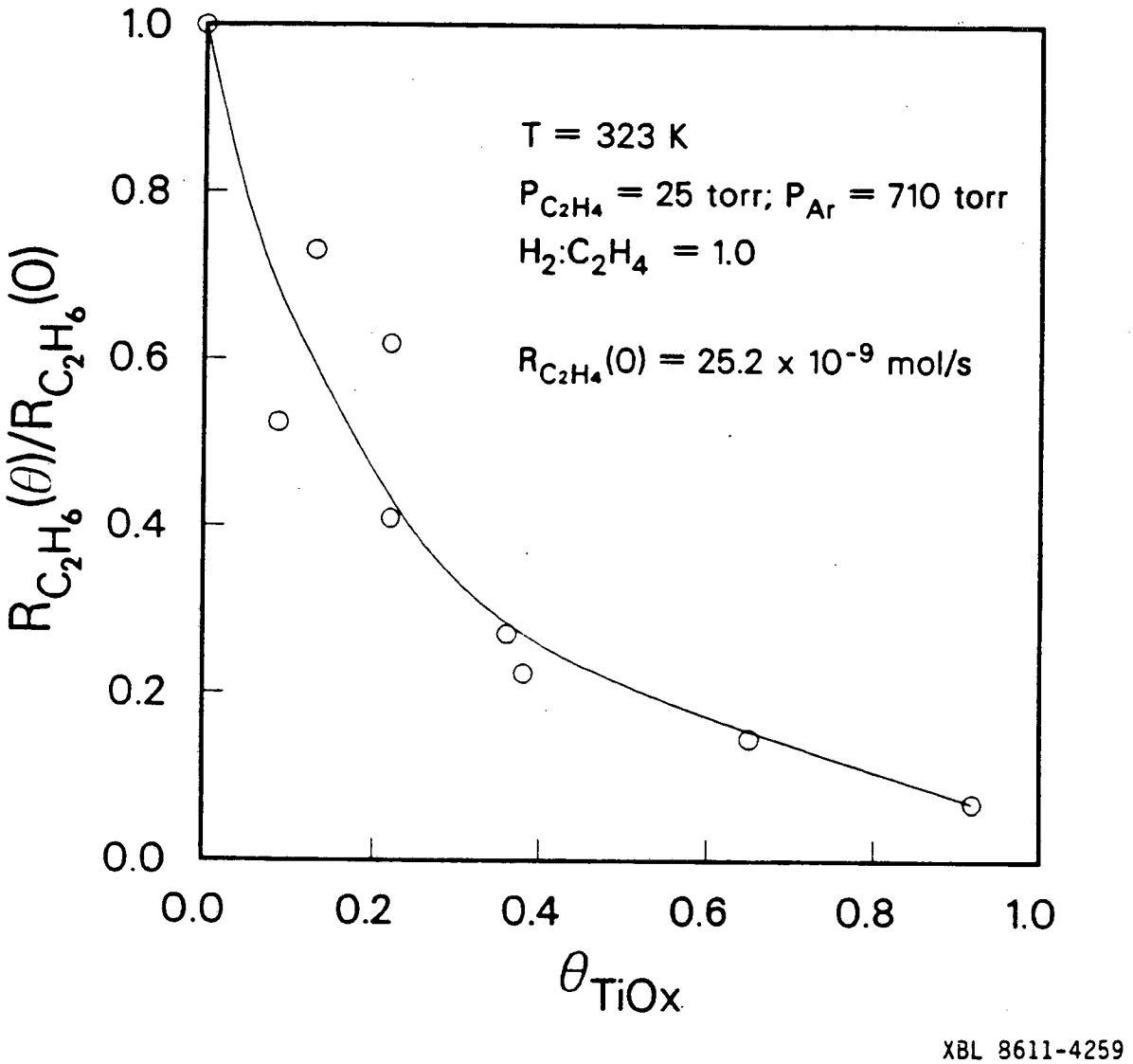

Figure 5.49: Relative ethylene hydrogenation rate on TiO_x-promoted Rh as a function of TiO_x coverage. Reaction conditions were: 323 K, 25 torr C_2H_4, 25 torr H_2, and 710 torr Ar. The rate for clean Rh was 25.2 x 10^{-9} mole/s.

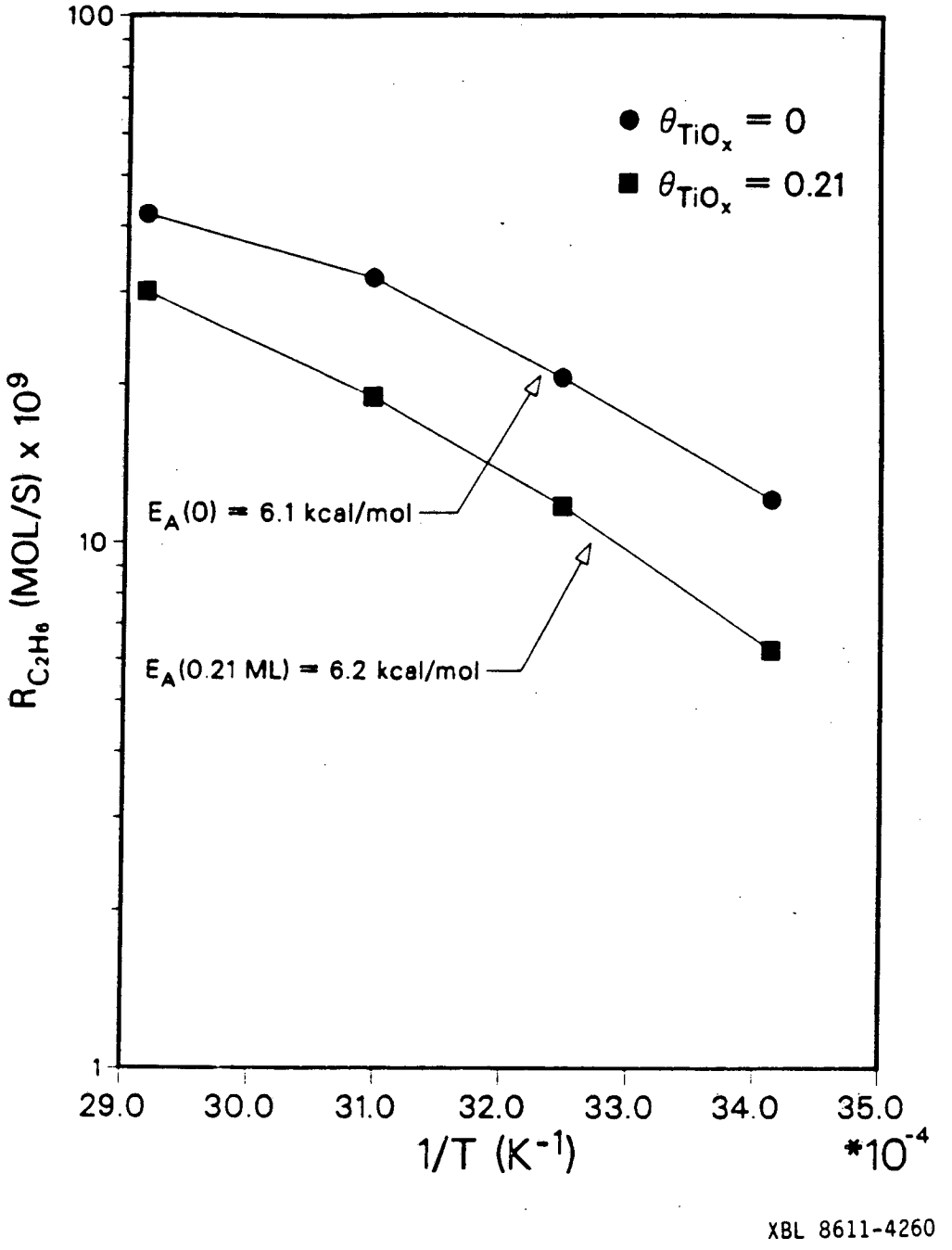

Figure 5.50: Temperature dependence of the ethylene hydrogenation rate over clean Rh foil and TiO_x/Rh (0.21 ML). Except for the temperature variation, reaction conditions were identical to those reported in Fig. 5.49.

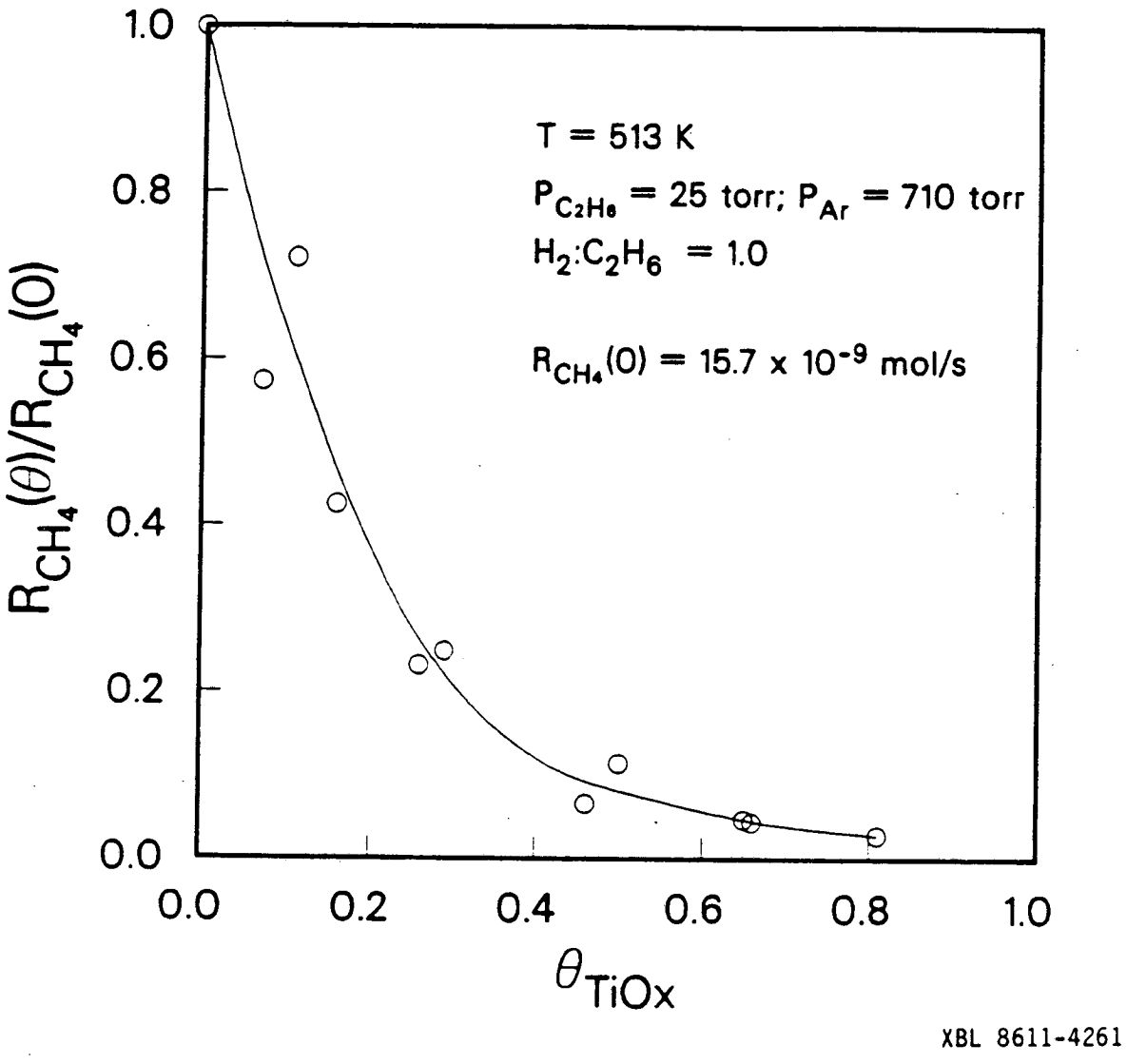

Figure 5.51: Relative ethane hydrogenolysis rate on TiO_x-promoted Rh as a function of TiO_x coverage. Reaction conditions were: 513 K, 25 torr C_2H_6, 25 torr H_2, and 710 torr Ar. The rate for clean Rh was 15.2 x 10^{-9} mole/s.

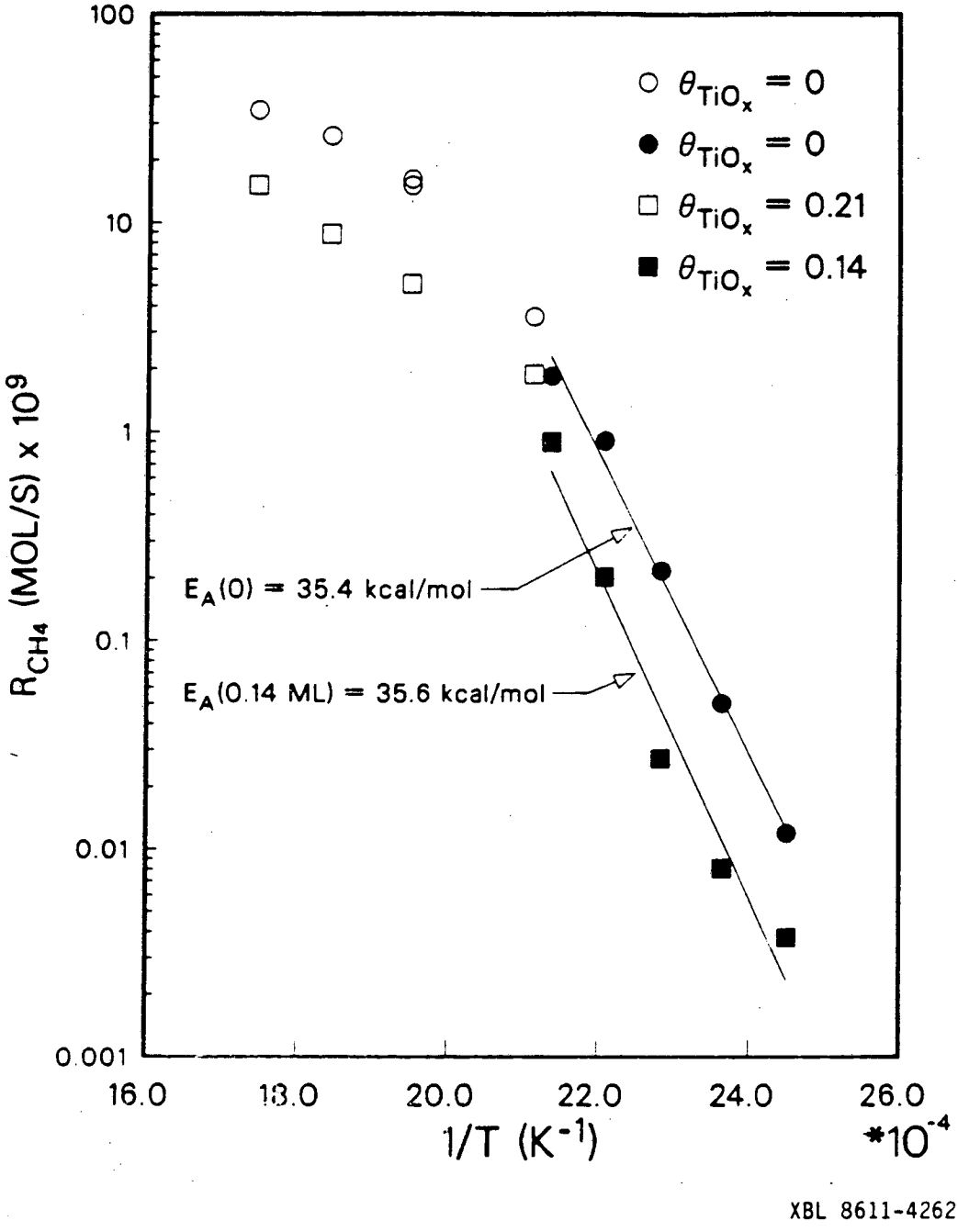

Figure 5.52: Temperature dependence of the ethylene hydrogenation rate over clean Rh foil and TiO_x/Rh (0.14 and 0.21 ML). Except for the temperature variation, reaction conditions were identical to those reported in Fig. 5.51.

Chapter 6

DISCUSSION

6.1 OXIDE OVERLAYER CHARACTERIZATION

6.1.1 Overlayer Coverage and Structure

The AES uptake plots of Figs. 5.5 and 5.13 reveal that both alumina and titania overlayers develop on the rhodium surface through the Stranski-Krastanov growth behavior, *i.e.*, growth of a two-dimensional monolayer followed by three-dimensional growth at higher coverages. Although deposited metals do not usually wet oxide substrates, in the reverse system, an oxide may be expected to spread over a metal surface. This is a result of the higher surface energy of exposed metal relative to the oxide [72], which in turn, leads to significant metal/metal oxide interaction. For oxide-supported metals, if the interaction is particularly strong, such as between titania and Group VIII metals, it may lead to the migration of oxide species from the support onto the surface of the metal particles. Once the free metal surface is covered, the driving force for layered growth is eliminated and minimization of surface area becomes the overriding criterion.

The degree of attenuation of the rhodium substrate signal at monolayer coverage was 0.45 for AlO_x/Rh and 0.34 for TiO_x/Rh. Metal-on-metal growth studies, though, show typical attenuation factors of 0.5–0.6 for 300–400 eV electrons (see Table 2.1). The larger attenuation for an oxide monolayer may be attributed to a more complex structure to the mono-

layer. Specifically, the two-component monolayer may likely exhibit a three-dimensional morphology which leads to a thicker "monolayer" than expected in a conventional one-component overlayer. For similar atomic densities, a metal oxide monolayer may then attenuate the substrate signal more than a metal monolayer due to the greater number of atoms covering the substrate.

Further information regarding the morphology of the oxide overlayers is difficult to obtain and has not been pursued in this study. Low energy electron diffraction (LEED) of the oxides on rhodium single crystals may provide information on the location of overlayer species relative to the substrate atoms if the metal oxide occupies positions at regular intervals on the substrate surface lattice. The width of LEED substrate spots may indicate the size of uncovered Rh domains and hence, the dispersion of the metal oxide on the surface. The application of scanning tunneling microscopy (STM) to this system would also provide information about the dispersion of metal oxide overlayers.

Determination of the relative positions of the metal and oxygen in the overlayer is not possible with the techniques on hand and would require techniques sensitive to M–O bond lengths and bond angles on the surface (HREELS, SEXAFS, *etc.*). However, if a distribution of bond lengths and orientations exists, even these techniques would prove ineffective. Perhaps the only plausible picture of the oxide overlayers at this level of understanding would be an extrapolation of the bulk morphologies. Examples of these for alumina [137] and titania [138,139] are shown in Fig. 6.1. The extent of distortion from these structures will depend on such factors as the degree of interaction (of both metal and oxygen) with the substrate, the preferred oxide orientation, substrate surface topology, and overlayer preparation conditions.

Attempts to clarify the oxide overlayer structures must be left to future investigations. Further discussion of the morphologies will be restricted to the nature of the metal/metal oxide interface at the periphery of oxide islands.

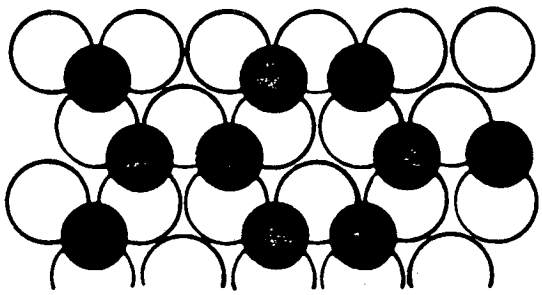

(a)

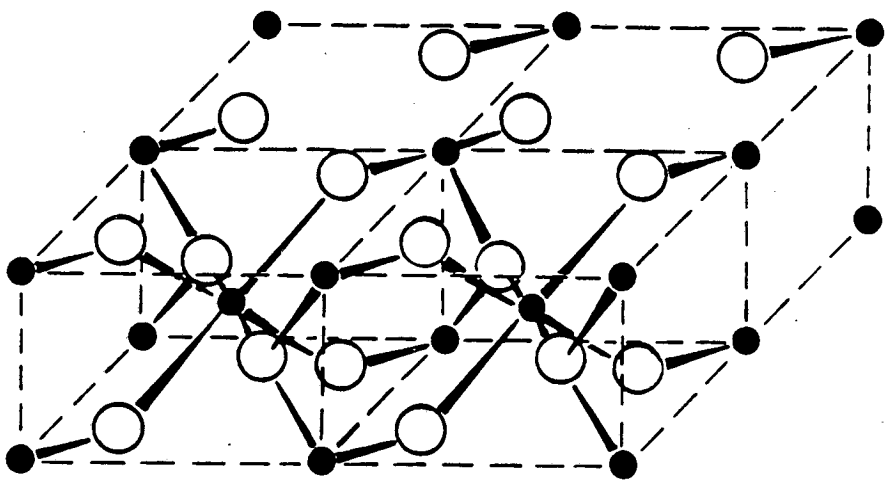

(b)

Figure 6.1: The bulk structures of (a) α-Al_2O_3 [137] and (b) TiO_2 (rutile) [138,139].

6.1.2 Overlayer Stoichiometry

Although overlayer morphological identification is not feasible with the available techniques, the oxide can be characterized in terms of the oxygen-to-metal ratio with AES and XPS. The comparison by AES of the oxide overlayers prepared in this study with bulk alumina and titania samples demonstrates the nearly-complete stoichiometry of the oxide overlayers. These observations are reinforced by XPS analyses showing the aluminum in the 3+ oxidation state and titanium predominantly in the 4+ state.

The differences in the effects of the aluminum and titanium oxides on the chemisorption and catalytic properties of rhodium can be related to their relative ease of reduction. While no reduction of the Al^{3+} by CO titration occurs, treatment in 50 torr hydrogen at 753 K induces reduction of no more than 10% of the Al^{3+} to Al^{0}. No intermediate cation states are thermodynamically stable. The inertness of the alumina overlayer to reducing conditions parallels the trends in Figs. 5.8 and 5.9 where alumina appears to only block CO chemisorption and hydrogenation sites in proportion to the coverage. Thus alumina acts as an inert contaminant on the surface of rhodium.

By comparison, reduction of titania is facile provided there is an adequate supply of a reducing agent on the surface. The treatment of titania on gold in a reducing atmosphere fails to produce any Ti^{3+} features in the XPS spectrum (Fig. 5.17) while conversion of more than 60% of the Ti^{4+} to Ti^{3+} is possible for titania on rhodium (Fig. 5.16). Clearly, reduction by gas-phase hydrogen does not take place. However, even exposure to CO followed by heating produces a significant quantity of Ti^{3+} in the rhodium-supported overlayer. Reduction of the titanium to the 2+ oxidation state can be accomplished by annealing sufficiently to cause diffusion of the oxide into the substrate.

It is also evident from Figure 5.24 that the process of overlayer reduction with H_2 is rapid, reaching the final state of reduction in less than 30 seconds at 753 K. The reduction may even be carried in the UHV chamber if desired.

Operation of the AES electron gun has also been observed to reduce surface titania as

evidenced by the AES O/Ti ratio. Though reduction to only ~TiO has been seen, other authors have noted more extreme oxygen removal upon impingement by an AES electron beam [64].

The process of reducing titania in the aforementioned examples is facilitated by the existence of Magnelli phases of composition Ti_nO_{2n-1}. The energetics of partial reduction to these suboxides are not prohibitively difficult—unlike complete reduction to Ti metal. Another factor which can aid titania reduction is the possible formation of Brewer–Engels-type alloys between the titanium and rhodium. The stability of this interaction provides an additional driving force for the removal of oxygen from the titania overlayer. No direct evidence for this interaction is provided by the results presented in this study, but, as will be seen later, the CO chemisorption results suggest that after H_2 reduction, redispersion of TiO_x islands on the rhodium surface occurs, increasing the amount of TiO_x–Rh interface.

Figs. 5.20 and 5.22 show increases in the Ti^{3+} and –OH percentages in the titania overlayer as lower coverages are reached. Since the perimeter-to-area ratio of the overlayer also rises with lower coverages, it appears that the much of the Ti^{3+} and –OH species reside at the periphery of titania islands. The higher degree of Ti^{3+} formation seen after H_2 reduction, as compared with after CO titration, reflects the greater ease of breaking Ti–O bonds at the island periphery. In the case of the –OH percentage in the overlayer, there is little dependence on pretreatment conditions. The severing of Ti–O bonds can be accomplished by the reduction of hydroxyl groups at the island perimeter to form water or by reduction of Ti–O–Ti to Ti–OH. These two schemes predict changes in opposite directions for the –OH percentage with pretreatment conditions. Taken together, they may cancel resulting in the observed negligible dependence on pretreatment conditions.

6.2 CO CHEMISORPTION

6.2.1 The Suppression of CO Chemisorption on Rhodium by Oxide Overlayers

Comparison of the coverage dependence of CO chemisorption on the AlO_x/Rh and TiO_x/Rh surfaces reveals striking differences in the effects of these oxide overlayers. Alumina was found to inhibit CO chemisorption in direct proportion to its coverage suggesting that alumina is present on the surface as an inert contaminant. In contrast, titania overlayers exhibit a further suppression of CO chemisorption capacity beyond that expected from blocking Rh sites underneath. It is emphasized that the coverages for these two oxides were determined by the same method (AES intensity–vs.–dosing time plots) and that the behavior exhibited in these determinations was very similar.

The additional suppression of CO chemisorption by titania is most likely to arise from effects at the TiO_x-Rh interface. Inhibition of CO chemisorption at Rh atoms along the perimeters of TiO_x islands is envisioned to occur by two means: (1) partial blocking of neighboring Rh atoms by TiO_x species residing in multiple-Rh atom sites (*e.g.*, bridge, 3-fold hollow) and (2) "bonding" between TiO_x species and neighboring Rh atoms, which in turn, would weaken the bonding of CO to those Rh sites. The implication of these modes is that CO chemisorption at Rh sites on the periphery of TiO_x islands may still occur, but with a reduced bond energy. The normal bond strength of CO on rhodium, as determined from first-order desorption kinetics (Eqn. 2.12) [116,117], is about 29 kcal/mole (Figs. 5.2 and 6.2). The absence of any new desorption features ascribable to CO on the "peripheral" rhodium sites at temperatures as low as 150 K indicates that if CO is bound at these sites, it would indeed be weakly bound, with a bond energy of no more than 8 kcal/mole.

A simple thought process eliminates the possibility that mode 1 above operates alone. If CO chemisorption is suppressed only by partial blocking of "peripheral" Rh sites by TiO_x species, comparison of the results for TiO_x and AlO_x overlayers suggests that there is much

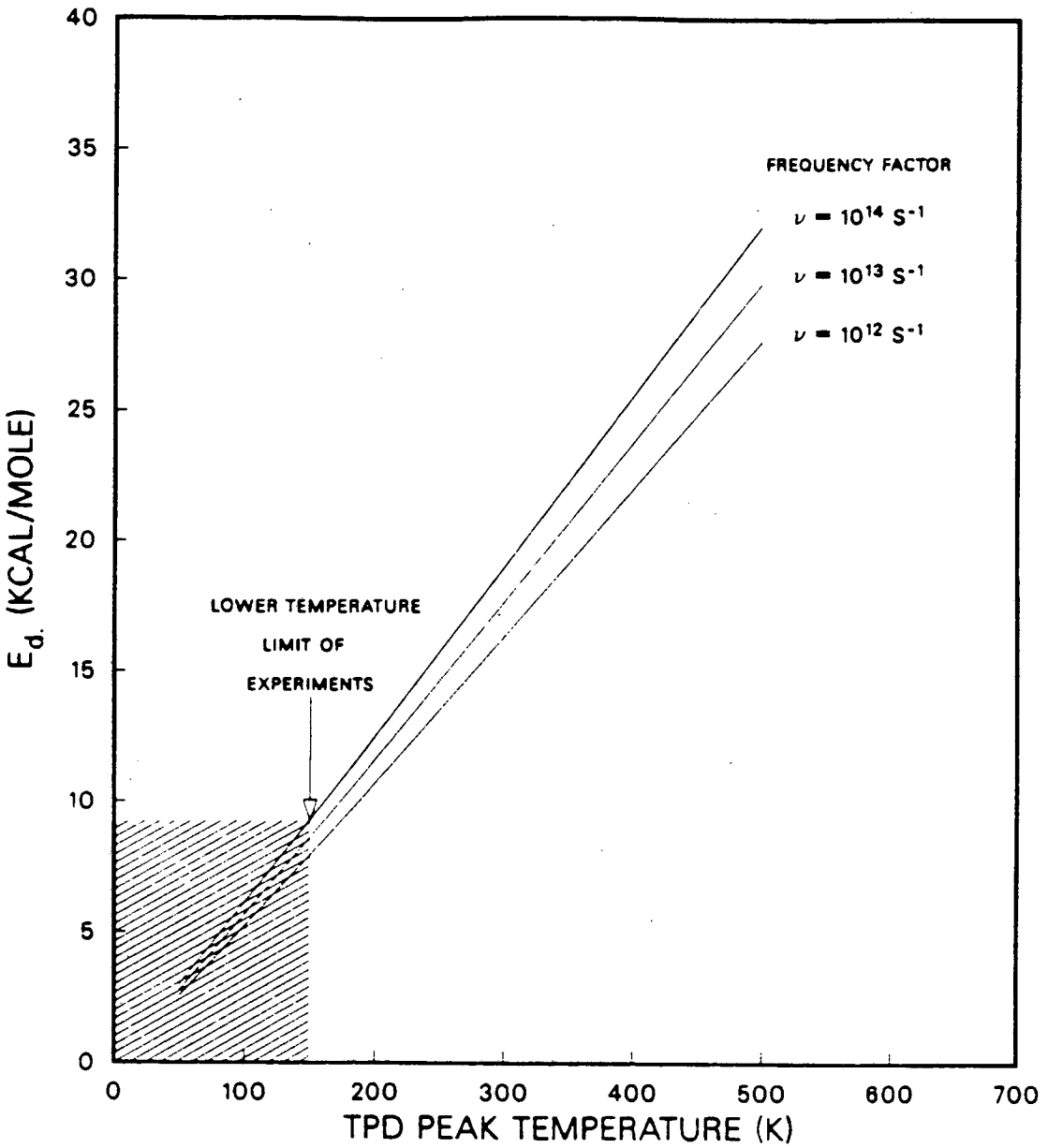

Figure 6.2: Desorption energy as a function of peak temperature for first-order desorption kinetics (from Eqn. 2.12).

more oxide perimeter for TiO_x than AlO_x (since AlO_x may have the same stereochemical effect on neighboring Rh atoms). This means that for identical coverages, TiO_x islands will be smaller than AlO_x islands, on the average, reflecting a higher dispersion. A higher dispersion for TiO_x must arise from a more substantial interaction between metal and metal oxide. The thermodynamically-favored Ti-Rh interaction described earlier provides the driving force for the greater dispersion of the TiO_x overlayer. This Ti-Rh interaction, though, leads to the second mode of suppression. Clearly, mode 1 cannot occur without mode 2.

Dwyer *et al.* detected a substantial concentration of Ti^{3+} species with XPS on a TiO_x-promoted Pt foil. Figure 5.20 shows that Ti^{3+} species are more prevalent at low TiO_x coverages where the perimeter-to-area ratio of TiO_x islands is higher. This trend reflects the stability of Ti^{3+} species at the oxide-metal interface. The density of states at the Fermi level of Rh atoms in the vicinity of the TiO_x-Rh interface may be influenced by these Ti^{3+} centers along the oxide island perimeter. Recent calculations by Feibelman and Hamann [50,51] have demonstrated that such perturbations can extend a few metal atom distances from the perturbing ion and could be responsible for changes in the chemisorptive properties of the affected metal atoms. Similar calculations by Joyner *et al.* [52] for the C/Ni system limit the local electronic effect to one atomic distance.

6.2.2 Modeling of CO Chemisorption on TiO_x/Rh

A description of the falloff in CO chemisorption capacity with TiO_x coverage can be provided from a model incorporating the ideas presented above. It is assumed that TiO_x islands nucleate at defect sites on the Rh surface and that the Rh sites covered by the islands, as well as those within m Rh–Rh bond distances (2.69 Å) of an island perimeter, are no longer available for CO chemisorption (at temperatures above 150 K). Rhodium sites affected by nearby Ti^{3+} centers are depicted in Fig. 6.3.

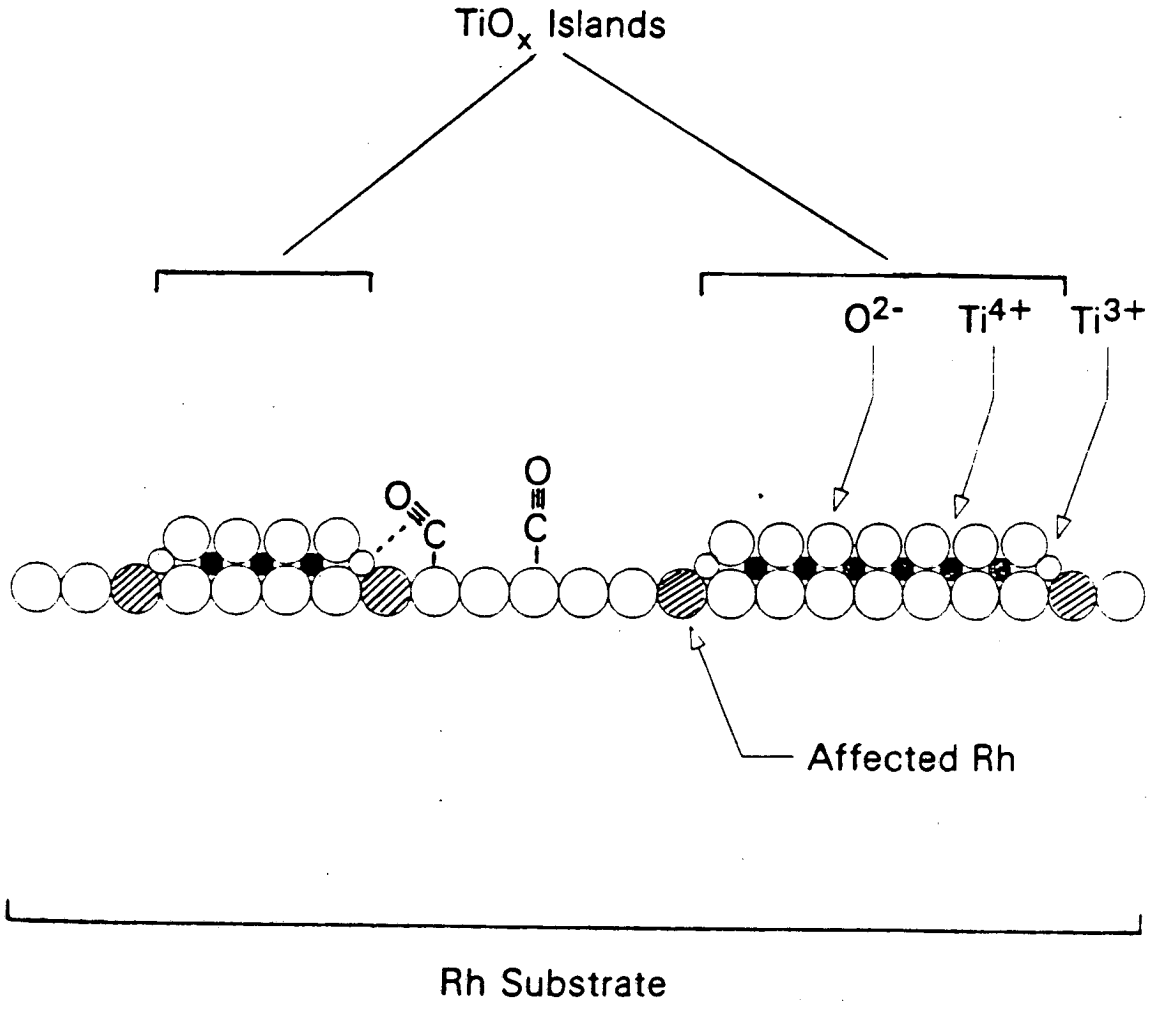

Figure 6.3: Schematic model for titania overlayers on rhodium.

Two approaches were taken to determine the number of Rh sites affected by nearby TiO_x species: one in terms of a mathematical expression and the other with a Monte Carlo simulation. The first requires uniform circular island growth around the nucleation sites and is essentially a continuum model. This leads to the following expression for the amount of CO that can be adsorbed at a given TiO_x coverage

$$A(\theta_{TiO_x})/A(0) = 1 - \pi[(\theta_{TiO_x}/\pi N)^{1/2} + m\delta]^2 N \qquad (6.1)$$

where $A(\theta_{TiO_x})$ is the CO coverage, N is the concentration of defect sites, and δ is the Rh-Rh bond distance (2.69 Å). This formulation accurately describes the data for CO adsorption over the range $0 \leq \theta_{TiO_x} \leq 0.3$ when, m=1 and N = 4.5 x 10^{13} cm^{-2} (Fig. 6.4). For $0.30 \leq \theta_{TiO_x} \leq \pi/4$, the overlap between excluded perimeter areas has to be taken into account to avoid counting it twice. By adopting a regular arrangement of TiO_x islands, the overlap can be calculated and subtracted from the excluded perimeter area. Equation 6.1 is then modified to

$$A(\theta_{TiO_x})/A(0) = 1 - R_0^2 N[\pi - 4\pi(\phi/360) + 4\sin(\phi/2)\cos(\phi/2)] \qquad (6.2)$$

where $\phi = 2\sin^{-1}[1 - 1/4R_0^2N]$

and $\pi[1/2 - \sqrt{N}m\delta]^2 \leq \theta \leq \pi/4$

for a square-lattice array of nucleation sites, the fit of the experimental data is extended by Eqn. 6.2 to nearly $\theta_{TiO_x} = 1.0$, as shown in Figure 6.4. The dependences on N and m in this model are shown in Figs. 6.5 and 6.6, respectively. It is also interesting to note that the density of TiO_x islands predicted by Eqs. 6.1–6.2 is roughly within an order of magnitude of that observed for Au, Pb, and Co islands nucleating on Pt(100), Cu(111), and Cu(100), respectively [134,135,136].

The Monte Carlo simulation of TiO_x growth was performed on a Commodore Model 8032 personal computer. A BASIC program was written to generate an array of points

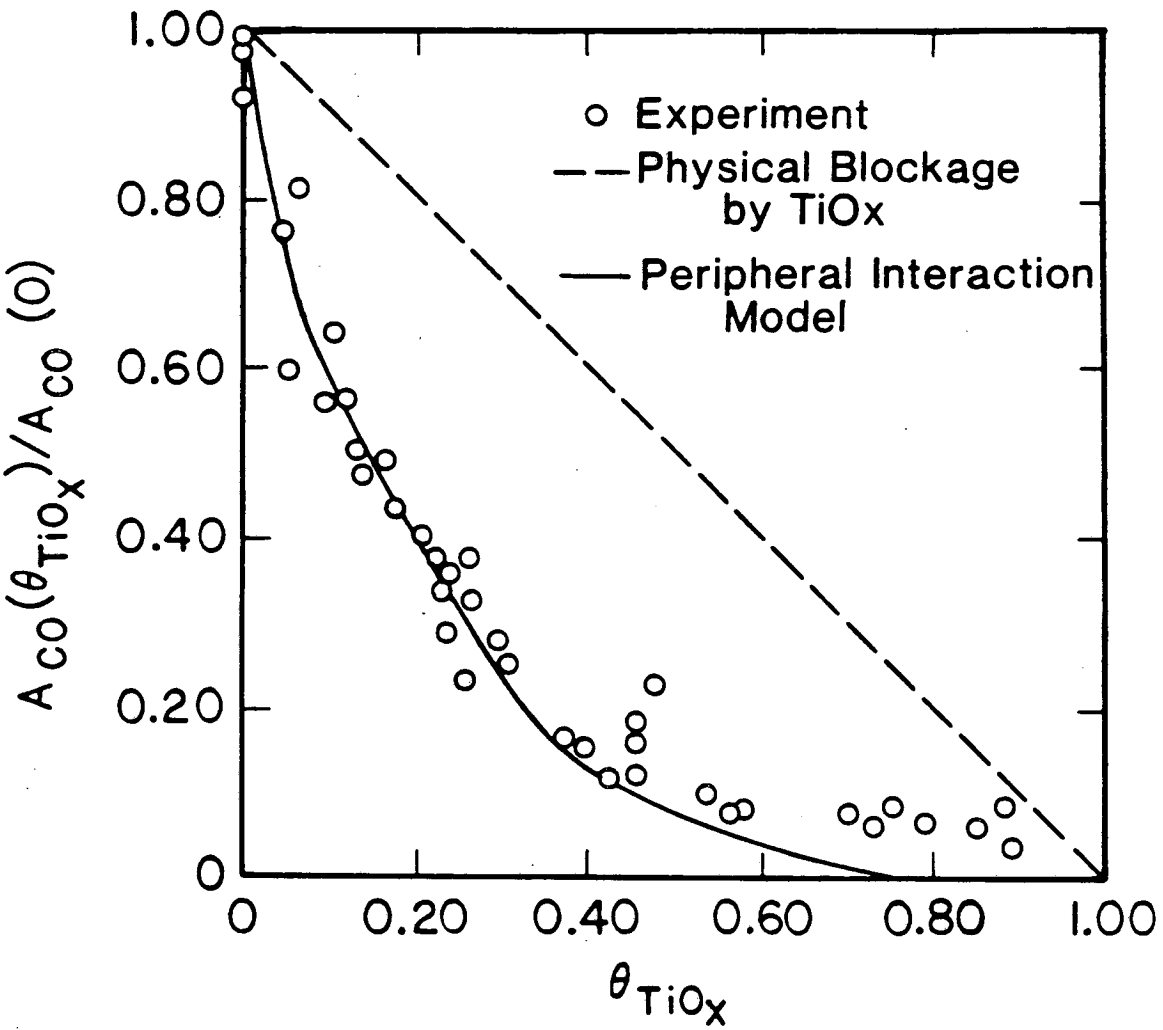

Figure 6.4: Comparison of island edge model and experiment for the dependence of CO coverage on TiO_x coverage. The solid line is given by Eqns. 6.1 and 6.2 for m = 1 and N = 4.5 x 10^{13} cm^{-2}.

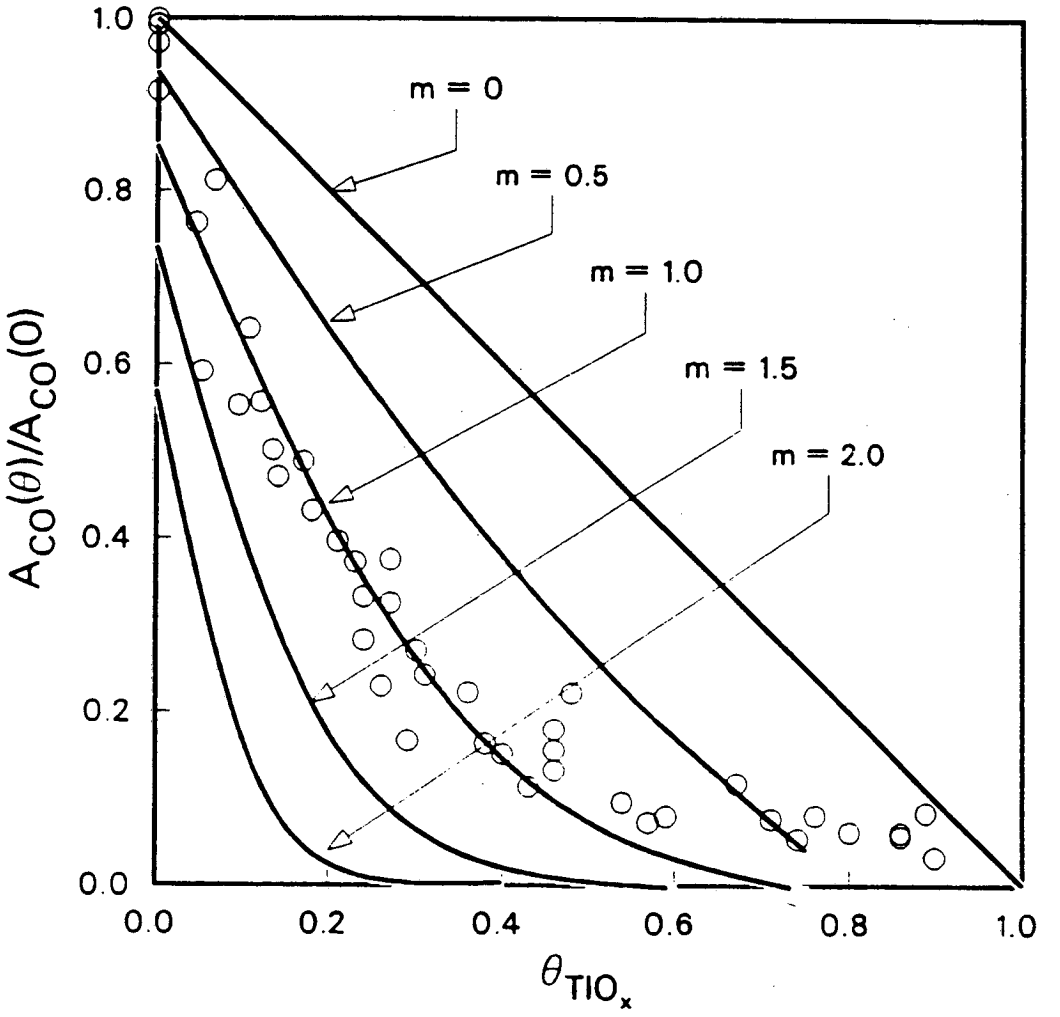

Figure 6.5: The effect of interaction distance on the predicted amount of CO chemisorbed on the TiO_x/Rh surface (Eqns. 6.1 and 6.2). The parameter m represents the number of Rh–Rh bond distances outward from the perimeter of TiO_x islands (N = 4.5 x 10^{13} cm^{-2}).

displayed on the visual memory representing the Rh surface. Nucleation sites were randomly chosen up to a pre-selected concentration. Island growth then proceeded by randomly blocking out points bordering the nucleation sites or along existing islands.. The number of rhodium atoms along the periphery of the TiO_x islands was then counted at various coverages. Although a square array was displayed, counting could be performed to simulate a hexagonal array by neglecting one pair of diagonally opposite corners as nearest neighbors. The code for this program appears in Appendix B.

Example visual displays appear in Fig. 6.7 showing clearly the irregular growth pattern

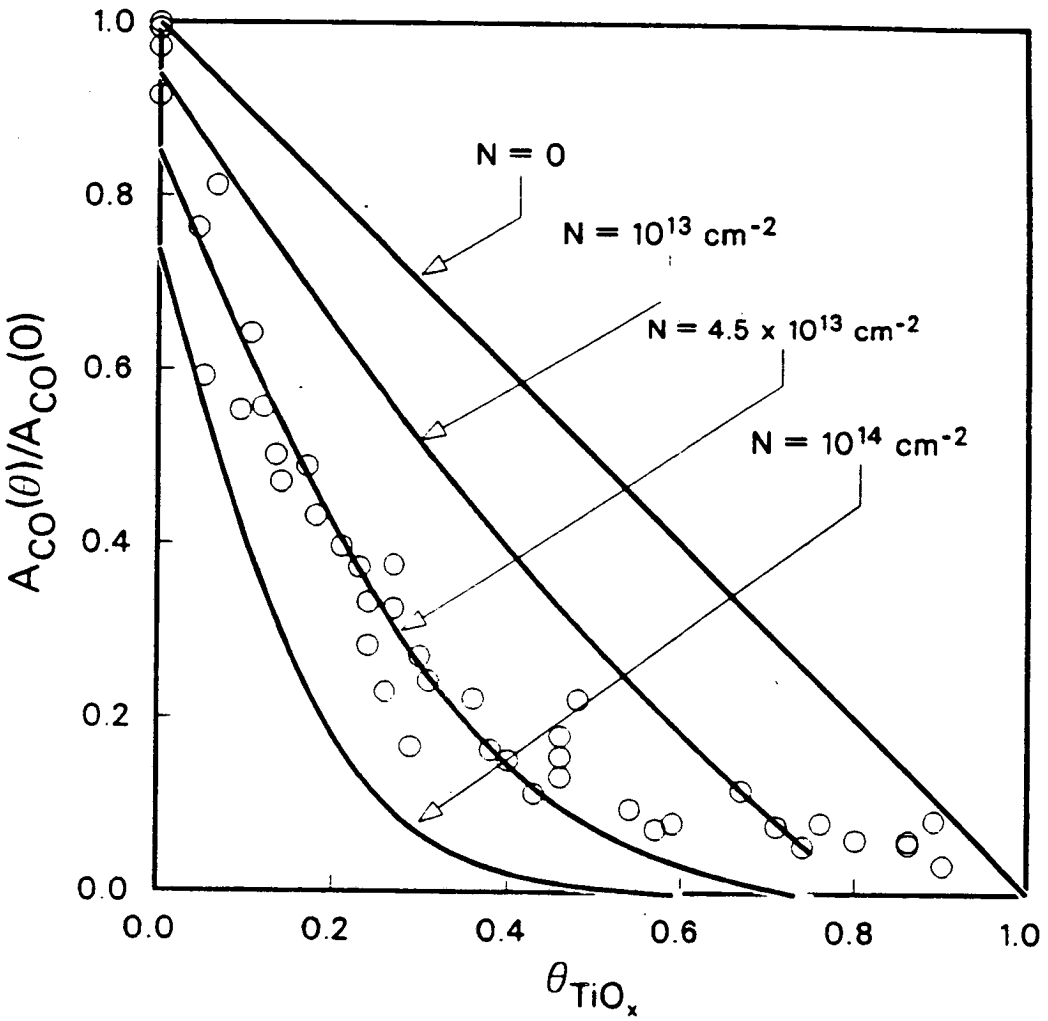

Figure 6.6: The effect of nucleation site density on the predicted amount of CO chemisorbed on the TiO_x/Rh surface (Eqns. 6.1 and 6.2). The parameter N represents the number of nucleation sites (m = 1).

of the islands which is believed to be more realistic than the assumptions associated with Eqn. 6.1. Figure 6.8 illustrates the expected CO chemisorption capacity as determined by the procedure just mentioned. For a 100 x 100 array and a nucleation site density of 4.5 x 10^{13} cm^{-2}, identical results are obtained to those from the uniform circular island growth model (compare Figs. 6.8 and 6.4). This indicates how even a simple depiction of the morphology of the surface, *i.e.*, uniformly-sized circular oxide islands, provides an adequate description on the macroscopic scale. The power of the Monte Carlo simulation lies in its flexibility and the ease of counting different types of sites while maintaining a closer link to

the actual surface morphology.

6.2.3 Effects of H_2 Reduction

At a fixed value of θ_{TiO_x}, we have observed that increasing the reduction temperature can result in a further suppression of the CO chemisorption capacity and a shift in CO TPD peak temperature to lower temperatures. These changes are accompanied by a decrease in the O/Ti ratio. The principal question now is whether the changes in CO chemisorption characteristics are due to the changes in the stoichiometry of the TiO_x layer, or to other causes. For example, one might imagine that with increasing reduction temperature, the number of TiO_x islands remains constant but that the magnitude of m associated with each island increases due to the decrease in the value of x. To fit the data for T_{red} = 753 K shown in Fig. 5.30, this interpretation would require m to increase from 1 to 1.25. The fractional value would indicate that only some of the next-nearest neighboring Rh atoms are affected. As an alternative, m may remain constant and the dispersion of the islands increase, thereby creating more perimeter. In this case, N would have to increase from 4.5 x 10^{13} cm^{-2} to 7.5 x 10^{13} cm^{-2} to fit the data.

Of the two alternatives presented above, the second seems more plausible than the first. From Fig. 5.36 it is evident that the reduction temperature influences the suppression of CO chemisorption only above a threshold temperature. It is also observed that the threshold temperature decreases with increasing TiO_x coverage. On the other hand, the O/Ti ratio of the overlayer decreases continually with increasing reduction temperature. What this suggests is that the reduction in O/Ti ratio is not directly responsible for the observed changes in CO chemisorption. Instead, the reduction in the O/Ti ratio facilitates the break-up of the TiO_x islands, once the O/Ti ratio has fallen below some critical value. Thus we contend that the suppression in CO chemisorption with increasing temperature, above the threshold value seen in Fig. 5.36, is the result of an increase in the number of

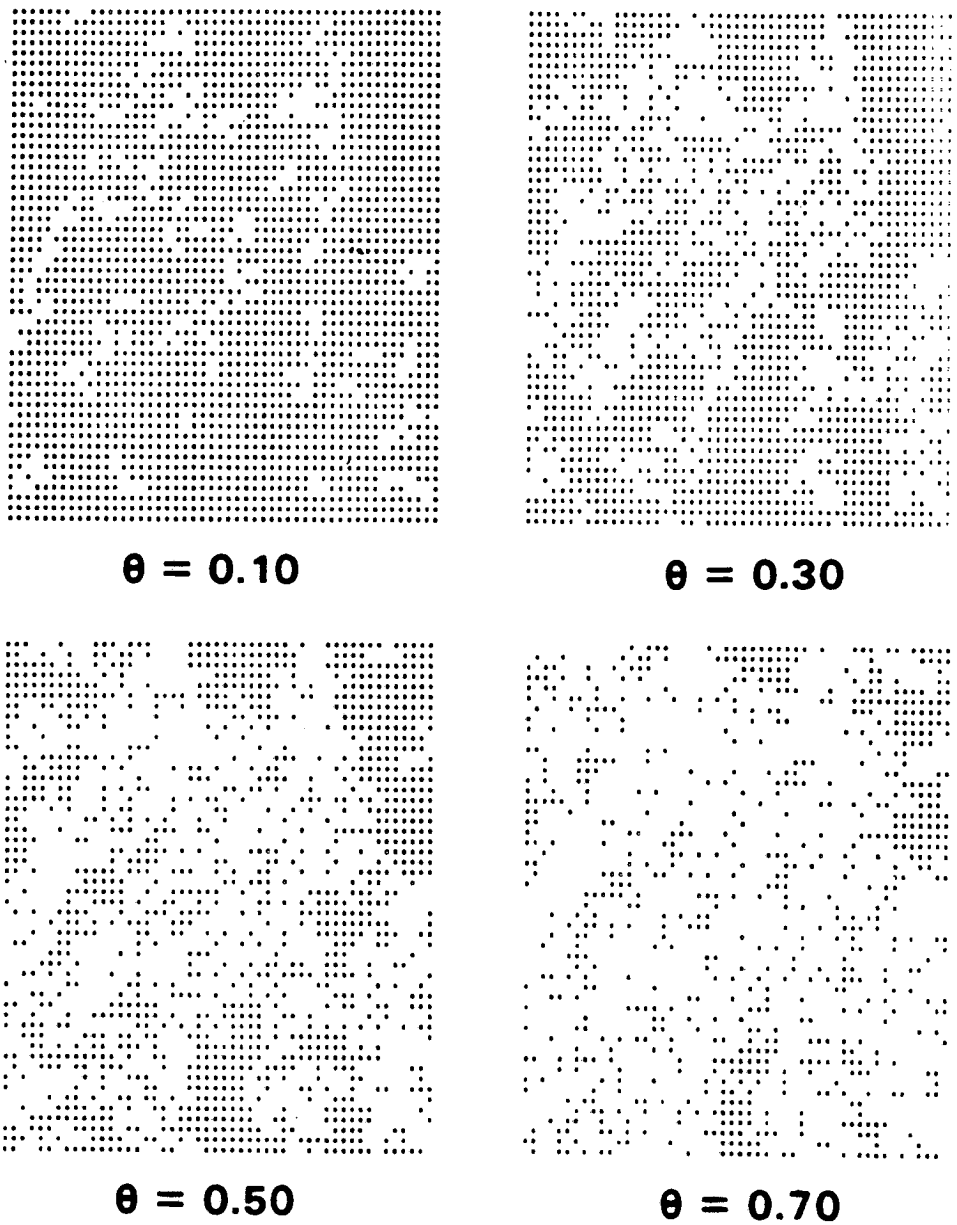

Figure 6.7: Computer simulation of titania island growth around fixed nucleation sites. Example visual displays for a 50 x 50 array are shown corresponding to coverages of (a) 0.10, (b) 0.30, (c) 0.50, and (d) 0.70 ML. A nucleation site density of 4.5 x 10^{13} cm-2 was employed.

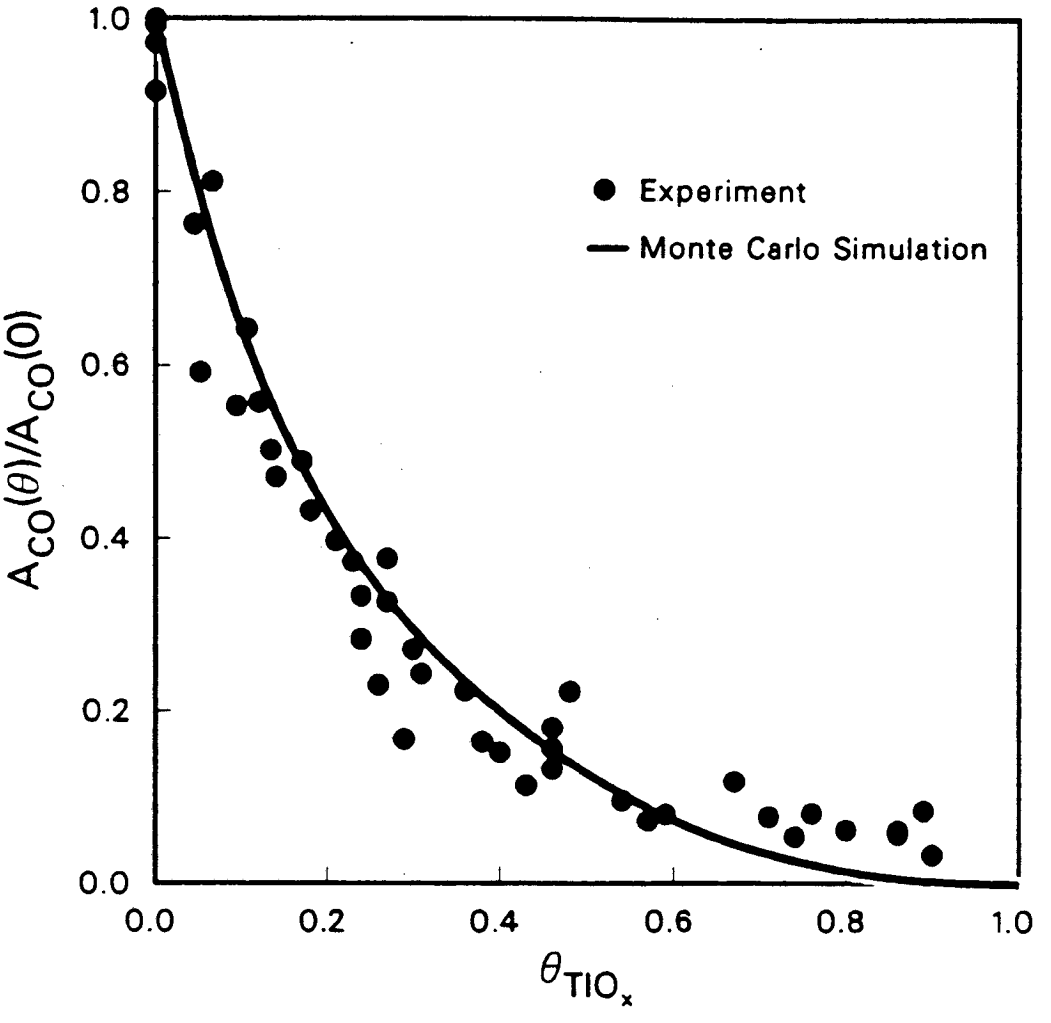

Figure 6.8: Comparison of the island edge model from a Monte Carlo simulation of TiO_x island growth with experiment data for the dependence of CO chemisorption on TiO_x coverage. All exposed Rh atoms were counted except for those adjacent to the perimeter of TiO_x islands. A nucleation site density of 4.5 x 10^{13} cm^{-2} was employed.

TiO_x islands and hence the perimeter area surrounding the islands.

6.3 CO HYDROGENATION

6.3.1 Reaction over AlO_x/Rh

It has already been noted that the presence of alumina overlayers results in the suppression of CO chemisorption on rhodium in direct proportion to the coverage. The same behavior is exhibited for CO hydrogenation on AlO_x/Rh indicating that alumina only physically blocks active sites for this reaction. The kinetic parameters and selectivity of this system are identical to those of the clean rhodium surface and agree well with those found for Al_2O_3–supported rhodium (see Table 6.1).

The degree of deactivation after one hour of reaction was largely independent of AlO_x coverage, averaging at roughly 80% of the initial activity. Also, no additional carbon was deposited on the surface in the presence of alumina. Clearly, alumina has no effect on the kinetics or deactivation of CO hydrogenation on rhodium.

6.3.2 Methane Formation over TiO_x/Rh

As indicated in Figure 5.38, a clear enhancement in methanation activity occurs for TiO_x coverages under 0.3 ML while at higher coverages, the rate diminishes gradually to a level well below that for clean Rh. This behavior was also observed by Chung *et al.* [88] for TiO_x deposited on a Ni(111) surface. Increases in activity of Pt foil [69], Pt–black [60], SiO_2–supported Pd [140], and SiO_2–supported Rh [141] have been found upon promotion with TiO_x.

It is apparent from Figs. 5.39 to 5.41 that at TiO_x coverages comparable to those where

Table 6.1: KINETICS FOR CO HYDROGENATION

LOADING (wt% Rh)	T (K)	H_2:CO	P_{tot} (atm)	$N^a_{CH_4}$ (x 10^3)	E^b_A	n (H_2)	m (CO)	SELECTIVITY x_{C_1}	x_{C_2}	x_{C_3}	Ref.
Rhodium											
—	573	3:1	0.9	150	24			0.89	0.09	0.03	[123]
—	573	2:1	6	260	25	1.0	-1.0	0.95	0.04	0.01	[122]
—	**553**	**2:1**	**1**	**37**	**24.4**	**1.0**	**-1.0**	**0.90**	**0.09**	**0.01**	*
Al_2O_3—Rhodium											
1	538	3:1	1	13	24.0	1.04	-0.20	0.89	0.09	0.02	[127]
1	548	3:1	1	11	24.0	0.90	-0.42	0.85	0.03	0.03	[142]
2.3	513	20:3	1	3.6	23.7			0.93	0.05	0	[143]
0.35	543	1:1	1	0.21				0.87	0.06	0.04	[144]
[c]	**553**	**2:1**	**1**	**11**	**24.7**	**1.1**	**-0.6**	**0.90**	**0.09**	**0.01**	*
TiO_2—Rhodium											
2	538			~11	33.2	1.7	-0.10				[13]
1	548	3:1	1	62	18.3	0.75	-0.88	0.75	0.04	0.03	[127]
7.8	573	3:1	1	5.4	36.2			0.77	0.03	0.04	[145]
3	573	1:2	10	0.22	41.5			0.50	0.32		[146]
[d]	**553**	**2:1**	**1**	**72**	**19.0**	**2.4**	**-0.3**	**0.67**	**0.22**	**0.11**	*

*This work

[a]Turnover frequency (molecules/site-s)

[b]Activation energy (kcal/mole)

[c] ~0.4 ML AlO_x/Rh

[d] ~0.2 ML TiO_x/Rh

R_{CH_4} reaches a maximum, the value of E_A is smaller, and the values of m and n are larger compared to the values of these parameters for clean Rh. A reduction in E_A has also been reported by Demmin *et al.* [69] for a TiO_x-promoted Pt foil and by Rieck and Bell [140] for TiO_x-promoted Pd/SiO_2. A sharp increase in hydrogen order was also observed by Vannice [13] for TiO_2-supported Rh in comparison with Al_2O_3-supported Rh, while only a slight change in the CO partial pressure dependence was found (see Table 6.1).

The influence of TiO_x on the CO hydrogenation activity of Group VIII metals has been attributed to Ti^{3+} ions present at the perimeter of small TiO_x islands decorating the metal surface [14,24,147,148,149,150,151,152]. For a TiO_x-promoted Pt foil, Dwyer *et al.* [67] detected a substantial concentration of Ti^{3+} species with x-ray photoelectron spectroscopy. XPS studies for TiO_x on Rh presented earlier have shown that the percentage of Ti^{3+} in the formed by either CO or H_2 reduction increases with lower TiO_x coverage. Since the perimeter-to-area ratio of overlayer islands also rises with lower TiO_x coverages, these results suggest that Ti-O bonds near the periphery of TiO_x islands are more prone to attack by reducing agents chemisorbed on the Rh metal. The oxygen deficient Ti^{3+} species along the oxide island periphery may then interact with the oxygen end of CO adsorbed on nearby metal sites, as shown in Fig. 6.9. When CO is adsorbed on Rh sites adjacent to the Rh-Ti boundary, the C-O bond is long enough for the oxygen to reach the Ti^{3+} ion. The acid-base interaction between CO and the oxophilic Ti^{3+} should enhance the dissociation of CO—an essential step in the formation of methane.

To explain the observed methanation rate dependence on TiO_x coverage, we can propose that an ensemble of Ti^{3+} and Rh sites near the periphery of the islands are the active sites where an enhancement in rate occurs. The simplest ensemble that can be considered would include a single Rh site at the periphery. To determine the number of Rh atoms at the titania island periphery, the Monte Carlo simulation of TiO_x island growth around fixed nucleation sites was employed with the nucleation site density determined in the CO chemisorption modeling (4.5×10^{13} cm^{-2}). Counting the number of these "peripheral" rhodium sites by use of the Monte Carlo simulation produces a function reaching a maximum at $\theta_{TiO_x} \approx$

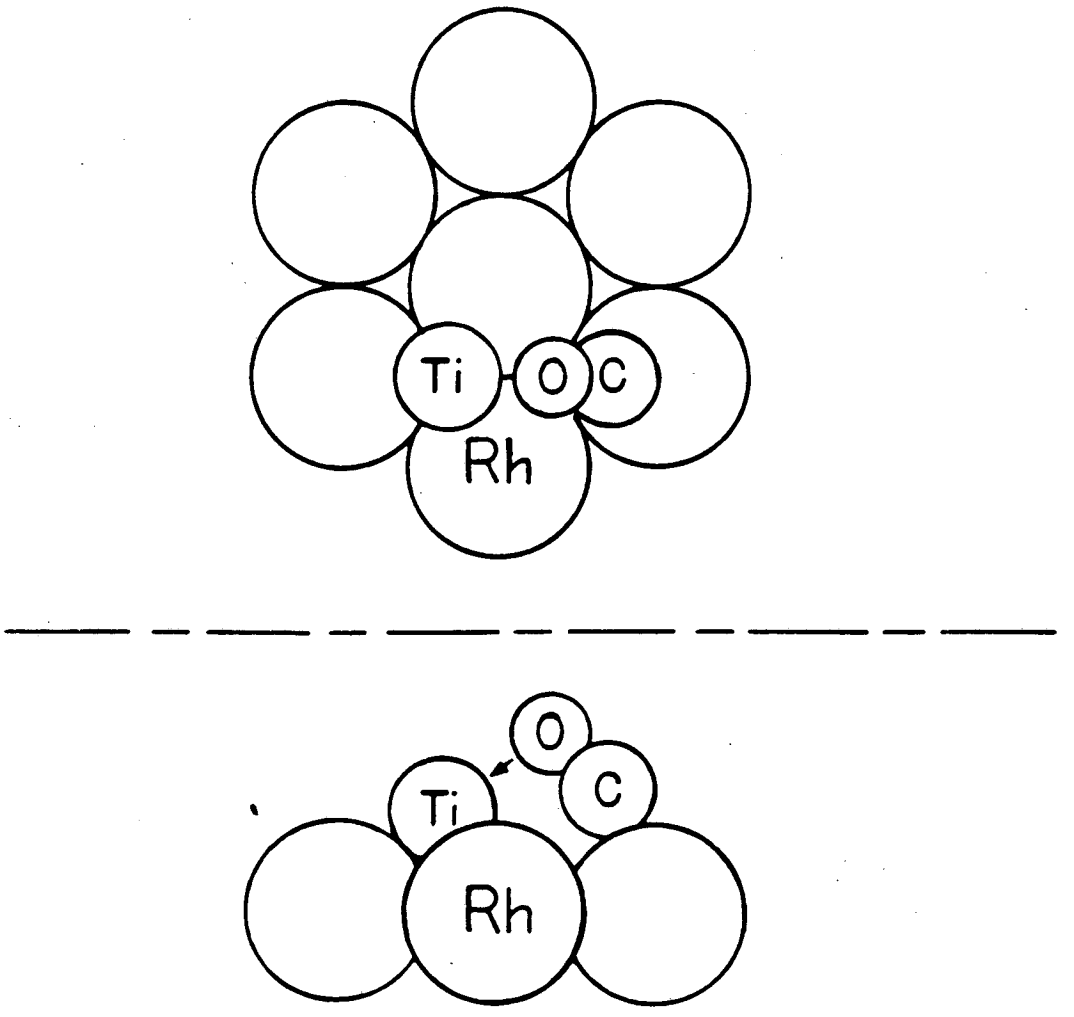

Figure 6.9: A possible configuration for the bonding of CO between peripheral Ti^{3+} sites and the Rh substrate.

0.35 ML, corresponding to the maximum chemisorption suppression at low pressures (Fig. 6.10). Neither the position of the maximum nor the shape of the curve agree with the trend of the experimental data.

A model which does give agreement with the observed trends is one in which a site pair consisting of a "peripheral" Rh site and an adjacent, non-"peripheral" Rh site has an intrinsically higher methanation activity. If it is assumed that the contribution of these peripheral site pairs to the total methanation rate is proportional to the product of the surface concentrations of each constituent site, then the total methanation rate in this model becomes

$$R_{CH_4} = S_T[n_o r_o + (\frac{n_p}{n_T})(\frac{n_{p'}}{n_T})r_{pp'}] \tag{6.3}$$

where r_o and $r_{pp'}$ represent the intrinsic methanation rates per unit catalyst area for the Rh sites unaffected by TiO_x and the highly active site pairs near the perimeter of the TiO_x islands, respectively. The numbers of each type of site present—exposed, "peripheral", adjacent to "peripheral", and the total—are given by n_o, n_p, $n_{p'}$, and n_T, respectively.

The number densities of the various types of site at various TiO_x coverages were determined through use of the Monte Carlo simulation. The values of n_o, n_p, and $n_{p'}$ were combined with the experimentally observed reaction rate for clean Rh, r_o, in Eqn. 6.3 to yield the total reaction rate as a function of coverage. The value of $r_{pp'}$ was chosen so that the maximum value of the predicted rate agrees with the maximum in the observed methanation rate. For this condition to be met, $r_{pp'}/r_o = 43$. The dependence of the calculated rate on the TiO_x coverage, described by Eqn. 6.3, is shown in Fig. 6.11 (solid curve), along with the experimental points presented in Fig. 5.38, for comparison. Good agreement is seen between the location of the predicted rate maximum and that of the experimental data. The width of the calculated peak, though, is broader than that exhibited by the data.

Another feature of this model is that it accounts for the extrema in kinetic parameters observed in Figs. 5.41 to 5.43. At low coverages ($\leq$ 0.3 ML), the rate is dominated by

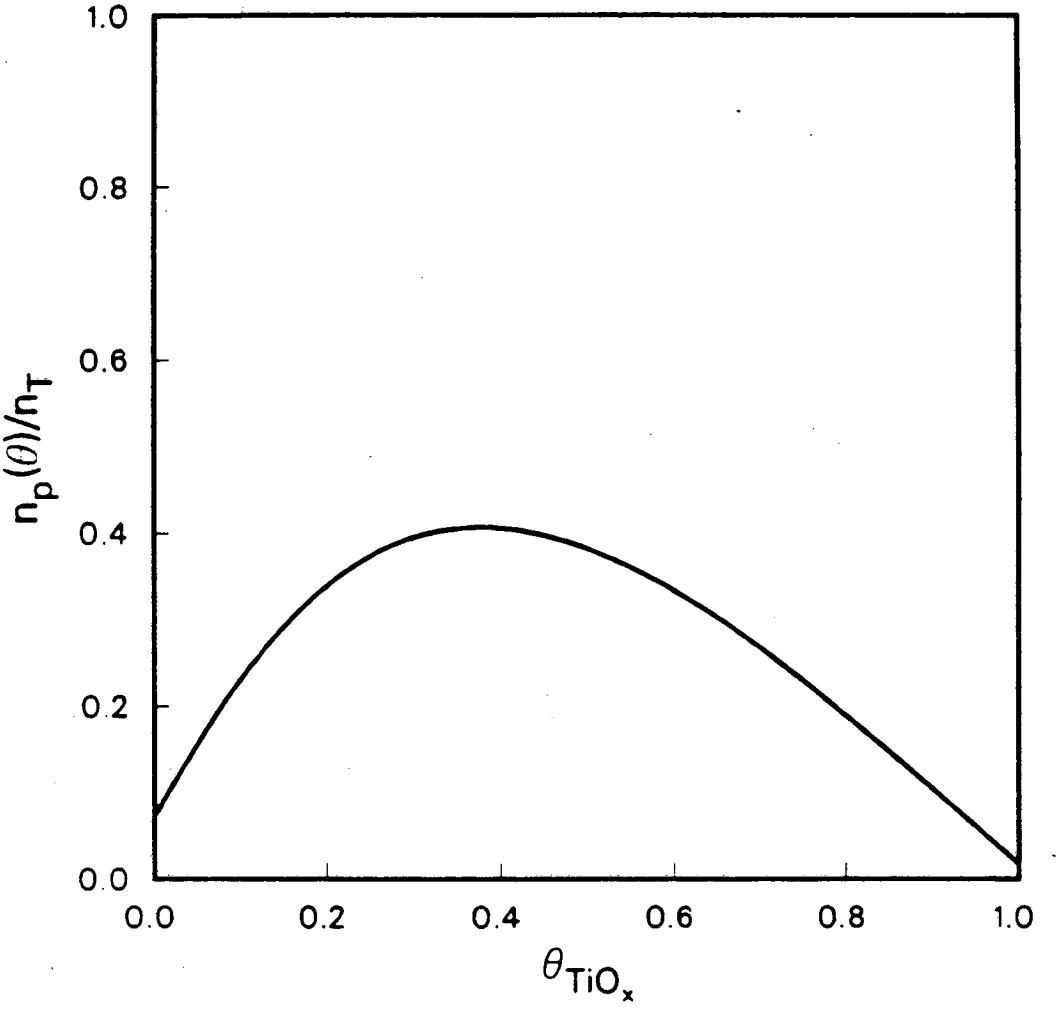

Figure 6.10: Amount of "peripheral" Rh sites as a function of TiO_x coverage based on a model in which CO chemisorption (at room temperature) is excluded at these sites (determined by subtracting the curve found in Fig. 5.30 (non-reduced) from the total amount of exposed Rh atoms.

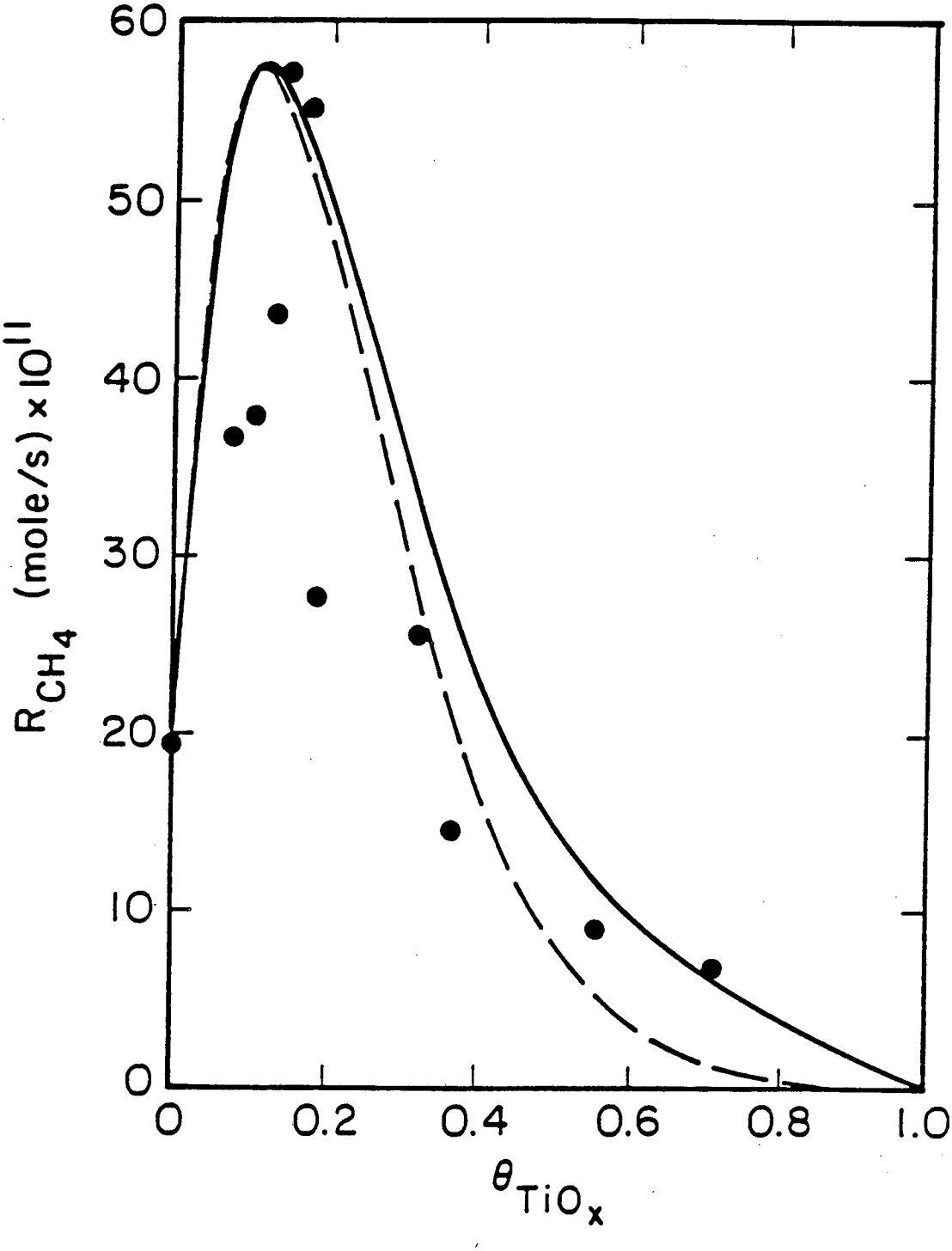

Figure 6.11: A comparison between the predicted methanation rate and the experimental data (●) as a function of TiO_x coverage. Solid curve— peripheral Rh sites active for both the Ti^{3+}-assisted reaction pathway and the normal reaction pathway. Dashed curve—peripheral Rh sites active only in the Ti^{3+}-assisted pathway.

the reaction occurring at the TiO_x/Rh interface, as reflected by the changes in activation energy and partial pressure dependences. At higher coverages, this contribution diminishes rapidly until kinetics typifying CO hydrogenation on clean Rh dominate.

At coverages approaching one monolayer, virtually all exposed, surface Rh atoms border TiO_x islands. These Rh sites may catalyze CO hydrogenation either through the mechanism normally occurring on Rh metal or through the Ti^{3+}-assisted pathway, depending on the prevalence of Ti^{3+} species at the metal/oxide interface under reaction conditions. The number of sites, n_o, catalyzing the reaction through the normal CO hydrogenation mechanism on bare Rh is therefore taken to be the total number of exposed Rh atoms.

The quantity, n_o, can be taken as the number of Rh atoms that could chemisorb CO at low pressures. The plot of predicted rate versus TiO_x in this case is depicted by the dashed curve in Fig. 6.11. However, with n_o defined in this manner, the model does not predict the extrema in kinetic parameters of Figs. 5.41 to 5.43.

Through bonding with the oxygen in CO, Ti^{3+} is oxidized to the +4 oxidation state. Regeneration of the Ti^{3+} site must occur for this reaction pathway to be followed again. One scheme for the reduction of Ti^{4+} back to Ti^{3+} is given below

1. $Ti^{4+}—O—M + H(a) \rightleftharpoons Ti^{4+}—OH \quad (M = Rh \text{ or } Ti^{4+})$
2. $Ti^{4+}—OH + H(a) \rightleftharpoons Ti^{3+} + H_2O$

The high reaction order of 2.6 with respect to hydrogen in the Ti^{3+}-assisted reaction pathway suggests that five or six hydrogenation steps are crucial in determining the overall reaction rate; Reactions 1 and 2 comprise two of these steps. In contrast, for bare Rh, where CO dissociation is believed to be rate-determining, the first-order H_2 dependence suggests that only two hydrogenation steps are important. Consequently, changes in the abundance of hydrogen on the surface are expected to affect the Ti^{3+}-assisted methanation rate to a greater extent.

As higher TiO_x coverages are reached, there is a reduction in the number of exposed

non-"peripheral" sites relative to the number of "peripheral" Rh sites. Furthermore, the high dispersion of the oxide overlayer serves to break up Rh–Rh pairs necessary for the chemisorption and dissociation of molecular hydrogen. The supply of surface hydrogen decreases rapidly with coverage and the impact on the Ti^{3+}-assisted reaction pathway, where the H_2 partial pressure dependence is nearly cubic, is much greater than on the normal pathway, where the dependence is only linear. At the microscopic level, this means that at near-monolayer coverages, there is insufficient surface hydrogen to maintain the Ti^{3+}-assisted reaction rate and so the slower pathway, in which CO dissociation is rate-determining, is the principal contributant.

The absence of any effect from pre-reduction of the sample upon reaction rate, as observed in this study and others [17,22,24,38] may be related to the active role of Ti^{3+} species in CO hydrogenation. Whether pre-oxidized or pre-reduced, the oxidation state (and perhaps also the morphology) of the oxide overlayer may be determined by the reaction conditions, where both H_2 and H_2O are present. In particular, the percentage of Ti^{3+} after reaction was found to be only weakly dependent on the pretreatment conditions (Fig. 5.27).

4.2 Formation of C_{2+} Hydrocarbons

Comparison of Figs. 5.44 to 5.46 with Figs. 5.41 to 5.43 shows two principal patterns: (1) the kinetics of ethane formation are similar to those of methane formation and (2) the kinetics of ethylene and propylene formation are likewise similar. Significant differences are seen only in the case of the CO partial pressure dependence (*e.g.*, -1.0 order for CH_4 and +0.5 order for C_2H_4) and these can be attributed to the requirement of additional surface carbon to form large hydrocarbons. Of particular interest is the difference in hydrogen partial pressure dependences between paraffins and olefins. The methane and ethane hydrogen orders are between 1/2 and 1 greater than for ethylene and propylene. Similar behavior was noted by Dictor and Bell [153] for unsupported Fe and by Kellner and Bell [154] for Al_2O_3-supported Ru. In both of these studies, a difference in order of roughly 1/2 was seen

between paraffins and olefins.

6.3.3 Deactivation of the Catalyst

Figs. 5.11 and 5.47 showed a decay in activity after one hour of reaction as a function of oxide coverage. Clearly, the coverages where higher methanation rates occurred were accompanied by higher degrees of catalyst coking as evidenced by the normalized rates and the normalized AES carbon intensities as a function of TiO_x coveage. The carbon signal reaches a maximum of about 0.44, compared with 0.12 for AlO_x/Rh, and at a TiO_x coverage near the point where the amount of oxide periphery is expected to reach a maximum ($\approx$ 0.35 ML based on the chemisorption modeling). Thus it appears that the additional carbon is deposited at the TiO_x/Rh interface along the periphery of TiO_x islands.

6.4 ETHYLENE HYDROGENATION AND ETHANE HYDROGENOLYSIS

Titania overlayers have been shown to enhance the hydrogenation of CC over rhodium, but as is apparent from Figs. 5.49 and 5.51, do not increase the rates of ethylene hydrogenation or ethane hydrogenolysis several possible hydrogenation steps). Rather, the rates of the latter two reactions diminish more rapidly than does the amount of exposed Rh with TiO_x coverage. The trends appear similar to that of CO chemisorption capacity as a function of coverage, but for reasons discussed below, the possible occurrence of mass transfer effects precludes any strong quantitative connections between the reactions and CO chemisorption behavior.

Clearly, the presence of TiO_x on the surface does not translate into higher hydrogenation rates. No enhancement in the rates appears to occur at the TiO_x–Rh interface which

suggests the necessity of a functional group, such as a carbonyl, on a reactant molecule for an interaction with Ti^{3+} to take place. The suppression in activity in both reactions can be attributed to three effects: (1) the coverage of Rh sites by TiO_x, (2) the break-up of ensembles by TiO_x on which the hydrocarbon reaction takes place, and (3) the break-up of Rh-Rh pairs for the chemisorption and dissociation of molecular hydrogen (as in Section 6.3.2). The ensemble size necessary for ethane hydrogenolysis has been investigated by other authors [155] and their conclusions point to a cluster of <4 metal atoms. Similar results might be expected in the case of ethylene hydrogenation. The precise numbers of Rh atoms per ensemble in either reaction cannot be relied upon too heavily until they can be confirmed by alternative means.

Inspection of Figs. 5.50 and 5.52 reveals that surface TiO_x has no appreciable effect on the activation energies for these reactions. This is further evidence that TiO_x does not appear to take an active role in these reactions. However, the activation energy for ethylene hydrogenation is only about half of that observed for supported Rh catalysts [124,125] and the activation energy for ethane hydrogenolysis is only about one-third of reported values (T = 513 K) [30,133]. These low activation energies, which are independent of the presence of TiO_x, may be due to interphase mass transfer limitations. At lower hydrogenolysis temperatures, where the corresponding reaction rate was significantly reduced, a normal activation energy was obtained. A calculation of the expected mass transfer rate during reaction conditions indicates that this should only marginally be a problem. Yet mass transfer limitations appear to be the most likely explanation for both diminished activation energies. Further study of this problem is warranted.

The effect of mass transfer limitations on the rate versus TiO_x coverage plots of Figs. 5.49 and 5.51 would be to diminish the rate dependence with coverage. If interphase transport is much slower than the surface reaction rate, then the overall rate would be independent of TiO_x coverage and would appear as a horizontal line. For Figs. 5.49 and 5.51, the actual surface rates are expected to decline more steeply with coverage than as they actually appear. In the case of CO hydrogenation, the rate is more than 30 times less active

than the ethylene hydrogenation and ethane hydrogenolysis reactions and so mass transport considerations do not apply.

Chapter 7

CONCLUSIONS AND RECOMMENDATIONS

7.1 CONCLUSIONS—EXPERIMENTAL

Oxide overlayers ($\leq$3 ML) on rhodium foil have been prepared in ultra-high vacuum through deposition of aluminum or titanium with subsequent oxidation. The AlO_x/Rh and TiO_x/Rh surfaces were characterized in terms of the oxide growth and chemisorption properties with surface analytical tools (AES, XPS, TPD) and in terms of their catalytic properties.

Both alumina and titania overlayers develop through the Stranski-Krastanov mechanism, i.e., formation of a two-dimensional monolayer followed by three-dimensional growth. As prepared, the two oxide overlayers, AlO_x and TiO_y, were only slightly substoichiometric, with x = 2.8 and y = 1.9.

The similarities between the two oxide overlayers end at this point. *Whereas reduction of the alumina overlayer is difficult, reduction of the titania with H_2 or CO is facile.* At low TiO_x coverages, nearly 70% of the titanium is in the 3+ oxidation state following reduction in 50 torr H_2 at 753 K. Under similar conditions, titania deposited on a gold foil could not be reduced, suggesting the need for an active metal, such as Rh, to dissociate H_2.

Thermal desorption and catalytic results indicate that *alumina acts only as an inert*

contaminant on the rhodium surface, physically blocking sites active for CO chemisorption and CO hydrogenation. The CO chemisorption capacity of alumina on rhodium was found to decrease linearly with increasing alumina coverage. The same trend was observed for the methanation rate as a function of coverage with no changes in selectivity occurring (~90 mol% CH_4 for all coverages). Alumina appears to have no effect on the rate of deactivation as well as the amount of carbon deposited on the surface.

Titania overlayers were found to induce a sharp suppression in CO chemisorption which could only partly be attributed to site-blocking by the oxide. A further reduction in the CO chemisorpton capacity occurred upon hydrogen reduction at temperatures above ~520 K. While a downward shift in desorption temperature was noted for high TiO_x coverages or after hydrogen reduction, no new significant desorption features appeared, even at temperatures as low as 150 K.

A three-fold enhancement in CO hydrogenation activity occurred for a TiO_x coverage of 0.15 ML. This was accompanied by dramatic changes in the kinetic parameters, suggesting an alternative reaction pathway for Rh in the presence of TiO_x. In addition, there was an increase in selectivity toward ethylene and propylene. The presence of surface titania also led to a greater rate of deactivation and carbon deposition during reaction.

In contrast, *both the ethylene hydrogenation and ethane hydrogenolysis rates were substantially diminished by TiO_x on the surface.* Both activities were suppressed at least to the extent exhibited by CO chemisorption, but the actual amounts may be masked by mass transfer effects. The activation energies of these two reactions remained unchanged when TiO_x was added indicating that changes in mechanisms are unlikely. Comparison with the CO hydrogenation results suggests the need for a functional group, such as –C=O, for the Ti^{3+}-assisted reaction pathway to occur.

7.2 CONCLUSIONS—MODELING

The modification of the chemisorption and catalytic properties of Rh by TiO_x overlayers can

be attributed to processes occurring at the TiO_x/M interface at the TiO_x island periphery. In particular, XPS results point to the existence of Ti^{3+} sites along the periphery of TiO_x islands. These species may interact with neighboring Rh atoms, reducing the bond order of those Rh atoms, and thereby substantially weaken CO chemisorption. Under conditions for CO hydrogenation, these Ti^{3+} sites may interact with the oxygen of chemisorbed CO to enhance dissociation of the C–O bond and therefore the surface activity.

The suppression of CO chemisorption on a TiO_x/Rh surface has been successfully modeled by excluding CO chemisorption at Rh sites bordering as well as underneath TiO_x islands. The morphology of TiO_x species on the surface was simulated with two approaches: uniform circular islands grown around fixed nucleation sites and a Monte Carlo simulation of random island growth around randomly chosen nucleation sites. The number of Rh atoms bordering TiO_x islands can then be counted. Comparison of the results of either approach with the experimental data suggests a nucleation site density of 4.5 x 10^{13} cm^{-2} (a 2.8% site density). The high dispersion inferred from the nucleation site density probably reflects a high degree of Brewer-Engels–type alloying between the TiO_x species and the Rh.

Modeling of the methanation rate as a function of TiO_x coverage suggests a higher activity on two-site ensembles along the TiO_x island periphery. Whereas the Monte Carlo simulation (with the same dispersion as in the CO chemisorption modeling) yields a broad function with a maximum at 0.35 ML for a one-site ensemble, the two-site ensemble gives a sharper function reaching a peak at 0.10 ML. This agrees more closely with the experimental results. The model also allows for the return of the kinetic parameters at near-monolayer coverages to values typical of bare Rh. At the high TiO_x coverages, the supply of adsorbed hydrogen is inadequate to maintain Ti in the 3+ oxidation state and so the contribution from the Ti^{3+}-assisted reaction pathway is diminished.

7.3 RECOMMENDATIONS

While this work has demonstrated the importance of the titania/rhodium interface in CO chemisorption and hydrogenation, further exploration of metal oxide/metal systems is required to clarify the nature of the interactions taking place.

Structural information is vitally important. Knowledge concerning the positions and orientations of the overlayer atoms relative to the substrate could supply valuable information on the interaction between oxide overlayer and metal substrate and the participation of the metal oxide/metal interface in reactions. Although the determination of surface structures of this type are extremely difficult, the application of scanning tunneling microscopy (STM) and low energy electron diffraction (LEED) with single crystal substrates may provide a basis for understanding the overlayer structure relative to the substrate.

The effect of oxide overlayers on the chemisorption of other molecules should be investigated. Titania has already been shown to suppress CO chemisorption; chemisorption of other molecules, such as H_2 or NO, may be similarly affected. Perhaps some molecules may show no effect at all. Chemisorption on the oxide, for example by CO_2 or H_2O, may even be affected by the metal substrate. Finally, exploring the effect of oxide dispersion through the variation of adsorbate molecule size (H_2 vs. CO or C_3H_8 vs C_6H_{14}) may prove interesting.

By studying the reactions of hydrocarbons with -C=O groups on TiO_x/M surfaces, the role of "peripheral" Ti^{3+} in dissociation of the C-O bond may be investigated further. Other probe reactions include: the reduction of NO to N_2 by CO; CO + H_2 + C_2H_4 to form propanaldehyde; and reactions of hydrocarbons with other functional groups (*e.g.*, -COOH, -OH). Hydrocarbon hydrogenation and hydrogenolysis activities have already been shown to be suppressed by TiO_x on the surface. Perhaps these diminished activities can be related to the dispersion of the TiO_x overlayer.

Finally, *interactions between metal oxides and metals are not unique to the TiO_x/Rh system and other oxide/substrate systems should be studied.* Other suitable oxides include:

SiO_2, MnO_2, ZrO_2, V_2O_5, and La_2O_3. Some of these oxides may exhibit an interaction intermediate in strength compared with Al_2O_3 and TiO_2. Variation of the substrate is also possible and some of the likely candidates are: Ni, Ru, Fe, Pt, and Cu. Alloying between Pt and Ti makes the formation of a TiO_x overlayer extremely difficult and for this reason, a Pt substrate is not recommended. Also, the TiO_x/Ni and TiO_x/Pt systems have already been studied extensively in other research groups. Preliminary work with a Au substrate has been performed and may prove valuable when investigating the properties of the oxide overlayer.

Bibliography

[1] G.M. Schwab, J. Block, W. Müller, and D. Schultze, *Naturwissenschaftern*, **44**, 582 (1957).

[2] G.M. Schwab, J. Block, and D. Schultze, *Angew. Chem.*, **71**, 101 (1958).

[3] G.M. Schwab, "Advances in Catalysis," Vol. 27, p.1, Academic Press, New York, 1978.

[4] Z.G. Szabó, F. Solymosi, and I. Batta, *Z. Phys. Chem. N.F.*, **17**, 125 (1958).

[5] Z.G. Szabó, F. Solymosi, and I. Batta, *Z. Phys. Chem. N.F.*, **23**, 56 (1960).

[6] F. Solymosi, *Catal. Rev*, **1**, 233 (1967).

[7] R.F. Baddour and R.F. Deibert, *J. Phys. Chem.*, **70**, 2173 (1966).

[8] S.J. Tauster, S.C. Fung, and R.L. Garten, *J. Am. Chem. Soc.*, **100**, 170 (1978).

[9] S.J. Tauster, and S.C. Fung, *J. Catal*, **55**, 29 (1978).

[10] S.J. Tauster, S.C. Fung, R.T.K. Baker, and J.A. Horsley, *Science*, **211**, 1121 (1981).

[11] J.S. Smith, P.A. Thrower, and M.A. Vannie, *J. Catal.*, **68**, 270 (1981).

[12] P. Mériaudeau, O.H. Ellestad, M. Dufaux, and C. Naccache, *J. Catal.*, **75**, 243 (1982).

[13] M.A. Vannice, *J. Catal.*, **74**, 199 (1982).

[14] R. Burch and A.R. Flambard, *J. Catal.*, **78**, 389 (1982).

[15] J.M. Herrmann and P. Pichat, *J. Catal.*, **78**, 425 (1982).

[16] M.A. Vannice, C.C. Twu, and S.H. Moon, *J. Catal.*, **79**, 70 (1982).

[17] M.A. Vannice, C.C. Twu, and S.H. Moon, *J. Catal.*, **82**, 213 (1983).

[18] D.E. Resasco and G.L. Haller, *J. Phys. Chem.*, **88**, 4552 (1984).

[19] X.-Z. Jiang, T.F. Hayden, and J.A. Dumesic, *J. Catal.*, **83**, 168 (1983).

[20] C.H. Bartholomew and R.B. Pannell, *J. Catal.*, **65**, 390 (1980).

[21] S.-M. Fang and J.M. White, *J. Catal.*, **83**, 1 (1983).

[22] F. Solymosi, I. Tombácz, and M. Kocsis, *J. Catal.*, **75**, 78 (1982).

[23] R. Burch and A.R. Flambard, *J. Catal.*, **85**, 16 (1984).

[24] J.D. Bracey and R. Burch, *J. Catal.*, **86**, 384 (1984).

[25] V. Rives-Arnau and G. Munuera, *Appl. Surf. Sci.*, **6**, 122 (1980).

[26] R. Nakamura, S. Nakai, K. Sugiyama, and E. Echigoya, *Bull. Chem. Soc. Jpn.*, **54**, 1950 (1981).

[27] R. Nakamura, K. Yamagami, S. Nishiyama, H. Niiyama, and E. Echigoya, *Chem. Lett.*, **2**, 275 (1981).

[28] N.K. Pande and A.T. Bell, *J. Catal.*, **98**, 7 (1986).

[29] D.E. Resasco and G.L. Haller, *J. Catal.*, **82**, 279 (1983).

[30] E.I. Ko and R.L. Garten, *J. Catal.*, **68**, 233 (1981).

[31] E.I. Ko and G. Marcelin, *J. Catal.*, **93**, 201 (1985).

[32] A. Sárkány and P. Tétényi, *React. Kinet. Catal. Lett.*, **12**, 297 (1979).

[33] D.J.C. Yates, W.F. Taylor, J.H. Sinfelt, *J. Am. Chem. Soc.*, **86**, 2996 (1964).

[34] L. Brewer, *Acta Met.*, **15**, 553 (1967).

[35] L. Brewer and P.R. Wengert, *Metall. Trans.*, **4**, 83 (1973).

[36] P.T. Meschter and W.L. Worrell, *Metall. Trans. A*, **7A**, 299 (1977).

[37] J.A. Horsley, *J. Am. Chem. Soc.*, **101**, 2870 (1979).

[38] S.R. Morris, R.B. Moyes, and P.B. Wells, in "Studies in Surface Science and Catalysis" (B. Imelik *et al.*, Eds.), Vol. 11, p.247, Elsevier, Amsterdam (1982).

[39] T. Huizinga and R. Prins, *J. Phys. Chem.*, **85**, 2158 (1981).

[40] B.A. Sexton, A.E. Hughes, and K. Foger, *J. Catal.*, **77**, 85 (1982).

[41] R.T.K. Baker, E.B. Prestridge, and L.L. Murrell, *J. Catal.*, **79**, 348 (1983).

[42] R.T.K. Baker, E.B. Prestridge, and L.L. Murrell, *J. Catal.*, **56**, 390 (1979).

[43] M.K. Bahl, S.C. Tsai, and Y.W. Chung, *Phys. Rev. B*, **21**(4), 1344 (1980).

[44] C.C. Kao, S.C. Tsai, M.K. Bahl, Y.W. Chung, and W.J. Lo, *Surf. Sci.*, **95**, 1 (1980).

[45] S.C. Fung, *J. Catal.*, **76**, 225 (1982).

[46] D.N. Belton, Y.-M. Sun, and J.M. White, *J. Phys. Chem.*, **88**, 1690 (1984).

[47] J.M. Herrmann, *J. Catal.*, **89**, 404 (1984).

[48] V. Ponec in "Studies in Surface Science and Catalysis" (B. Imelik *et al.*, Eds.), Vol. 11, p. 63, Elsevier, Amsterdam (1982).

[49] U. Bardi, G.A. Somorjai, and P.N. Ross, *J. Catal.*, **85**, 272 (1984).

[50] P.J. Feibelman and D.R. Hamann, *Phys. Rev. Lett.*, **52**, 61 (1984).

[51] P.J. Feibelman and D.R. Hamann, *Surf. Sci.*, **149**, 48 (1985).

[52] R.W. Joyner, J.B. Pendry, D.K. Saladin, and S.R. Tennison, *Surf. Sci.*, **138**, 84 (1984).

[53] J. Santos, J. Phillips, and J.A. Dumesic, *J. Catal.*, **81**, 147 (1983).

[54] P. Turlier, J.A. Dalmon, and B.A. Martin, in "Studies in Surface Science and Catalysis" (B. Imelik *et al.*, Eds.), Vol. 11, p. 203 (1982).

[55] H.R. Sadeghi and V.E. Henrich, *J. Catal.*, **87**, 279 (1984).

[56] S. Takatani and Y.-W. Chung, *J. Catal.*, **90**, 75 (1984).

[57] D.N. Belton, Y.-M. Sun, and J.M. White, *J. Phys. Chem.*, **88**, 5172 (1984).

[58] R.T.K. Baker, J.J. Chludzinski, and J.A. Dumesic, *J. Catal.*, **93**, 312 (1985).

[59] E.L. Kugler and R.L. Garten, U.S. Patent #4,273,724 (1981).

[60] D.J. Dwyer, J.L. Robbins, S.D. Cameron, N. Dudash, and J. Hardenbergh, *ACS Symposium Ser.*, No. 298, "Strong Metal Support Interaction" (R.T.K. Baker, S.J. Tauster, and J.A. Dumesic, Eds.), p. 21, 1986.

[61] N.K. Pande and A.T. Bell, *Appl. Catal.*, **20**, 109 (1986).

[62] G.B. Raupp and J.A. Dumesic, *J. Phys. Chem.*, **88**, 660 (1984).

[63] G.B. Raupp and J.A. Dumesic, *J. Catal.*, **95**, 587 (1985).

[64] C.S. Ko and R.J. Gorte, *J. Catal.*, **90**, 59 (1984).

[65] C.S. Ko and R.J. Gorte, *Surf. Sci.*, **161**, 597 (1985).

[66] C.S. Ko and R.J. Gorte, *Surf. Sci.*, **155**, 296 (1985).

[67] D.J. Dwyer, S.D. Cameron, and J. Gland, *Surf. Sci.*, **159**, 430 (1985).

[68] Y.-W. Chung, G. Xiong, and C.-C. Kao, *J. Catal.*, **85**, 237 (1984).

[69] R.A. Demmin, C.S. Ko, and R.J. Gorte, *J. Phys. Chem.*, **89**, 1151 (1985).

[70] R.A. Demmin and R.J. Gorte, *J. Catal.*, **98**, 577 (1986).

[71] D. Briggs and M.P. Seah, "Practical Surface Analysis by Auger and X-Ray Photoelectron Spectroscopy," John Wiley & Sons, 1983.

[72] G.A. Somorjai, "Chemistry in Two Dimensions," Cornell University Press, 1981.

[73] P.W. Palmberg, G.E. Riach, R.E. Weber, and N.C. MacDonald, "Handbook of Auger Electron Spectroscopy," Physical Electronics Industries, Eden Prairie, MN, 1972.

[74] R.W. Vook, *Inter. Metals Rev.*, **27**, 209 (1982).

[75] J.P. Biberian and G.A. Somorjai, *Surf. Sci.*, **2**, 352 (1979).

[76] E. Bauer, *Appl. Surf. Sci.*, **11/12**, 479 (1982).

[77] J.W.A. Sachtler, M.A. Van Hove, J.P. Biberian, and G.A. Somorjai, *Surf. Sci.*, **110**, 19 (1981).

[78] R.C. Yeates, Ph.D. Thesis, University of California, Berkeley, California, 1985.

[79] J.H. Ho and R.W. Vook, *J. Cryst. Growth*, **44**, 561 (1978).

[80] C. Binns and C. Norris, *Surf. Sci.*, **116**, 338 (1982).

[81] A. Sepulveda and G.E. Rhead, *Surf. Sci.*, **66**, 436 (1977).

[82] M.-G. Barthès and G.E. Rhead, *Surf. Sci.*, **80**, 421 (1979).

[83] C. Argile and G.E. Rhead, *Surf. Sci.*, **78**, 115 (1978).

[84] L. Gonzalez, Ph.D. Thesis, Universidad Autonoma de Madrid, 1982.

[85] G. Praline, N. Pacia, J.J. Ehrhardt, A. Cassuto, and J.P. Langeron, *Surf. Sci.*, **105**, 289 (1981).

[86] U. Bardi, G.A. Somorjai, and P.N. Ross, personal communication.

[87] P.W. Davies, M.A. Quinlan, and G.A. Somorjai, *Surf. Sci.*, **121**, 290 (1982).

[88] C. Argile and G.E. Rhead, *Surf. Sci.*, **78**, 125 (1978).

[89] H. Tokutaka, K. Nishimori, and K. Takashima, *Surf. Sci.*, **86**, 54 (1979).

[90] M.-G. Barthès and G.E. Rhead, *Surf. Sci.*, **85**, L211 (1979).

[91] K. Lewis and G.A. Somorjai, results to be published.

[92] G. Le Lay, M. Manneville, and J.J. Métois, *Surf. Sci.*, **123**, 117 (1982).

[93] R.A. Metzger and F.G. Allen, *Surf. Sci.*, **137**, 397 (1984).

[94] W. Kirstein, B. Krüger, and F. Thieme, *Surf. Sci.*, **176**, 505 (1986).

[95] L. Gonzalez, R. Miranda, M. Salmeron, J.A. Vergés, F. Ynduráin, *Phys. Rev. B*, **24**(6), 3245 (1981).

[96] D. Godbey and G.A. Somorjai, to be published.

[97] U. Gradmann and G. Waller, *Surf. Sci.*, **116**, 539 (1982).

[98] P.R. Davis, *Surf. Sci.*, **91**, 385 (1980).

[99] W. Schlenk and E. Bauer, *Surf. Sci.*, **93**, 9 (1980).

[100] Ch. Park, E. Bauer, and H. Poppa, *Surf. Sci.*, **154**, 371 (1985).

[101] D. Godbey and G.A. Somorjai, to be published.

[102] D.R. Strongin and G.A. Somorjai, to be published.

[103] U. Bardi, P.N. Ross, and G.A. Somorjai, *J. Vac. Sci. Technol. A*, **2**(1), 40 (1984).

[104] K. Christmann, G. Ertl, and H. Shimuzu, *J. Catal.*, **61**, 397 (1980).

[105] C. Harendt, K. Christmann, W. Hirschwald, and J.C. Vickerman, *Surf. Sci.*, **165**, 413 (1986).

[106] R. Siuda, *Surf. Sci.*, **123**, L667 (1982).

[107] A. Rolland, J. Bernardini, M.-G. Barthès-Labrousse, *Surf. Sci.*, **143**, 579 (1984).

[108] G.C. Smith, H.A. Padmore, and C. Norris, *Surf. Sci.*, **119**, L287 (1982).

[109] D.R. Strongin and G.A. Somorjai, unpublished results.

[110] S.R. Bare, D.R. Strongin, and G.A. Somorjai, *J. Phys. Chem.*, **90**, 4726 (1986).

[111] S. Nakanishi and T. Horiguchi, *Surf. Sci.*, **133**, 605 (1983).

[112] D.C. Jackson, T.E. Gallon, and A. Chambers, *Surf. Sci.*, **36**, 381 (1973).

[113] G. Ertl and J. Küppers, "Low Energy Electrons and Surface Chemistry," Verlag Chemie, 1974.

[114] C.D. Wagner, W.M. Riggs, L.E. Davis, J.F. Moulder, and G.E. Muilenberg (Editor), "Handbook of X-Ray Photoelectron Spectroscopy," Perkin-Elmer Corporation, Physical Electronics Division, Eden Prairie, MN, 1979.

[115] S. Doniach and M. Šunjić, *J. Phys. C*, **3**, 285 (1970).

[116] P.A. Redhead, *Vacuum*, **12**, 203 (1962).

[117] R.P.H. Gasser, "An Introduction to Chemisorption and Catalysis by Metals," Oxford University Press, 1985.

[118] D.G. Castner, B.A. Sexton, and G.A. Somorjai, *Surf. Sci.*, **71**, 519 (1978).

[119] P.A. Thiel, E.D. Williams, J.T. Yates, Jr., and W.H. Weinberg, *Surf. Sci.*, **84**, 54 (1974).

[120] R.J. Baird, R.C. Ku, and P. Wynblatt, *Surf. Sci.*, **97**, 346 (1980).

[121] P.R. Watson and G.A. Somorjai, *J. Phys. Chem.*, **86**, 3993 (1982).

[122] M.A. Logan and G.A. Somorjai, *J. Catal.*, **95**, 317 (1985).

[123] D.J. Dwyer, K. Yoshida, and G.A. Somorjai, "Adv. in Chem. Series," no. 178 (E.L. Kugler and F.W. Steffgen, Eds.), p. 65 (1979).

[124] G.C. Bond, G. Webb, P.B. Wells, and J.M. Winterbottom, *Trans. Faraday Soc.*, **62**, 443 (1966).

[125] F. Pinna, M. Gonizzi, G. Strukul, G. Cocco, and S. Enzo, *J. Catal.*, **82**, 171 (1983).

[126] U. Bardi and P.N. Ross, *J. Vac. Sci. Technol. A*, **2**(4), 1461 (1984).

[127] G.D. Davis, M. Natan, and K.A. Anderson, *Appl. Surf. Sci.*, **15**, 321 (1983).

[128] G.B. Raupp and J.A. Dumesic, *J. Phys. Chem.*, **89**, 5240 (1985).

[129] C.M. Greenlief, J.M. White, C.S. Ko, and R.J. Gorte, *J. Phys. Chem.*, **89**, 5025 (1985).

[130] C.R. Brundle and A.F. Carley, *Chem. Phys. Lett.*, **31**(3), 423 (1975).

[131] S.L.T. Andersson, *J. Chem. Soc.*, **75**, 1356 (1979).

[132] K. Wandelt, *Surf. Sci. Reports*, **2**, 1 (1982).

[133] J.H. Sinfelt, *Catal. Rev.*, **3**, 175 (1969).

[134] M. Salmeron, S. Ferrer, M. Jazzar, and G.A. Somorjai, *Phys. Rev. B*, **28**, 1158 (1983).

[135] C. Ocal, E. Martinez, and S. Ferrer, *Surf. Sci.*, **136**, 571 (1984).

[136] F. Falo, I. Cano, and M. Salmeron, *Surf. Sci.*, **143**, 303 (1984).

[137] B.C. Gates, J.R. Katzer, and G.C.A. Schuit, "Chemistry of Catalytic Processes," McGraw-Hill Book Company, 1979.

[138] Y.-W. Chung, W.J. Lo, and G.A. Somorjai, *Surf. Sci.*, **64**, 588 (1977).

[139] J.E. Huheey, "Inorganic Chemistry, Principles of Structure and Reactivity," 2nd Ed., Harper & Row, 1978.

[140] J.S. Rieck and A.T. Bell, *J. Catal.*, 1986, in press.

[141] N.K. Pande, Ph.D. Thesis, University of California, Berkeley, CA, 1985.

[142] M.A. Vannice, *J. Catal.*, **37**, 449 (1975).

[143] T. Iizuka, Y. Tanaka, and K. Tanabe, *J. Catal.*, **76**, 1 (1982).

[144] J.R. Budge, B.F. Løucke, B.G. Gates, and J. Toran, *J. Catal.*, **91**, 272 (1985).

[145] F. Solymosi, I. Tombácz, and J. Koszta, *J. Catal.*, **95**, 578 (1985).

[146] S.C. Chuang, J.G. Goodwin, Jr., and I. Wender, *J. Catal.*, **95**, 435 (1985).

[147] J.B.F. Anderson, J.D. Bracey, R. Burch, A.R. Flambard, in "Proceedings, 8th International Congress on Catalysis," Vol. V, p. 111. Berlin, 1984.

[148] M.A. Vannice and C. Sudhakar, *J. Phys. Chem.*, **88**, 2429 (1984).

[149] C. Sudhakar and M.A. Vannice, *J. Catal.*, **95**, 227 (1985).

[150] W.M.H. Sachtler, in "Proceedings, 8th International Congress on Catalysis," Vol. V, p. 151. Berlin, 1984.

[151] W.M.H. Sachtler, D.F. Shriver, W.B. Hollenberg, and A.F. Long, *J. Catal.*, **92**, 429 (1985).

[152] J.S. Rieck and A.T. Bell, *J. Catal.*, **96**, 88 (1985).

[153] R.A. Dictor and A.T. Bell, *Appl. Catal.*, **20**, 145 (1986).

[154] C.S. Kellner and A.T. Bell, *J. Catal.*, **70**, 418 (1981).

[155] M. Boudart and G. Djéga-Mariadassou, "Kinetics of Heterogeneous Catalytic Reactions," Princeton University Press, 1984.

[156] J.L. Gland, *Surf. Sci.*, **93**, 487 (1980).

Appendix A

FURTHER ANALYSIS OF OXIDE OVERLAYERS

A.1 ALTERNATIVE MEANS FOR DETERMINING OVERLAYER COVERAGE

An alternative method for the determination of oxide overlayer coverage has been employed in some studies [64,65]. The method involves comparing the AES O/Rh ratio for TiO_x on Rh with the ratio measured for O_2 chemisorbed (at saturation) on Rh. At 90 K, saturation coverage of O_2 on Rh resulted in an AES O/Rh ratio of 0.07 [65].

The difficulty in this method lies in applying the O/Rh value to the TiO_x overlayer. First of all, the actual coverage corresponding to saturation coverage of O_2 is uncertain. Saturation coverage is likely between 0.25 and 0.75 ML and may be a 2 x 2 overlayer (as with Pt [156]). However, the O/Rh ratio is of little value without a precise measure of the coverage.

If it is assumed that saturation coverage does correspond to 0.25 ML oxygen (a 2 x 2 overlayer), then the next step is to determine a basis for comparison with the AES O/Rh ratio of the TiO_x overlayer. The stoichiometry of the oxide overlayer is now important. Gorte *et al.* [65] observed an oxide overlayer of stoichiometry TiO. Based on this information, an AES O/Rh ratio of 0.19 was interpreted as "monolayer" coverage with a corresponding

33% attenuation in the Rh signal.

In the present work, monolayer coveage was determined from the linear break in an AES intensity-vs.-evaporation time plot. The O/Rh ratio corresponding to monolayer coverage was 0.96 for an oxide stoichiometry near TiO_2. If the oxide overlayer is "allowed" to have a three-dimensional structure, *i.e.*, the monolayer is actually a bi-layer, then the monolayer equivalent of oxygen atoms on the surface is 2/3 x 2 ML = 1.33 ML, compared with 0.25 ML for the 2 x 2 oxygen overlayer. Taking into account the attenuation of the Rh signal (66%) yields a predicted AES O/Rh ratio of 0.85 at monolayer coverage. This represents a difference of only 13%. These calculations are illustrated below. Clearly, the method of coverage determination involving comparison of O/Rh ratios is consistent with both Gorte's calibration and the one presented here, although CO chemisorption data indicate a factor of three or four difference between these two calibrations.

For monolayer coverage for AlO_x on Rh (as determined from Fig. 5.5), an AES O/Rh ratio of about 0.43 was observed. The predicted value for a two-dimensional bi-layer is 0.63. However, since the degree of attenuation is smaller (α larger) for AlO_x/Rh compared with TiO_x/Rh at monolayer coverage, the assumption of a full bi-layer may not be valid. If the second layer is only half occupied, with O atoms on top, an AES O/Rh ratio of 0.50 might be expected.

The problem in this method lies in assumptions made of the oxide overlayer structure. One cannot compare O/Rh ratios in a meaningful manner unless the orientation of oxygen in the overlayer is known. For example, for a TiO overlayer, if the oxide exists as a lattice of Ti atoms on the surface with oxygen atoms sitting on top, twice as many oxygen atoms will exist on the surface compared with the case of O and Ti in the same plane. This method, therefore, is only as good as the available knowledge regarding the structure of the oxide overlayer. In the absence of this knowledge, many results are possible, depending on the structure assumed.

TiO_x/Rh Calculations:

I_{Rh}

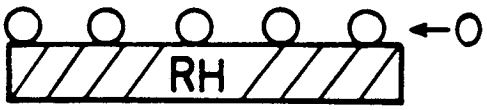

0.25 ML O on Rh $\qquad \frac{I_O}{I_{Rh}} = 0.07$

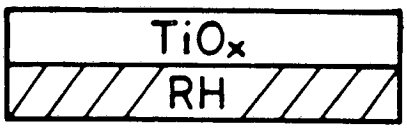

1 ML ($\equiv$ 2 ML—bi-layer) $\qquad \frac{I_O}{I_{Rh}} = ?$

#O atoms = (2 ML atoms) x $\frac{2}{5} = \frac{4}{5}$ ML

$\alpha = 0.34$: for a 1 atom thick monolayer, $\alpha' = \sqrt{0.34} = 0.58$

O on Rh: $\frac{I_O}{I_{Rh}} = 0.07 = \frac{y}{\underbrace{1-\frac{1-\sqrt{0.34}}{4}}_{\text{0.25 ML attenuation of Rh}}} = 1.116\ y$

$\Rightarrow y = 0.0627$

TiO_2 on Rh: $\frac{I_O}{I_{Rh}} = \left(\frac{\frac{2}{5}\text{x2ML}}{0.25\text{ML}}\right) \frac{y}{1-0.66} \frac{\overbrace{1+\frac{1}{5}(0.58)}^{\text{attenuation of 1st layer O signal by 2nd layer O}}}{\frac{4}{5}} = 0.88$

Observed: $\frac{I_O}{I_{Rh}} = 0.96$

AlO_x/Rh Calculations:

I_{Rh}

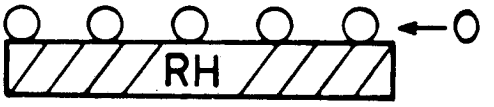

0.25 ML O on Rh $\qquad \frac{I_O}{I_{Rh}} = 0.07$

1 ML ($\equiv$ 2 ML—bi-layer) $\qquad \frac{I_O}{I_{Rh}} = ?$

#O atoms = (2 ML atoms) x $\frac{3}{5}$ = 1.1 ML

$\alpha = 0.45$: for a 1 atom thick monolayer, $\alpha' = \sqrt{0.45} = 0.67$

O on Rh: $\frac{I_O}{I_{Rh}} = 0.07 = \frac{y}{\underbrace{1-\frac{1-0.67}{4}}_{\text{0.25 ML attenuation of Rh}}} = 1.090\ y$

$\Rightarrow y = 0.0642$

attenuation of 1st layer O signal by 2nd layer O

Al_2O_3 on Rh: $\frac{I_O}{I_{Rh}} = \left(\frac{\frac{3}{5}x2ML}{0.25ML}\right) \frac{y}{1-0.66} \overbrace{\frac{1+\frac{1}{3}(0.58)}{1.1}} = 0.66$

#O atoms = ("1.5 ML" atoms) x $\frac{5}{5} = 1.1$ ML

$\alpha = 0.45$: for a "1.5 atom" thick monolayer, $\alpha' = \alpha^{\frac{1}{1.5}} = 0.45^{\frac{1}{1.5}} = 0.59$

O on Rh: $\frac{I_O}{I_{Rh}} = 0.07 = \frac{y}{1-\underbrace{\frac{1-0.59}{4}}_{\text{0.25 ML attenuation of Rh}}} = 1.090\ y$

$\Rightarrow y = 0.0628$

Al_2O_3 on Rh: $\frac{I_O}{I_{Rh}} = \left(\frac{\frac{5}{4}x1.5ML}{0.25ML}\right)\frac{y}{1-0.55} = 0.50$

Observed: $\frac{I_O}{I_{Rh}} = 0.43$

A.2 THE EFFECT OF THREE-DIMENSIONAL OVERLAYER GROWTH ON COVERAGE DETERMINATION

An analysis of the impact of three-dimensional overlayer growth on the measured AES substrate signal is presented here. Calculations were performed by assuming an overlayer geometry at a given coverage and calculating the attenuation of the substrate (Rh (302 eV)) signal. A value of α (the coverage) of 0.55 was taken. As seen from Table 2-1, this value is in the range observed for 280–360 eV electrons for overlayers of one atomic distance thickness. Since an attenuation corresponding to $\alpha = 0.34$ was observed for TiO_x/Rh, this analysis represents a worst-case scenario to test the validity of the coverage determination in Fig. 5.13.

Six overlayer geometries were employed, each comprised of stacked layers in which the angle formed between successive layers and the surface plane is specified. The overlayer geometries corresponding to angles of 0°, 18.4°, 32°,45°, 50° , and 78.7° are depicted in Fig. A.1 for a monolayer equivalent of 0.78 ML. The effect from only one island, of rectangular cross-section, on a section of substrate of arbitrary length was considered.

Fig. A.2 shows the resulting AES intensity-vs.-evaporation time plot for the various overlayer geometries. The AES intensities were normalized with respect to the bare substrate signal and the evaporation times normalized to give a 66% attenuation at the same time for all growth angles. This was done to compare with the analogous plot for TiO_x growth in Fig. 5.13(b). By comparison of the regions of initial decline in both plots, it is not possible to rule out the existence of three-dimensional growth of TiO_x for angles under, say, 45°. However, since a break does not occur at a substrate attenuation of 0.34 (remember $\alpha = 0.55$), the curves fall well below the trend for layer-by-layer growth displayed in Fig. 5.13(b). Consequently, the growth of titania on rhodium cannot be adequately described by three-dimensional growth.

The expected CO TPD area-versus-coverage plot for three-dimensional overlayer growth,

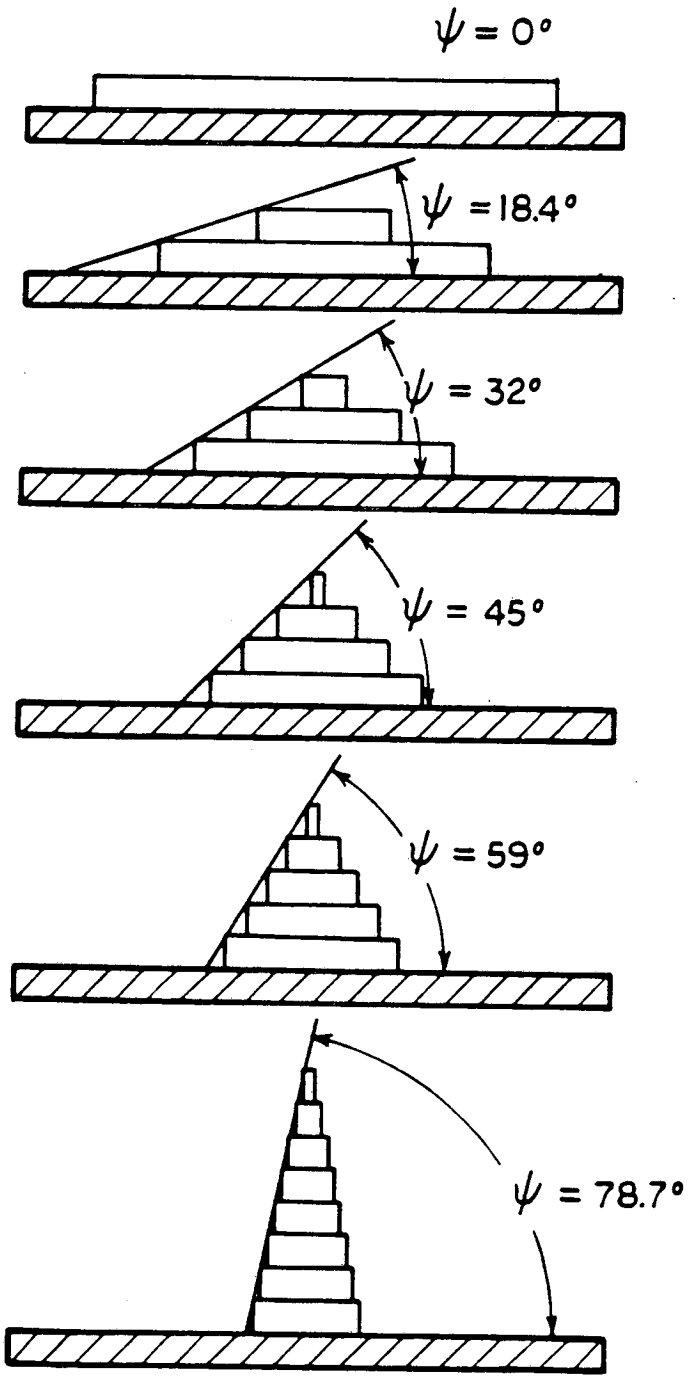

Figure A.1: Model geometries of overlayer growth. The extent of three-dimensional growth is characterized by the angle ψ between the surface and the incline of an overlayer "island".

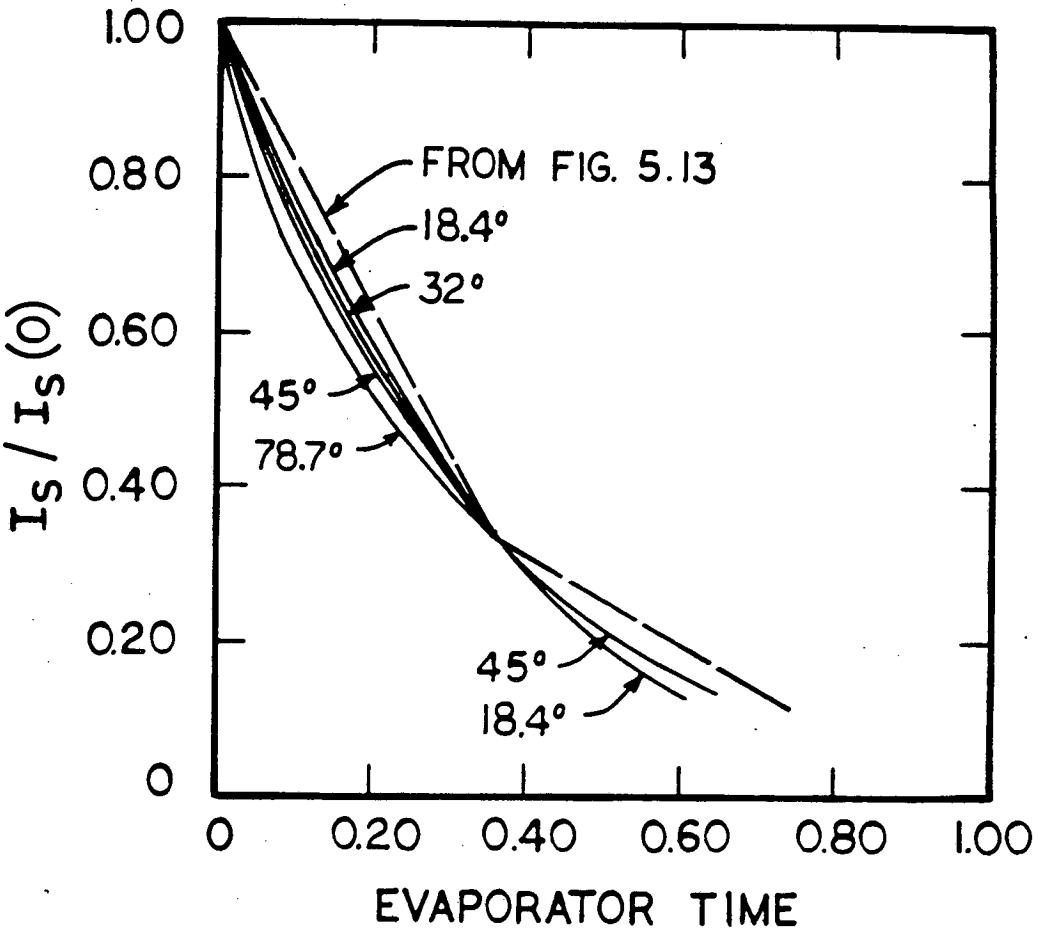

Figure A.2: A plot of the raw AES substrate intensity as a function of evaporation time. The curvature arising from three-dimensional growth is clearly visible for angles above 32°. The dosing times for an attenuation of 0.34 were set equivalent for comparison with Fig. 5-13(b).

assuming CO chemisorbs *at all exposed Rh sites*, appears in Fig. A.3. When three-dimensional growth occurs, the "apparent" coverage (measured by AES) does not accurately reflect the actual amount of surface Rh covered. As the "apparent" coverage increases, there is a nonlinear decrease in the CO chemisorption capacity. However, the amount of CO chemisorbed is always greater than that expected from the coverage. If coverage is determined from an attenuation of 66% at monolayer coverage, the CO TPD area-vs.-coverage plot of Fig. A.4 results. Three-dimensional growth can account for the behavior in Fig.

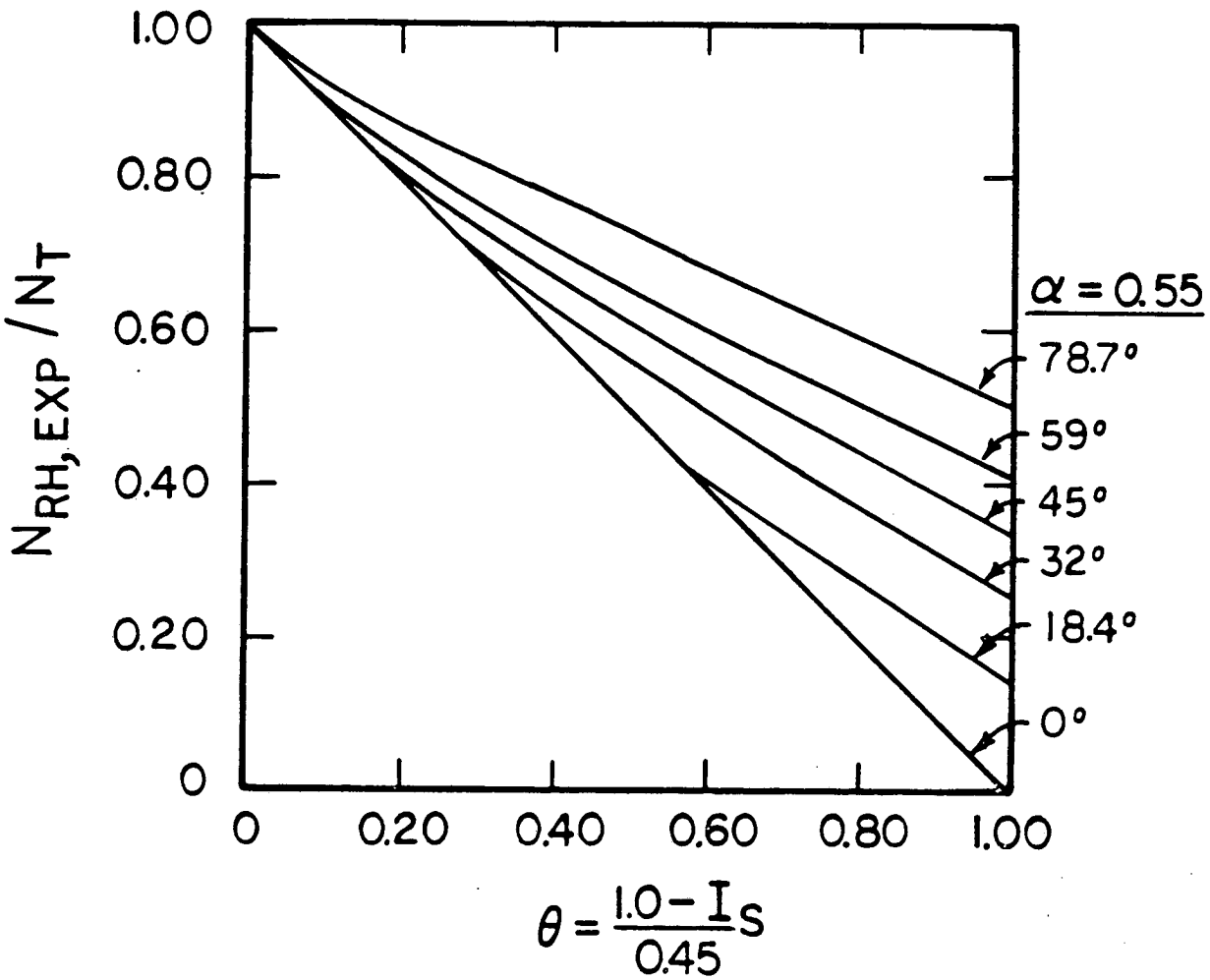

Figure A.3: The expected CO TPD peak area-vs.-coverage plots with three-dimensional overlayer growth and assuming CO chemisorbs at all exposed Rh atoms. $\alpha = 0.55$.

5.30 only if $\alpha = 0.77$ for monolayer coverage—an improbable value in light of the other overlayer studies in Table 2.1.

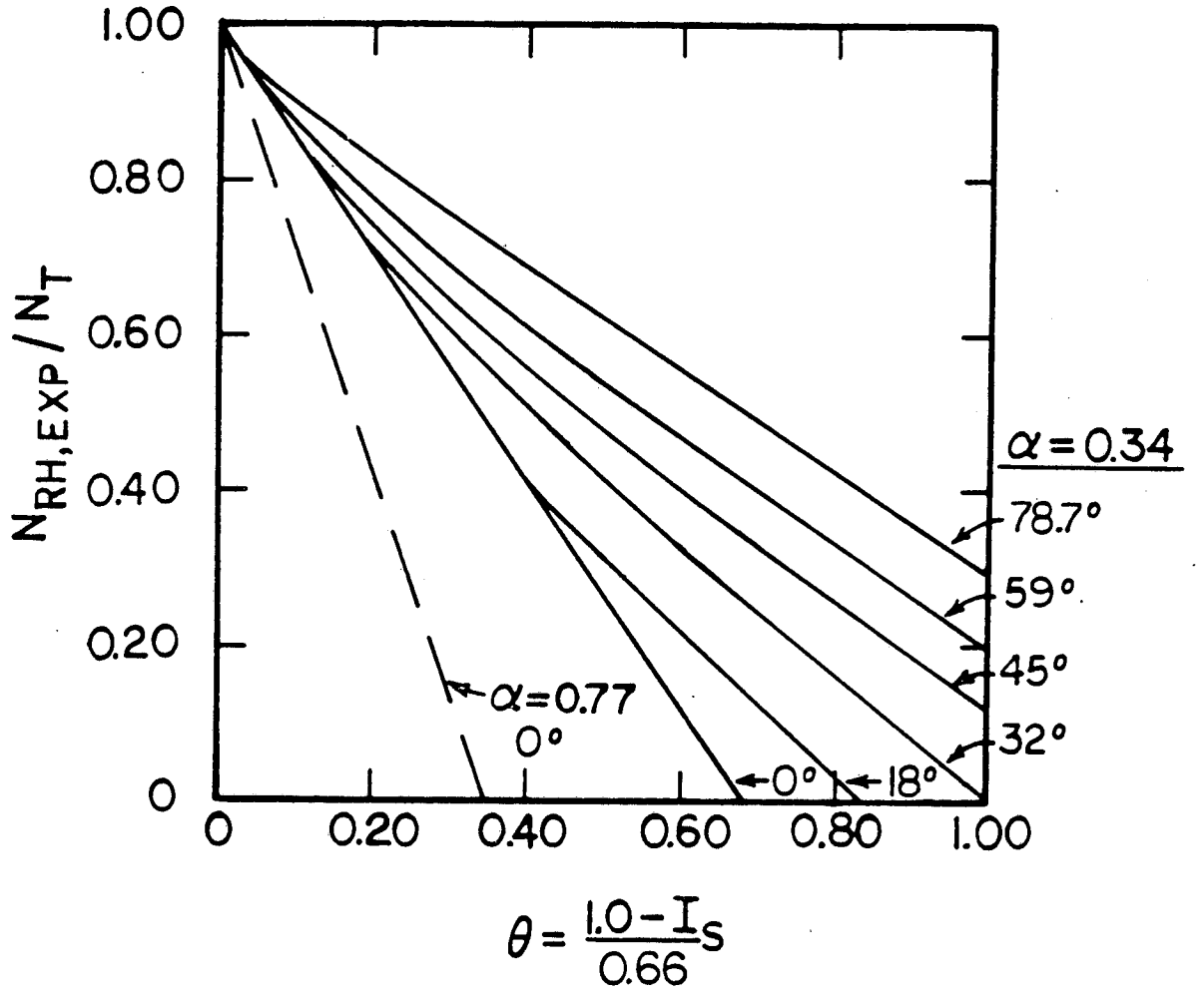

Figure A.4: The expected CO TPD peak area-vs.-coverage plots with three-dimensional overlayer growth and assuming CO chemsiorbs at all exposed Rh atoms. α taken as 0.34 with monolayer coverage actually at $\alpha = 0.55$—as a "worst case" evaluation of Fig. 5-30.

Appendix B

COMPUTER PROGRAMS

B.1 XPS DATA ACQUISITION AND ANALYSIS PROGRAM

The following program (written by Dr. Bruce Beard) was modified to allow fitting of XPS spectra with peaks of Doniach-Šunjić lineshape (see Chapter 2). This program has a total of six function: (1) data acquisition, (2) analysis of stored data (Gaussian fit), (3) analysis of stored data (Doniach-Šunjić fit), (4) printing out raw data, (5) checking the contents of a data file, and (6) forming a data file of raw/analyzed data for future transferral to a mainframe computer. This program calculates a quantity, "deviation from the fit," by a sum of the squares of the difference between fitted and raw curves. However, there appears to be a "bug" in this part of the routine.

If any changes are to be made to this program, please adjust the timing loop (statement 4510) accordingly to match the IBM PC data acquisition timing with that of the Tracor multi-channel analyzer. Otherwise, an incomplete spectrum will be transferred to the IBM PC.

```
10 ' program electron spectroscopy
20 DIM X(520), Y(520), F(8,520), P(6,4), LOW(6), AREA(6), B(300), HF(6)
25 DIM Al(6),GAMMA(6),XB(3),YB(3),XE(256)
30 DEF SEG=&HB100     'SET ADDRESS LOCATION OF THE LAV MASTER BOARD.
40 POKE 3,4           'SET OUTPUT OF D/A THAT CONTROLS MCA DATA DUMP TO ~5 V.
50 POKE 2,0
55 NP=512
60 CMIN=0
70 SURSCN=0
75 PI=3.14159
80 'This is the main routine from which the remainder
90 'of the program is routed. Functions of this program include
100 'data collection, display, and a variety of routines
110 'necessary for the fittng analysis of XPS spectra.
120 'N represents the # of peaks to be fitted to the spectrum.
122 'This program was written by Dr.Bruce C. Beard in 1984. Modifications
123 'have been made to include peak subtraction, survey scan plotting,
124 'and more stream-lined data entry for fitting.
125 'This program was modified in Aug. 1986 by Marc Levin to allow for
126 'Doniach-Sunjic fitting of XPS spectra.  This modification includes
127 'subroutines for computing the Gamma function and a parabolic baseline
128 'from three points.  Changes were also made in the display routine to
129 'make it more efficient.
130 CLS
140 SCREEN 0
150 LOCATE 5,27
160 PRINT "SIX ROUTES ARE AVAILABLE"
170 LOCATE  6,23:PRINT "1.  Data Acquisition, XPS or AES"
180 LOCATE  7,23:PRINT "2.  Analysis of Stored Data--Gaussian Fit"
190 LOCATE  8,23:PRINT "3.  Analysis of Stored Data--Doniach-Sunjic Fit"
200 LOCATE  9,23:PRINT "4.  Hard Copy of Raw Data"
210 LOCATE 10,23:PRINT "5.  Check Contents of a Data File"
215 LOCATE 11,23:PRINT "6.  Disk Copy of Smoothed Data"
220 LOCATE 12,23:PRINT "9.  To Stop Program"
250 LOCATE 14,18
260 PRINT "Enter number for the desired option"
270 LOCATE 16,30
280 INPUT "OPTION ?  ",IDEX
290 SURSCN=0
300 FLG=0
310 IF IDEX=1 THEN GOSUB 3540
320 IF IDEX=2 THEN GOSUB 420
330 IF IDEX=3 THEN GOSUB 7420
340 IF IDEX=4 THEN GOSUB 5100
350 IF IDEX=5 THEN GOSUB 5250
355 IF IDEX=6 THEN GOSUB 7000
360 IF IDEX=9 THEN STOP
380 INPUT "Any further options (Y OR N)?",YN$
385 IF YN$<>"N" AND YN$<>"Y" THEN 380
390 IF YN$="Y" THEN 130
400 STOP
410 '
420 'Subroutine data analysis
430 'This routine fits data to as many as six gaussian components,
440 'satellite peak removal, baseline addition, and smoothing
450 ' are all available from this conrtolling subroutine.
460 '
465 LOCATE 2,23:PRINT "ANALYSIS OF STORED DATA--GAUSSIAN FIT"
470 GOSUB 3920
480 GOSUB 1770
```

```
490 GOSUB 2390
491 '
492 IF SURSCN=0 GOTO 500
493 INPUT "Hard copy (Y OR N)?   ",YN$
494 IF YN$<>"N" AND YN$<>"Y" THEN 493
495 IF YN$="N" THEN 130
496 GOSUB 2390
497 GOSUB 4620
498 GOTO 130
499 '
500 INPUT "Shall any smoothing of the data be performed (Y OR N)?  ",YN$
505 IF YN$<>"N" AND YN$<>"Y" THEN 500
510 IF YN$="Y" THEN GOSUB 1910
520 INPUT "Shall satellite removal be performed (Y OR N)?  ",YN$
525 IF YN$<>"N" AND YN$<>"Y" THEN 520
530 IF YN$="Y" THEN GOSUB 1580
540 INPUT "How many components to this spectrum?  ",N
550 IF N>6 GOTO 570 ELSE GOTO 590
560 BEEP
570 PRINT N,"IS TOO LARGE A VALUE FOR THE NUMBER OF COMPONENTS, TRY AGAIN"
580 GOTO 540
590 Z=N+2
600 PRINT"Enter the parameters for each component, Amp, eV, FWHM,"
610 FOR L=1 TO N
620 PRINT "Parameters for component #",L
630 FOR J=1 TO 3
640 PRINT "Enter p("L,J")"
650 INPUT P(L,J)
660 NEXT J
670 NEXT L
680 INPUT "PARAMETERS ENTERED CORRECTLY (Y OR N)?   ",YN$
685 IF YN$<>"N" AND YN$<>"Y" THEN 680
690 IF YN$="N" THEN GOTO 600
700 '
710 'CALCULATES THE GAUSSIAN LINE SHAPE FOR EACH OF THE COMPONENTS AND'
720 'THE SUMMATION; ALSO THE BACKGROUND INTENSITY DROP AND THE BASE-
730 'LINE CONTRIBUTION FROM EACH COMPONENT.
740 '
750 INPUT "Enter beginning and ending background reference channels ",FRT1,BCK1
760 FRT=0: BCK=0: DEL=0
770 FOR K=1 TO 10
780 FRT=FRT+Y(FRT1+K)
790 BCK=BCK+Y(BCK1+K)
800 NEXT K
810 DEL=FRT/10-BCK/10
820 '
830 'TOTAL PEAK HEIGHTS
840 '
850 HGT=0
860 FOR K=1 TO N
870 HGT=HGT+P(K,1)
880 NEXT K
890 '
900 'CALCULATE THE BASELINE AND PEAKS
910 '
920 FOR K=1 TO N
930 HF(K)=P(K,1)/HGT
940 FOR J%=1 TO 256
950 DX=(X(J%)-P(K,2))/P(K,3)
960 F(K+1,J%)=P(K,1)*(1/EXP(DX*DX))
```

```
970 F(1,J%)=HF(K)*DEL/(1+EXP(-DX))
980 B(J%)=B(J%)+F(1,J%)
990 F(K+1,J%)=F(K+1,J%)+F(1,J%)
1000 F(Z,J%)=F(Z,J%)+F(K+1,J%)
1010 NEXT J%
1020 NEXT K
1030 '
1040 IF FLG=7 GOTO 1440
1050 IF FLG=5 THEN GOSUB 5880
1060 '
1070 'Section to allow for the correction of the parameters
1080 '
1090 GOSUB 2810
1100 LOCATE 24,1
1110 INPUT "Changes in the fit (Y OR N)?  ",YN$
1115 IF YN$<>"N" AND YN$<>"Y" THEN 1110
1120 IF YN$="Y" THEN GOTO 1130 ELSE 1270
1130 INPUT "Shall the number of components be changed (Y OR N)?  ",YN$
1135 IF YN$<>"N" AND YN$<>"Y" THEN 1130
1140 IF YN$="Y" GOTO 540
1150 INPUT "Change background?, (answer 0), or component # ?", L
1160 IF L=0 THEN GOTO 750
1170 IF L>N THEN BEEP ELSE GOTO 1200
1180 PRINT "Enter a number between 1 and  ",N
1190 GOTO 1150
1200 PRINT "Parameters for component # ",L
1210 FOR J=1 TO 3
1220 PRINT "Old P("L,J") value is:" ,P(L,J)
1230 INPUT "Enter new Value  ", CHECK
1240 IF CHECK=0 THEN GOTO 1250 ELSE P(L,J)=CHECK
1250 NEXT J
1260 GOTO 850
1270 '
1280 CLS
1290 LOCATE 5,25
1300 PRINT "THREE OPTIONS ARE AVAILABLE"
1310 LOCATE 8,25
1320 PRINT "1. PLOT FITTED SPECTRUM"
1330 LOCATE 10,25
1340 PRINT "2. SUBTRACT FITTED COMPONENTS"
1345 LOCATE 12,25: PRINT "3. EXIT ANALYSIS SECTION
1350 LOCATE 13,25
1360 BEEP
1370 INPUT " ENTER OPTION  ",IDEX
1380 IF IDEX=2 GOTO 5880
1385 IF IDEX=3 THEN RETURN
1387 IF IDEX<>1 GOTO 1370
1390 FLG=7
1400 GOTO 850
1410 '
1420 ' Calcuate area of each component.
1430 '
1440 FOR I=1 TO N
1450 AREA(I)=P(I,1)*P(I,3)*2.5066
1460 NEXT I
1470 '
1480 'Final display of fit with all the parameters, specimen description
1490 ' the area of each peak, and standard deviation of the fit.
1500 '
1510 LOCATE 17,15
```

```
1520 INPUT "** TURN ON THE PRINTER * STRIKE CARRIAGE RETURN **",YN$
1530 GOSUB 2810
1540 GOSUB 4650
1550 INPUT "PERFORM SUBTRACTION (Y OR N)? ",YN$
1555 IF YN$<>"N" AND YN$<>"Y" THEN 1550
1560 IF YN$="Y" THEN FLG=5:GOTO 850
1570 RETURN
1580 ' Subroutine Satpeak
1590 ' This routine removes the naturally occuring satellite peaks from the
1600 ' Mg Ka X-ray emission line used for XPS analysis.
1610 AU2=.085
1620 AU3=.045
1630 XINC=(X(1)-X(512))/256
1640 IAU2%=(8.45/XINC)
1650 IAU3%=(10.15/XINC)
1660 FOR J%=1 TO 256
1670 ID2=J%-IAU2%
1680 ID3=J%-IAU3%
1690 IF ID2<1 THEN ID2=1
1700 IF ID3<1 THEN ID3=1
1710 A3=Y(ID2)*AU2+Y(ID3)*AU3
1720 Y(J%)=Y(J%)-A3
1730 NEXT J%
1740 GOSUB 2390
1750 RETURN
1760 '
1770 'Subroutine loadx
1780 'This routine generates the x-array based on the number of channels
1790 'and the eV range.
1800 '
1810 XINC=(X(1)-X(512))/256
1820 IF X(1)>X(512) THEN GOTO 1870
1830 FOR I%=2 TO 256
1840 X(I%)=X(I%-1)+XINC
1850 NEXT I%
1860 GOTO 1900
1870 FOR I%=2 TO 256
1880 X(I%)=X(I%-1)-XINC
1890 NEXT I%
1900 RETURN
1905 '
1910 'Subroutine Smooth
1920 'This routine is a modified six point smoothing routine
1930 'where the operator is able to choose the degree of smoothing
1940 'by the use of a discriminator, the larger the disc value
1950 ' the smaller the change caused by the smoothing routine.
1960 INPUT "Enter the discriminator value   ",DISC
1970 GOSUB 2090
1980 SPRED=DISC*SQR(CMAX)
1990 FOR J%=4 TO 253
2000 AV=(Y(J%-3)+Y(J%-2)+Y(J%-1)+Y(J%+1)+Y(J%+2)+Y(J%+3))/6
2010 DIF=Y(J%)-AV
2020 ADIF=ABS(DIF)
2030 IF ADIF<SPRED THEN GOTO 2040 ELSE Y(J%)=AV
2040 NEXT J%
2050 GOSUB 2390
2060 INPUT "MORE SMOOTHING (Y OR N)? ",YN$
2065 IF YN$<>"N" AND YN$<>"Y" THEN 2060
2070 IF YN$="Y" THEN 1960
2080 RETURN
```

```
2085 '
2090 'Subroutine Maxmin
2100 'This routine determines the maximum and minimum values in the
2110 'data array
2120 CMAX=-50000!
2130 CMIN=90000!
2140 FOR J%=1 TO NP
2150 IF Y(J%)<CMIN THEN CMIN=Y(J%)
2160 IF Y(J%)>CMAX THEN CMAX=Y(J%)
2170 NEXT J%
2180 RETURN
2185 '
2190 'Subroutne normalize
2200 'this routine normalizes the data array to betwwen 0 and 1.
2210 CC=CMAX-CMIN
2220 FOR J%=1 TO NP
2230 Y(J%)=(Y(J%)-CMIN)/CC
2240 NEXT J%
2250 RETURN
2255 '
2260 'Subroutine SDFIT
2270 'This routne calculates the standard devaiton between the
2280 ' raw data and the fitted array, giving an indication of the
2290 ' goodness of the fitting paramters used.
2300 SUM=0
2310 FOR J%=1 TO 256
2320 F(Z,J%)=F(Z,J%)/CC
2330 SUM=SUM+(F(Z,J%)-Y(J%))^2
2340 F(Z,J%)=F(Z,J%)*CC
2350 NEXT J%
2360 SD=SQR(SUM/256)
2370 RETURN
2380 '
2390 'Subroutine Show
2400 ' This is a display routine which makes a simple plot of the data
2410 '
2420 SCREEN 2
2430 GOSUB 2090
2440 GOSUB 2190
2450 CLS
2460 LINE (99,15)-(611,15)
2470 LINE (611,15)-(611,175)
2480 LINE (611,175)-(99,175)
2490 LINE (99,175)-(99,15)
2500 '
2510 FOR I=1 TO 6
2520 LOCATE 7+I,6
2530 PRINT MID$ ("COUNTS",I,1)
2540 NEXT I
2550 '
2560 LOCATE 3,8
2570 PRINT CMAX
2580 LOCATE 22,8
2590 PRINT CMIN
2600 LOCATE 23,37
2602 IF X(1)<X(512) THEN GOTO 2614
2610 PRINT "BINDING ENERGY(eV)"
2612 GOTO 2620
2614 PRINT "KINETIC ENERGY(eV)"
2620 LOCATE 23,10
```

```
2630 PRINT X(1)
2640 LOCATE 23,74
2650 PRINT X(512)
2660 '
2670 IF SURSCN=1 THEN GOSUB 6230
2680 IF SURSCN=1 THEN GOTO 2790
2690 '
2700 I=0
2710 FOR J=1 TO NP
2720 COLMN=98+I
2730 I=I+(512/NP)
2740 Y(J)=Y(J)-1
2750 F(1,J)=(Y(J)*-160)+15
2755 'LPRINT J;COLMN;Y(J);F(1,J)
2760 PSET(COLMN,F(1,J))
2770 Y(J)=(Y(J)+1)*CC
2780 NEXT J
2790 RETURN
2800 '
2810 'Subroutine Shwal
2820 'Routine show-all plots the results of the data anaysis by displaying
2830 'the raw data, the fitted line, and each component in the fitted line.
2840 '
2850 '
2860 GOSUB 2090
2870 '
2880 CLS
2890 LINE (99,15)-(611,15)
2900 LINE (611,15)-(611,175)
2910 LINE (611,175)-(99,175)
2920 LINE (99,175)-(99,15)
2990 '
3000 FOR I=1 TO 10
3010 LOCATE 6+I,3
3020 PRINT MID$ ("NORMALIZED",I,1)
3030 NEXT I
3040 '
3050 FOR I=1 TO 6
3060 LOCATE 8+I,6
3070 PRINT MID$ ("COUNTS",I,1)
3080 NEXT I
3090 '
3100 LOCATE 2,8
3110 PRINT "1"
3140 '
3150 'normalize raw and fitted array,normalize components, and inert to 0 to -1
3160 '
3170 CC=CMAX-CMIN
3180 FOR J=1 TO 256
3190 Y(J)=(Y(J)-CMIN)/CC
3200 '
3205 FOR K=1 TO N+2
3210 F(K,J)=F(K,J)/CC
3215 NEXT K
3220 '
3230 ' plot raw data as a point plot ,raw data for plot in f(1,j)
3240 '
3250 PSET (97+2*J,160-Y(J)*160+15)
3260 'Y(J)=Y(J)*CC+CMIN
3270 NEXT J
```

```
3280 '
3290 'plot fitted data and individual components as lines
3300 '
3330 FOR J=1 TO 256
3335 PSET (97+2*J,160-Y(J)*160+15)
3336 Y(J)=Y(J)*CC+CMIN
3340 FOR K=1 TO N+2
3350 LINE (97+2*J,160-F(K,J)*160+15)-(99+2*J,160-F(K,J+1)*160+15)
3360 F(K,J)=F(K,J)*CC
3370 NEXT K
3380 NEXT J
3390 '
3420 LOCATE 22,8
3430 PRINT "0"
3435 LOCATE 23,10
3440 PRINT X(1)
3450 LOCATE 23,37
3455 IF X(1)<X(512) THEN GOTO 3466
3460 PRINT "BINDING ENERGY(eV)"
3464 GOTO 3470
3466 PRINT "KINETIC ENERGY(eV)"
3470 LOCATE 23,74
3480 PRINT X(512)
3520 RETURN
3530 '
3540 'Subroutine Data Acquisiton
3550 'Controls the input of data into the computer assuring
3560 'all of the pertinent details are present.
3570 INPUT "Enter the energy values X(1),X(512)",X(1),X(512)
3580 'date of analysis obtained from system
3590 V$=DATE$
3600 INPUT "Enter specimen description.",SPMN$
3610 PRINT "Enter the analysis conditions, transition, RC, Resolution,"
3620 INPUT "Vmult, Excitation Energy.",CON$
3630 INPUT "How many scans ?",SCANS$
3640 IF X(1)>X(512) THEN GOSUB 4290 ELSE GOSUB 5380
3650 '
3660 BEEP
3670 '
3680 'data collection completed
3690 '
3700 NP=512
3705 GOSUB 2390
3710 INPUT "Shall this data be stored (Y OR N)?",YN$
3715 IF YN$<>"N" AND YN$<>"Y" THEN 3710
3720 IF YN$="N" THEN 3740
3722 GOSUB 3760
3725 INPUT"HARD COPY OF STORED DATA (Y OR N)?",YN$
3730 IF YN$<>"N" AND YN$<>"Y" THEN 3725
3732 IF YN$="N" THEN RETURN
3734 GOSUB 3970
3736 GOSUB 2390
3738 GOSUB 4650
3740 RETURN
3750 '
3760 'Subroutine Store, This routine accepts the collected data and analysis
3770 ' discription and places them on the data disk for future reference.
3780 '
3790 INPUT "Enter the name under which this data shall be filed",NAM$
3800 OPEN NAM$ FOR OUTPUT AS #1
```

```
3810 PRINT #1, SPMN$
3820 PRINT #1, V$
3830 PRINT #1, SCANS$
3840 PRINT #1, CON$
3850 PRINT #1, X(1),X(512)
3860 FOR J=1 TO 512
3870 PRINT#1, Y(J)
3880 NEXT J
3890 CLOSE #1
3900 RETURN
3910 '
3920 'Subroutine Recall, This routine retreves the desired data file from
3930 'the data disk, loading all the information into the proper string
3940 'or array.
3950 LOCATE 16,13
3960 INPUT "What is the name of the desired data file?  ",NAM$
3970 OPEN NAM$ FOR INPUT AS #1
3980 INPUT #1, SPMN$
3990 INPUT #1, V$
4000 INPUT #1, SCANS$
4010 INPUT #1, CON$
4020 INPUT #1, X(1),X(512)
4030 FOR J%=1 TO 512
4040 INPUT #1, Y(J%)
4050 NEXT J%
4060 '
4070 BEDIF=X(1)-X(512)
4080 IF BEDIF<100 THEN GOTO 4140
4090 PRINT "Binding energy difference has been found to be > 100 eV"
4100 INPUT "Shall all 512 data points be displayed (Y OR N)? ",YN$
4105 IF YN$<>"N" AND YN$<>"Y" THEN 4100
4110 IF YN$="N" THEN 4140
4120 SURSCN=1
4130 GOTO 4200
4140 '
4150 ' Reduce the 512 data points to 256 for numeric evaluation
4160 '
4170 FOR K%=1 TO 256
4180 Y(K%)=(Y(2*K%-1)+Y(2*K%))/2
4190 NEXT K%
4200 'y(1) and y(2) are noisy channels, thus they
4210 'are set to the average of three points which follow.
4220 Y(1)=(Y(3)+Y(4)+Y(5))/3
4230 Y(2)=(Y(4)+Y(5)+Y(6))/3
4240 IF SURSCN=1 THEN GOTO 4260
4250 NP=256
4260 CLOSE #1
4270 RETURN
4280 '
4290  'Subroutine XPSAQ
4300 'This is a data retreal reutine taking data from the Tracor MCA
4310 'into the PC, correcting for the number of channels used in the
4320 'A/D conversion and the vertical scale factor of the MCA.
4330 '
4420 PRINT "********SET OUPUT RATE OF MCA TO 40 MS/CHAN*******"
4430 INPUT "Enter the vertical scale factor from the MCA",VSF
4440 DEF SEG=&HB100
4450 POKE 5,0                        'SELECT A/D CHANNEL
4460 POKE 3,0
4470 POKE 2,200                     'SET D/A #1 TO 0 VOLTS START DATA OUT
```

```
4480 FOR J=1 TO 512
4490 POKE 6,1                          'START CONVERSION
4500 Y(J)=256*PEEK (6) + PEEK (5)
4510 FOR Z=1 TO 60:NEXT Z 'MCA OUTPUT SPEED 40 MS/CHAN--READJUSTED FOR ESCA1
4520 NEXT J
4530 BEEP
4540 POKE 3,4                         'RESET D/A TO 5 V
4550 POKE 2,0
4560 '
4570 FOR I%=1 TO 512
4580 Y(I%)=Y(I%)*VSF/2048         'OUTPUT OF MCA ONLY 0-5, DA SET FOR 0-10
4590 NEXT I%
4600 '
4610 RETURN
4620 'Screen dump routine for the IBM PC to an HP Think-Jet printer
4630 'This routine was written by David Dahlgren,
4640 '
4650 DIM IMASK%(10)
4660 IMASK%(0)=1:IMASK%(1)=2:IMASK%(2)=4:IMASK%(3)=8:IMASK%(4)=16:IMASK%(5)=32
4670 IMASK%(6)=64:IMASK%(7)=128
4680 DEF SEG=&HB800
4690 OFST%=&H2000
4700 LPRINT               'CLEAR PRINTER
4710 LPRINT CHR$(27)+CHR$(64)
4720 WIDTH "LPT1:",255    'QUENCH CARRIAGE RETURNS
4730 LPRINT CHR$(27)+CHR$(65)+CHR$(8);        '16 DOT LINE FEED
4740 FOR         ROW%=0 TO 49
4750 IROW%=ROW%*160
4760 LPRINT CHR$(27)+CHR$(75)+CHR$(128)+CHR$(2);      'RECEIVE 640 BYTES
4770   FOR COL%=0 TO 79
4780    ICOL%=IROW%+COL%
4790    CH%=0                         'START WITH BLANK
4800    FOR BIT%=7 TO 0 STEP  -1
4810      MASK%=IMASK%(BIT%)
4820      IF (PEEK(ICOL%+80+OFST%) AND MASK%)>0 THEN CH%=CH% OR 3
4830      IF (PEEK(ICOL%+80) AND MASK%)>0       THEN CH%=CH% OR 12
4840      IF (PEEK(ICOL%+OFST%) AND MASK%)>0    THEN CH%=CH% OR 48
4850      IF (PEEK(ICOL%) AND MASK%)>0          THEN CH%=CH% OR 192
4860      LPRINT CHR$(CH%);:CH%=0
4870    NEXT
4880   NEXT
4890   LPRINT
4900 NEXT
4910 LPRINT CHR$(27)+CHR$(50)
4920 LOCATE 24,1
4930 LPRINT "Data file name:",NAM$
4940 LPRINT "Specimen",SPMN$
4950 LPRINT "Analysis Date:",V$
4960 LPRINT "Analysis Conditions",CON$
4970 LPRINT "Number of Scans:",SCANS$
4980 INPUT "Shall the fitting parameters & areas be printed (Y OR N)?",YN$
4985 IF YN$<>"N" AND YN$<>"Y" THEN 4980
4990 IF YN$="N" THEN 5070
5000 LPRINT
5010 LPRINT "PEAK #","COUNTS","POSITION (eV)","WIDTH (eV)","ASYMMETRY","AREA"
5020 FOR J=1 TO N
5030 LPRINT J,P(J,1),P(J,2),P(J,3),P(J,4),AREA(J)
5040 NEXT J
5045 LPRINT XB(1),YB(1),XB(2),YB(2),XB(3),YB(3)
5050 GOSUB 2260
```

```
5060 LPRINT "Deviation of the Fit",SD
5070 RETURN
5080 '
5090 '
5100 'Subroutine display files, Reads a data file from the disk, allows for
5110 'satellite removal and smoothing before the spectrum is sent to the
5120 'screen dump.
5130 GOSUB 3920
5140 GOSUB 2390
5150 INPUT "Shall satellite removal be performed (Y OR N)?",YN$
5155 IF YN$<>"N" AND YN$<>"Y" THEN 5150
5160 IF YN$="Y" THEN GOSUB 1580
5170 INPUT "Shall any smoothing be performed (Y OR N)?",YN$
5175 IF YN$<>"N" AND YN$<>"Y" THEN 5170
5180 IF YN$="Y" THEN GOSUB 1910
5190 INPUT "TURN ON PRINTER!!! STRIKE RETURN WHEN READY",YN$
5200 GOSUB 2390
5210 GOSUB 4650
5220 RETURN
5230 '
5240 '
5250 'Subroutine file check. Reads data files, lists specimen description
5260 'and analysis date.
5270 GOSUB 3920
5280 GOSUB 2390
5290 PRINT SPMN$
5300 PRINT "Analysis Date:",V$
5310 INPUT "Shall data analysis be performed (Y OR N)?",YN$
5315 IF YN$<>"N" AND YN$<>"Y" THEN 5310
5320 IF YN$="Y" THEN 490 ELSE GOTO 5340
5330 RETURN
5340 INPUT "Is a hard copy of the raw data desired (Y OR N)?",YN$
5345 IF YN$<>"N" AND YN$<>"Y" THEN 5340
5350 IF YN$="Y" THEN GOSUB 2390 ELSE 5370
5360 GOSUB 4620
5370 RETURN
5380 'SUBROUTINE AUGERAQ
5390 'Acquires Auger data, controls output of diriving voltage
5400 'converts analog data to digital values, sums and averages
5410 'signal over the desired number of scans.
5420 '
5430 DEF SEG=&HB100
5440 '
5450 POKE 5,1            'SET A/D CONVERSION CHANNEL
5460 H=0
5470 '
5480 INPUT "How many scans to be collected?",S
5490 '
5500 FOR I%=1 TO S
5510 '
5520 FOR J=8 TO 15
5530 POKE 1,J
5540 FOR K=0 TO 255 STEP 8       'VOLTAGE STEPS 0V TO 5V
5550 POKE 0,K
5560 FOR L=1 TO 20: NEXT L       'DEAD LOOP TO ALLOW VOLTAGES TO STABALIZE
5570 H=H+1
5580 POKE 6,1                    'START A/D CONVERSION
5590 Y(H)=Y(H) + (256 * PEEK(6) + PEEK(5))     'CONVERT AND SUM
5600 NEXT K
5610 NEXT J
```

```
5620 FOR J=0 TO 7                    'VOLTAGE STEPS 5V TO 10V
5630 FOR K=0 TO 255 STEP 8
5640 POKE 1,J
5650 POKE 0,K
5660 FOR L=1 TO 20: NEXT L           'DEAD LOOP TO ALLOW VOLTAGES TO STABALIZE
5670 H=H+1
5680 POKE 6,1                        'START A/D CONVERSION
5690 Y(H)=Y(H)+(256*PEEK(6)+PEEK(5))
5700 NEXT K
5710 NEXT J
5720 '
5730 POKE 1,8       'RESET D/A TO 0 VOLTS AHEAD OF TIME TO ALLOW THE OUTPUT
5740 POKE 0,0       'AT THE BEGINNING OF THE NEXT SCAN TO BE 0 VOLTS
5750 '
5760 H=0
5770 '
5780 NEXT I%
5790 '
5800 FOR J%=1 TO 512
5810 Y(J%)=Y(J%)/S           'AVERAGE RESULTS OVER THE NUMBER OF SCANS
5820 NEXT J%
5830 '
5840 BEEP
5850 RETURN
5860 '
5870 '
5880 '                       SUBROUTINE SUBTRACTION
5890 ' THIS ROUTINE TAKES THE FITTED COMPONENTS THAT ARE TO THE OPERATORS
5900 ' LIKING AND REMOVES THEM FROM THE RAW DATA FILE TO LEAVE A DIFFERENCE
5910 ' SPECTRUM. FURTHER FITTING AND OUTPUT OPTION FOLLOW THIS ROUTINE SUCH
5920 ' THAT COMPARISONS MAY BE MADE FROM BEFORE AND AFTER SUBTRACTIONS.
5930 '
5960 '
5970 FOR I%=1 TO 256
5980 Y(I%)=Y(I%)-F(Z,I%)
5990 NEXT I%
6000 '
6010 FLG=0
6020 '
6030 GOSUB 2390
6040 INPUT "ANY SMOOTHING (Y OR N)? ",YN$
6045 IF YN$<>"N" AND YN$<>"Y" THEN 6040
6050 IF YN$="Y" THEN GOSUB 1910
6060 LOCATE 24,1
6070 INPUT "HARD COPY (Y OR N)?",YN$
6075 IF YN$<>"N" AND YN$<>"Y" THEN 6070
6080 IF YN$="N" THEN GOTO 6110
6090 GOSUB 2390
6100 GOSUB 4650
6110 '
6120 FOR K=1 TO Z
6130 FOR I%=1 TO 256
6140 F(K,I%)=0
6150 NEXT I%
6160 NEXT K
6170 '
6180 FOR I%=1 TO 256
6190 B(I%)=0
6200 NEXT I%
6210 RETURN
```

```
6220 '
6230 'SUBROUTINE SURVEY SCAN PLOT
6240 'This is a short routine to just plot out the data array for a
6250 ' survey scan. All 512 data points are displayed.
6260 '
6270 FOR J=1 TO 512
6280 COLMN=98+J
6290 Y(J)=Y(J)-1
6300 F(1,J)=(Y(J)*-160)+15
6310 PSET(COLMN,F(1,J))
6320 Y(J)=(Y(J)+1)*CC
6330 NEXT J
6340 RETURN
7000 'Subroutine DiskStore.  This routine reads a datafile, allow removal
7002 'of satellites, allow for smoothing, and then saves the data on disk
7004 'for eventual transferral to the VAX system.
7010 GOSUB 3920
7015 GOSUB 2390
7020 INPUT "Is satellite removal to be performed (Y OR N)?", YN$
7025 IF YN$<>"N" AND YN$<>"Y" THEN 7020
7030 IF YN$="Y" THEN GOSUB 1580
7035 INPUT "Is any smoothing to be performed (Y OR N)?", YN$
7040 IF YN$<>"N" AND YN$<>"Y" THEN 7035
7045 IF YN$="Y" THEN GOSUB 1910
7050 INPUT "Enter the name under which this data is to be filed", NAM$
7055 OPEN NAM$ FOR OUTPUT AS #1
7060 PRINT #1, SPMN$
7065 PRINT #1, V$
7070 PRINT #1, SCANS$
7075 PRINT #1, CON$
7080 PRINT #1, X(1),X(512)
7085 FOR J=1 TO 256
7090 XE(J)=X(1) - (X(1)-X(512))/256*(J-1)
7092 PRINT #1, XE(J),Y(J)
7094 NEXT J
7098 INPUT "Is a disk copy of the deconvoluted spectra desired?", YN$
7099 IF YN$<>"N" AND YN$<>"Y" THEN 7098
7100 IF YN$="N" THEN 7394
7105 CLS
7110 LOCATE 2,19:PRINT "ANALYSIS OF STORED DATA (DONIACH-SUNJIC FIT)"
7120 GOSUB 1770
7125 GOSUB 2390
7130 '
7135 IF SURSCN=0 GOTO 7160
7140 GOSUB 2390
7145 GOSUB 4620
7150 GOTO 130
7155 '
7160 INPUT "How many components to this spectrum?  ",N
7165 IF N>6 GOTO 7175 ELSE GOTO 7195
7170 BEEP
7175 PRINT N,"IS TOO LARGE A VALUE FOR THE NUMBER OF COMPONENTS, TRY AGAIN"
7180 GOTO 7160
7195 Z=N+2
7200 PRINT"Enter the parameters for each component, Amp, eV, FWHM,ASYM"
7205 FOR L=1 TO N
7210 PRINT "Parameters for component #",L
7215 FOR J=1 TO 4
7220 PRINT "Enter p("L,J")"
7225 INPUT P(L,J)
```

```
7230 NEXT J
7235 NEXT L
7240 INPUT "PARAMETERS ENTERED CORRECTLY (Y OR N)?   ",YN$
7245 IF YN$<>"N" AND YN$<>"Y" THEN 7240
7250 IF YN$="N" THEN GOTO 7200
7255 '
7260 'THE SUMMATION; ALSO THE BACKGROUND INTENSITY DROP AND THE BASE-
7265 'LINE CONTRIBUTION FROM EACH COMPONENT.
7270 '
7275 GOSUB 2390
7280 INPUT "ENTER 1ST BASELINE REFERENCE POINT (CHANNEL,HEIGHT) ",XB(1),YB(1)
7285 INPUT "ENTER 2ND BASELINE REFERENCE POINT (CHANNEL,HEIGHT) ",XB(2),YB(2)
7290 INPUT "ENTER 3RD BASELINE REFERENCE POINT (CHANNEL,HEIGHT) ",XB(3),YB(3)
7295 GOSUB 9200
7300 '
7305 '
7310 '
7320 'CALCULATE THE BASELINE AND PEAKS
7325 FOR J%=1 TO 256
7330 F(Z,J%) = F(1,J%)
7335 NEXT J%
7340 '
7345 FOR K=1 TO N
7347 PRINT #1, "K = ", K
7350 A1(K)=1-P(K,4)
7355 GOSUB 9000
7360 FOR J%=1 TO 256
7362 M1=COS(PI*P(K,4)/2 + A1(K)*ATN((P(K,2)-X(J%))/P(K,3)))
7364 M2=((X(J%)-P(K,2))^2 + P(K,3)^2)^(A1(K)/2)
7366 F(K+1,J%)=P(K,1)*GAMMA(K)*M1/M2
7368 B(J%)=B(J%)+F(1,J%)
7370 F(Z,J%)=F(Z,J%)+F(K+1,J%)
7371 PRINT #1, X(J%),F(K+1,J%)
7372 NEXT J%
7374 NEXT K
7378 PRINT #1, "TOTAL"
7380 FOR J% =1 TO 256
7385 PRINT #1, X(J%),F(Z,J%)
7390 NEXT J%
7394 CLOSE #1
7395 RETURN
7410 '
7420 'Subroutine data analysis
7430 'This routine fits data to as many as six Doniach-Sunjic components,
7440 'satellite peak removal, baseline addition, and smoothing
7450 ' are all available from this conrtolling subroutine.
7460 '
7462 CLS
7465 LOCATE 2,19:PRINT "ANALYSIS OF STORED DATA (DONIACH-SUNJIC FIT)"
7470 GOSUB 3920
7480 GOSUB 1770
7490 GOSUB 2390
7491 '
7492 IF SURSCN=0 GOTO 7500
7493 INPUT "Hard copy (Y OR N)?   ",YN$
7494 IF YN$<>"N" AND YN$<>"Y" THEN 7493
7495 IF YN$="N" THEN 130
7496 GOSUB 2390
7497 GOSUB 4620
7498 GOTO 130
```

```
7499 '
7500 INPUT "Shall any smoothing of the data be performed (Y OR N)?  ",YN$
7505 IF YN$<>"N" AND YN$<>"Y" THEN 7500
7510 IF YN$="Y" THEN GOSUB 1910
7520 INPUT "Shall satellite removal be performed (Y OR N)?  ",YN$
7525 IF YN$<>"N" AND YN$<>"Y" THEN 7520
7530 IF YN$="Y" THEN GOSUB 1580
7540 INPUT "How many components to this spectrum?  ",N
7550 IF N>6 GOTO 7570 ELSE GOTO 7175
7560 BEEP
7570 PRINT N,"IS TOO LARGE A VALUE FOR THE NUMBER OF COMPONENTS, TRY AGAIN"
7580 GOTO 7540
7590 Z=N+2
7600 PRINT"Enter the parameters for each component, Amp, eV, FWHM,ASYM"
7610 FOR L=1 TO N
7620 PRINT "Parameters for component #",L
7630 FOR J=1 TO 4
7640 PRINT "Enter p("L,J")"
7650 INPUT P(L,J)
7660 NEXT J
7670 NEXT L
7680 INPUT "PARAMETERS ENTERED CORRECTLY (Y OR N)?   ",YN$
7685 IF YN$<>"N" AND YN$<>"Y" THEN 7680
7690 IF YN$="N" THEN GOTO 7600
7700 '
7720 'THE SUMMATION; ALSO THE BACKGROUND INTENSITY DROP AND THE BASE-
7730 'LINE CONTRIBUTION FROM EACH COMPONENT.
7735 '
7740 GOSUB 2390
7741 INPUT "ENTER 1ST BASELINE REFERENCE POINT (CHANNEL,HEIGHT) ",XB(1),YB(1)
7742 INPUT "ENTER 2ND BASELINE REFERENCE POINT (CHANNEL,HEIGHT) ",XB(2),YB(2)
7743 INPUT "ENTER 3RD BASELINE REFERENCE POINT (CHANNEL,HEIGHT) ",XB(3),YB(3)
7795 GOSUB 9200
7800 '
7820 '
7850 '
7900 'CALCULATE THE BASELINE AND PEAKS
7905 FOR J%=1 TO 256
7907 F(Z,J%) = F(1,J%)
7909 NEXT J%
7910 '
7920 FOR K=1 TO N
7925 A1(K)=1-P(K,4)
7930 GOSUB 9000
7940 FOR J%=1 TO 256
7955 M1=COS(PI*P(K,4)/2 + A1(K)*ATN((P(K,2)-X(J%))/P(K,3)))
7960 M2=((X(J%)-P(K,2))^2 + P(K,3)^2)^(A1(K)/2)
7970 F(K+1,J%)=P(K,1)*GAMMA(K)*M1/M2
7980 B(J%)=B(J%)+F(1,J%)
8000 F(Z,J%)=F(Z,J%)+F(K+1,J%)
8010 NEXT J%
8020 NEXT K
8030 '
8050 IF FLAG=5 THEN GOSUB 5880
8060 '
8065 'Section to allow for the correction of the parameters
8070 '
8075 GOSUB 2810
8080 LOCATE 24,1
8085 INPUT "Changes in the fit (Y OR N)?  ",YN$
```

```
8090 IF YN$<>"N" AND YN$<>"Y" THEN 8085
8095 IF YN$="N" THEN 8270
8100 INPUT "Shall the number of components be changed (Y OR N)?  ",YN$
8105 IF YN$<>"N" AND YN$<>"Y" THEN 8100
8110 IF YN$="Y" THEN 7540
8115 INPUT "Change background?, (answer 0), or component # ?", L
8120 IF L<>0 THEN 8145
8125 FOR J=1 TO 3
8127 PRINT"BASELINE REFERENCE POINT NUMBER";J;":",XB(J),YB(J)
8129 INPUT"ENTER NEW CHANNEL";XT
8130 IF XT=0 THEN 8133
8131 INPUT"ENTER NEW HEIGHT";YT
8132 XB(J)=XT:YB(J)=YT
8133 NEXT J
8134 FOR J=1 TO 256
8135 F(Z,J)=F(Z,J)-F(1,J)
8136 NEXT J
8137 GOSUB 9200
8139 GOTO 8200
8140 IF YN$="Y" THEN 7540
8145 IF L>N THEN BEEP ELSE GOTO 8160
8150 PRINT "Enter a number between 1 and  ",N
8155 GOTO 8115
8160 PRINT "Parameters for component # ",L
8165 FOR J=1 TO 4
8170 PRINT "Old P("L,J") value is:" ,P(L,J)
8175 INPUT "Enter new Value  ", CHECK
8180 IF CHECK=0 THEN GOTO 8185 ELSE P(L,J)=CHECK
8185 NEXT J
8200 FOR J=1 TO 256
8205 IF L=0 THEN 8245
8210 F(Z,J)=F(Z,J)-F(L+1,J)
8215 A1(L)=1-P(L,4):K=L
8220 GOSUB 9000
8225 M1=COS(PI*P(L,4)/2 + A1(L)*ATN((P(L,2)-X(J))/P(L,3)))
8230 M2=((X(J)-P(L,2))^2 + P(L,3)^2)^(A1(L)/2)
8235 F(L+1,J)=P(L,1)*GAMMA(L)*M1/M2
8240 B(J)=B(J)+F(1,J)
8245 F(Z,J)=F(Z,J)+F(L+1,J)
8250 NEXT J
8260 GOTO 8050
8270 '
8280 CLS
8290 LOCATE 5,25
8300 PRINT "FOUR OPTIONS ARE AVAILABLE"
8310 LOCATE 8,25
8320 PRINT "1. PLOT FITTED SPECTRUM"
8330 LOCATE 10,25
8340 PRINT "2. SUBTRACT FITTED COMPONENTS"
8345 LOCATE 12,25: PRINT "3. CONTINUE SPECTRUM FITTING
8350 LOCATE 14,25: PRINT "4. EXIT ANALYSIS SECTION
8360 LOCATE 16,25:BEEP
8370 INPUT " ENTER OPTION  ",IDEX
8380 IF IDEX=2 GOTO 5880
8385 IF IDEX=3 THEN GOTO 8065
8390 IF IDEX=4 THEN RETURN
8395 IF IDEX<>1 GOTO 8370
8400 '
8410 '
8420 ' Calcuate area of each component (Simpson's Rule Integration)
```

```
8425 '
8430 FOR K=1 TO N
8435 AREA(K)=0
8440 FOR J%=2 TO 256
8445 IF J%=2 OR J%=256 THEN AREA(K)=AREA(K)+F(K+1,J%):GOTO 8460
8450 IF J%/2*2=J% THEN AREA(K)=AREA(K)+2*F(K+1,J%):GOTO 8460
8455 AREA(K)=AREA(K)+4*F(K+1,J%)
8460 NEXT J%
8462 AREA(K)=AREA(K)/3
8465 NEXT K
8470 '
8480 'Final display of fit with all the parameters, specimen description
8490 ' the area of each peak, and standard deviation of the fit.
8500 '
8510 LOCATE 17,15
8520 INPUT "** TURN ON THE PRINTER * STRIKE CARRIAGE RETURN **",YN$
8530 GOSUB 2810
8540 GOSUB 4650
8550 INPUT "PERFORM SUBTRACTION (Y OR N)? ",YN$
8555 IF YN$<>"N" AND YN$<>"Y" THEN 8550
8560 IF YN$="Y" THEN FLG=5:GOTO 7850
8570 RETURN
9000 'SUBROUTINE GAMMA
9010 'THIS SUBROUTINE CALCULATES THE GAMMA FUNCTION FOR 1-ALPHA BY A
9020 'POLYNOMIAL APPROXIMATION (FROM HANDBOOK OF MATHEMATICAL FUNCTIONS
9030 'BY ABRAMOWITZ AND STEGUN).  THE VALUE OF X SHOULD BE BETWEEN 0 AND
9040 '1 FOR THIS APPROXIMATION, OR  0<ALPHA<1.
9050 GAMMA(K)=1 - .577192*A1(K) + .988206*A1(K)^2 - .897057*A1(K)^3
9060 GAMMA(K)=GAMMA(K)+.918207*A1(K)^4 - .756704*A1(K)^5 + .482199*A1(K)^6
9070 GAMMA(K)=GAMMA(K)-.193528*A1(K)^7 + .035868*A1(K)^8
9080 GAMMA(K)=GAMMA(K)/A1(K)
9090 RETURN
9200 'SUBROUTINE BASELINE
9210 'THIS SUBROUTINE GENERATES THE PARABOLIC BASELINE FROM THE THREE
9220 'POINTS ENTERED IN THE D-S ANALYSIS SECTION
9230 M3=(XB(3)-XB(1))*(XB(2)-XB(1))
9240 M4=(XB(2)-XB(1))*(XB(3)-XB(2))
9250 M5=(XB(3)-XB(1))*(XB(3)-XB(2))
9260 AA=(XB(3)*XB(2)*YB(1)/M3)-(XB(3)*XB(1)*YB(2)/M4)+(XB(2)*XB(1)*YB(3)/M5)
9270 BB=-(XB(3)+XB(2))*YB(1)/M3 + (XB(3)+XB(1))*YB(2)/M4-(XB(1)+XB(2))*YB(3)/M5
9280 CC=YB(1)/M3 - YB(2)/M4 + YB(3)/M5
9290 FOR J% = 1 TO 256
9300 F(1,J%)=AA + BB*J% + CC*J%^2
9310 NEXT J%
9320 RETURN
```

B.2 MONTE CARLO SIMULATION PROGRAM

This program was written to simulate TiO_x island growth on a (111) or (100) surface. It was written for a Commodore 8032 personal computer equipped with visual memory. The program is composed of several steps:

(1) Displaying an N x N grid

(2) Randomly choosing nucleation sites (at a user-specified density)

(3) Randomly growing islands around these sites to coverages at 0.05 ML intervals

(4) Counting of sites (of a particular type)

Several programs of this form were written so as to count each type of site (*e.g.*, peripheral, adjacent-to-peripheral). Typically 100 x 100 "hexagonal" (~(111) surface) grids were employed with a nucleation site density of 4.5×10^{13} cm^{-2}. Due to the extraordinary amount of time required to execute this program, a column of dots to the right of the grid will appear to indicate the current row at which counting is occurring and to reassure the user that the program is indeed running.

```
1 DIM X(500),Y(500),RF(50),RR(50),RN(50)
2 PRINT"":CLEAR:F=0
3 PRINT"                    NEAR-PERIPHERY SITE COUNTING (W/ PLOT)":PRINT"":PRINT""
4 PRINT"CONTINUOUS MODE (Y OR N)":INPUT F1$:IF F1$="Y" THEN F=1
5 PRINT"NEAR-PERIPHERAL CALCULATION (Y OR N)?":INPUT F2$
6 IF F2$="Y" THEN F2=1
7 PRINT"ENTER LATTICE TYPE (S=SQUARE OR H=HEXAGONAL)"
8 INPUT LA$:IF LA$="S" OR LA$="H" GOTO 10
9 GOTO 7
10 PRINT"ENTER GRID SIZE (X,Y)":INPUT NX,NY
12 PRINT"ENTER NUCLEATION SITE DENSITY":INPUT N
15 PRINT"ENTER INITIAL TIO2 COVERAGE":INPUT THETA
17 IF F=1 THEN PRINT"ENTER FINAL TIO2 COVERAGE":INPUT TF
18 PRINT"ENTER RANDOM NUMBER SEED":INPUT SE:U1=RND(SE)
20 U%=NX:NX=U%:U%=NY:NY=U%:PRINT""
25 CLEAR:POKE49151,3:DOTL1,1
30 FOR J=1 TO NY
35 LINE 102,2*J,2*NX+100,2*J
40 NEXT
60 N%=N*1.6E15*(NX*NY)
70 MOVE 100,190:AUTEXT "SEEDING: N=":AUTEXT STR$(N%)
75 AUTEXT "(";STR$(N);" SITES/CM2)"
80 FOR I=1 TO N%
90 U1=RND(1):V1=RND(1)
100 U%=NX*U1:V%=NY*V1:I1=2*U%+102:J1=2*V%+2
110 MOVE I1,J1:RDPIX VAR:IF VAR=2 THEN I=I-1:GOTO 120
115 WRPI:X(I)=I1:Y(I)=J1
117 N1=N1+1
120 NEXT I
121 IF N1 <N% THEN PRINT"SEED MISMATCH":STOP
124 DOTL1,0
125 N1=N%
126 COV=N1/(NX*NY)
135 MOVE 100,150:AUTEXT "ISLAND GROWTH:"
125 MOVE 110,170:AUTEXT"COVERAGE="
130 MOVE 150,170:AUTEXT STR$(C)
131 C=COV:POKE 16,170:AUTEXT STR$(COV)
132 IF C<=(N)*N)/2 THEN 170
135 U1=RND(1):V1=RND(1)
140 U%=NX*U1:V%=NY*V1:U%=2*U%+102:V%=2*V%+2
145 MOVE U%,V%:RDPIX VAR:IF VAR=2 GOTO 135
147 FOR I=1 TO 3
148 FOR J=1 TO 3
149 I1=U%+2*(I-2):J1=V%+2*(J-2)
150 IF I1>102 THEN I1=I1+2*NX
151 IF I1>2*NX+100 THEN I1=I1-2*NX
152 IF J1>2 THEN J1=J1+2*NY
153 IF J1>2*NY THEN J1=J1-2*NY
154 MOVE I1,J1:RDPIX VAR
155 IF VAR=2 THEN N1=N1+1:MOVE U%,V%:WRPIX:COV=N1/(NX*NY):GOTO 130
156 NEXT J
157 NEXT I
160 GOTO 135
170 MOVE 100,150:AUTEXT"PERIPHERAL COUNTING:"
180 R0=0:R1=0:R2=0
190 SUM=0
200 FOR J=1 TO N:J1=2*J
210 FOR I=1 TO N:I1=2*I+100
220 MOVE I1,J1:RDPIX VAR:IF VAR=2 GOTO 250
230 SUM=0
231 FOR I1=1 TO 3:I2=J1+2*(I1-2)
232 FOR I1=1 TO 3:I2=I1+2*(I1-2)
233 IF LA$="H" AND I1-I1=0 GOTO 235
234 IF L2>102 THEN L2=L2+2*NX
235 IF L2>2*NX+100 THEN L2=L2-2*NX
236 IF L2<2 THEN L2=L2+2*NY
237 IF L2>2*NY THEN L2=L2-2*NY
240 MOVE I1,L2:RDPIX VAR:SUM=SUM+VAR
245 NEXT I1
246 NEXT I1
247 IF SUM=0 AND LA$="H" THEN R1=R1+1:GOTO 250
248 IF SUM=8 AND LA$="S" THEN R1=R1+1:GOTO 250
249 R0=R0+1:IF F2=1 THEN GOSUB 400
250 NEXT I
251 MOVE 28,J1:WRPIX
255 NEXT J
270 RC=R1/(N)*N1)
271 RCOV=R0/(N)*N1)
280 I=I+1:RF(I)=RC:RR(I)=RC/(NX*NY)
281 MOVE 110,130:AUTEXT"UNAFFECTED AREA=":
282 MOVE 205,130:AUTEXT STR$(RCOV)
283 MOVE 110,140:AUTEXT"PERIPHERAL AREA=":
284 MOVE 205,140:AUTEXT STR$(RCOV)
300 IF F=1 THEN PRINT THETA,RR(I):PRINT RF(I),RN(I)
301 IF F=0 THEN PRINT THETA,RR(I):PRINT RF(I)
303 IF F=1 GOTO 315
305 THETA=THETA+0.05:IF TF<THETA THEN GOSUB 500:STOP
310 GOTO 350
315 PRINT"SIMULATION COMPLETED"
320 PRINT"NEW COVERAGE? (Y OR N)"
325 INPUT A$
330 IF A$="N" THEN STOP
340 PRINT"ENTER NEW COVERAGE"
345 INPUT THETA
350 PRINT""
```

```
MOVE 110,150:AUTEXT"UNAFFECTED AREA=":
MOVE 205,150:AUTEXT STR$(PCOV)
MOVE 110,140:AUTEXT"PERIPHERAL AREA=":
MOVE 205,140:AUTEXT STR$(PCOV)
MOVE 100,160:AUTEXT"PERIPHERAL COUNTING:"
GOTO 130
FOR L1=1 TO 5:L2=J1+2*(L1-3)
FOR R1=1 TO 5:R2=J1+2*(R1-3)
IF ABS(L1-3)=2 AND ABS(R1-3)=2 GOTO 430
IF I$="5" GOTO 425
IF L1+L1=4 OR L1+L1=8 GOTO 430
IF R2<102 THEN R2=R2+2*NX
IF R2>2*NX+100 THEN R2=R2-2*NX
IF L2<2 THEN L2=L2+2*NY
IF L2>2*NY THEN L2=L2-2*NY
MOVE R2,L2:EPEEK VAR:IF VAR=2 THEN R2=R2+1:RETURN
NEXT R1
NEXT L1
RETURN
CLEAR
DRAW 1,0:LINE 102,30,202,30
THETA=0
LINE 102,30,102,130
MOVE 115,20:AUTEXT"0.2":MOVE 135,20:AUTEXT"0.4"
MOVE 155,20:AUTEXT"0.6":MOVE 175,20:AUTEXT"0.8"
MOVE 195,20:AUTEXT"1.0":MOVE 130,10:AUTEXT"TIOX COVERAGE"
MOVE 72,40:AUTEXT"0.2":MOVE 72,60:AUTEXT"0.4"
MOVE 72,80:AUTEXT"0.6":MOVE 72,100:AUTEXT"0.8"
MOVE 72,120:AUTEXT"1.0"
FOR I = 1 TO 11
THETA=THETA+0.05
PRINT"COVERAGE=",THETA
PRINT"ENTER RH*/**":INPUT R1
I1=THETA*100+102
Q=(1-PEEK)*1000+30:MOVE I1,Q:WRPIX
NEXT I
RETURN
```

LAWRENCE BERKELEY LABORATORY
TECHNICAL INFORMATION DEPARTMENT
UNIVERSITY OF CALIFORNIA
BERKELEY, CALIFORNIA 94720